ChemRxiv™

doi.org/10.26434/chemrxiv.11605698.v2

Bond-Length Distributions for Ions Bonded to Oxygen: Results for the Transition Metals and Quantification of the Factors Underlying Bond-Length Variation in Inorganic Solids

Olivier Charles Gagné, Frank Christopher Hawthorne

Submitted date: 20/02/2020 • Posted date: 20/02/2020

Licence: CC BY-NC-ND 4.0

Citation information: Gagné, Olivier Charles; Hawthorne, Frank Christopher (2020): Bond-Length Distributions for Ions Bonded to Oxygen: Results for the Transition Metals and Quantification of the Factors Underlying Bond-Length Variation in Inorganic Solids. ChemRxiv. Preprint.
https://doi.org/10.26434/chemrxiv.11605698.v2

Bond-length distributions are examined for 63 transition-metal ions bonded to O2- in 147 configurations, for 7522 coordination polyhedra and 41,488 bond distances, providing baseline statistical knowledge of bond lengths for transi-tion metals bonded to O2-. A priori bond valences are calculated for 140 crystal structures containing 266 coordination poly-hedra for 85 transition-metal ion configurations with anomalous bond-length distributions. Two new indices, Δ□□□□□ and Δ□□□□□, are proposed to quantify bond-length variation arising from bond-topological and crystallographic effects in extended solids. Bond-topological mechanisms of bond-length variation are [1] non-local bond-topological asymmetry, and [2] multi-ple-bond formation; crystallographic mechanisms are [3] electronic effects (with inherent focus on coupled electronic-vibra-tional degeneracy in this work), and [4] crystal-structure effects. The Δ□□□□□ and Δ□□□□□ indices allow one to determine the primary cause(s) of bond-length variation for individual coordination polyhedra and ion configurations, quantify the dis-torting power of cations via electronic effects (by subtracting the bond-topological contribution to bond-length variation), set expectation limits regarding the extent to which functional properties linked to bond-length variations may be optimized in a given crystal structure (and inform how optimization may be achieved), and more. We find the observation of multiple bonds to be primarily driven by the bond-topological requirements of crystal structures in solids. However, we sometimes observe multiple bonds to form as a result of electronic effects (e.g. the pseudo Jahn-Teller effect); resolution of the origins of multiple-bond formation follows calculation of the Δ□□□□□ and Δ□□□□□ indices on a structure-by-structure basis. Non-local bond-topological asymmetry is the most common cause of bond-length variation in transition-metal oxides and oxysalts, followed closely by the pseudo Jahn-Teller effect (PJTE). Non-local bond-topological asymmetry is further suggested to be the most widespread cause of bond-length variation in the solid state, with no a priori limitations with regard to ion identity. Overall, bond-length variations resulting from the PJTE are slightly larger than those resulting from non-local bond-topological asym-metry, comparable to those resulting from the strong JTE, and less than those induced by π-bond formation. From a compar-ison of a priori and observed bond valences for ~150 coordination polyhedra in which the strong JTE

or the PJTE is the main reason underlying bond-length variation, the Jahn-Teller effect is found not to have a symbiotic relation with the bond-topo-logical requirements of crystal structures. The magnitude of bond-length variations caused by the PJTE decreases in the fol-lowing order for octahedrally coordinated d0 transition metals oxyanions: Os8+ > Mo6+ > W6+ >> V5+ > Nb5+ > Ti4+ > Ta5+ > Hf4+ > Zr4+ > Re7+ >> Y3+ > Sc3+. Such ranking varies by coordination number; for [4], it is Re7+ > Ti4+ > V5+ > W6+ > Mo6+ > Cr6+ > Os8+ >> Mn7+; for [5], it is Os8+ > Re7+ > Mo6+ > Ti4+ > W6+ > V5+ > Nb5+. We conclude that non-octahedral coordinations of d0 ion configurations are likely to occur with bond-length variations that are similar in magnitude to their octahedral counterparts. However, smaller bond-length variations are expected from the PJTE for non-d0 transition-metal oxyanions.

File list (2)

Transition metals for ACS_OCG-FCH - Supporting.pdf (7.57 MiB)	view on ChemRxiv • download file
Transition metals for ACS_OCG-FCH.pdf (3.84 MiB)	view on ChemRxiv • download file

SUPPORTING INFORMATION FOR "BOND-LENGTH DISTRIBUTIONS FOR IONS BONDED TO OXYGEN: RESULTS FOR THE TRANSITION METALS AND QUANTIFICATION OF THE FACTORS UNDERLYING BOND-LENGTH VARIATION IN INORGANIC SOLIDS"

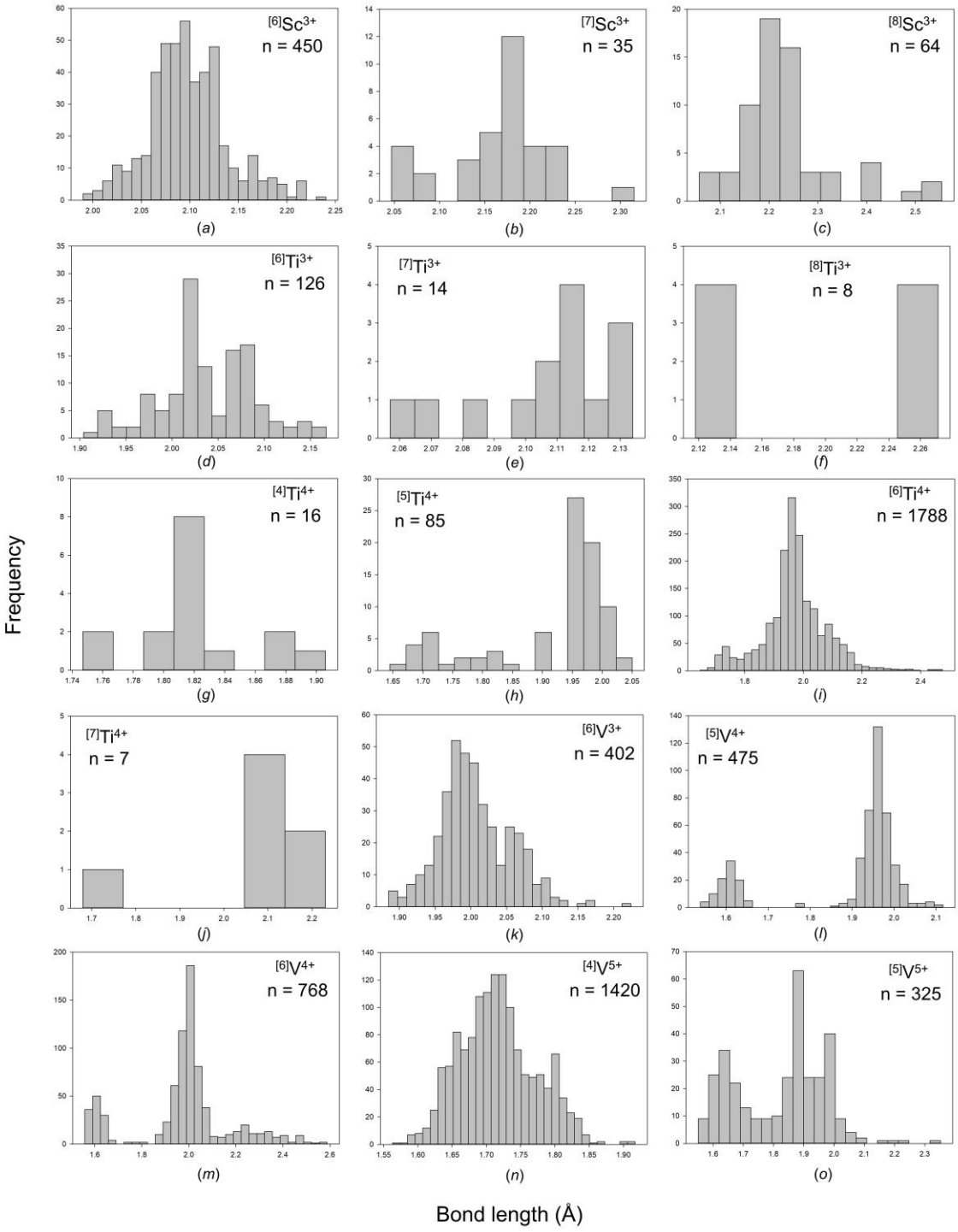
[6]Sc3+
n = 450
(a)
[7]Sc3+
n = 35
(b)
[8]Sc3+
n = 64
(c)
[6]Ti3+
n = 126
(d)
[7]Ti3+
n = 14
(e)
[8]Ti3+
n = 8
(f)
[4]Ti4+
n = 16
(g)
[5]Ti4+
n = 85
(h)
[6]Ti4+
n = 1788
(i)
[7]Ti4+
n = 7
(j)
[6]V3+
n = 402
(k)
[5]V4+
n = 475
(l)
[6]V4+
n = 768
(m)
[4]V5+
n = 1420
(n)
[5]V5+
n = 325
(o)
Frequency
Bond length (Å)

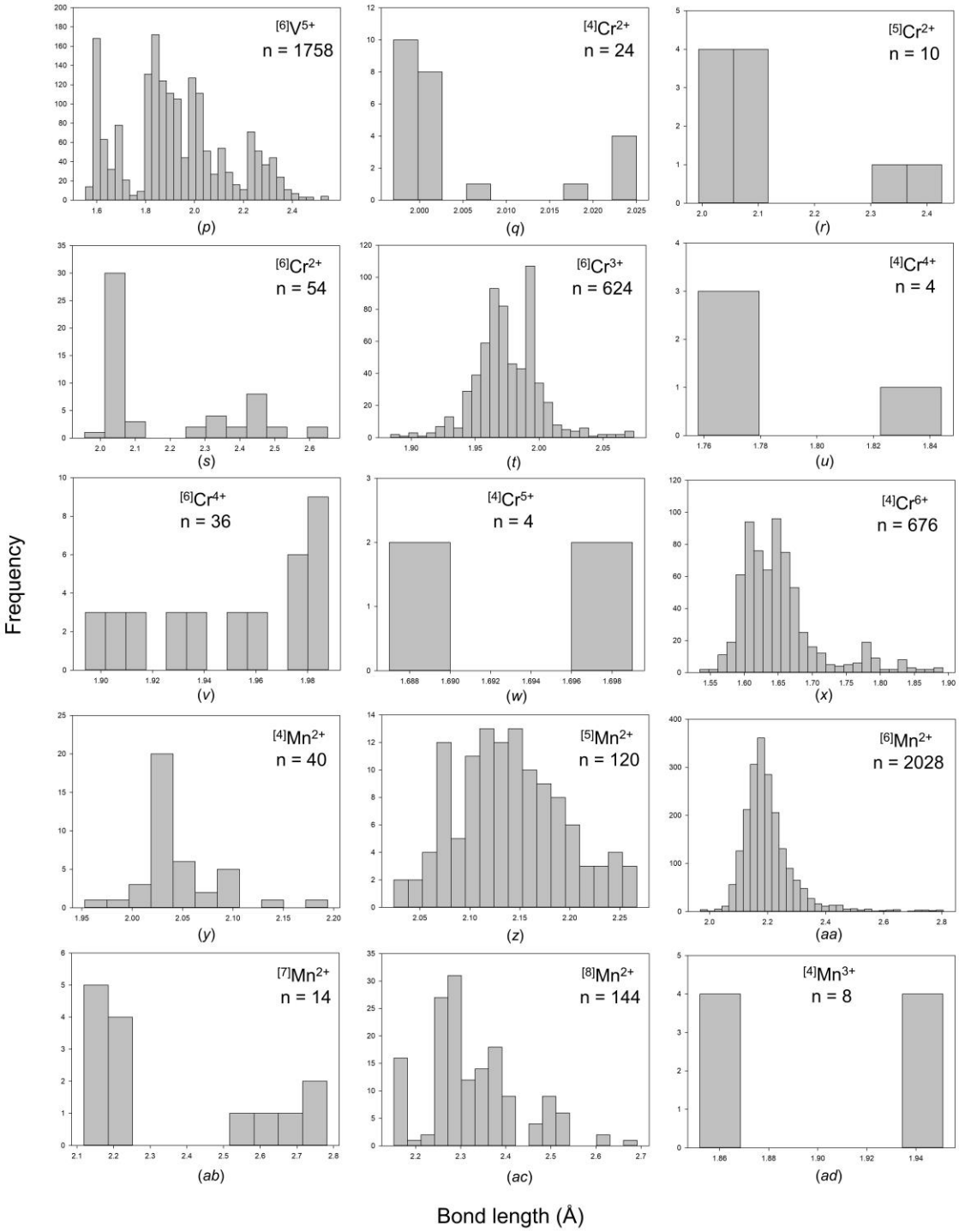
[6]V5+
n = 1758
(p)
[4]Cr2+
n = 24
(q)
[5]Cr2+
n = 10
(r)
[6]Cr2+
n = 54
(s)
[6]Cr3+
n = 624
(t)
[4]Cr4+
n = 4
(u)
[6]Cr4+
n = 36
(v)
[4]Cr5+
n = 4
(w)
[4]Cr6+
n = 676
(x)
[4]Mn2+
n = 40
(y)
[5]Mn2+
n = 120
(z)
[6]Mn2+
n = 2028
(aa)
[7]Mn2+
n = 14
(ab)
[8]Mn2+
n = 144
(ac)
[4]Mn3+
n = 8
(ad)
Frequency
Bond length (Å)

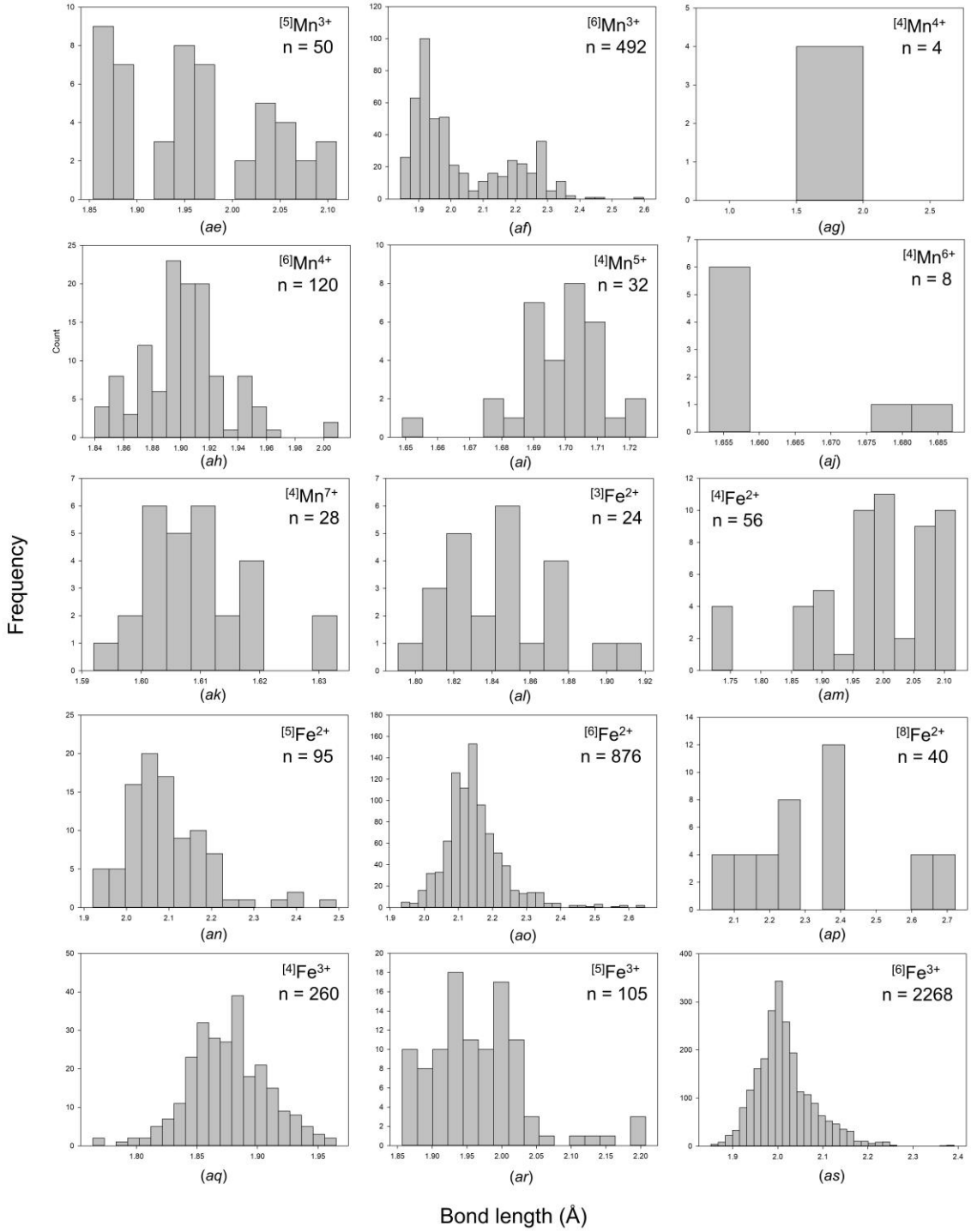
[5]Mn3+
n = 50
(ae)
[6]Mn3+
n = 492
(af)
[4]Mn4+
n = 4
(ag)
[6]Mn4+
n = 120
(ah)
[4]Mn5+
n = 32
(ai)
[4]Mn6+
n = 8
(aj)
[4]Mn7+
n = 28
(ak)
[3]Fe2+
n = 24
(al)
[4]Fe2+
n = 56
(am)
[5]Fe2+
n = 95
(an)
[6]Fe2+
n = 876
(ao)
[8]Fe2+
n = 40
(ap)
[4]Fe3+
n = 260
(aq)
[5]Fe3+
n = 105
(ar)
[6]Fe3+
n = 2268
(as)
Count
Frequency
Bond length (Å)

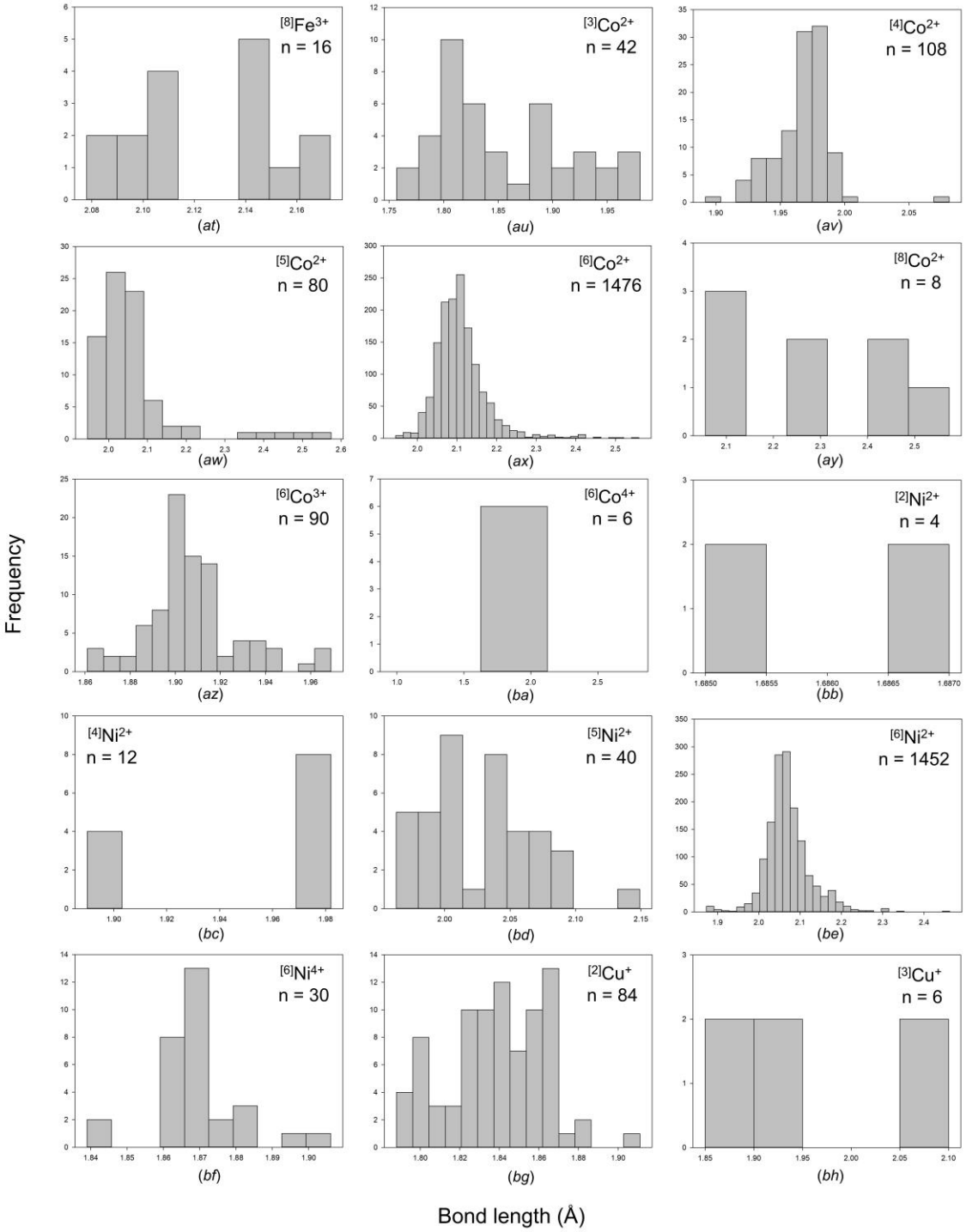
Frequency
[8]Fe3+
n = 16
(at)
[3]Co2+
n = 42
(au)
[4]Co2+
n = 108
(av)
[5]Co2+
n = 80
(aw)
[6]Co2+
n = 1476
(ax)
[8]Co2+
n = 8
(ay)
[6]Co3+
n = 90
(az)
[6]Co4+
n = 6
(ba)
[2]Ni2+
n = 4
(bb)
[4]Ni2+
n = 12
(bc)
[5]Ni2+
n = 40
(bd)
[6]Ni2+
n = 1452
(be)
[6]Ni4+
n = 30
(bf)
[2]Cu+
n = 84
(bg)
[3]Cu+
n = 6
(bh)
Bond length (Å)

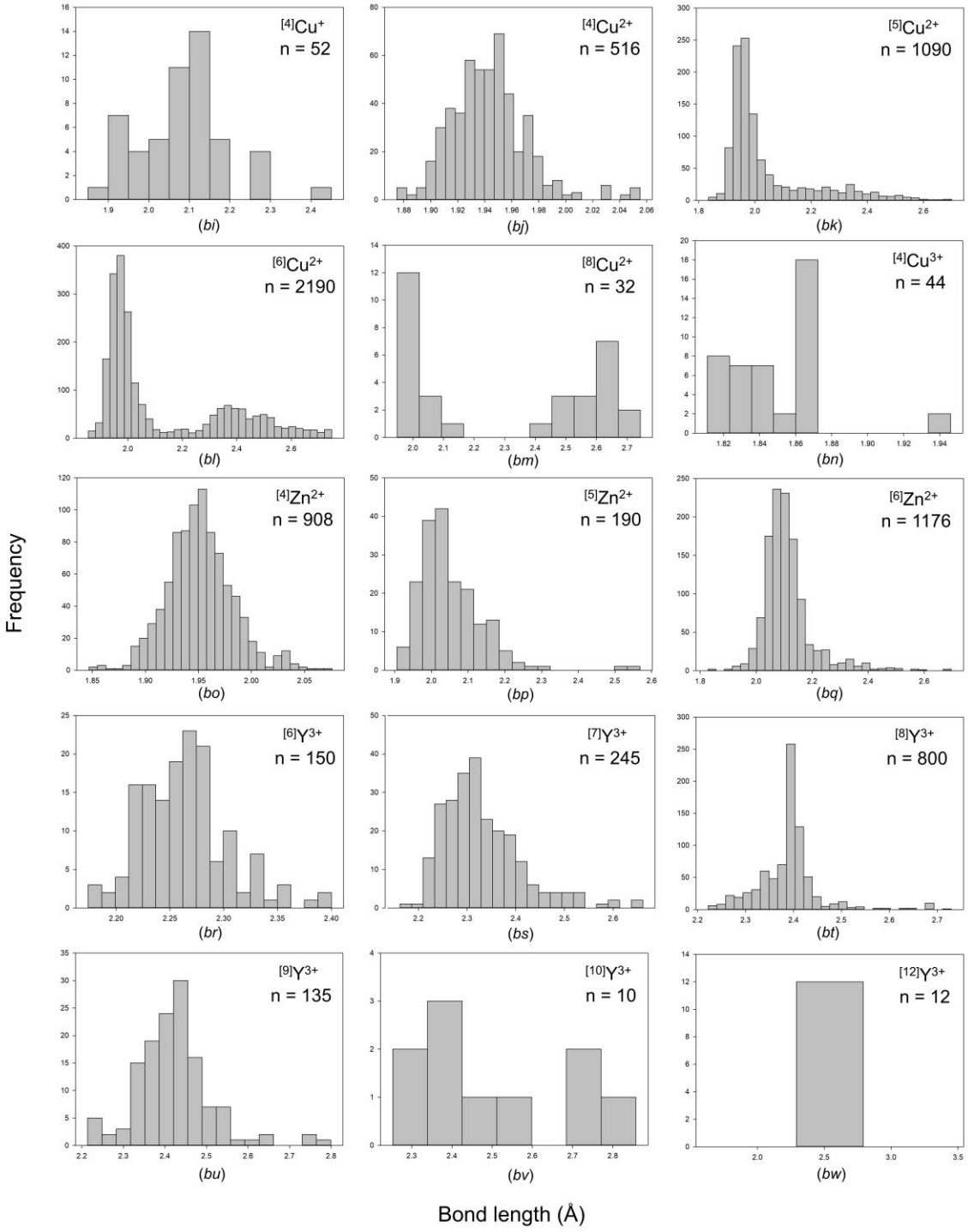
[4]Cu+
n = 52
(bi)
[4]Cu2+
n = 516
(bj)
[5]Cu2+
n = 1090
(bk)
[6]Cu2+
n = 2190
(bl)
[8]Cu2+
n = 32
(bm)
[4]Cu3+
n = 44
(bn)
[4]Zn2+
n = 908
(bo)
[5]Zn2+
n = 190
(bp)
[6]Zn2+
n = 1176
(bq)
[6]Y3+
n = 150
(br)
[7]Y3+
n = 245
(bs)
[8]Y3+
n = 800
(bt)
[9]Y3+
n = 135
(bu)
[10]Y3+
n = 10
(bv)
[12]Y3+
n = 12
(bw)
Frequency
Bond length (Å)

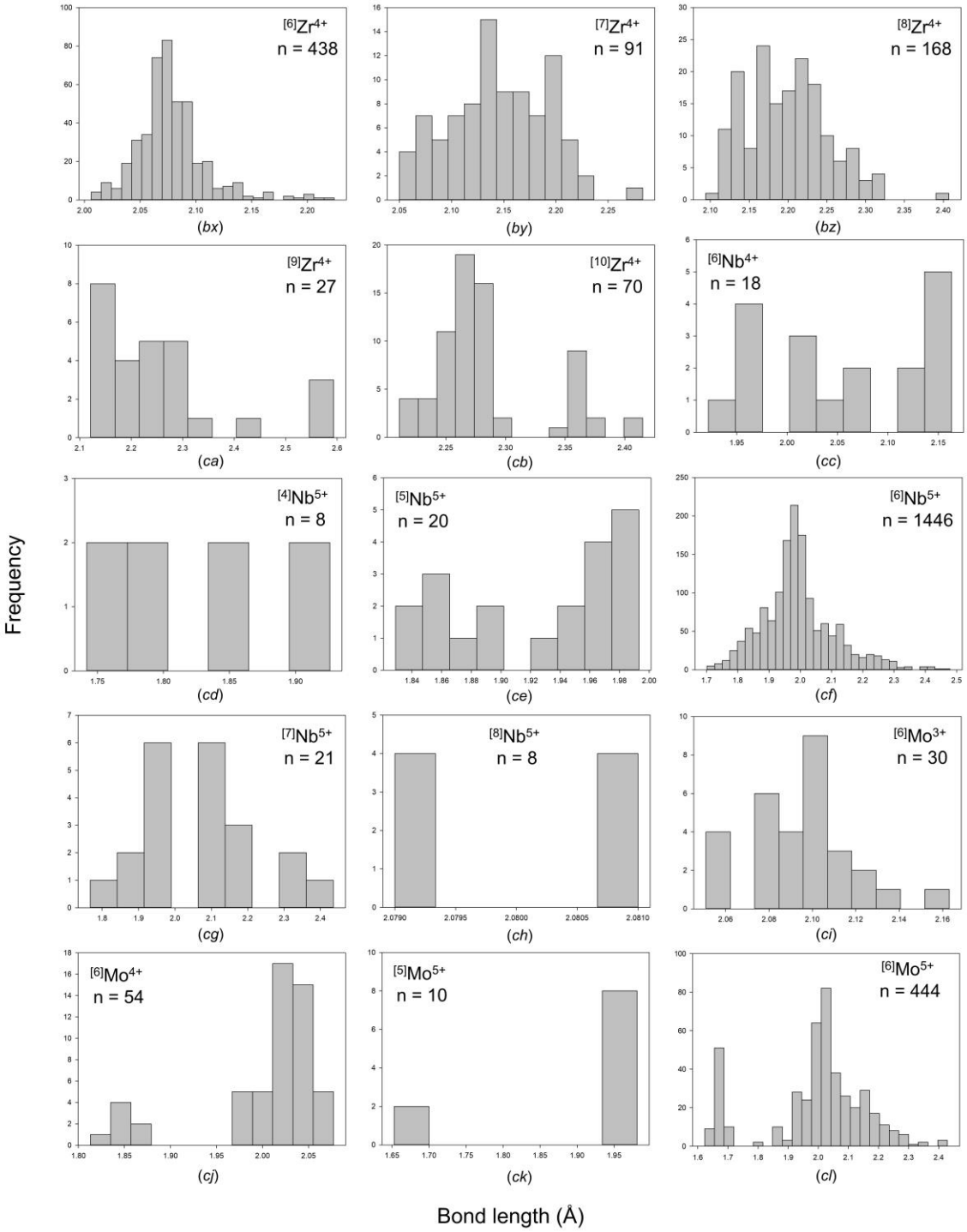
[6]Zr4+
n = 438
(bx)
[7]Zr4+
n = 91
(by)
[8]Zr4+
n = 168
(bz)
[9]Zr4+
n = 27
(ca)
[10]Zr4+
n = 70
(cb)
[6]Nb4+
n = 18
(cc)
[4]Nb5+
n = 8
(cd)
[5]Nb5+
n = 20
(ce)
[6]Nb5+
n = 1446
(cf)
[7]Nb5+
n = 21
(cg)
[8]Nb5+
n = 8
(ch)
[6]Mo3+
n = 30
(ci)
[6]Mo4+
n = 54
(cj)
[5]Mo5+
n = 10
(ck)
[6]Mo5+
n = 444
(cl)
Frequency
Bond length (Å)

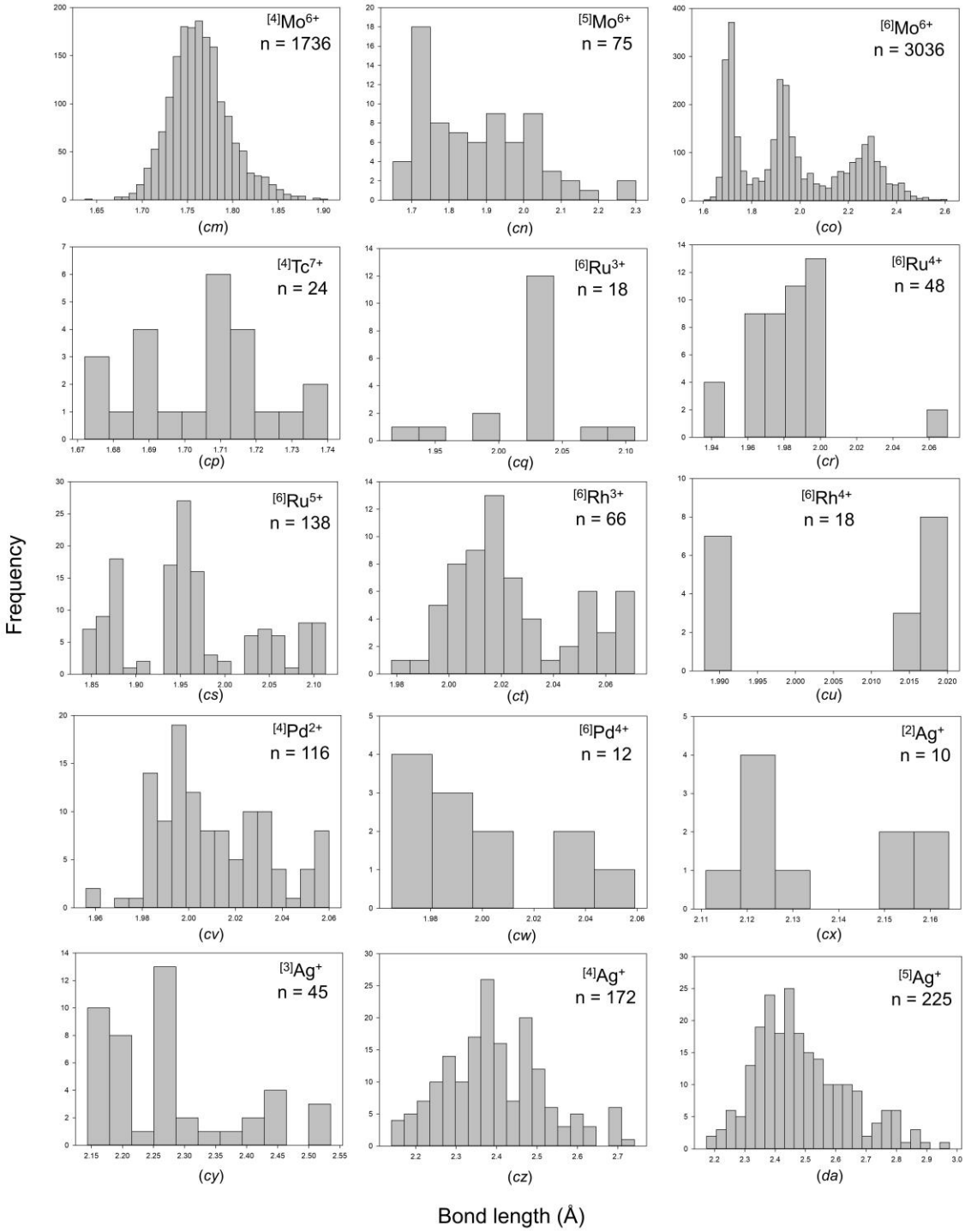
[4]Mo6+
n = 1736
(cm)
[5]Mo6+
n = 75
(cn)
[6]Mo6+
n = 3036
(co)
[4]Tc7+
n = 24
(cp)
[6]Ru3+
n = 18
(cq)
[6]Ru4+
n = 48
(cr)
[6]Ru5+
n = 138
(cs)
[6]Rh3+
n = 66
(ct)
[6]Rh4+
n = 18
(cu)
[4]Pd2+
n = 116
(cv)
[6]Pd4+
n = 12
(cw)
[2]Ag+
n = 10
(cx)
[3]Ag+
n = 45
(cy)
[4]Ag+
n = 172
(cz)
[5]Ag+
n = 225
(da)
Frequency
Bond length (Å)

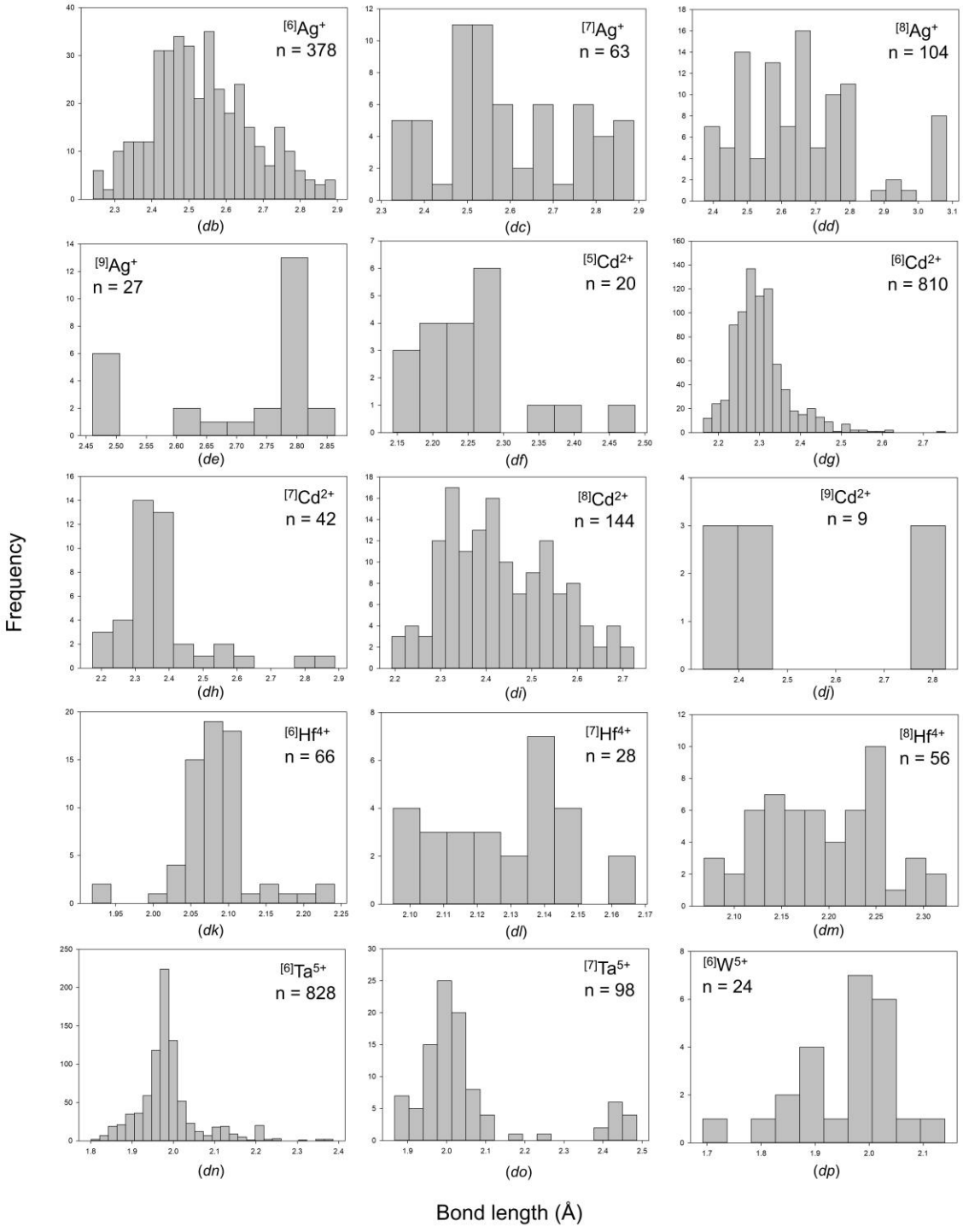
Frequency
[6]Ag+
n = 378
(db)
[7]Ag+
n = 63
(dc)
[8]Ag+
n = 104
(dd)
[9]Ag+
n = 27
(de)
[5]Cd2+
n = 20
(df)
[6]Cd2+
n = 810
(dg)
[7]Cd2+
n = 42
(dh)
[8]Cd2+
n = 144
(di)
[9]Cd2+
n = 9
(dj)
[6]Hf4+
n = 66
(dk)
[7]Hf4+
n = 28
(dl)
[8]Hf4+
n = 56
(dm)
[6]Ta5+
n = 828
(dn)
[7]Ta5+
n = 98
(do)
[6]W5+
n = 24
(dp)
Bond length (Å)

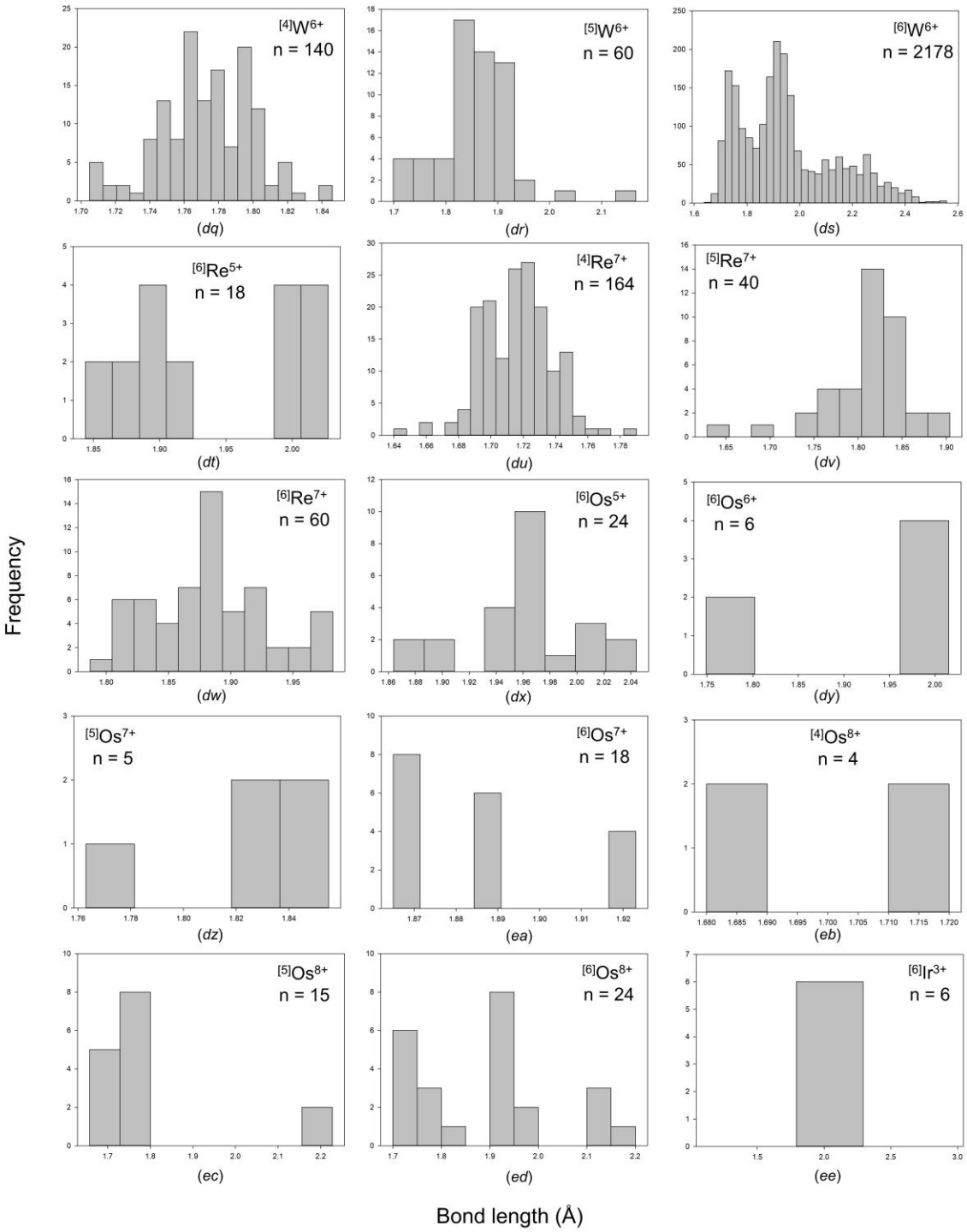
[4]W6+
n = 140
(dq)
[5]W6+
n = 60
(dr)
[6]W6+
n = 2178
(ds)
[6]Re5+
n = 18
(dt)
[4]Re7+
n = 164
(du)
[5]Re7+
n = 40
(dv)
[6]Re7+
n = 60
(dw)
[6]Os5+
n = 24
(dx)
[6]Os6+
n = 6
(dy)
[5]Os7+
n = 5
(dz)
[6]Os7+
n = 18
(ea)
[4]Os8+
n = 4
(eb)
[5]Os8+
n = 15
(ec)
[6]Os8+
n = 24
(ed)
[6]Ir3+
n = 6
(ee)
Frequency
Bond length (Å)

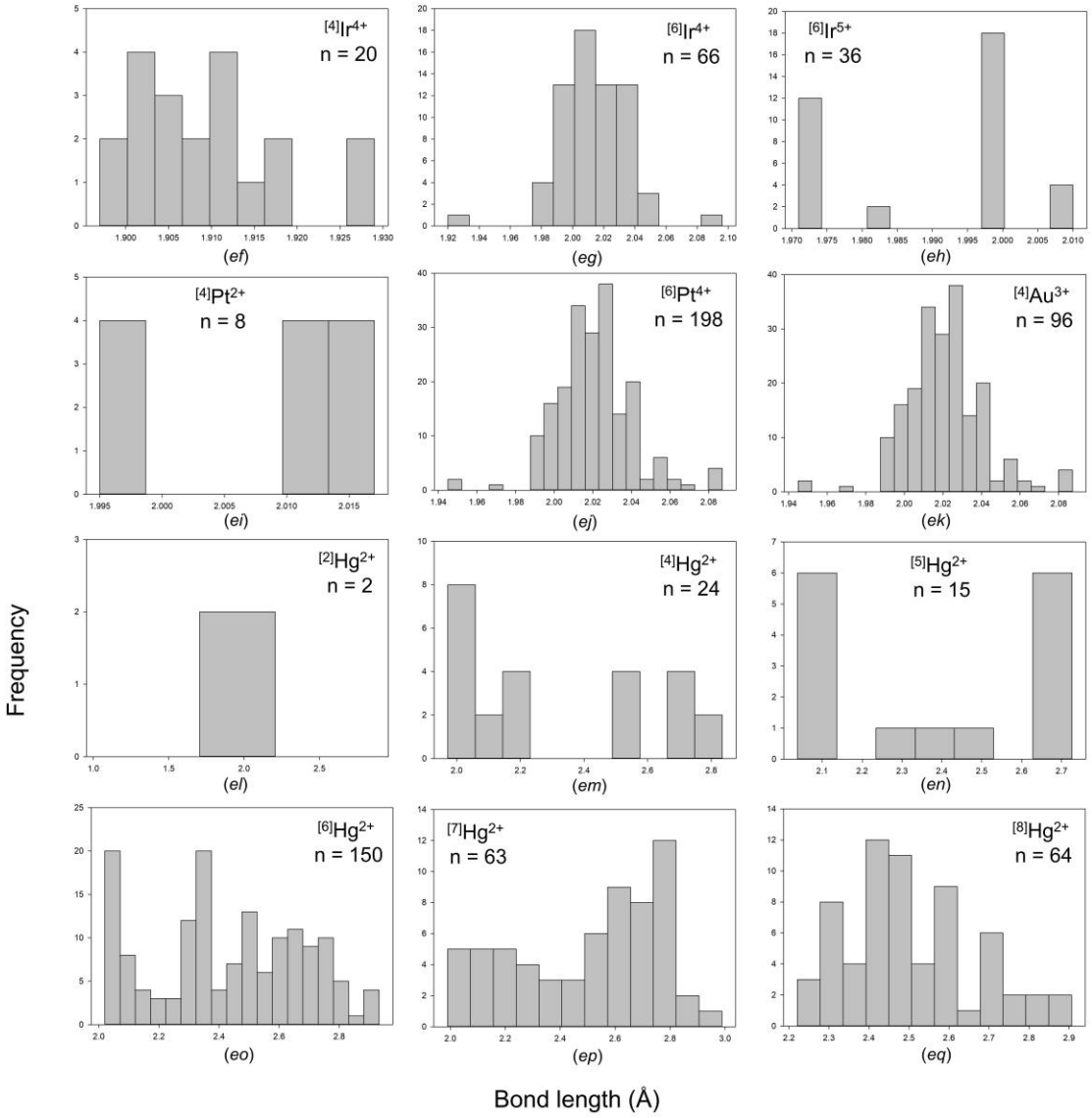

Figure S1: Bond-length distributions for all configurations of the transition metal ions bonded to O^{2-}: (*a*) $^{[6]}Sc^{3+}$, (*b*) $^{[7]}Sc^{3+}$, (*c*) $^{[8]}Sc^{3+}$, (*d*) $^{[6]}Ti^{3+}$, (*e*) $^{[7]}Ti^{3+}$, (*f*) $^{[8]}Ti^{3+}$, (*g*) $^{[4]}Ti^{4+}$, (*h*) $^{[5]}Ti^{4+}$, (*i*) $^{[6]}Ti^{4+}$, (*j*) $^{[7]}Ti^{4+}$, (*k*) $^{[6]}V^{3+}$, (*l*) $^{[5]}V^{4+}$, (*m*) $^{[6]}V^{4+}$, (*n*) $^{[4]}V^{5+}$, (*o*) $^{[5]}V^{5+}$, (*p*) $^{[6]}V^{5+}$, (*q*) $^{[4]}Cr^{2+}$, (*r*) $^{[5]}Cr^{2+}$, (*s*) $^{[6]}Cr^{2+}$, (*t*) $^{[6]}Cr^{3+}$, (*u*) $^{[4]}Cr^{4+}$, (*v*) $^{[6]}Cr^{4+}$, (*w*) $^{[4]}Cr^{5+}$, (*x*) $^{[4]}Cr^{6+}$, (*y*) $^{[4]}Mn^{2+}$, (*z*) $^{[5]}Mn^{2+}$, (*aa*) $^{[6]}Mn^{2+}$, (*ab*) $^{[7]}Mn^{2+}$, (*ac*) $^{[8]}Mn^{2+}$, (*ad*) $^{[4]}Mn^{3+}$, (*ae*) $^{[5]}Mn^{3+}$, (*af*) $^{[6]}Mn^{3+}$, (*ag*) $^{[4]}Mn^{4+}$, (*ah*) $^{[6]}Mn^{4+}$, (*ai*) $^{[4]}Mn^{5+}$, (*aj*) $^{[4]}Mn^{6+}$, (*ak*) $^{[4]}Mn^{7+}$, (*al*) $^{[3]}Fe^{2+}$, (*am*) $^{[4]}Fe^{2+}$, (*an*) $^{[5]}Fe^{2+}$, (*ao*) $^{[6]}Fe^{2+}$, (*ap*) $^{[8]}Fe^{2+}$, (*aq*) $^{[4]}Fe^{3+}$, (*ar*) $^{[5]}Fe^{3+}$, (*as*) $^{[6]}Fe^{3+}$, (*at*) $^{[8]}Fe^{3+}$, (*au*) $^{[3]}Co^{2+}$, (*av*) $^{[4]}Co^{2+}$, (*aw*) $^{[5]}Co^{2+}$, (*ax*) $^{[6]}Co^{2+}$, (*ay*) $^{[8]}Co^{2+}$, (*az*) $^{[6]}Co^{3+}$, (*ba*) $^{[6]}Co^{4+}$, (*bb*) $^{[2]}Ni^{2+}$, (*bc*) $^{[4]}Ni^{2+}$, (*bd*) $^{[5]}Ni^{2+}$, (*be*) $^{[6]}Ni^{2+}$, (*bf*) $^{[6]}Ni^{4+}$, (*bg*) $^{[2]}Cu^{+}$, (*bh*) $^{[3]}Cu^{+}$, (*bi*) $^{[4]}Cu^{+}$, (*bj*) $^{[4]}Cu^{2+}$, (*bk*) $^{[5]}Cu^{2+}$, (*bl*) $^{[6]}Cu^{2+}$, (*bm*) $^{[8]}Cu^{2+}$, (*bn*) $^{[4]}Cu^{3+}$, (*bo*) $^{[4]}Zn^{2+}$, (*bp*) $^{[5]}Zn^{2+}$, (*bq*) $^{[6]}Zn^{2+}$, (*br*) $^{[6]}Y^{3+}$, (*bs*) $^{[7]}Y^{3+}$, (*bt*) $^{[8]}Y^{3+}$, (*bu*) $^{[9]}Y^{3+}$, (*bv*) $^{[10]}Y^{3+}$, (*bw*) $^{[12]}Y^{3+}$, (*bx*) $^{[6]}Zr^{4+}$, (*by*) $^{[7]}Zr^{4+}$, (*bz*) $^{[8]}Zr^{4+}$, (*ca*) $^{[9]}Zr^{4+}$, (*cb*) $^{[10]}Zr^{4+}$, (*cc*) $^{[6]}Nb^{4+}$, (*cd*) $^{[4]}Nb^{5+}$, (*ce*) $^{[5]}Nb^{5+}$, (*cf*) $^{[6]}Nb^{5+}$, (*cg*) $^{[7]}Nb^{5+}$, (*ch*) $^{[8]}Nb^{5+}$, (*ci*) $^{[6]}Mo^{3+}$, (*cj*) $^{[6]}Mo^{4+}$, (*ck*) $^{[5]}Mo^{5+}$, (*cl*) $^{[6]}Mo^{5+}$, (*cm*) $^{[4]}Mo^{6+}$, (*cn*) $^{[5]}Mo^{6+}$, (*co*) $^{[6]}Mo^{6+}$, (*cp*) $^{[4]}Tc^{7+}$, (*cq*) $^{[6]}Ru^{3+}$, (*cr*) $^{[6]}Ru^{4+}$, (*cs*) $^{[6]}Ru^{5+}$, (*ct*) $^{[6]}Rh^{3+}$, (*cu*) $^{[6]}Rh^{4+}$, (*cv*) $^{[4]}Pd^{2+}$, (*cw*) $^{[6]}Pd^{4+}$, (*cx*) $^{[2]}Ag^{+}$, (*cy*) $^{[3]}Ag^{+}$, (*cz*) $^{[4]}Ag^{+}$, (*da*) $^{[5]}Ag^{+}$, (*db*) $^{[6]}Ag^{+}$, (*dc*) $^{[7]}Ag^{+}$, (*dd*) $^{[8]}Ag^{+}$, (*de*) $^{[9]}Ag^{+}$, (*df*) $^{[5]}Cd^{2+}$, (*dg*) $^{[6]}Cd^{2+}$, (*dh*) $^{[7]}Cd^{2+}$, (*di*) $^{[8]}Cd^{2+}$, (*dj*) $^{[9]}Cd^{2+}$, (*dk*) $^{[6]}Hf^{4+}$, (*dl*) $^{[7]}Hf^{4+}$, (*dm*) $^{[8]}Hf^{4+}$, (*dn*) $^{[6]}Ta^{5+}$, (*do*) $^{[7]}Ta^{5+}$, (*dp*) $^{[6]}W^{5+}$, (*dq*) $^{[4]}W^{6+}$, (*dr*) $^{[5]}W^{6+}$, (*ds*) $^{[6]}W^{6+}$, (*dt*) $^{[6]}Re^{5+}$, (*du*) $^{[4]}Re^{7+}$, (*dv*) $^{[5]}Re^{7+}$, (*dw*) $^{[6]}Re^{7+}$, (*dx*) $^{[6]}Os^{5+}$, (*dy*) $^{[6]}Os^{6+}$, (*dz*) $^{[5]}Os^{7+}$, (*ea*) $^{[6]}Os^{7+}$, (*eb*) $^{[4]}Os^{8+}$, (*ec*) $^{[5]}Os^{8+}$, (*ed*) $^{[6]}Os^{8+}$, (*ee*) $^{[6]}Ir^{3+}$, (*ef*) $^{[4]}Ir^{4+}$, (*eg*) $^{[6]}Ir^{4+}$, (*eh*) $^{[6]}Ir^{5+}$, (*ei*) $^{[4]}Pt^{2+}$, (*ej*) $^{[6]}Pt^{4+}$, (*ek*) $^{[4]}Au^{3+}$, (*el*) $^{[2]}Hg^{2+}$, (*em*) $^{[4]}Hg^{2+}$, (*en*) $^{[5]}Hg^{2+}$, (*eo*) $^{[6]}Hg^{2+}$, (*ep*) $^{[7]}Hg^{2+}$, (*eq*) $^{[8]}Hg^{2+}$.

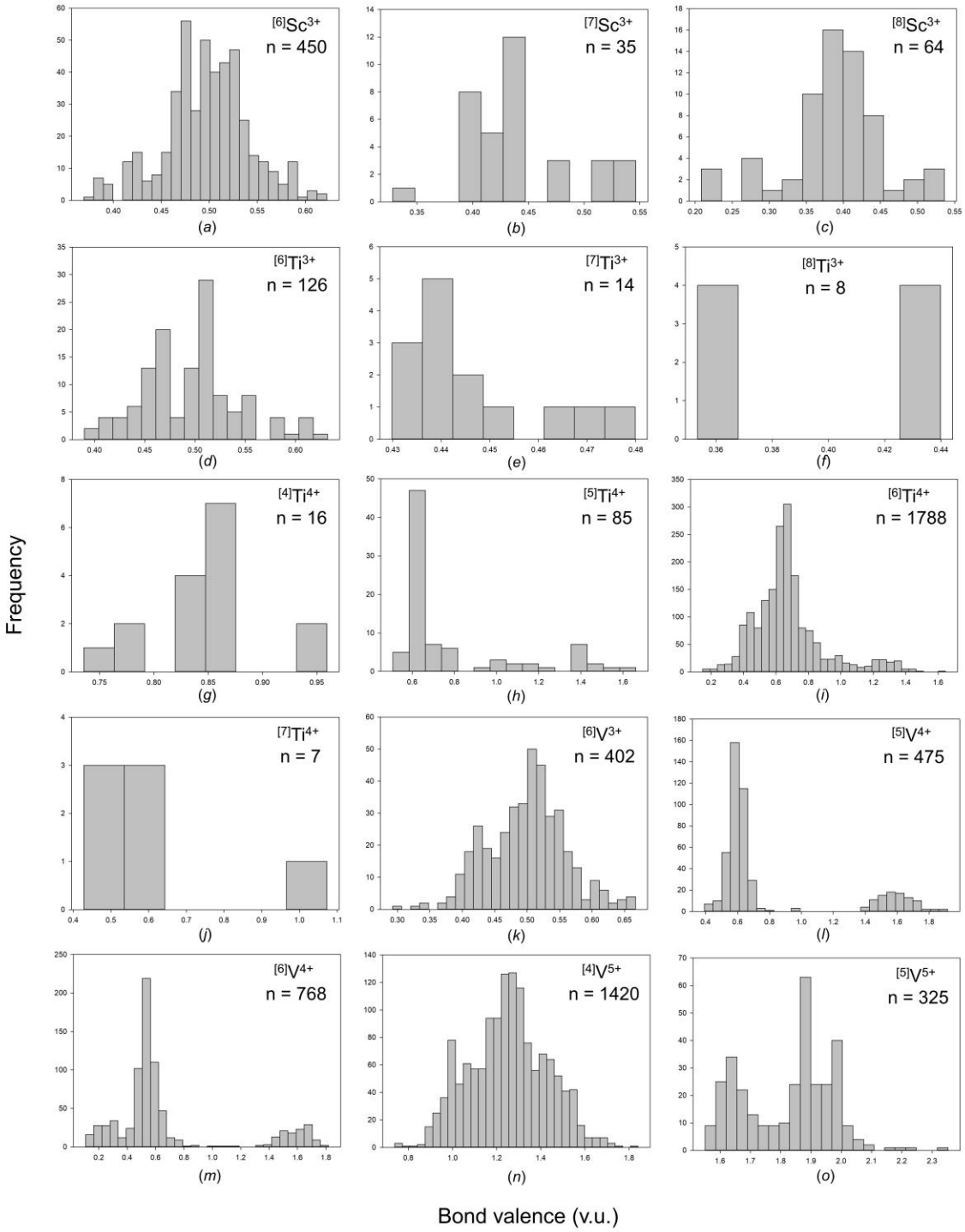
[6]Sc3+
n = 450
(a)
[7]Sc3+
n = 35
(b)
[8]Sc3+
n = 64
(c)
[6]Ti3+
n = 126
(d)
[7]Ti3+
n = 14
(e)
[8]Ti3+
n = 8
(f)
[4]Ti4+
n = 16
(g)
[5]Ti4+
n = 85
(h)
[6]Ti4+
n = 1788
(i)
[7]Ti4+
n = 7
(j)
[6]V3+
n = 402
(k)
[5]V4+
n = 475
(l)
[6]V4+
n = 768
(m)
[4]V5+
n = 1420
(n)
[5]V5+
n = 325
(o)
Frequency
Bond valence (v.u.)

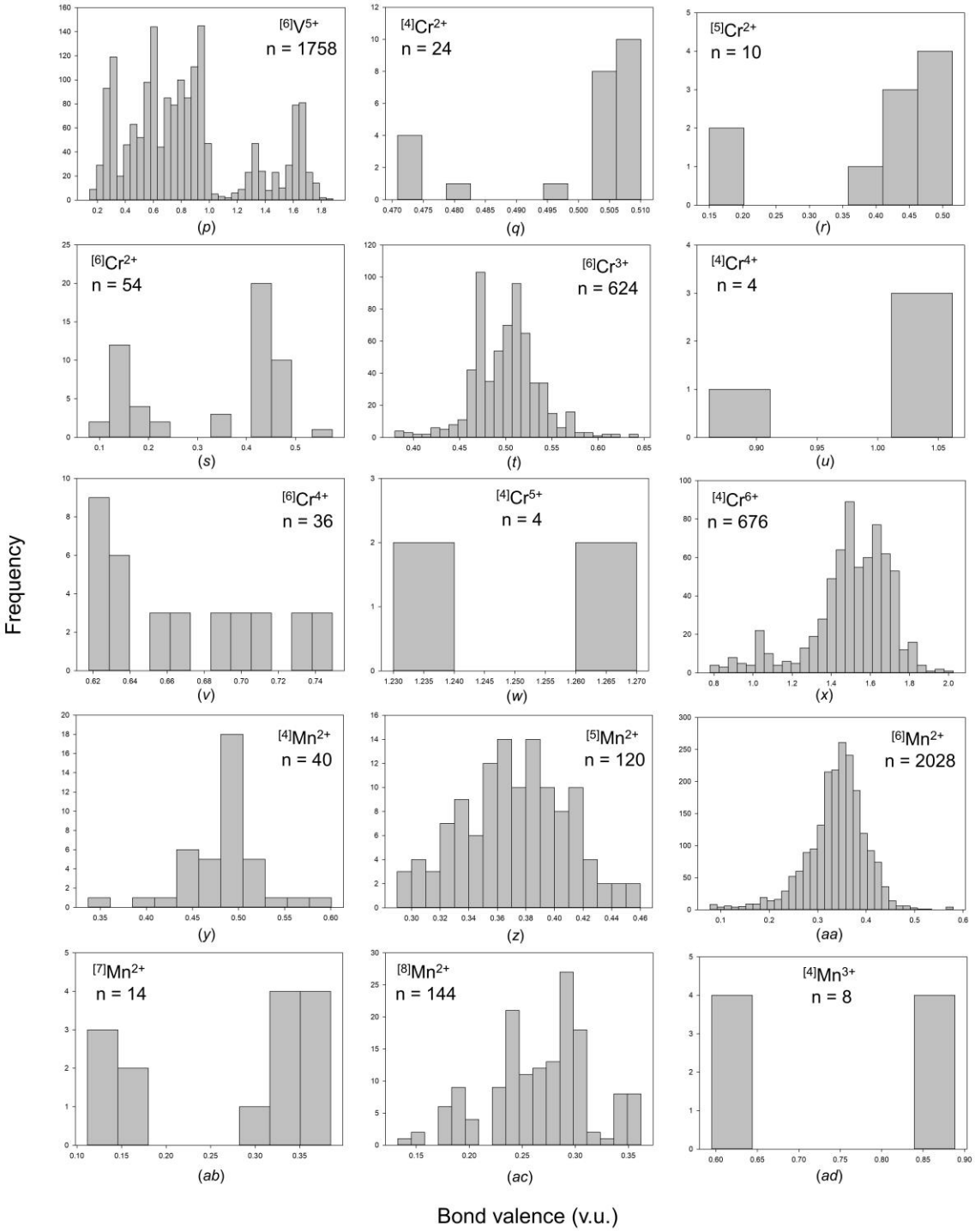
[6]V5+
n = 1758
(p)
[4]Cr2+
n = 24
(q)
[5]Cr2+
n = 10
(r)
[6]Cr2+
n = 54
(s)
[6]Cr3+
n = 624
(t)
[4]Cr4+
n = 4
(u)
[6]Cr4+
n = 36
(v)
[4]Cr5+
n = 4
(w)
[4]Cr6+
n = 676
(x)
[4]Mn2+
n = 40
(y)
[5]Mn2+
n = 120
(z)
[6]Mn2+
n = 2028
(aa)
[7]Mn2+
n = 14
(ab)
[8]Mn2+
n = 144
(ac)
[4]Mn3+
n = 8
(ad)
Frequency
Bond valence (v.u.)

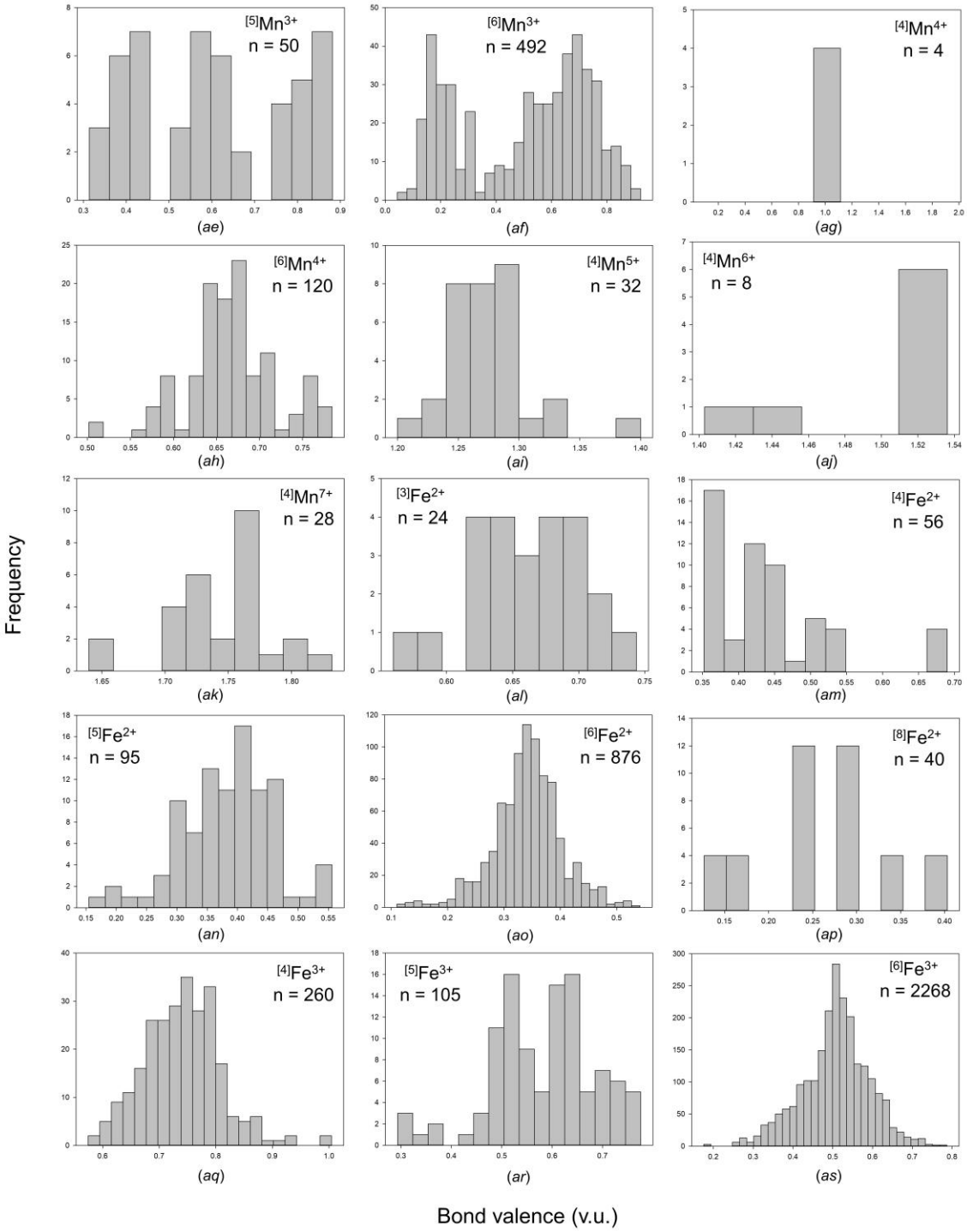
[5]Mn3+
n = 50
(ae)
[6]Mn3+
n = 492
(af)
[4]Mn4+
n = 4
(ag)
[6]Mn4+
n = 120
(ah)
[4]Mn5+
n = 32
(ai)
[4]Mn6+
n = 8
(aj)
[4]Mn7+
n = 28
(ak)
[3]Fe2+
n = 24
(al)
[4]Fe2+
n = 56
(am)
[5]Fe2+
n = 95
(an)
[6]Fe2+
n = 876
(ao)
[8]Fe2+
n = 40
(ap)
[4]Fe3+
n = 260
(aq)
[5]Fe3+
n = 105
(ar)
[6]Fe3+
n = 2268
(as)
Frequency
Bond valence (v.u.)

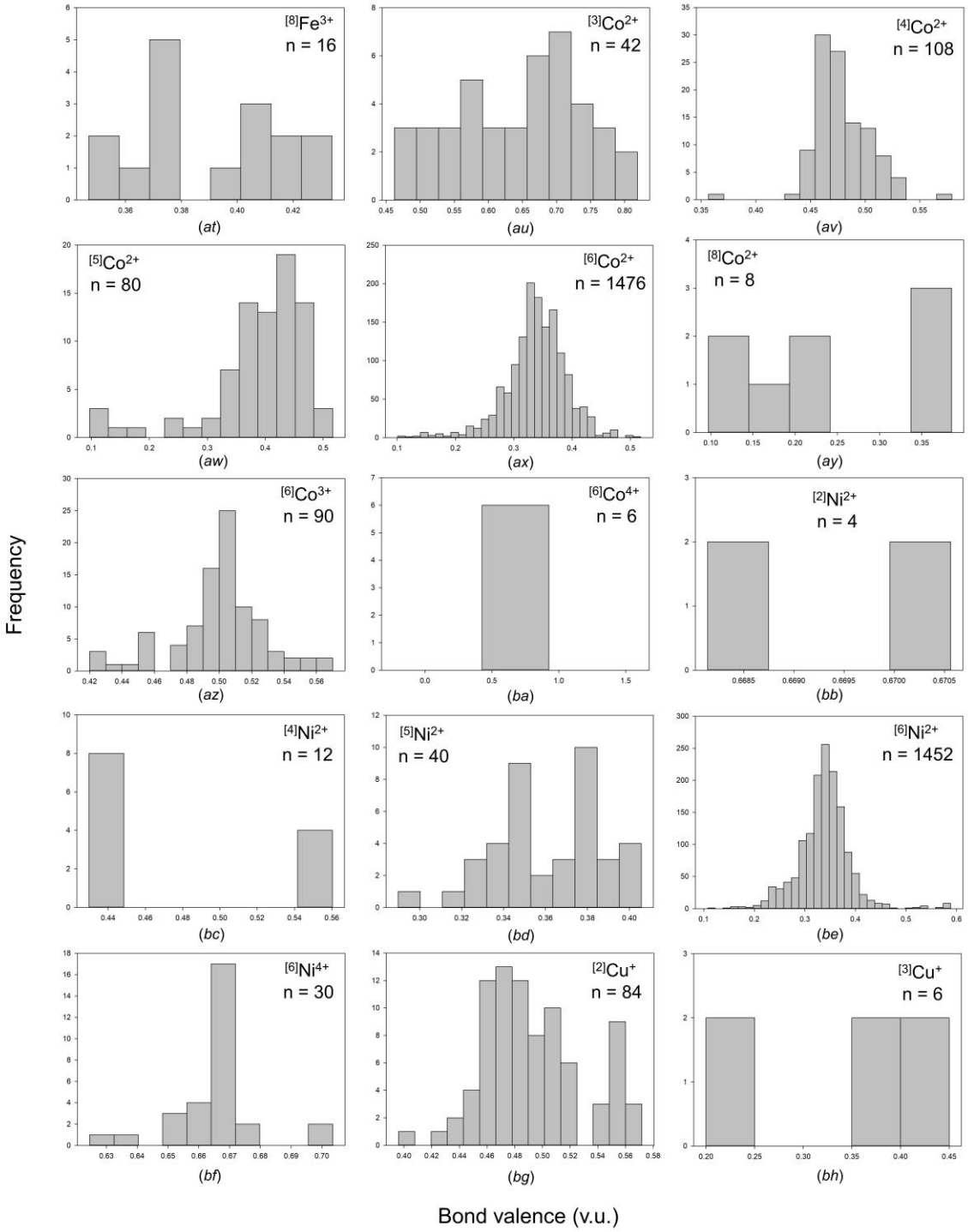
Frequency
[8]Fe3+
n = 16
(at)
[3]Co2+
n = 42
(au)
[4]Co2+
n = 108
(av)
[5]Co2+
n = 80
(aw)
[6]Co2+
n = 1476
(ax)
[8]Co2+
n = 8
(ay)
[6]Co3+
n = 90
(az)
[6]Co4+
n = 6
(ba)
[2]Ni2+
n = 4
(bb)
[4]Ni2+
n = 12
(bc)
[5]Ni2+
n = 40
(bd)
[6]Ni2+
n = 1452
(be)
[6]Ni4+
n = 30
(bf)
[2]Cu+
n = 84
(bg)
[3]Cu+
n = 6
(bh)
Bond valence (v.u.)

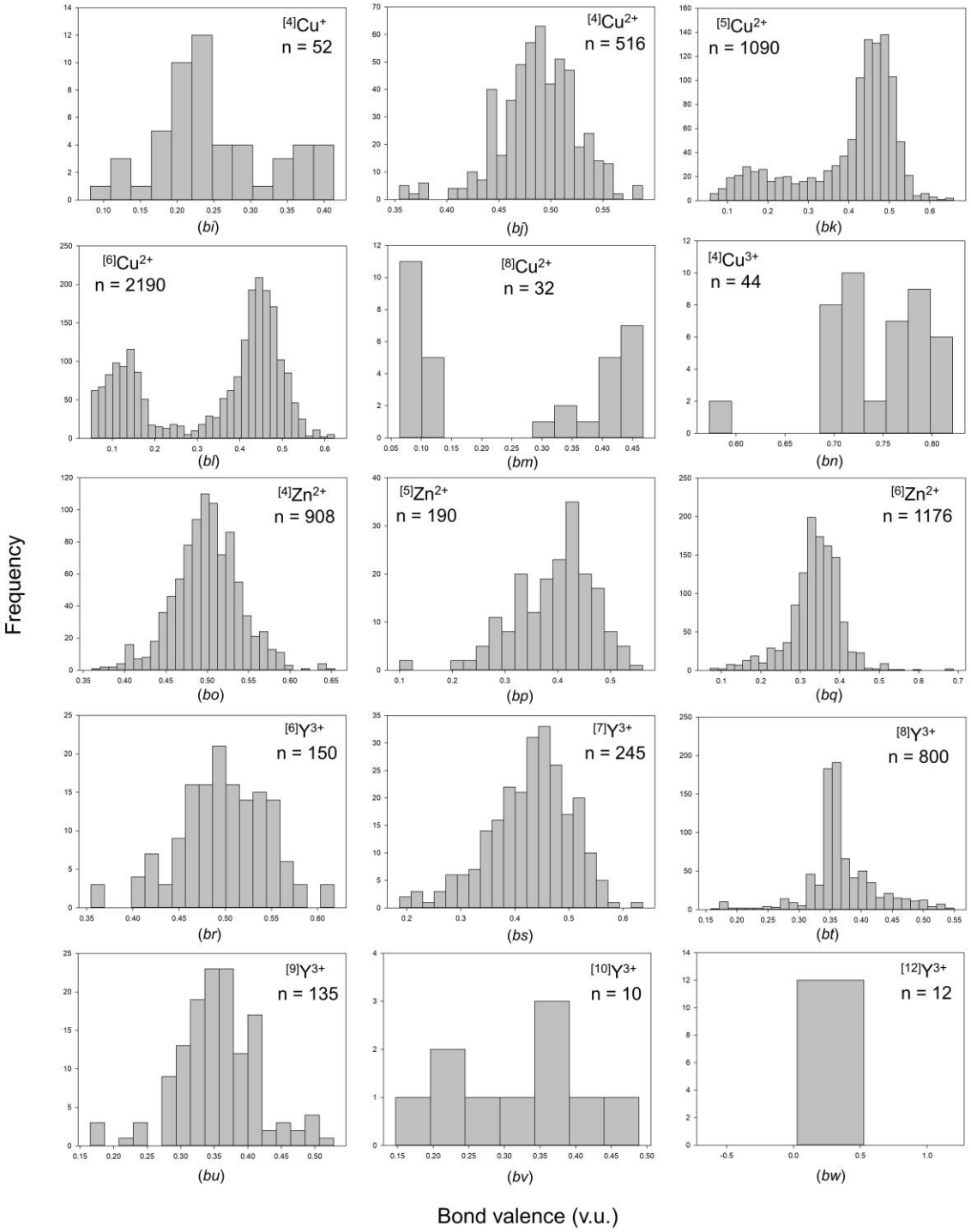
[4]Cu+
n = 52
(bi)
[4]Cu2+
n = 516
(bj)
[5]Cu2+
n = 1090
(bk)
[6]Cu2+
n = 2190
(bl)
[8]Cu2+
n = 32
(bm)
[4]Cu3+
n = 44
(bn)
[4]Zn2+
n = 908
(bo)
[5]Zn2+
n = 190
(bp)
[6]Zn2+
n = 1176
(bq)
[6]Y3+
n = 150
(br)
[7]Y3+
n = 245
(bs)
[8]Y3+
n = 800
(bt)
[9]Y3+
n = 135
(bu)
[10]Y3+
n = 10
(bv)
[12]Y3+
n = 12
(bw)
Frequency
Bond valence (v.u.)

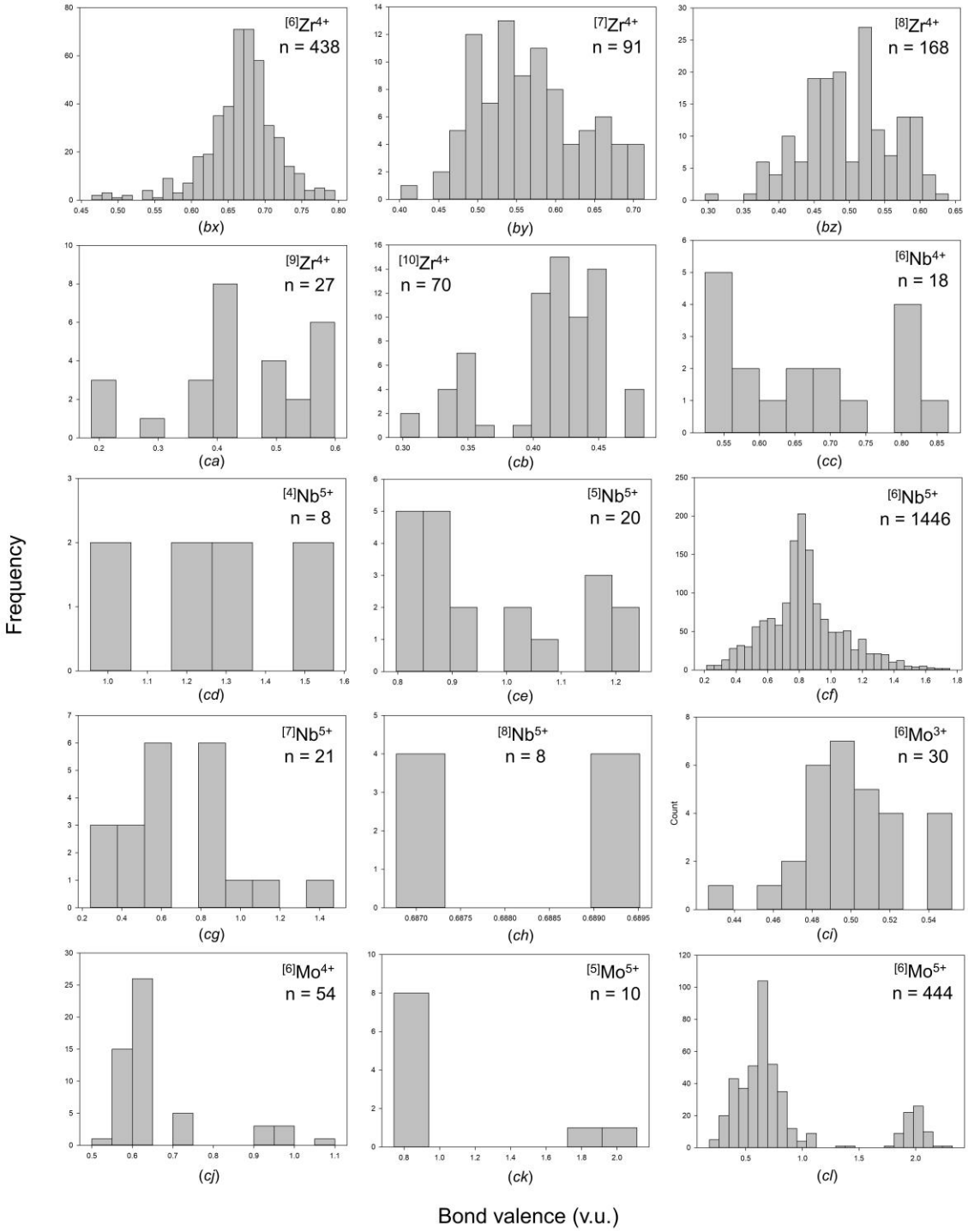
[6]Zr4+
n = 438
(bx)
[7]Zr4+
n = 91
(by)
[8]Zr4+
n = 168
(bz)
[9]Zr4+
n = 27
(ca)
[10]Zr4+
n = 70
(cb)
[6]Nb4+
n = 18
(cc)
[4]Nb5+
n = 8
(cd)
[5]Nb5+
n = 20
(ce)
[6]Nb5+
n = 1446
(cf)
[7]Nb5+
n = 21
(cg)
[8]Nb5+
n = 8
(ch)
[6]Mo3+
n = 30
(ci)
[6]Mo4+
n = 54
(cj)
[5]Mo5+
n = 10
(ck)
[6]Mo5+
n = 444
(cl)
Frequency
Count
Bond valence (v.u.)

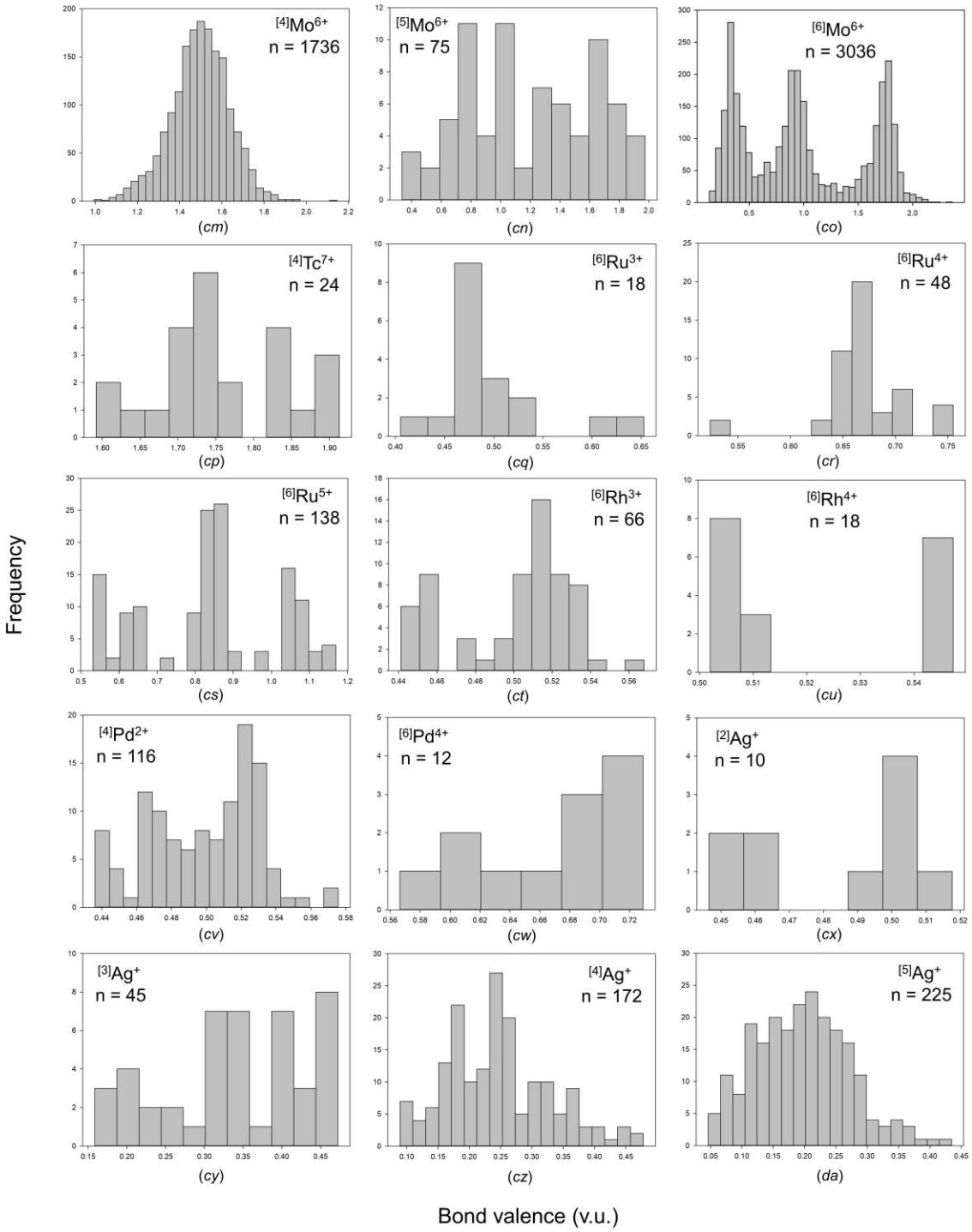
[4]Mo6+
n = 1736
(cm)
[5]Mo6+
n = 75
(cn)
[6]Mo6+
n = 3036
(co)
[4]Tc7+
n = 24
(cp)
[6]Ru3+
n = 18
(cq)
[6]Ru4+
n = 48
(cr)
[6]Ru5+
n = 138
(cs)
[6]Rh3+
n = 66
(ct)
[6]Rh4+
n = 18
(cu)
[4]Pd2+
n = 116
(cv)
[6]Pd4+
n = 12
(cw)
[2]Ag+
n = 10
(cx)
[3]Ag+
n = 45
(cy)
[4]Ag+
n = 172
(cz)
[5]Ag+
n = 225
(da)
Frequency
Bond valence (v.u.)

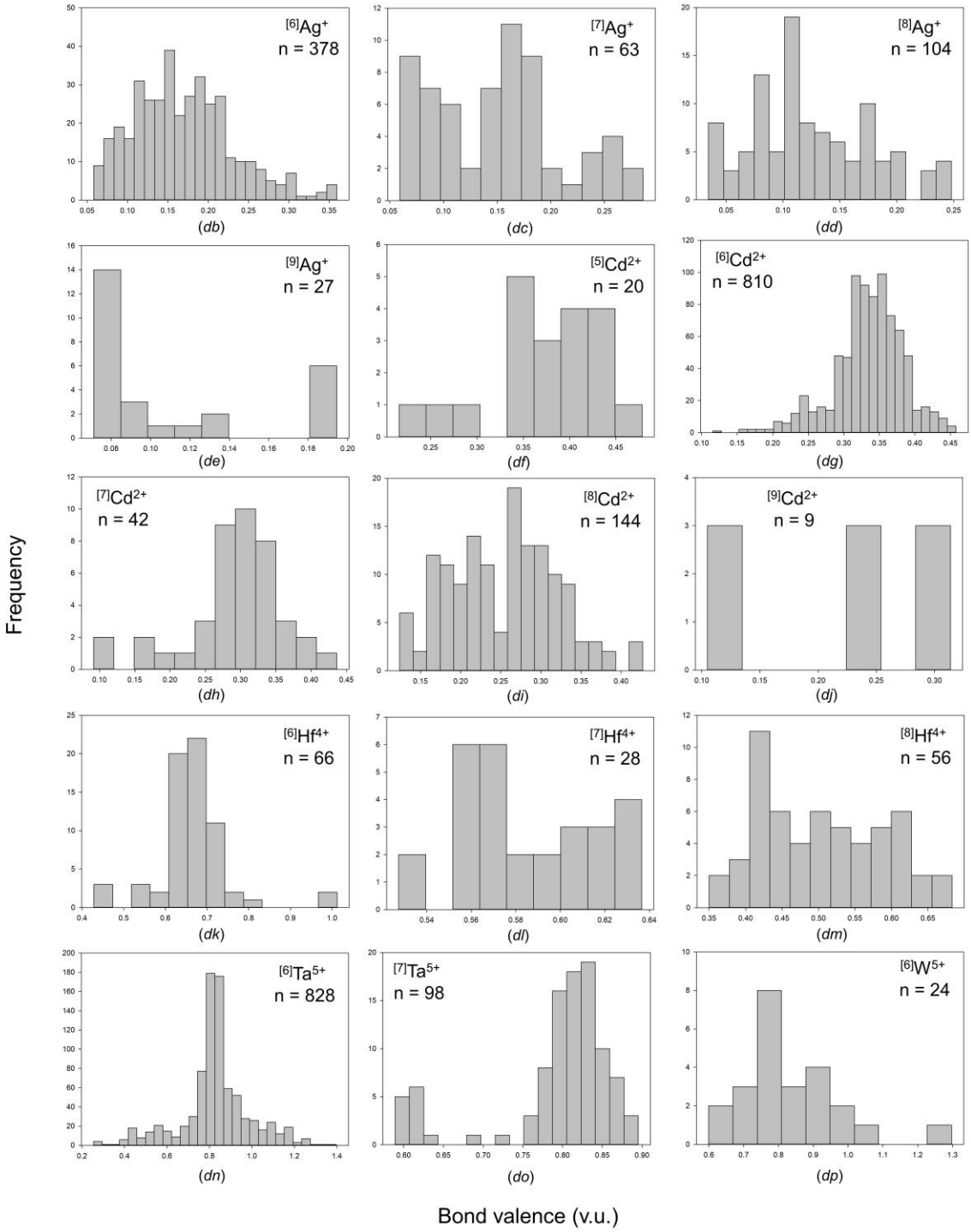
[6]Ag+
n = 378
(db)
[7]Ag+
n = 63
(dc)
[8]Ag+
n = 104
(dd)
[9]Ag+
n = 27
(de)
[5]Cd2+
n = 20
(df)
[6]Cd2+
n = 810
(dg)
[7]Cd2+
n = 42
(dh)
[8]Cd2+
n = 144
(di)
[9]Cd2+
n = 9
(dj)
[6]Hf4+
n = 66
(dk)
[7]Hf4+
n = 28
(dl)
[8]Hf4+
n = 56
(dm)
[6]Ta5+
n = 828
(dn)
[7]Ta5+
n = 98
(do)
[6]W5+
n = 24
(dp)
Frequency
Bond valence (v.u.)

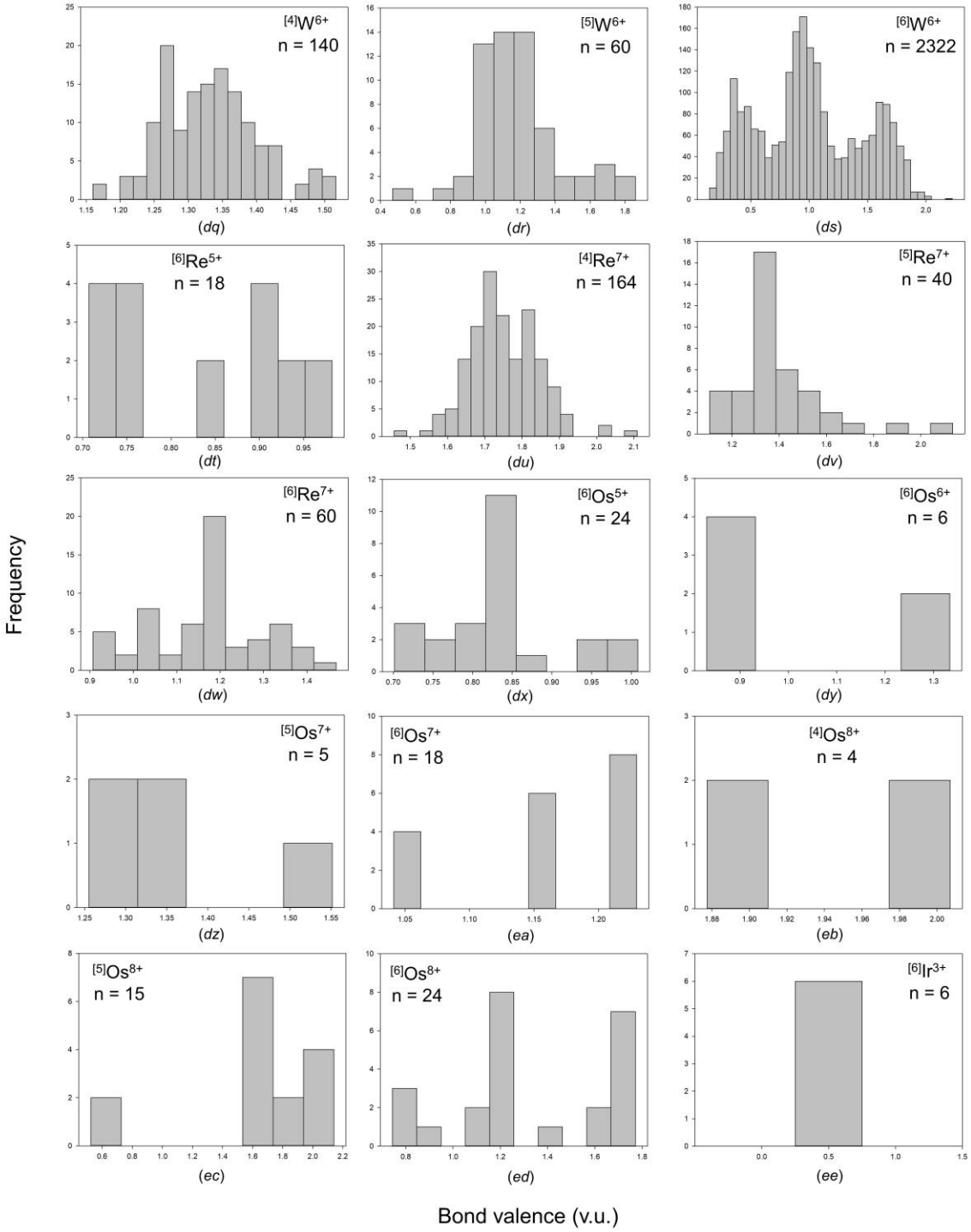
[4]W6+
n = 140
(dq)
[5]W6+
n = 60
(dr)
[6]W6+
n = 2322
(ds)
[6]Re5+
n = 18
(dt)
[4]Re7+
n = 164
(du)
[5]Re7+
n = 40
(dv)
[6]Re7+
n = 60
(dw)
[6]Os5+
n = 24
(dx)
[6]Os6+
n = 6
(dy)
[5]Os7+
n = 5
(dz)
[6]Os7+
n = 18
(ea)
[4]Os8+
n = 4
(eb)
[5]Os8+
n = 15
(ec)
[6]Os8+
n = 24
(ed)
[6]Ir3+
n = 6
(ee)
Frequency
Bond valence (v.u.)

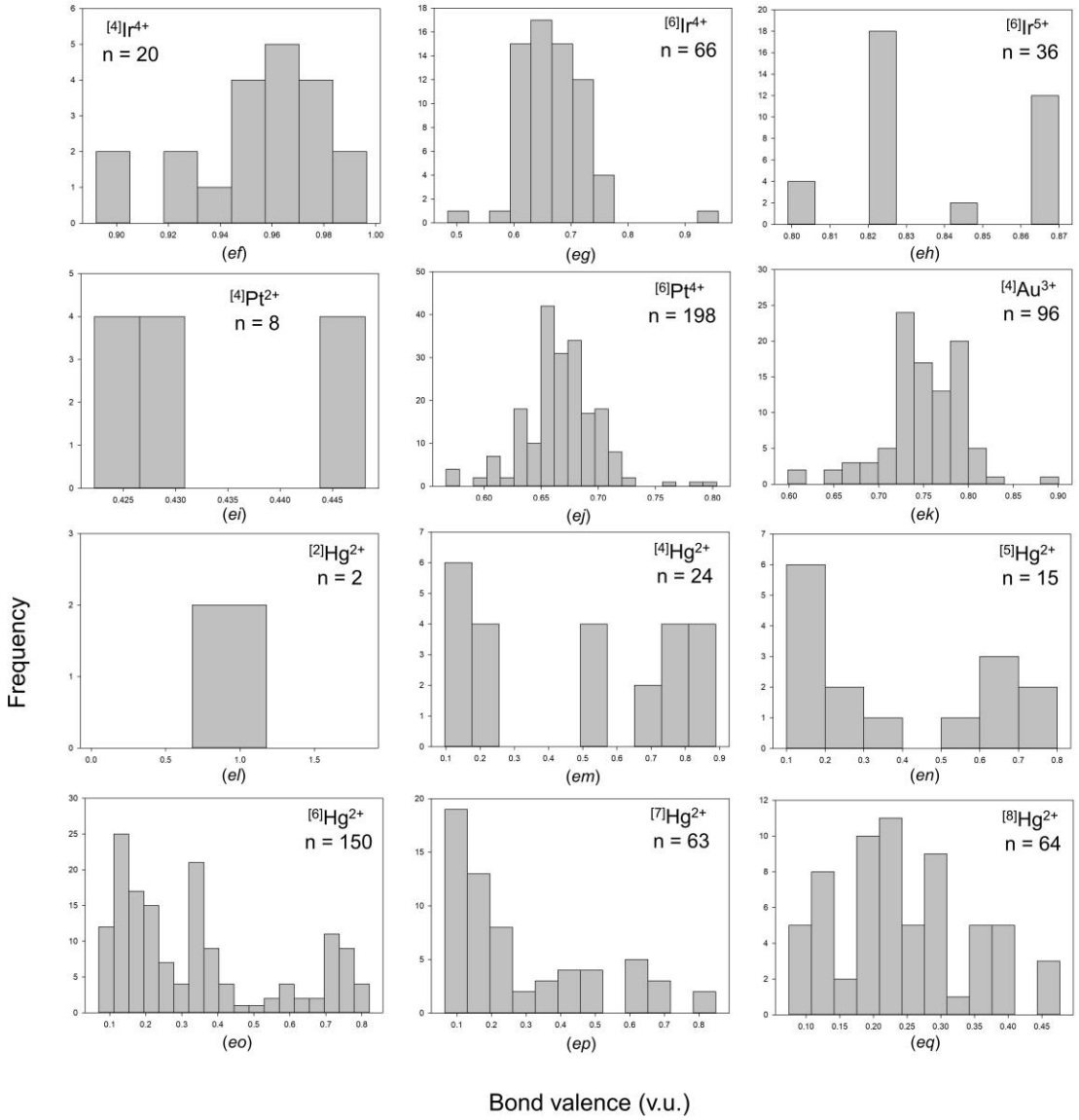

Figure S2: Bond-valence distributions for all configurations of the transition metal ions bonded to O^{2-}: (*a*) $^{[6]}Sc^{3+}$, (*b*) $^{[7]}Sc^{3+}$, (*c*) $^{[8]}Sc^{3+}$, (*d*) $^{[6]}Ti^{3+}$, (*e*) $^{[7]}Ti^{3+}$, (*f*) $^{[8]}Ti^{3+}$, (*g*) $^{[4]}Ti^{4+}$, (*h*) $^{[5]}Ti^{4+}$, (*i*) $^{[6]}Ti^{4+}$, (*j*) $^{[7]}Ti^{4+}$, (*k*) $^{[6]}V^{3+}$, (*l*) $^{[5]}V^{4+}$, (*m*) $^{[6]}V^{4+}$, (*n*) $^{[4]}V^{5+}$, (*o*) $^{[5]}V^{5+}$, (*p*) $^{[6]}V^{5+}$, (*q*) $^{[4]}Cr^{2+}$, (*r*) $^{[5]}Cr^{2+}$, (*s*) $^{[6]}Cr^{2+}$, (*t*) $^{[6]}Cr^{3+}$, (*u*) $^{[4]}Cr^{4+}$, (*v*) $^{[6]}Cr^{4+}$, (*w*) $^{[4]}Cr^{5+}$, (*x*) $^{[4]}Cr^{6+}$, (*y*) $^{[4]}Mn^{2+}$, (*z*) $^{[5]}Mn^{2+}$, (*aa*) $^{[6]}Mn^{2+}$, (*ab*) $^{[7]}Mn^{2+}$, (*ac*) $^{[8]}Mn^{2+}$, (*ad*) $^{[4]}Mn^{3+}$, (*ae*) $^{[5]}Mn^{3+}$, (*af*) $^{[6]}Mn^{3+}$, (*ag*) $^{[4]}Mn^{4+}$, (*ah*) $^{[6]}Mn^{4+}$, (*ai*) $^{[4]}Mn^{5+}$, (*aj*) $^{[4]}Mn^{6+}$, (*ak*) $^{[4]}Mn^{7+}$, (*al*) $^{[3]}Fe^{2+}$, (*am*) $^{[4]}Fe^{2+}$, (*an*) $^{[5]}Fe^{2+}$, (*ao*) $^{[6]}Fe^{2+}$, (*ap*) $^{[8]}Fe^{2+}$, (*aq*) $^{[4]}Fe^{3+}$, (*ar*) $^{[5]}Fe^{3+}$, (*as*) $^{[6]}Fe^{3+}$, (*at*) $^{[8]}Fe^{3+}$, (*au*) $^{[3]}Co^{2+}$, (*av*) $^{[4]}Co^{2+}$, (*aw*) $^{[5]}Co^{2+}$, (*ax*) $^{[6]}Co^{2+}$, (*ay*) $^{[8]}Co^{2+}$, (*az*) $^{[6]}Co^{3+}$, (*ba*) $^{[6]}Co^{4+}$, (*bb*) $^{[2]}Ni^{2+}$, (*bc*) $^{[4]}Ni^{2+}$, (*bd*) $^{[5]}Ni^{2+}$, (*be*) $^{[6]}Ni^{2+}$, (*bf*) $^{[6]}Ni^{4+}$, (*bg*) $^{[2]}Cu^{+}$, (*bh*) $^{[3]}Cu^{+}$, (*bi*) $^{[4]}Cu^{+}$, (*bj*) $^{[4]}Cu^{2+}$, (*bk*) $^{[5]}Cu^{2+}$, (*bl*) $^{[6]}Cu^{2+}$, (*bm*) $^{[8]}Cu^{2+}$, (*bn*) $^{[4]}Cu^{3+}$, (*bo*) $^{[4]}Zn^{2+}$, (*bp*) $^{[5]}Zn^{2+}$, (*bq*) $^{[6]}Zn^{2+}$, (*br*) $^{[6]}Y^{3+}$, (*bs*) $^{[7]}Y^{3+}$, (*bt*) $^{[8]}Y^{3+}$, (*bu*) $^{[9]}Y^{3+}$, (*bv*) $^{[10]}Y^{3+}$, (*bw*) $^{[12]}Y^{3+}$, (*bx*) $^{[6]}Zr^{4+}$, (*by*) $^{[7]}Zr^{4+}$, (*bz*) $^{[8]}Zr^{4+}$, (*ca*) $^{[9]}Zr^{4+}$, (*cb*) $^{[10]}Zr^{4+}$, (*cc*) $^{[6]}Nb^{4+}$, (*cd*) $^{[4]}Nb^{5+}$, (*ce*) $^{[5]}Nb^{5+}$, (*cf*) $^{[6]}Nb^{5+}$, (*cg*) $^{[7]}Nb^{5+}$, (*ch*) $^{[8]}Nb^{5+}$, (*ci*) $^{[6]}Mo^{3+}$, (*cj*) $^{[6]}Mo^{4+}$, (*ck*) $^{[5]}Mo^{5+}$, (*cl*) $^{[6]}Mo^{5+}$, (*cm*) $^{[4]}Mo^{6+}$, (*cn*) $^{[5]}Mo^{6+}$, (*co*) $^{[6]}Mo^{6+}$, (*cp*) $^{[4]}Tc^{7+}$, (*cq*) $^{[6]}Ru^{3+}$, (*cr*) $^{[6]}Ru^{4+}$, (*cs*) $^{[6]}Ru^{5+}$, (*ct*) $^{[6]}Rh^{3+}$, (*cu*) $^{[6]}Rh^{4+}$, (*cv*) $^{[4]}Pd^{2+}$, (*cw*) $^{[6]}Pd^{4+}$, (*cx*) $^{[2]}Ag^{+}$, (*cy*) $^{[3]}Ag^{+}$, (*cz*) $^{[4]}Ag^{+}$, (*da*) $^{[5]}Ag^{+}$, (*db*) $^{[6]}Ag^{+}$, (*dc*) $^{[7]}Ag^{+}$, (*dd*) $^{[8]}Ag^{+}$, (*de*) $^{[9]}Ag^{+}$, (*df*) $^{[5]}Cd^{2+}$, (*dg*) $^{[6]}Cd^{2+}$, (*dh*) $^{[7]}Cd^{2+}$, (*di*) $^{[8]}Cd^{2+}$, (*dj*) $^{[9]}Cd^{2+}$, (*dk*) $^{[6]}Hf^{4+}$, (*dl*) $^{[7]}Hf^{4+}$, (*dm*) $^{[8]}Hf^{4+}$, (*dn*) $^{[6]}Ta^{5+}$, (*do*) $^{[7]}Ta^{5+}$, (*dp*) $^{[6]}W^{5+}$, (*dq*) $^{[4]}W^{6+}$, (*dr*) $^{[5]}W^{6+}$, (*ds*) $^{[6]}W^{6+}$, (*dt*) $^{[6]}Re^{5+}$, (*du*) $^{[4]}Re^{7+}$, (*dv*) $^{[5]}Re^{7+}$, (*dw*) $^{[6]}Re^{7+}$, (*dx*) $^{[6]}Os^{5+}$, (*dy*) $^{[6]}Os^{6+}$, (*dz*) $^{[5]}Os^{7+}$, (*ea*) $^{[6]}Os^{7+}$, (*eb*) $^{[4]}Os^{8+}$, (*ec*) $^{[5]}Os^{8+}$, (*ed*) $^{[6]}Os^{8+}$, (*ee*) $^{[6]}Ir^{3+}$, (*ef*) $^{[4]}Ir^{4+}$, (*eg*) $^{[6]}Ir^{4+}$, (*eh*) $^{[6]}Ir^{5+}$, (*ei*) $^{[4]}Pt^{2+}$, (*ej*) $^{[6]}Pt^{4+}$, (*ek*) $^{[4]}Au^{3+}$, (*el*) $^{[2]}Hg^{2+}$, (*em*) $^{[4]}Hg^{2+}$, (*en*) $^{[5]}Hg^{2+}$, (*eo*) $^{[6]}Hg^{2+}$, (*ep*) $^{[7]}Hg^{2+}$, (*eq*) $^{[8]}Hg^{2+}$.

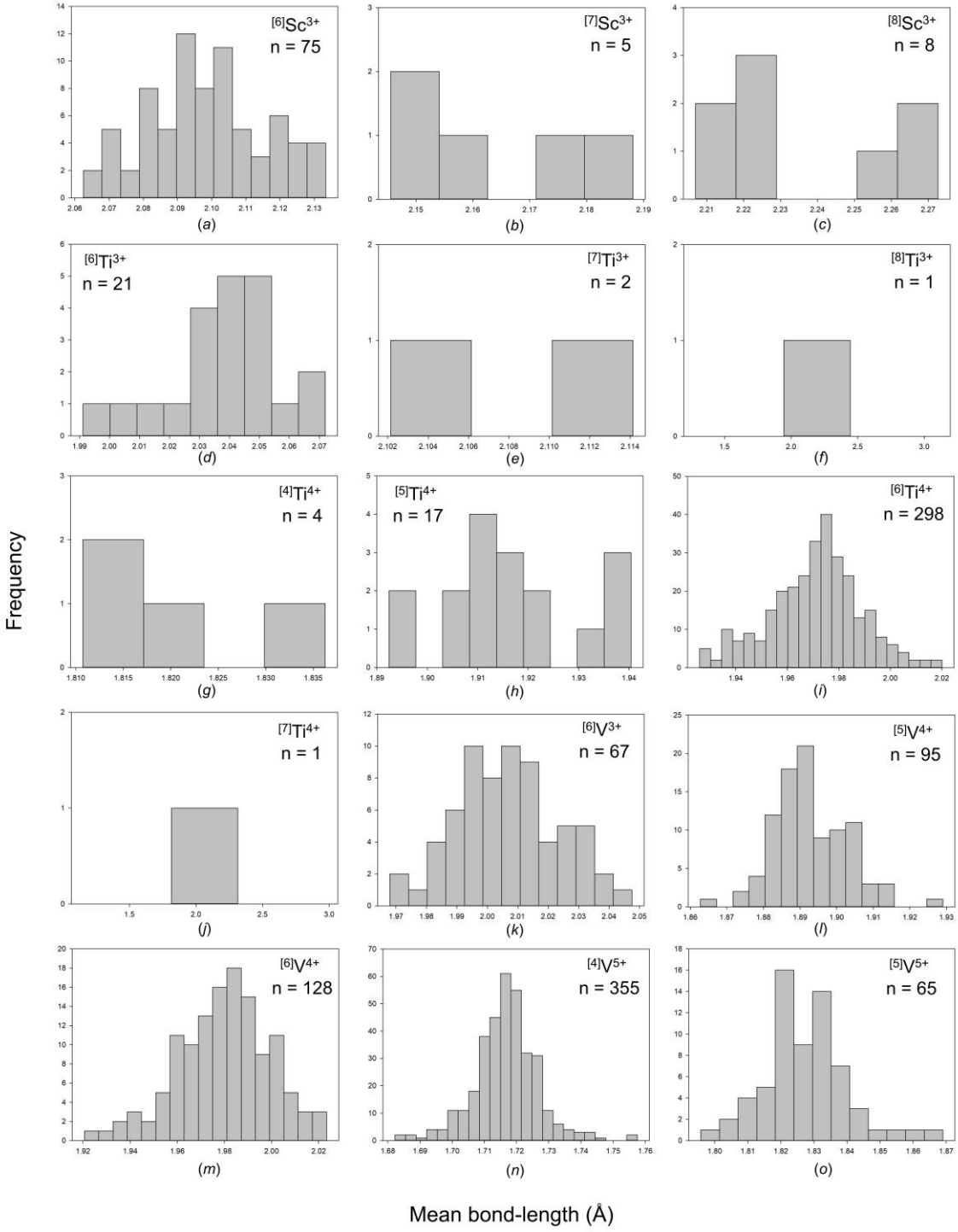
[6]Sc3+
n = 75
(a)
[7]Sc3+
n = 5
(b)
[8]Sc3+
n = 8
(c)
[6]Ti3+
n = 21
(d)
[7]Ti3+
n = 2
(e)
[8]Ti3+
n = 1
(f)
[4]Ti4+
n = 4
(g)
[5]Ti4+
n = 17
(h)
[6]Ti4+
n = 298
(i)
[7]Ti4+
n = 1
(j)
[6]V3+
n = 67
(k)
[5]V4+
n = 95
(l)
[6]V4+
n = 128
(m)
[4]V5+
n = 355
(n)
[5]V5+
n = 65
(o)
Frequency
Mean bond-length (Å)

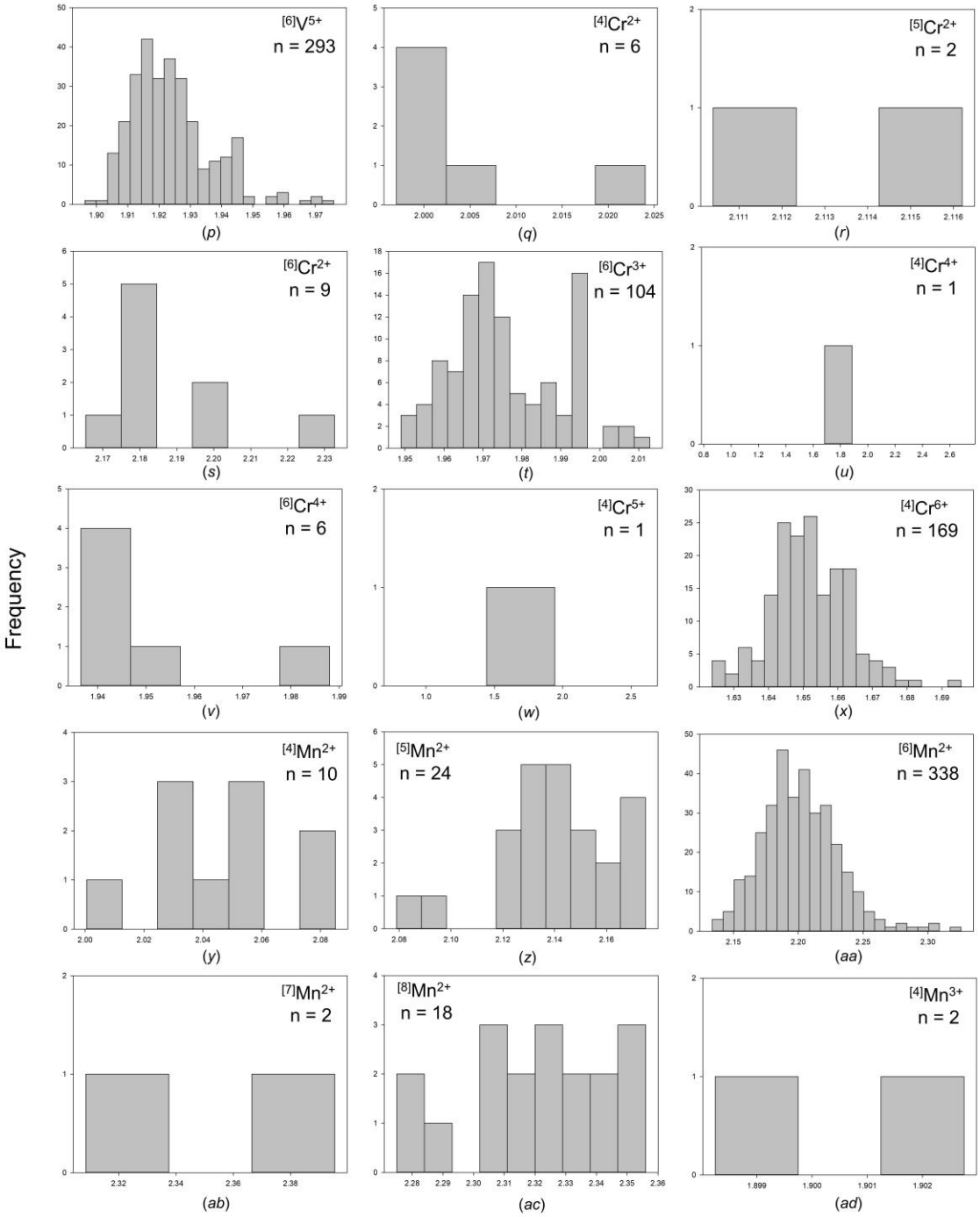
[6]V5+
n = 293
(p)
[4]Cr2+
n = 6
(q)
[5]Cr2+
n = 2
(r)
[6]Cr2+
n = 9
(s)
[6]Cr3+
n = 104
(t)
[4]Cr4+
n = 1
(u)
[6]Cr4+
n = 6
(v)
[4]Cr5+
n = 1
(w)
[4]Cr6+
n = 169
(x)
[4]Mn2+
n = 10
(y)
[5]Mn2+
n = 24
(z)
[6]Mn2+
n = 338
(aa)
[7]Mn2+
n = 2
(ab)
[8]Mn2+
n = 18
(ac)
[4]Mn3+
n = 2
(ad)
Frequency
Mean bond-length (Å)

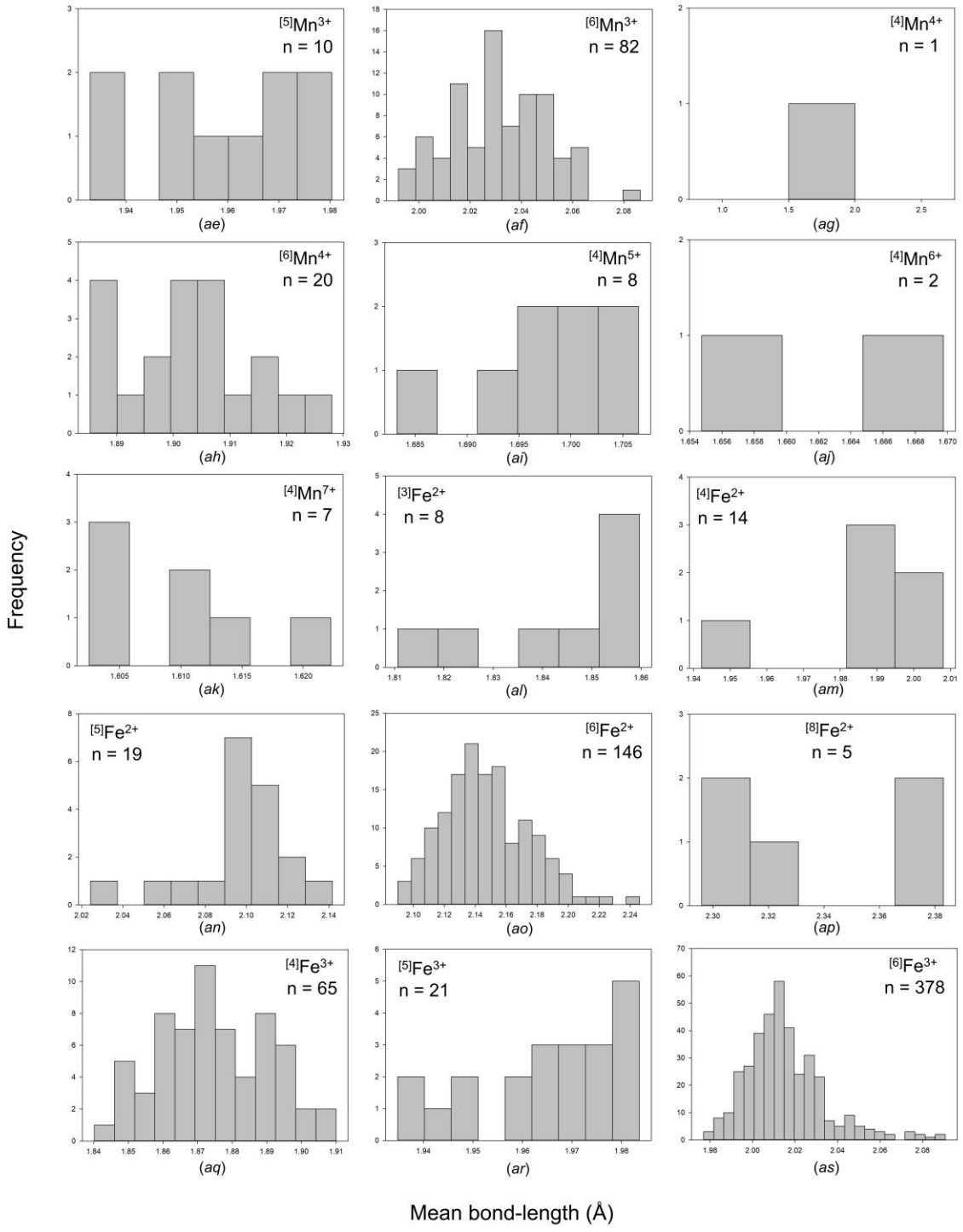
[5]Mn3+
n = 10
(ae)
[6]Mn3+
n = 82
(af)
[4]Mn4+
n = 1
(ag)
[6]Mn4+
n = 20
(ah)
[4]Mn5+
n = 8
(ai)
[4]Mn6+
n = 2
(aj)
[4]Mn7+
n = 7
(ak)
[3]Fe2+
n = 8
(al)
[4]Fe2+
n = 14
(am)
[5]Fe2+
n = 19
(an)
[6]Fe2+
n = 146
(ao)
[8]Fe2+
n = 5
(ap)
[4]Fe3+
n = 65
(aq)
[5]Fe3+
n = 21
(ar)
[6]Fe3+
n = 378
(as)
Frequency
Mean bond-length (Å)

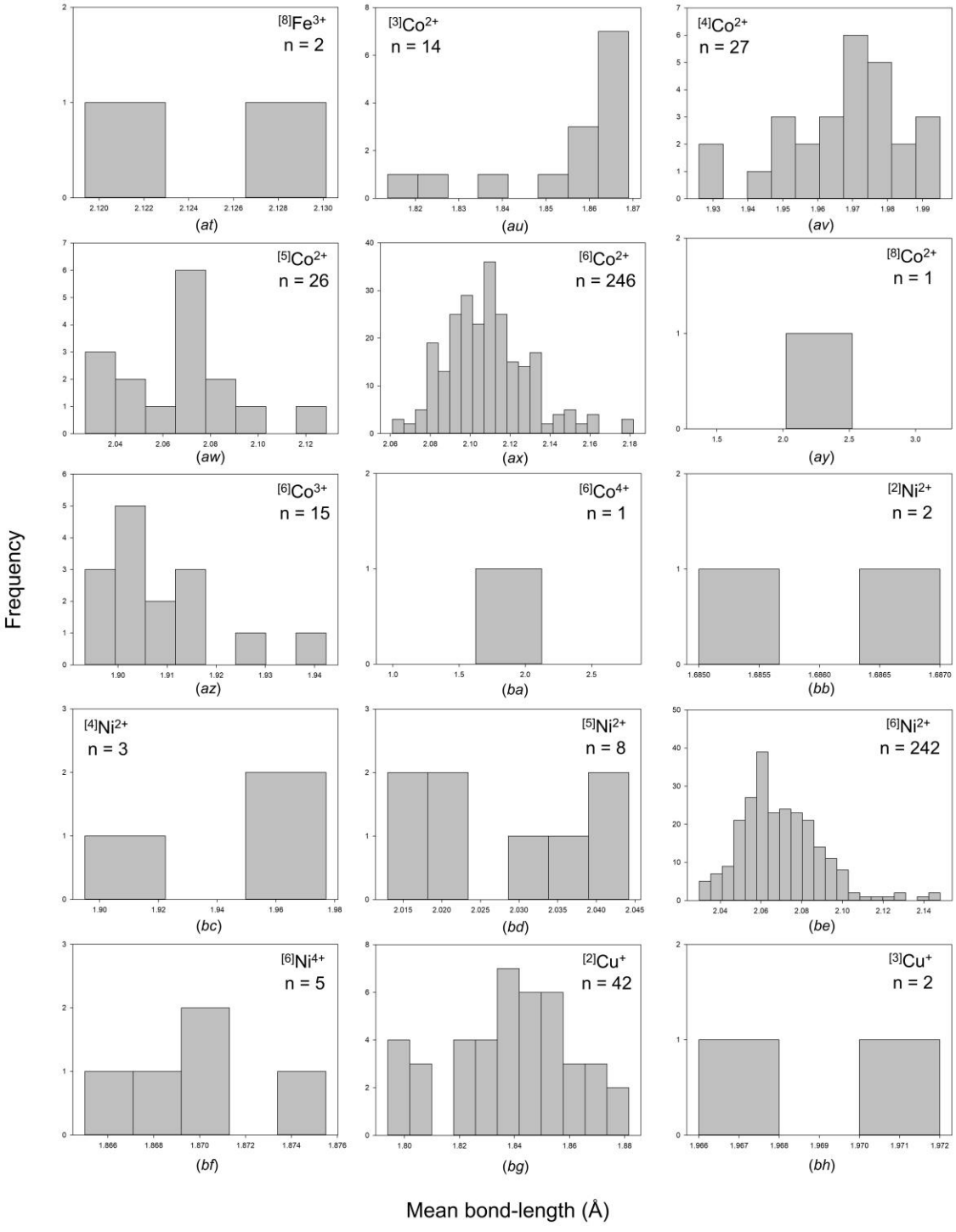
[8]Fe3+
n = 2
(at)
[3]Co2+
n = 14
(au)
[4]Co2+
n = 27
(av)
[5]Co2+
n = 26
(aw)
[6]Co2+
n = 246
(ax)
[8]Co2+
n = 1
(ay)
[6]Co3+
n = 15
(az)
[6]Co4+
n = 1
(ba)
[2]Ni2+
n = 2
(bb)
[4]Ni2+
n = 3
(bc)
[5]Ni2+
n = 8
(bd)
[6]Ni2+
n = 242
(be)
[6]Ni4+
n = 5
(bf)
[2]Cu+
n = 42
(bg)
[3]Cu+
n = 2
(bh)
Frequency
Mean bond-length (Å)

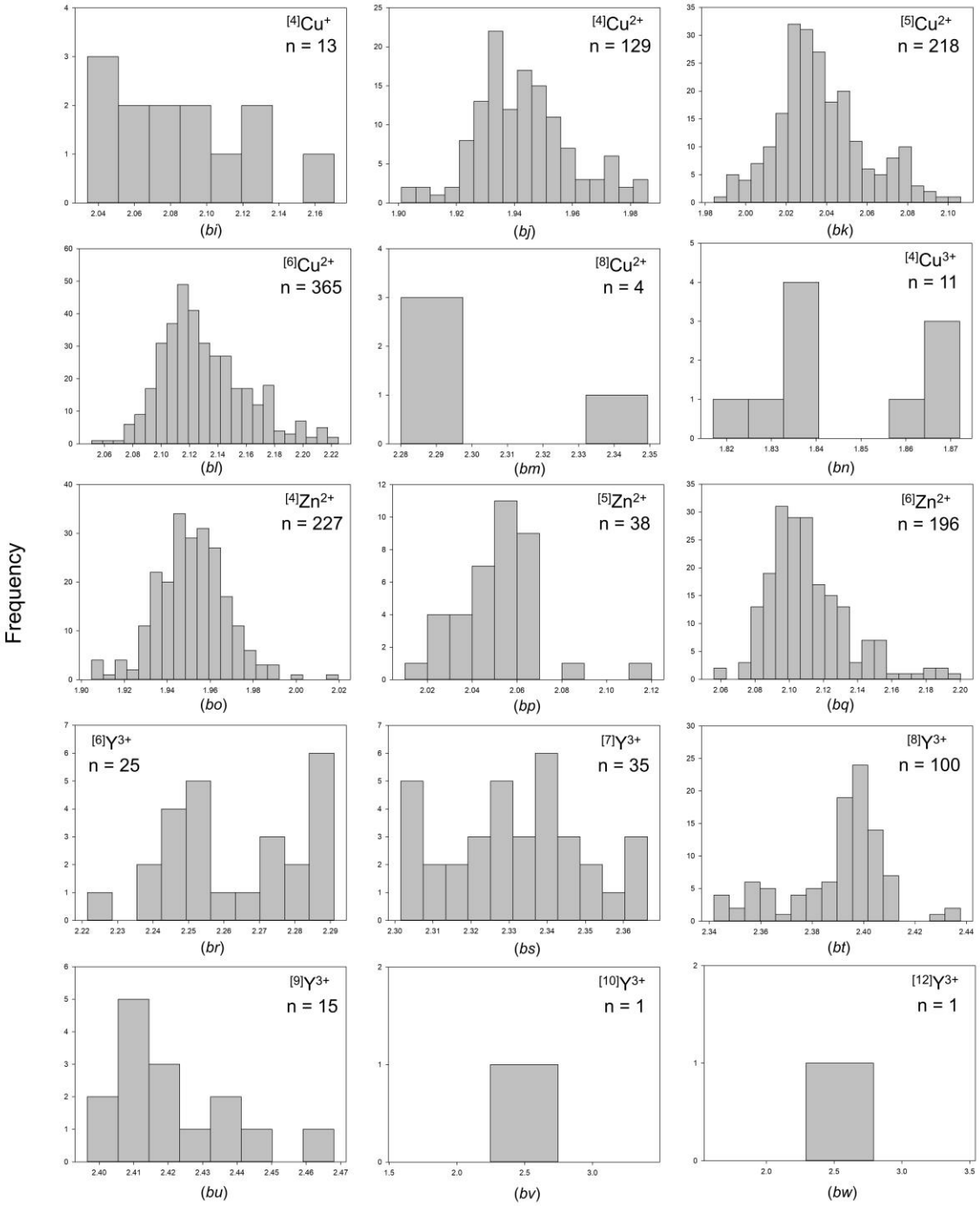
[4]Cu+
n = 13
(bi)
[4]Cu2+
n = 129
(bj)
[5]Cu2+
n = 218
(bk)
[6]Cu2+
n = 365
(bl)
[8]Cu2+
n = 4
(bm)
[4]Cu3+
n = 11
(bn)
[4]Zn2+
n = 227
(bo)
[5]Zn2+
n = 38
(bp)
[6]Zn2+
n = 196
(bq)
[6]Y3+
n = 25
(br)
[7]Y3+
n = 35
(bs)
[8]Y3+
n = 100
(bt)
[9]Y3+
n = 15
(bu)
[10]Y3+
n = 1
(bv)
[12]Y3+
n = 1
(bw)
Frequency
Mean bond-length (Å)

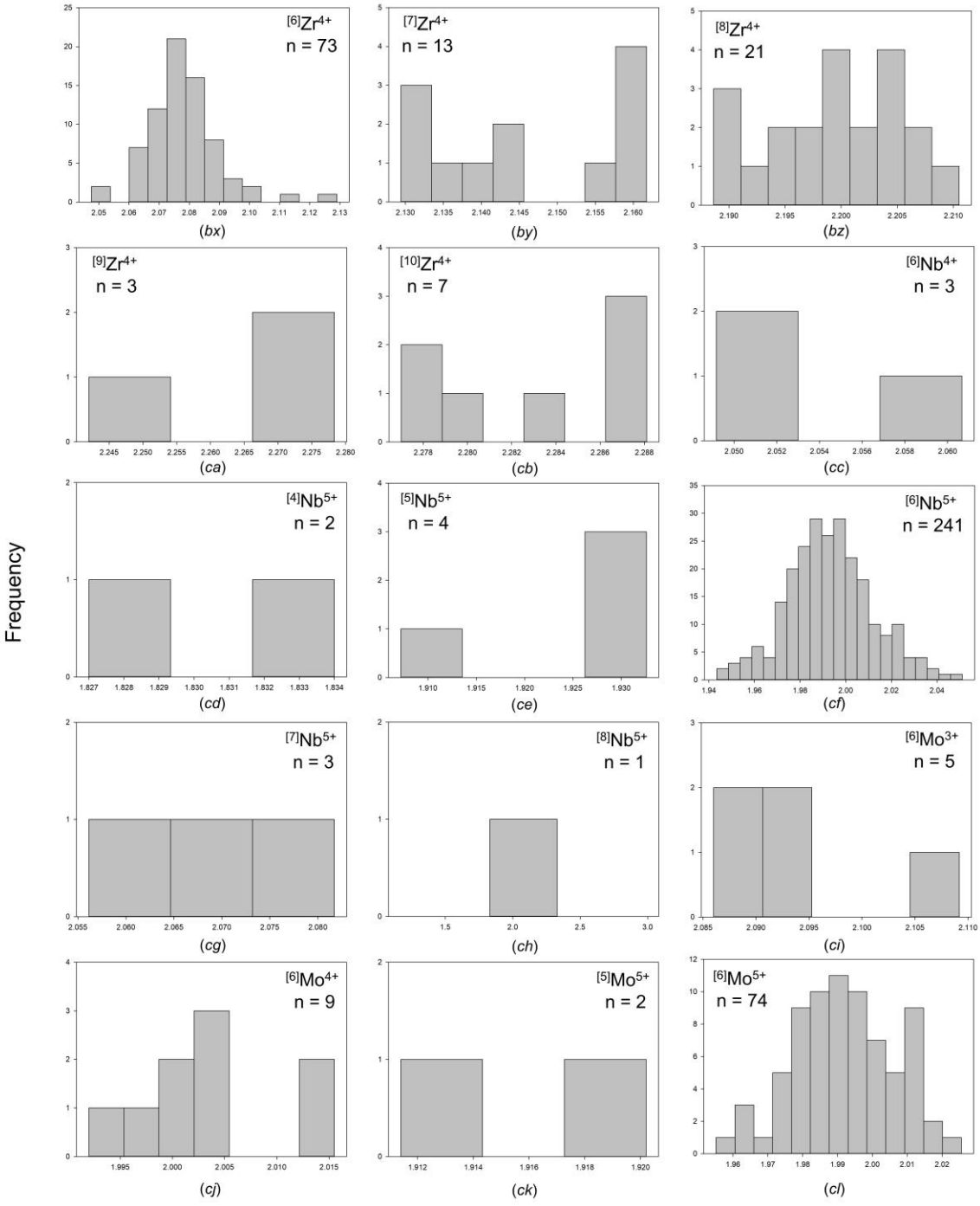
[6]Zr4+
n = 73
(bx)
[7]Zr4+
n = 13
(by)
[8]Zr4+
n = 21
(bz)
[9]Zr4+
n = 3
(ca)
[10]Zr4+
n = 7
(cb)
[6]Nb4+
n = 3
(cc)
[4]Nb5+
n = 2
(cd)
[5]Nb5+
n = 4
(ce)
[6]Nb5+
n = 241
(cf)
[7]Nb5+
n = 3
(cg)
[8]Nb5+
n = 1
(ch)
[6]Mo3+
n = 5
(ci)
[6]Mo4+
n = 9
(cj)
[5]Mo5+
n = 2
(ck)
[6]Mo5+
n = 74
(cl)
Frequency
Mean bond-length (Å)

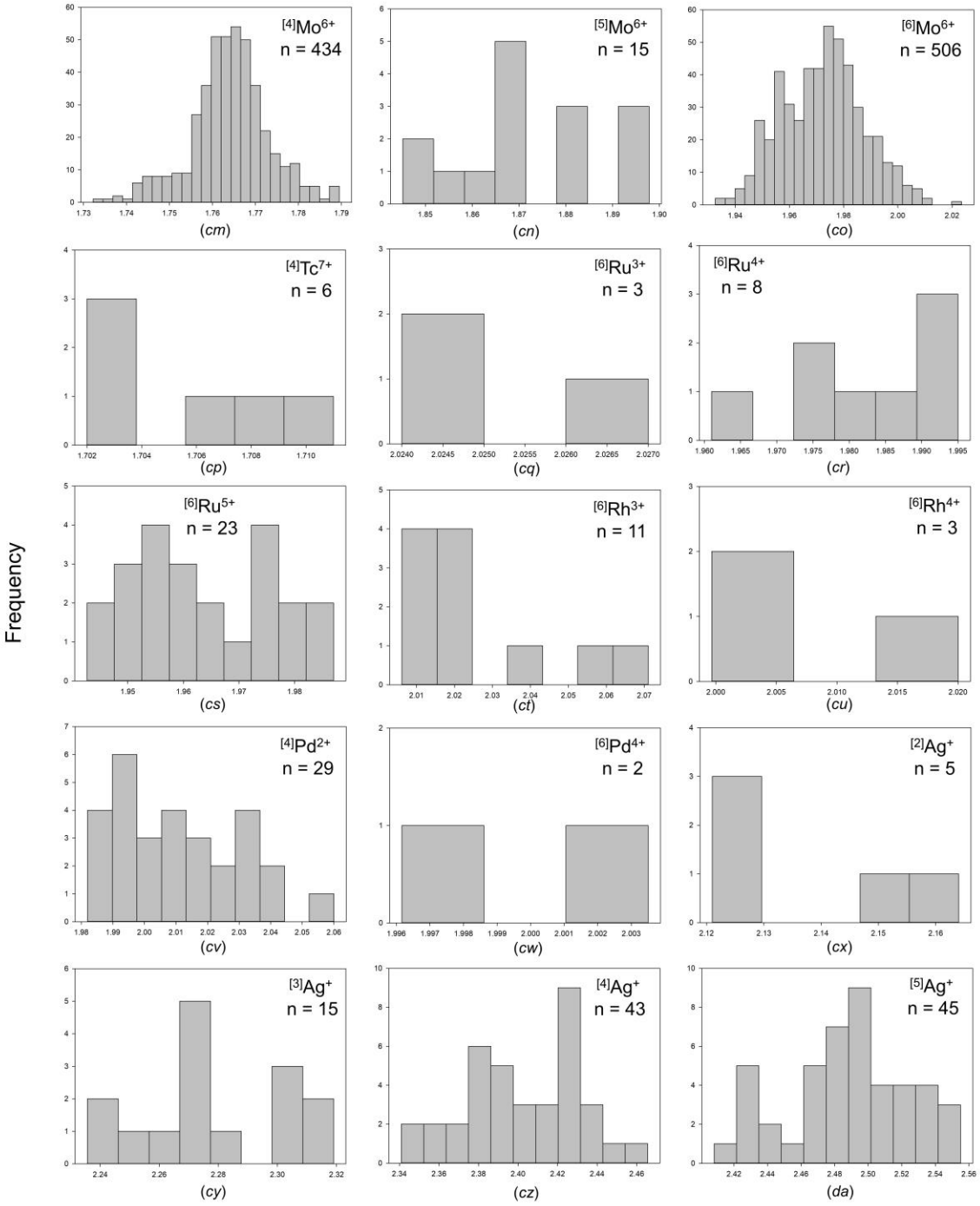
[4]Mo6+
n = 434
(cm)
[5]Mo6+
n = 15
(cn)
[6]Mo6+
n = 506
(co)
[4]Tc7+
n = 6
(cp)
[6]Ru3+
n = 3
(cq)
[6]Ru4+
n = 8
(cr)
[6]Ru5+
n = 23
(cs)
[6]Rh3+
n = 11
(ct)
[6]Rh4+
n = 3
(cu)
[4]Pd2+
n = 29
(cv)
[6]Pd4+
n = 2
(cw)
[2]Ag+
n = 5
(cx)
[3]Ag+
n = 15
(cy)
[4]Ag+
n = 43
(cz)
[5]Ag+
n = 45
(da)
Frequency
Mean bond-length (Å)

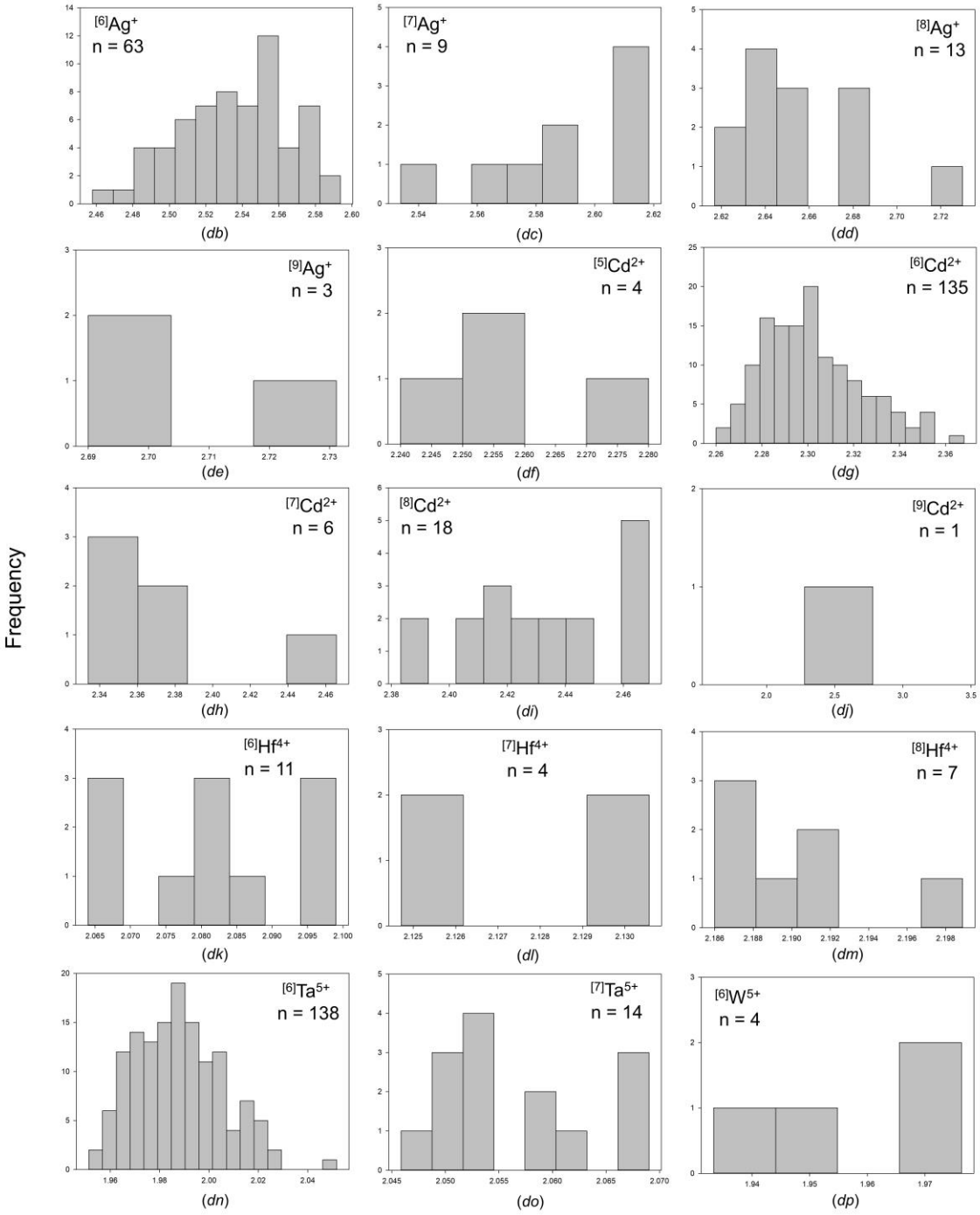
[6]Ag+
n = 63
(db)
[7]Ag+
n = 9
(dc)
[8]Ag+
n = 13
(dd)
[9]Ag+
n = 3
(de)
[5]Cd2+
n = 4
(df)
[6]Cd2+
n = 135
(dg)
[7]Cd2+
n = 6
(dh)
[8]Cd2+
n = 18
(di)
[9]Cd2+
n = 1
(dj)
[6]Hf4+
n = 11
(dk)
[7]Hf4+
n = 4
(dl)
[8]Hf4+
n = 7
(dm)
[6]Ta5+
n = 138
(dn)
[7]Ta5+
n = 14
(do)
[6]W5+
n = 4
(dp)
Frequency
Mean bond-length (Å)

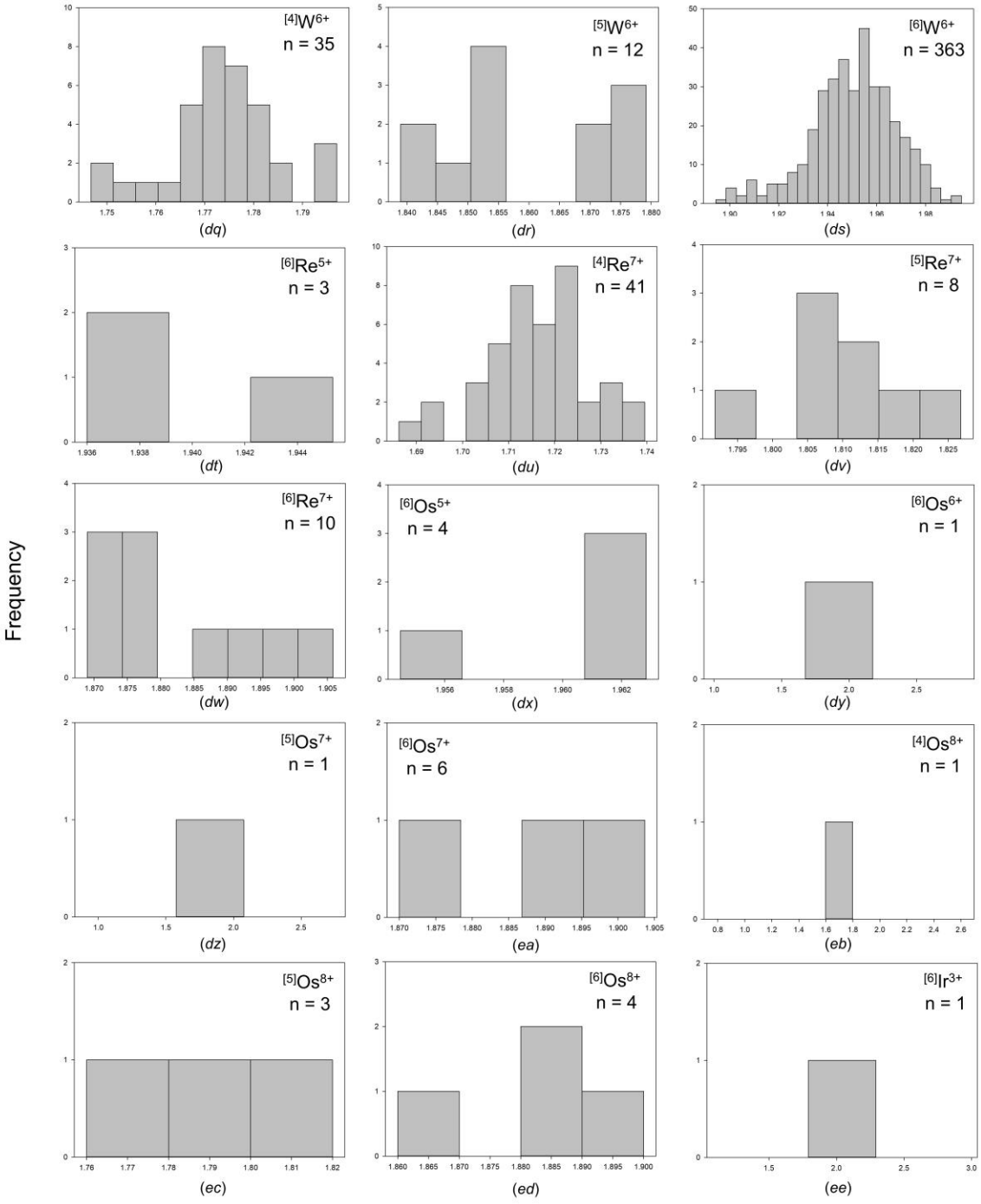
[4]W6+
n = 35
(dq)
[5]W6+
n = 12
(dr)
[6]W6+
n = 363
(ds)
[6]Re5+
n = 3
(dt)
[4]Re7+
n = 41
(du)
[5]Re7+
n = 8
(dv)
[6]Re7+
n = 10
(dw)
[6]Os5+
n = 4
(dx)
[6]Os6+
n = 1
(dy)
[5]Os7+
n = 1
(dz)
[6]Os7+
n = 6
(ea)
[4]Os8+
n = 1
(eb)
[5]Os8+
n = 3
(ec)
[6]Os8+
n = 4
(ed)
[6]Ir3+
n = 1
(ee)
Frequency
Mean bond-length (Å)

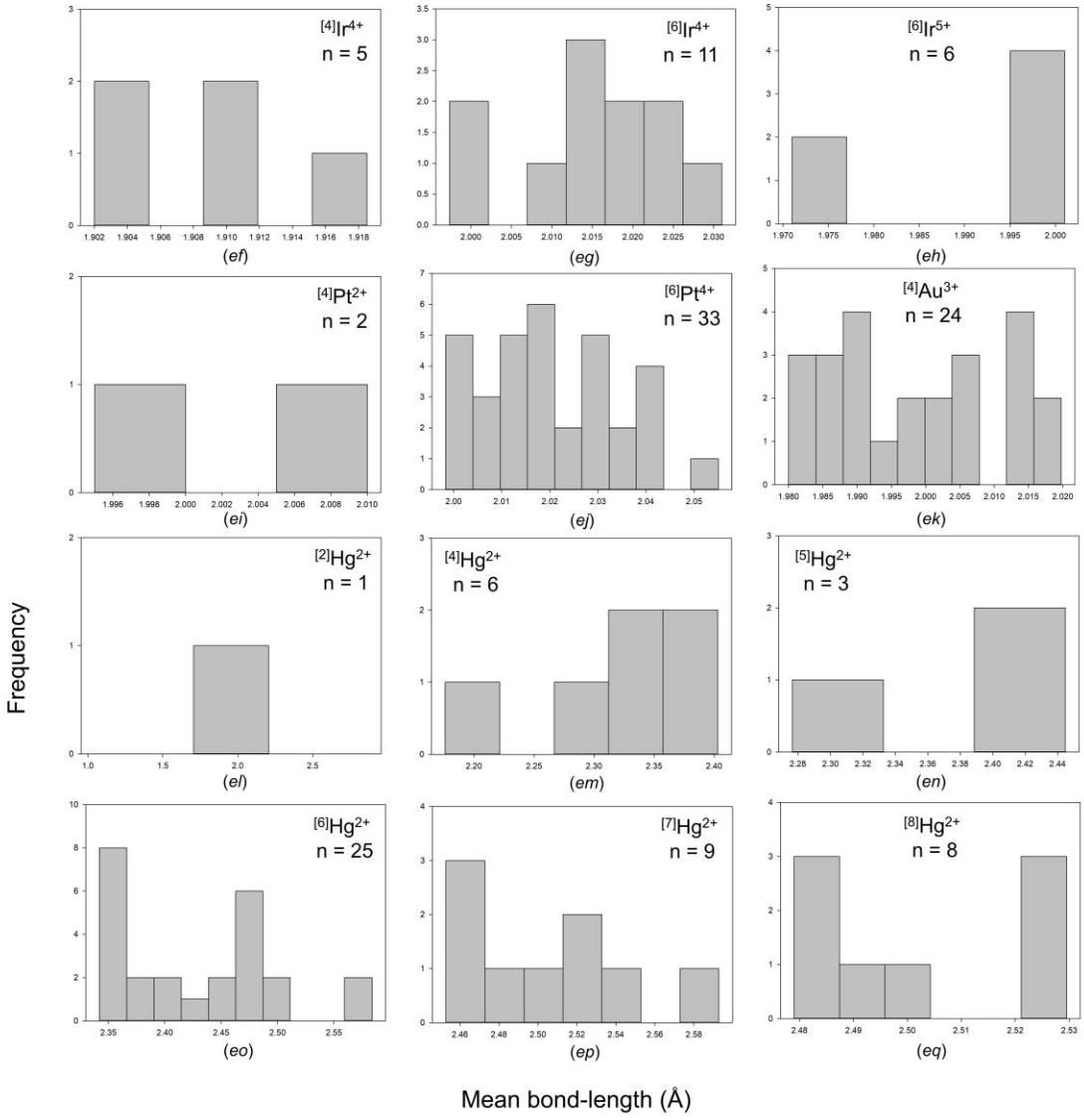

Figure S3: Mean bond-length distributions for all configurations of the transition metal ions bonded to O^{2-}: (*a*) $^{[6]}Sc^{3+}$, (*b*) $^{[7]}Sc^{3+}$, (*c*) $^{[8]}Sc^{3+}$, (*d*) $^{[6]}Ti^{3+}$, (*e*) $^{[7]}Ti^{3+}$, (*f*) $^{[8]}Ti^{3+}$, (*g*) $^{[4]}Ti^{4+}$, (*h*) $^{[5]}Ti^{4+}$, (*i*) $^{[6]}Ti^{4+}$, (*j*) $^{[7]}Ti^{4+}$, (*k*) $^{[6]}V^{3+}$, (*l*) $^{[5]}V^{4+}$, (*m*) $^{[6]}V^{4+}$, (*n*) $^{[4]}V^{5+}$, (*o*) $^{[5]}V^{5+}$, (*p*) $^{[6]}V^{5+}$, (*q*) $^{[4]}Cr^{2+}$, (*r*) $^{[5]}Cr^{2+}$, (*s*) $^{[6]}Cr^{2+}$, (*t*) $^{[6]}Cr^{3+}$, (*u*) $^{[4]}Cr^{4+}$, (*v*) $^{[6]}Cr^{4+}$, (*w*) $^{[4]}Cr^{5+}$, (*x*) $^{[4]}Cr^{6+}$, (*y*) $^{[4]}Mn^{2+}$, (*z*) $^{[5]}Mn^{2+}$, (*aa*) $^{[6]}Mn^{2+}$, (*ab*) $^{[7]}Mn^{2+}$, (*ac*) $^{[8]}Mn^{2+}$, (*ad*) $^{[4]}Mn^{3+}$, (*ae*) $^{[5]}Mn^{3+}$, (*af*) $^{[6]}Mn^{3+}$, (*ag*) $^{[4]}Mn^{4+}$, (*ah*) $^{[6]}Mn^{4+}$, (*ai*) $^{[4]}Mn^{5+}$, (*aj*) $^{[4]}Mn^{6+}$, (*ak*) $^{[4]}Mn^{7+}$, (*al*) $^{[3]}Fe^{2+}$, (*am*) $^{[4]}Fe^{2+}$, (*an*) $^{[5]}Fe^{2+}$, (*ao*) $^{[6]}Fe^{2+}$, (*ap*) $^{[8]}Fe^{2+}$, (*aq*) $^{[4]}Fe^{3+}$, (*ar*) $^{[5]}Fe^{3+}$, (*as*) $^{[6]}Fe^{3+}$, (*at*) $^{[8]}Fe^{3+}$, (*au*) $^{[3]}Co^{2+}$, (*av*) $^{[4]}Co^{2+}$, (*aw*) $^{[5]}Co^{2+}$, (*ax*) $^{[6]}Co^{2+}$, (*ay*) $^{[8]}Co^{2+}$, (*az*) $^{[6]}Co^{3+}$, (*ba*) $^{[6]}Co^{4+}$, (*bb*) $^{[2]}Ni^{2+}$, (*bc*) $^{[4]}Ni^{2+}$, (*bd*) $^{[5]}Ni^{2+}$, (*be*) $^{[6]}Ni^{2+}$, (*bf*) $^{[6]}Ni^{4+}$, (*bg*) $^{[2]}Cu^{+}$, (*bh*) $^{[3]}Cu^{+}$, (*bi*) $^{[4]}Cu^{+}$, (*bj*) $^{[4]}Cu^{2+}$, (*bk*) $^{[5]}Cu^{2+}$, (*bl*) $^{[6]}Cu^{2+}$, (*bm*) $^{[8]}Cu^{2+}$, (*bn*) $^{[4]}Cu^{3+}$, (*bo*) $^{[4]}Zn^{2+}$, (*bp*) $^{[5]}Zn^{2+}$, (*bq*) $^{[6]}Zn^{2+}$, (*br*) $^{[6]}Y^{3+}$, (*bs*) $^{[7]}Y^{3+}$, (*bt*) $^{[8]}Y^{3+}$, (*bu*) $^{[9]}Y^{3+}$, (*bv*) $^{[10]}Y^{3+}$, (*bw*) $^{[12]}Y^{3+}$, (*bx*) $^{[6]}Zr^{4+}$, (*by*) $^{[7]}Zr^{4+}$, (*bz*) $^{[8]}Zr^{4+}$, (*ca*) $^{[9]}Zr^{4+}$, (*cb*) $^{[10]}Zr^{4+}$, (*cc*) $^{[6]}Nb^{4+}$, (*cd*) $^{[4]}Nb^{5+}$, (*ce*) $^{[5]}Nb^{5+}$, (*cf*) $^{[6]}Nb^{5+}$, (*cg*) $^{[7]}Nb^{5+}$, (*ch*) $^{[8]}Nb^{5+}$, (*ci*) $^{[6]}Mo^{3+}$, (*cj*) $^{[6]}Mo^{4+}$, (*ck*) $^{[5]}Mo^{5+}$, (*cl*) $^{[6]}Mo^{5+}$, (*cm*) $^{[4]}Mo^{6+}$, (*cn*) $^{[5]}Mo^{6+}$, (*co*) $^{[6]}Mo^{6+}$, (*cp*) $^{[4]}Tc^{7+}$, (*cq*) $^{[6]}Ru^{3+}$, (*cr*) $^{[6]}Ru^{4+}$, (*cs*) $^{[6]}Ru^{5+}$, (*ct*) $^{[6]}Rh^{3+}$, (*cu*) $^{[6]}Rh^{4+}$, (*cv*) $^{[4]}Pd^{2+}$, (*cw*) $^{[6]}Pd^{4+}$, (*cx*) $^{[2]}Ag^{+}$, (*cy*) $^{[3]}Ag^{+}$, (*cz*) $^{[4]}Ag^{+}$, (*da*) $^{[5]}Ag^{+}$, (*db*) $^{[6]}Ag^{+}$, (*dc*) $^{[7]}Ag^{+}$, (*dd*) $^{[8]}Ag^{+}$, (*de*) $^{[9]}Ag^{+}$, (*df*) $^{[5]}Cd^{2+}$, (*dg*) $^{[6]}Cd^{2+}$, (*dh*) $^{[7]}Cd^{2+}$, (*di*) $^{[8]}Cd^{2+}$, (*dj*) $^{[9]}Cd^{2+}$, (*dk*) $^{[6]}Hf^{4+}$, (*dl*) $^{[7]}Hf^{4+}$, (*dm*) $^{[8]}Hf^{4+}$, (*dn*) $^{[6]}Ta^{5+}$, (*do*) $^{[7]}Ta^{5+}$, (*dp*) $^{[6]}W^{5+}$, (*dq*) $^{[4]}W^{6+}$, (*dr*) $^{[5]}W^{6+}$, (*ds*) $^{[6]}W^{6+}$, (*dt*) $^{[6]}Re^{5+}$, (*du*) $^{[4]}Re^{7+}$, (*dv*) $^{[5]}Re^{7+}$, (*dw*) $^{[6]}Re^{7+}$, (*dx*) $^{[6]}Os^{5+}$, (*dy*) $^{[6]}Os^{6+}$, (*dz*) $^{[5]}Os^{7+}$, (*ea*) $^{[6]}Os^{7+}$, (*eb*) $^{[4]}Os^{8+}$, (*ec*) $^{[5]}Os^{8+}$, (*ed*) $^{[6]}Os^{8+}$, (*ee*) $^{[6]}Ir^{3+}$, (*ef*) $^{[4]}Ir^{4+}$, (*eg*) $^{[6]}Ir^{4+}$, (*eh*) $^{[6]}Ir^{5+}$, (*ei*) $^{[4]}Pt^{2+}$, (*ej*) $^{[6]}Pt^{4+}$, (*ek*) $^{[4]}Au^{3+}$, (*el*) $^{[2]}Hg^{2+}$, (*em*) $^{[4]}Hg^{2+}$, (*en*) $^{[5]}Hg^{2+}$, (*eo*) $^{[6]}Hg^{2+}$, (*ep*) $^{[7]}Hg^{2+}$, (*eq*) $^{[8]}Hg^{2+}$.

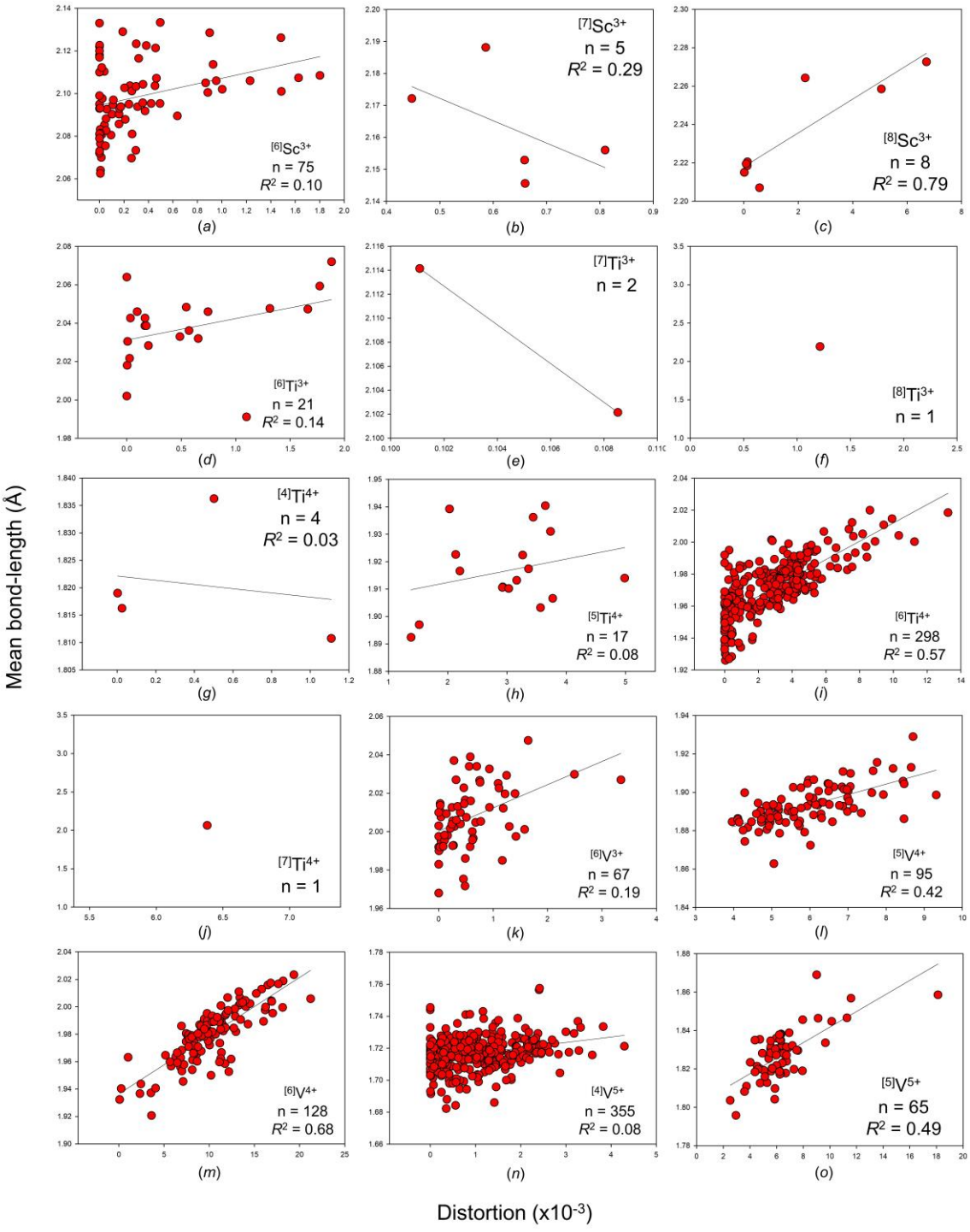
Mean bond-length (Å)
Distortion (x10-3)
(a) [6]Sc3+ n = 75 R2 = 0.10
(b) [7]Sc3+ n = 5 R2 = 0.29
(c) [8]Sc3+ n = 8 R2 = 0.79
(d) [6]Ti3+ n = 21 R2 = 0.14
(e) [7]Ti3+ n = 2
(f) [8]Ti3+ n = 1
(g) [4]Ti4+ n = 4 R2 = 0.03
(h) [5]Ti4+ n = 17 R2 = 0.08
(i) [6]Ti4+ n = 298 R2 = 0.57
(j) [7]Ti4+ n = 1
(k) [6]V3+ n = 67 R2 = 0.19
(l) [5]V4+ n = 95 R2 = 0.42
(m) [6]V4+ n = 128 R2 = 0.68
(n) [4]V5+ n = 355 R2 = 0.08
(o) [5]V5+ n = 65 R2 = 0.49

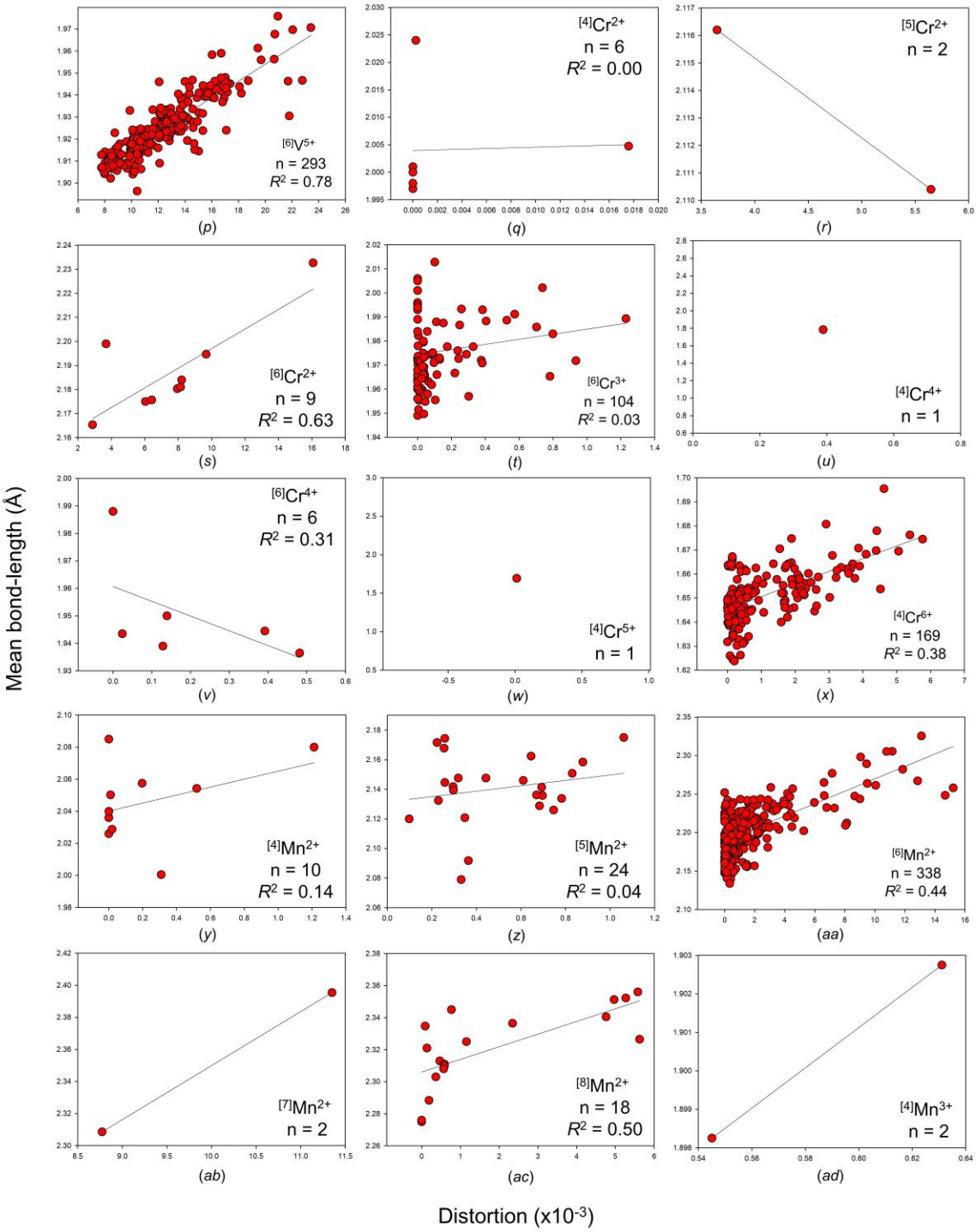
Mean bond-length (Å)
Distortion (x10-3)
[6]V5+
n = 293
R2 = 0.78
(p)
[4]Cr2+
n = 6
R2 = 0.00
(q)
[5]Cr2+
n = 2
(r)
[6]Cr2+
n = 9
R2 = 0.63
(s)
[6]Cr3+
n = 104
R2 = 0.03
(t)
[4]Cr4+
n = 1
(u)
[6]Cr4+
n = 6
R2 = 0.31
(v)
[4]Cr5+
n = 1
(w)
[4]Cr6+
n = 169
R2 = 0.38
(x)
[4]Mn2+
n = 10
R2 = 0.14
(y)
[5]Mn2+
n = 24
R2 = 0.04
(z)
[6]Mn2+
n = 338
R2 = 0.44
(aa)
[7]Mn2+
n = 2
(ab)
[8]Mn2+
n = 18
R2 = 0.50
(ac)
[4]Mn3+
n = 2
(ad)

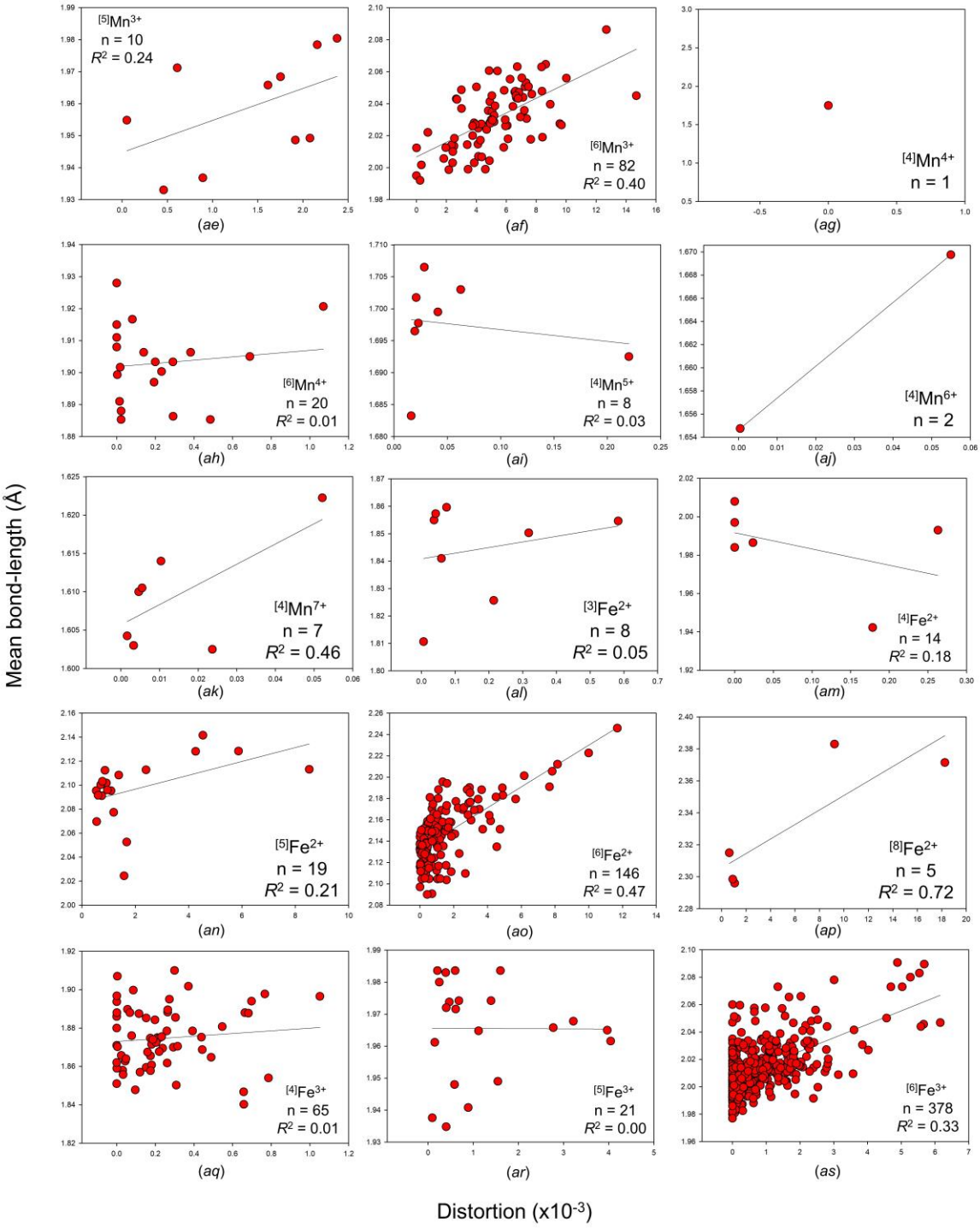
[5]Mn3+
n = 10
R2 = 0.24
(ae)
[6]Mn3+
n = 82
R2 = 0.40
(af)
[4]Mn4+
n = 1
(ag)
[6]Mn4+
n = 20
R2 = 0.01
(ah)
[4]Mn5+
n = 8
R2 = 0.03
(ai)
[4]Mn6+
n = 2
(aj)
[4]Mn7+
n = 7
R2 = 0.46
(ak)
[3]Fe2+
n = 8
R2 = 0.05
(al)
[4]Fe2+
n = 14
R2 = 0.18
(am)
[5]Fe2+
n = 19
R2 = 0.21
(an)
[6]Fe2+
n = 146
R2 = 0.47
(ao)
[8]Fe2+
n = 5
R2 = 0.72
(ap)
[4]Fe3+
n = 65
R2 = 0.01
(aq)
[5]Fe3+
n = 21
R2 = 0.00
(ar)
[6]Fe3+
n = 378
R2 = 0.33
(as)
Mean bond-length (Å)
Distortion (x10-3)

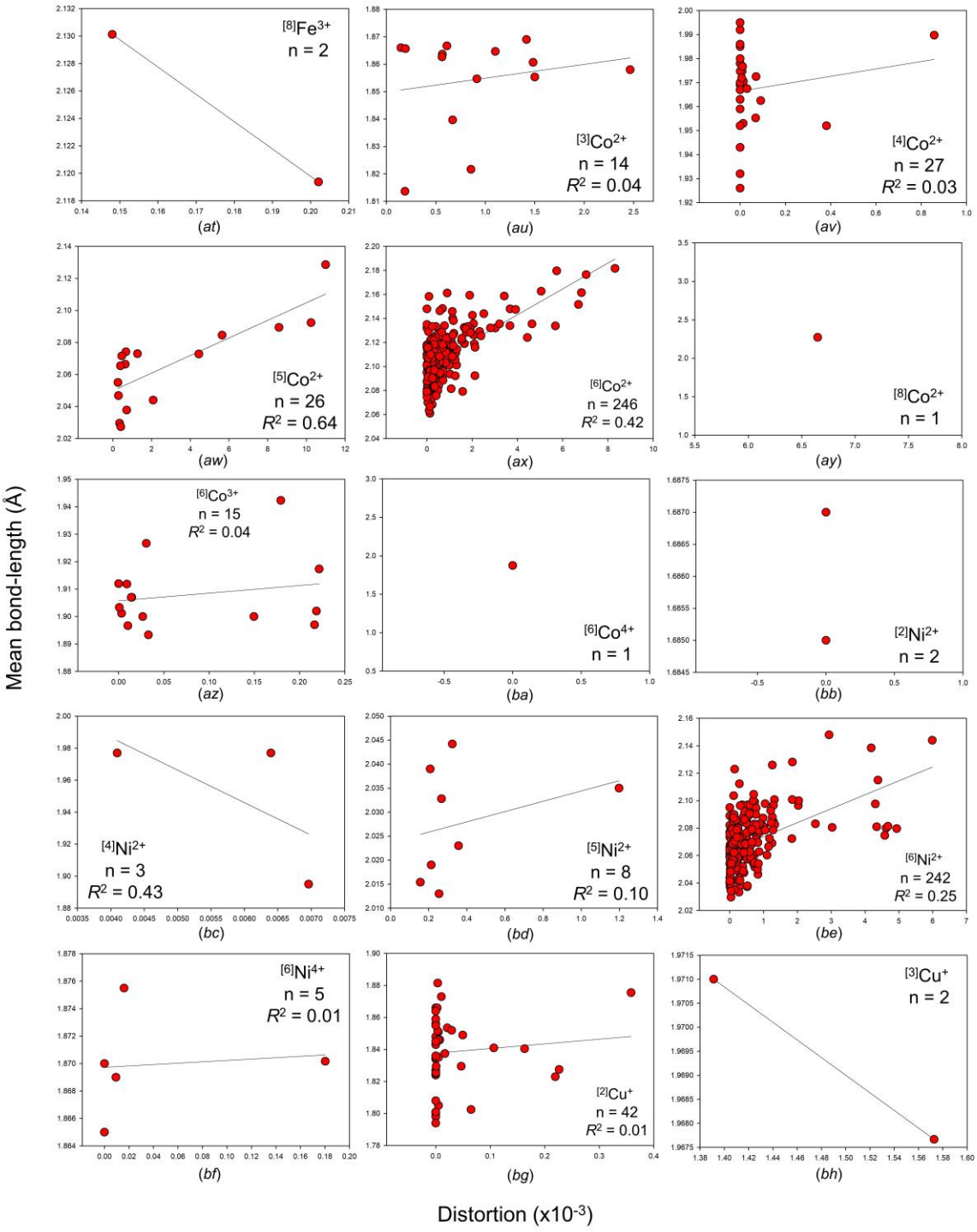
Mean bond-length (Å)
Distortion (x10-3)
[8]Fe3+
n = 2
(at)
[3]Co2+
n = 14
R2 = 0.04
(au)
[4]Co2+
n = 27
R2 = 0.03
(av)
[5]Co2+
n = 26
R2 = 0.64
(aw)
[6]Co2+
n = 246
R2 = 0.42
(ax)
[8]Co2+
n = 1
(ay)
[6]Co3+
n = 15
R2 = 0.04
(az)
[6]Co4+
n = 1
(ba)
[2]Ni2+
n = 2
(bb)
[4]Ni2+
n = 3
R2 = 0.43
(bc)
[5]Ni2+
n = 8
R2 = 0.10
(bd)
[6]Ni2+
n = 242
R2 = 0.25
(be)
[6]Ni4+
n = 5
R2 = 0.01
(bf)
[2]Cu+
n = 42
R2 = 0.01
(bg)
[3]Cu+
n = 2
(bh)

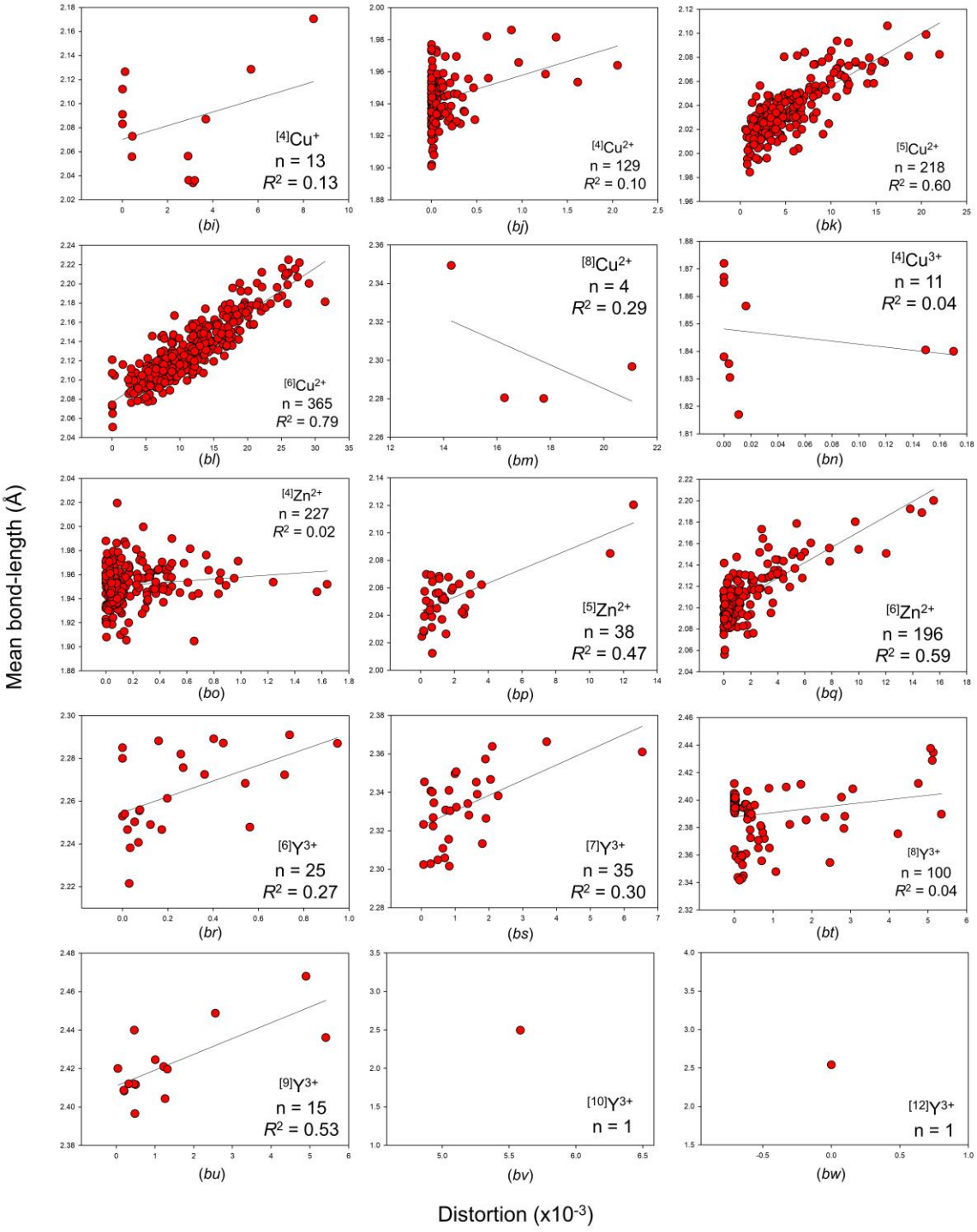
Mean bond-length (Å)
Distortion (x10-3)
[4]Cu+
n = 13
R2 = 0.13
(bi)
[4]Cu2+
n = 129
R2 = 0.10
(bj)
[5]Cu2+
n = 218
R2 = 0.60
(bk)
[6]Cu2+
n = 365
R2 = 0.79
(bl)
[8]Cu2+
n = 4
R2 = 0.29
(bm)
[4]Cu3+
n = 11
R2 = 0.04
(bn)
[4]Zn2+
n = 227
R2 = 0.02
(bo)
[5]Zn2+
n = 38
R2 = 0.47
(bp)
[6]Zn2+
n = 196
R2 = 0.59
(bq)
[6]Y3+
n = 25
R2 = 0.27
(br)
[7]Y3+
n = 35
R2 = 0.30
(bs)
[8]Y3+
n = 100
R2 = 0.04
(bt)
[9]Y3+
n = 15
R2 = 0.53
(bu)
[10]Y3+
n = 1
(bv)
[12]Y3+
n = 1
(bw)

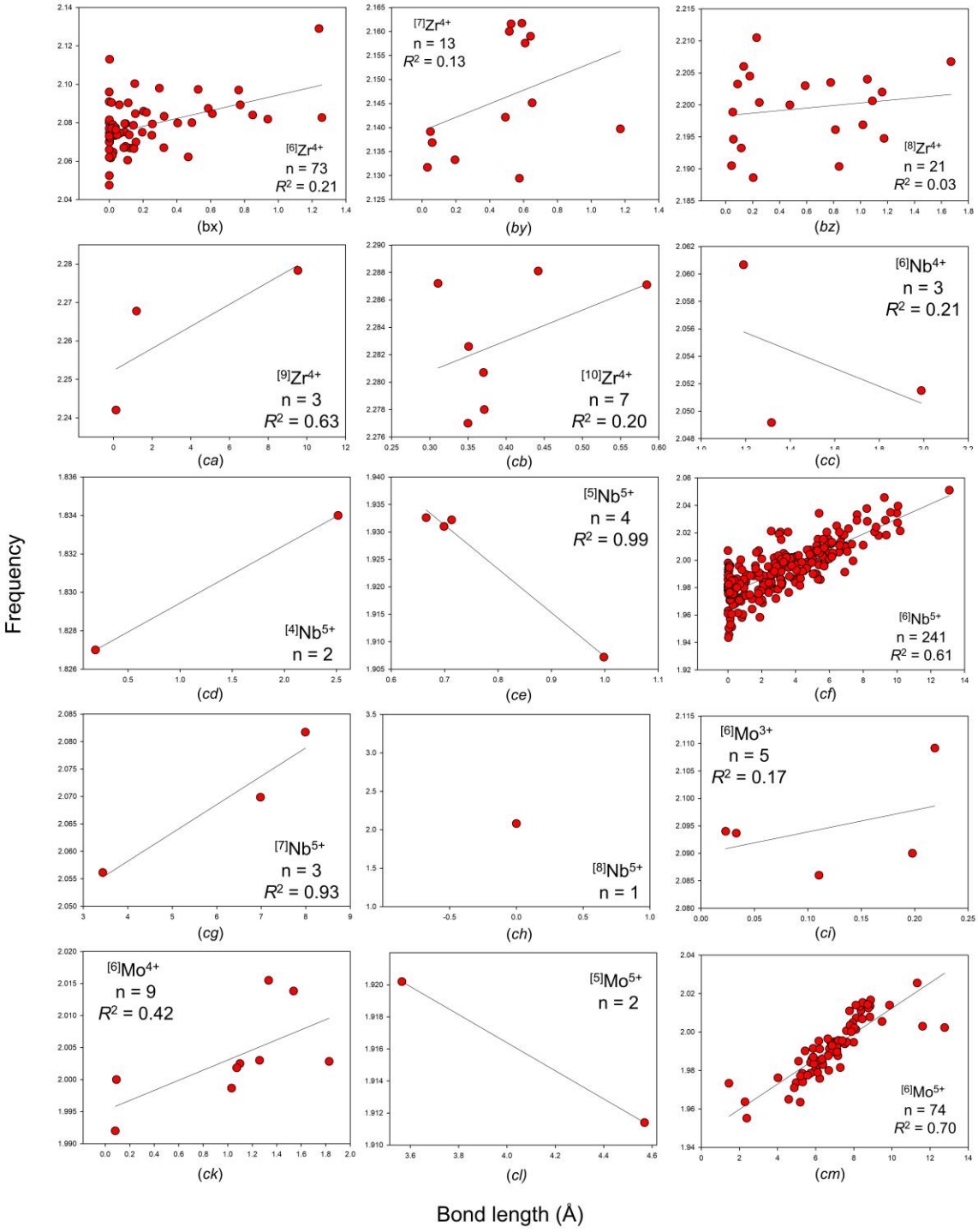
Frequency
Bond length (Å)
[6]Zr4+
n = 73
R2 = 0.21
(bx)
[7]Zr4+
n = 13
R2 = 0.13
(by)
[8]Zr4+
n = 21
R2 = 0.03
(bz)
[9]Zr4+
n = 3
R2 = 0.63
(ca)
[10]Zr4+
n = 7
R2 = 0.20
(cb)
[6]Nb4+
n = 3
R2 = 0.21
(cc)
[4]Nb5+
n = 2
(cd)
[5]Nb5+
n = 4
R2 = 0.99
(ce)
[6]Nb5+
n = 241
R2 = 0.61
(cf)
[7]Nb5+
n = 3
R2 = 0.93
(cg)
[8]Nb5+
n = 1
(ch)
[6]Mo3+
n = 5
R2 = 0.17
(ci)
[6]Mo4+
n = 9
R2 = 0.42
(ck)
[5]Mo5+
n = 2
(cl)
[6]Mo5+
n = 74
R2 = 0.70
(cm)

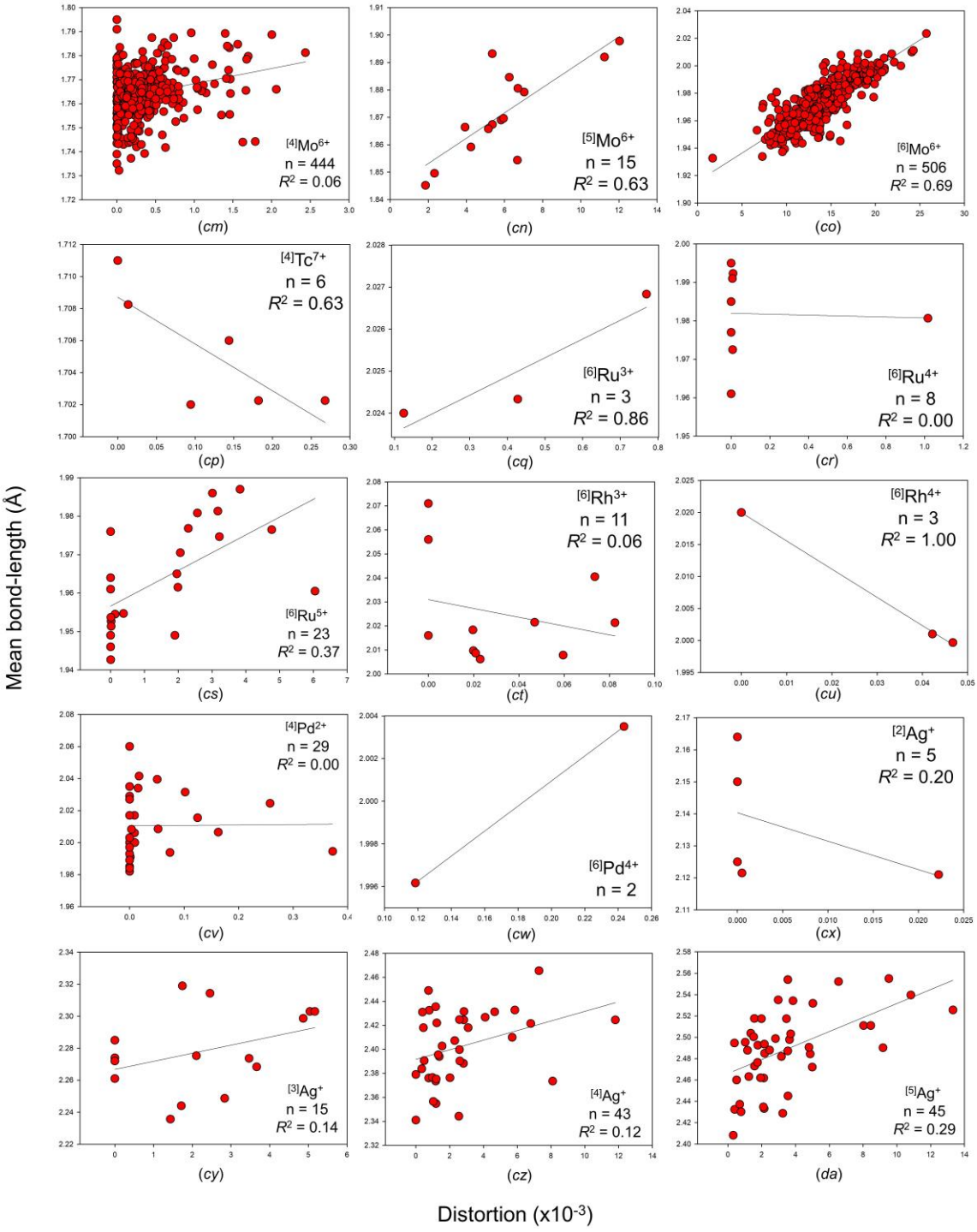
Mean bond-length (Å)
Distortion (x10-3)
[4]Mo6+
n = 444
R2 = 0.06
(cm)
[5]Mo6+
n = 15
R2 = 0.63
(cn)
[6]Mo6+
n = 506
R2 = 0.69
(co)
[4]Tc7+
n = 6
R2 = 0.63
(cp)
[6]Ru3+
n = 3
R2 = 0.86
(cq)
[6]Ru4+
n = 8
R2 = 0.00
(cr)
[6]Ru5+
n = 23
R2 = 0.37
(cs)
[6]Rh3+
n = 11
R2 = 0.06
(ct)
[6]Rh4+
n = 3
R2 = 1.00
(cu)
[4]Pd2+
n = 29
R2 = 0.00
(cv)
[6]Pd4+
n = 2
(cw)
[2]Ag+
n = 5
R2 = 0.20
(cx)
[3]Ag+
n = 15
R2 = 0.14
(cy)
[4]Ag+
n = 43
R2 = 0.12
(cz)
[5]Ag+
n = 45
R2 = 0.29
(da)

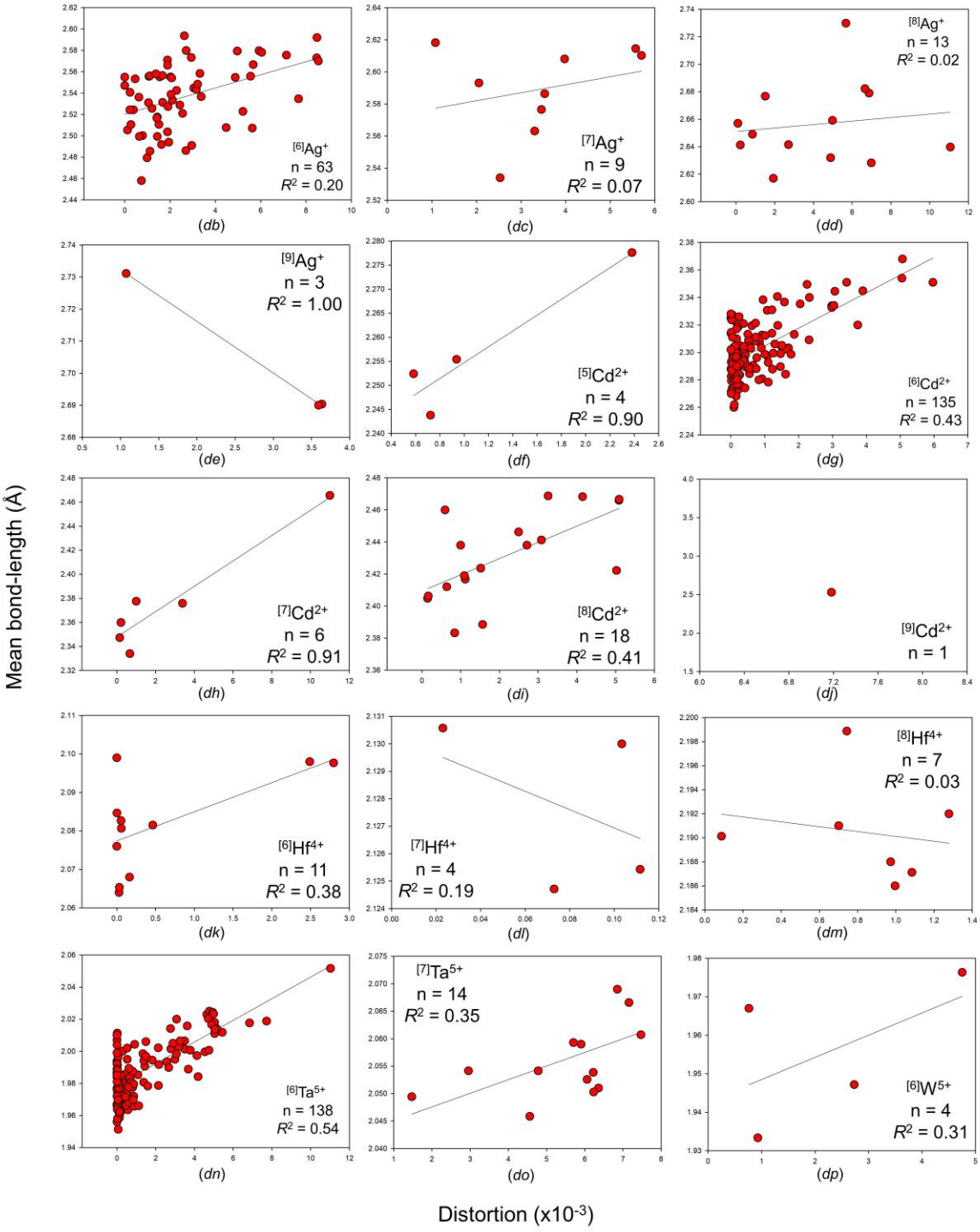
Mean bond-length (Å)
Distortion (x10-3)
(db) [6]Ag+ n = 63 R2 = 0.20
(dc) [7]Ag+ n = 9 R2 = 0.07
(dd) [8]Ag+ n = 13 R2 = 0.02
(de) [9]Ag+ n = 3 R2 = 1.00
(df) [5]Cd2+ n = 4 R2 = 0.90
(dg) [6]Cd2+ n = 135 R2 = 0.43
(dh) [7]Cd2+ n = 6 R2 = 0.91
(di) [8]Cd2+ n = 18 R2 = 0.41
(dj) [9]Cd2+ n = 1
(dk) [6]Hf4+ n = 11 R2 = 0.38
(dl) [7]Hf4+ n = 4 R2 = 0.19
(dm) [8]Hf4+ n = 7 R2 = 0.03
(dn) [6]Ta5+ n = 138 R2 = 0.54
(do) [7]Ta5+ n = 14 R2 = 0.35
(dp) [6]W5+ n = 4 R2 = 0.31

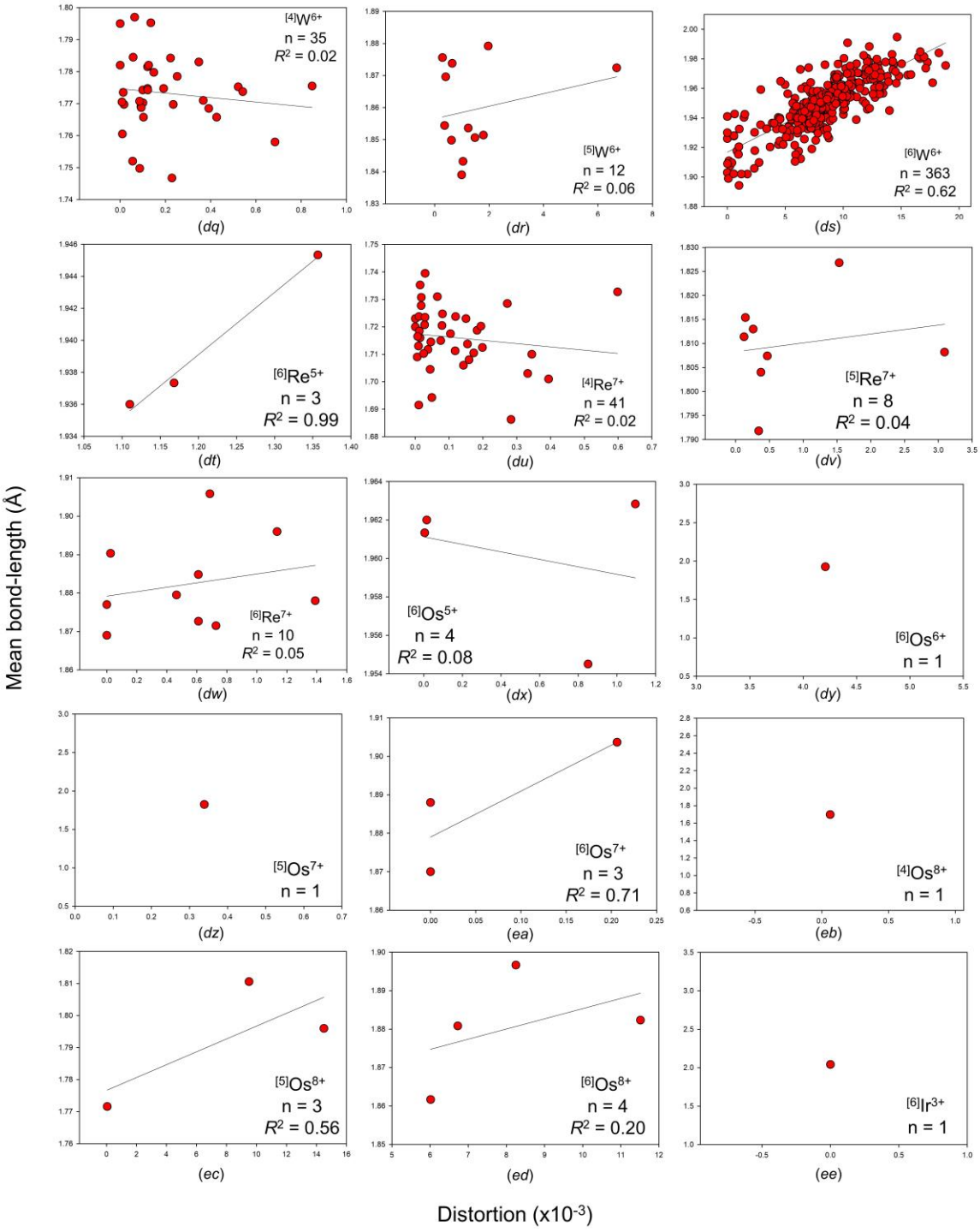
Mean bond-length (Å)
Distortion (x10-3)
[4]W6+
n = 35
R2 = 0.02
(dq)
[5]W6+
n = 12
R2 = 0.06
(dr)
[6]W6+
n = 363
R2 = 0.62
(ds)
[6]Re5+
n = 3
R2 = 0.99
(dt)
[4]Re7+
n = 41
R2 = 0.02
(du)
[5]Re7+
n = 8
R2 = 0.04
(dv)
[6]Re7+
n = 10
R2 = 0.05
(dw)
[6]Os5+
n = 4
R2 = 0.08
(dx)
[6]Os6+
n = 1
(dy)
[5]Os7+
n = 1
(dz)
[6]Os7+
n = 3
R2 = 0.71
(ea)
[4]Os8+
n = 1
(eb)
[5]Os8+
n = 3
R2 = 0.56
(ec)
[6]Os8+
n = 4
R2 = 0.20
(ed)
[6]Ir3+
n = 1
(ee)

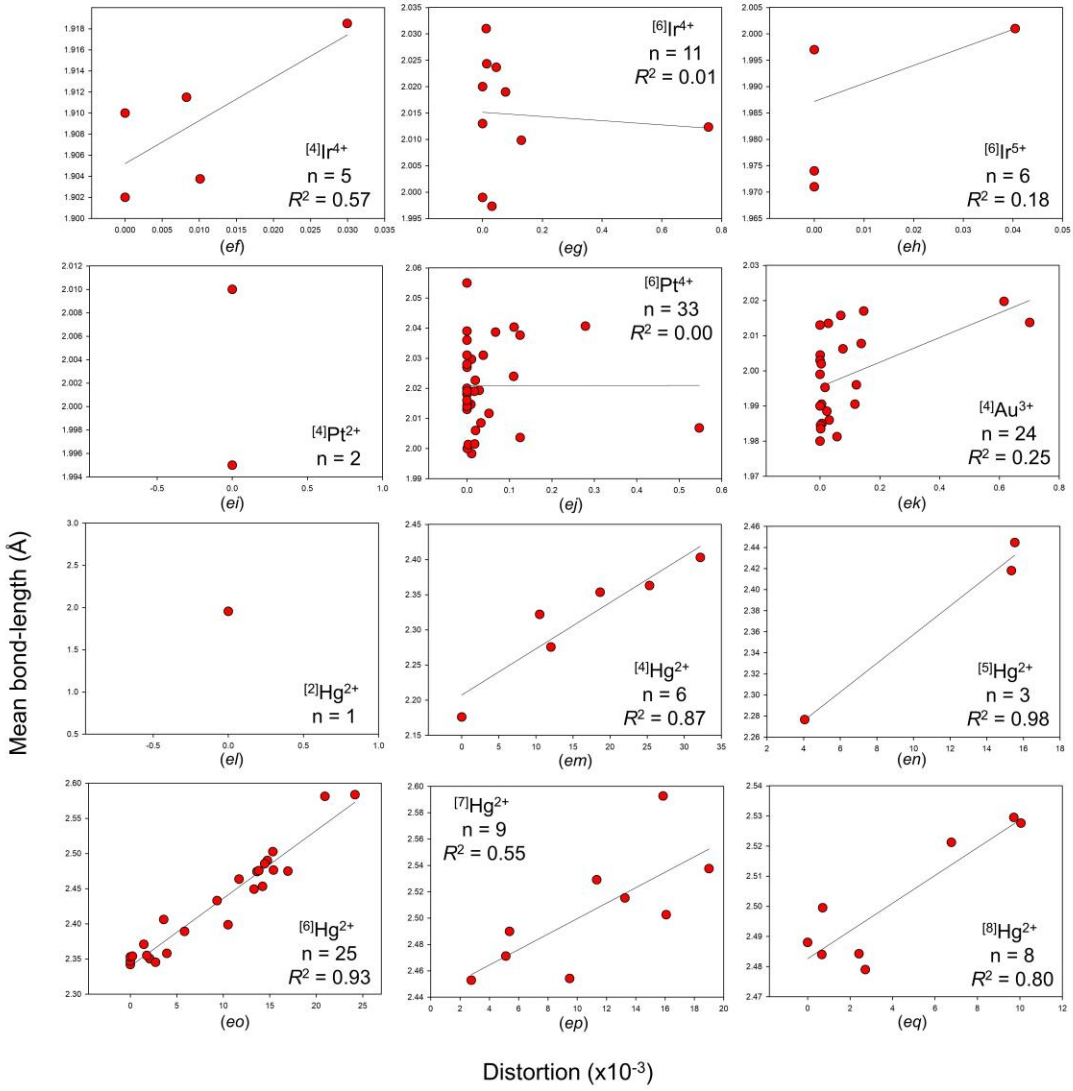

Figure S4: The effect of bond-length distortion on mean bond-length for all configurations of the transition metal ions bonded to O^{2-}: (*a*) $^{[6]}Sc^{3+}$, (*b*) $^{[7]}Sc^{3+}$, (*c*) $^{[8]}Sc^{3+}$, (*d*) $^{[6]}Ti^{3+}$, (*e*) $^{[7]}Ti^{3+}$, (*f*) $^{[8]}Ti^{3+}$, (*g*) $^{[4]}Ti^{4+}$, (*h*) $^{[5]}Ti^{4+}$, (*i*) $^{[6]}Ti^{4+}$, (*j*) $^{[7]}Ti^{4+}$, (*k*) $^{[6]}V^{3+}$, (*l*) $^{[5]}V^{4+}$, (*m*) $^{[6]}V^{4+}$, (*n*) $^{[4]}V^{5+}$, (*o*) $^{[5]}V^{5+}$, (*p*) $^{[6]}V^{5+}$, (*q*) $^{[4]}Cr^{2+}$, (*r*) $^{[5]}Cr^{2+}$, (*s*) $^{[6]}Cr^{2+}$, (*t*) $^{[6]}Cr^{3+}$, (*u*) $^{[4]}Cr^{4+}$, (*v*) $^{[6]}Cr^{4+}$, (*w*) $^{[4]}Cr^{5+}$, (*x*) $^{[4]}Cr^{6+}$, (*y*) $^{[4]}Mn^{2+}$, (*z*) $^{[5]}Mn^{2+}$, (*aa*) $^{[6]}Mn^{2+}$, (*ab*) $^{[7]}Mn^{2+}$, (*ac*) $^{[8]}Mn^{2+}$, (*ad*) $^{[4]}Mn^{3+}$, (*ae*) $^{[5]}Mn^{3+}$, (*af*) $^{[6]}Mn^{3+}$, (*ag*) $^{[4]}Mn^{4+}$, (*ah*) $^{[6]}Mn^{4+}$, (*ai*) $^{[4]}Mn^{5+}$, (*aj*) $^{[4]}Mn^{6+}$, (*ak*) $^{[4]}Mn^{7+}$, (*al*) $^{[3]}Fe^{2+}$, (*am*) $^{[4]}Fe^{2+}$, (*an*) $^{[5]}Fe^{2+}$, (*ao*) $^{[6]}Fe^{2+}$, (*ap*) $^{[8]}Fe^{2+}$, (*aq*) $^{[4]}Fe^{3+}$, (*ar*) $^{[5]}Fe^{3+}$, (*as*) $^{[6]}Fe^{3+}$, (*at*) $^{[8]}Fe^{3+}$, (*au*) $^{[3]}Co^{2+}$, (*av*) $^{[4]}Co^{2+}$, (*aw*) $^{[5]}Co^{2+}$, (*ax*) $^{[6]}Co^{2+}$, (*ay*) $^{[8]}Co^{2+}$, (*az*) $^{[6]}Co^{3+}$, (*ba*) $^{[6]}Co^{4+}$, (*bb*) $^{[2]}Ni^{2+}$, (*bc*) $^{[4]}Ni^{2+}$, (*bd*) $^{[5]}Ni^{2+}$, (*be*) $^{[6]}Ni^{2+}$, (*bf*) $^{[6]}Ni^{4+}$, (*bg*) $^{[2]}Cu^{+}$, (*bh*) $^{[3]}Cu^{+}$, (*bi*) $^{[4]}Cu^{+}$, (*bj*) $^{[4]}Cu^{2+}$, (*bk*) $^{[5]}Cu^{2+}$, (*bl*) $^{[6]}Cu^{2+}$, (*bm*) $^{[8]}Cu^{2+}$, (*bn*) $^{[4]}Cu^{3+}$, (*bo*) $^{[4]}Zn^{2+}$, (*bp*) $^{[5]}Zn^{2+}$, (*bq*) $^{[6]}Zn^{2+}$, (*br*) $^{[6]}Y^{3+}$, (*bs*) $^{[7]}Y^{3+}$, (*bt*) $^{[8]}Y^{3+}$, (*bu*) $^{[9]}Y^{3+}$, (*bv*) $^{[10]}Y^{3+}$, (*bw*) $^{[12]}Y^{3+}$, (*bx*) $^{[6]}Zr^{4+}$, (*by*) $^{[7]}Zr^{4+}$, (*bz*) $^{[8]}Zr^{4+}$, (*ca*) $^{[9]}Zr^{4+}$, (*cb*) $^{[10]}Zr^{4+}$, (*cc*) $^{[6]}Nb^{4+}$, (*cd*) $^{[4]}Nb^{5+}$, (*ce*) $^{[5]}Nb^{5+}$, (*cf*) $^{[6]}Nb^{5+}$, (*cg*) $^{[7]}Nb^{5+}$, (*ch*) $^{[8]}Nb^{5+}$, (*ci*) $^{[6]}Mo^{3+}$, (*cj*) $^{[6]}Mo^{4+}$, (*ck*) $^{[5]}Mo^{5+}$, (*cl*) $^{[6]}Mo^{5+}$, (*cm*) $^{[4]}Mo^{6+}$, (*cn*) $^{[5]}Mo^{6+}$, (*co*) $^{[6]}Mo^{6+}$, (*cp*) $^{[4]}Tc^{7+}$, (*cq*) $^{[6]}Ru^{3+}$, (*cr*) $^{[6]}Ru^{4+}$, (*cs*) $^{[6]}Ru^{5+}$, (*ct*) $^{[6]}Rh^{3+}$, (*cu*) $^{[6]}Rh^{4+}$, (*cv*) $^{[4]}Pd^{2+}$, (*cw*) $^{[6]}Pd^{4+}$, (*cx*) $^{[2]}Ag^{+}$, (*cy*) $^{[3]}Ag^{+}$, (*cz*) $^{[4]}Ag^{+}$, (*da*) $^{[5]}Ag^{+}$, (*db*) $^{[6]}Ag^{+}$, (*dc*) $^{[7]}Ag^{+}$, (*dd*) $^{[8]}Ag^{+}$, (*de*) $^{[9]}Ag^{+}$, (*df*) $^{[5]}Cd^{2+}$, (*dg*) $^{[6]}Cd^{2+}$, (*dh*) $^{[7]}Cd^{2+}$, (*di*) $^{[8]}Cd^{2+}$, (*dj*) $^{[9]}Cd^{2+}$, (*dk*) $^{[6]}Hf^{4+}$, (*dl*) $^{[7]}Hf^{4+}$, (*dm*) $^{[8]}Hf^{4+}$, (*dn*) $^{[6]}Ta^{5+}$, (*do*) $^{[7]}Ta^{5+}$, (*dp*) $^{[6]}W^{5+}$, (*dq*) $^{[4]}W^{6+}$, (*dr*) $^{[5]}W^{6+}$, (*ds*) $^{[6]}W^{6+}$, (*dt*) $^{[6]}Re^{5+}$, (*du*) $^{[4]}Re^{7+}$, (*dv*) $^{[5]}Re^{7+}$, (*dw*) $^{[6]}Re^{7+}$, (*dx*) $^{[6]}Os^{5+}$, (*dy*) $^{[6]}Os^{6+}$, (*dz*) $^{[5]}Os^{7+}$, (*ea*) $^{[6]}Os^{7+}$, (*eb*) $^{[4]}Os^{8+}$, (*ec*) $^{[5]}Os^{8+}$, (*ed*) $^{[6]}Os^{8+}$, (*ee*) $^{[6]}Ir^{3+}$, (*ef*) $^{[4]}Ir^{4+}$, (*eg*) $^{[6]}Ir^{4+}$, (*eh*) $^{[6]}Ir^{5+}$, (*ei*) $^{[4]}Pt^{2+}$, (*ej*) $^{[6]}Pt^{4+}$, (*ek*) $^{[4]}Au^{3+}$, (*el*) $^{[2]}Hg^{2+}$, (*em*) $^{[4]}Hg^{2+}$, (*en*) $^{[5]}Hg^{2+}$, (*eo*) $^{[6]}Hg^{2+}$, (*ep*) $^{[7]}Hg^{2+}$, (*eq*) $^{[8]}Hg^{2+}$.

Table S1 : *A priori* bond valences for crystal-structure refinements used in this work

1292: $Cu^{2+}{}_5O_2(PO_4)_2$					
	*Cu*1	*Cu*2	*Cu*3	*P*	∑
*O*1		0.367 ×2↓ ×2→		1.265	2
*O*2		0.551		1.449	2
*O*3	0.388 ×2↓		0.277 ×2↓ ×2→	1.059	2
*O*4		0.329	0.444	1.227	2
*O*5	0.612 ×2↓	0.385	0.501 ×2↓ ×2→		2
∑	2	2	2	5	

1640: $(Hg^{2+}(H_2O)_6)(Cl^{7+}O_4)_2$				
	Hg	*Cl*	*H*	∑
*O*1	0.333 ×6↓		0.833 ×2→	2
*O*2		1.667 ×3↓	0.167 ×2→	2
*O*3		2.000		2
∑	2	7	1	

2279: $Ba_3Cu^{2+}(Sb^{5+}{}_2O_9)$							
∑	*Ba*1	*Ba*2	*Ba*3	*Cu*	*Sb*1	*Sb*2	∑
*O*1	0.206 ×3↓	0.175 ×6↓ ×2→	0.152 ×3↓	0.396 ×3↓	0.896 ×3↓		2
*O*2	0.080 ×6↓ ×2→	0.149 ×3↓	0.026 ×3↓	0.270 ×3↓	0.770 ×3↓	0.724 ×3↓	2
*O*3	0.300 ×3↓	0.268 ×3↓	0.245 ×6↓ ×2→			0.943 ×3↓	2
∑	2	2	2	2	5	5	

8269: $Cr^{3+}(W^{5+}O_4)$			
	Cr	*W*	∑
*O*1	0.542 ×4↓ ×2→	0.917 ×2↓	2
*O*2	0.417	0.792 ×2↓ ×2→	2
*O*3	0.417	0.792 ×2↓ ×2→	2
∑	3	5	

14159: $Na2(Ni^{2+}O_2)$				
	*Na*1	*Na*2	*Ni*	∑
*O*1	0.219 ×2↓ ×2→	0.266 ×2↓ ×2→	0.516 ×2↓ ×2→	2
*O*2	0.188 ×3↓ ×3→	0.234 ×2↓ ×2→	0.484 ×2↓ ×2→	2
∑	1	1	2	

15505: $Y_3Re^{7+}O_8$					
	*Y*1	*Y*2	*Y*3	*Re*	∑
*O*1	0.495	0.486 ×2↓ ×2→	0.533		2
*O*2	0.495	0.486 ×2↓ ×2→	0.533		2

*O*3		0.254	0.302 ×2↓ ×2→	1.143	2
*O*4	0.282 ×2↓ ×2→	0.274		1.162	2
*O*5	0.361		0.399	1.240	2
*O*6	0.273	0.264	0.311	1.152	2
*O*7	0.273	0.264	0.311	1.152	2
*O*8	0.270 ×2↓ ×2→		0.309	1.150	2
∑	3	3	3	7	

15545: $Na_4Zr_2(SiO_4)_3$					
	*Na*1	*Na*2	*Zr*	*Si*	∑
*O*1	0.167 ×6↓	0.104 ×4↓ ×2→	0.646 ×3↓	0.979 ×2↓	2
*O*2		0.146 ×4↓ ×2→	0.688 ×3↓	1.021 ×2↓	2
∑	1	1	4	4	

17062: $Fe^{2+}_2(P_2O_7)$					
	*Fe*1	*Fe*2	*P*1	*P*2	∑
*O*1	0.333	0.333	1.333		2
*O*2	0.333	0.333	1.333		2
*O*3	0.333	0.333	1.333		2
*O*4			1.000	1.000	2
*O*5	0.333	0.333		1.333	2
*O*6	0.333	0.333		1.333	2
*O*7	0.333	0.333		1.333	2
∑	2	2	5	5	

20540: $Li_2[Os^{8+}O_4(OH)_2]$				
	*Li*1	*Li*2	*Os*	∑
*O*1	0.217 ×2↓	0.400 ×2↓	1.383 ×2↓	2
O2	0.417 ×2↓		1.583 ×2↓	2
*O*3	-0.133 ×2↓	0.050 ×4↓ ×2→	1.033 ×2↓	2
∑	1	1	8	

20611: $Rb(Os^{8+}_2O_8(OH))$				
	Rb	*Os*1	*Os*2	∑
*O*1	0.000 ×2↓ ×2→		2.000	2
*O*2	0.000 ×2↓ ×2→		2.000	2
*O*3	0.176 ×2↓ ×2→	1.647		2
*O*4	0.265	1.735		2
*O*5	0.000		2.000	2
*O*6	0.176 ×2↓ ×2→	1.647		2
*O*7	0.000 ×2↓ ×2→		2.000	2

*O*8	0.265	1.735		2
OH	-0.235	1.235		1
∑	1	8	8	

20670: $YCo^{2+}(BO_2)_5$								
	Co	*Y*	*B*1	*B*2	*B*3	*B*4	*B*5	∑
*O*1	0.300	0.246	0.715	0.738				2
*O*2	0.323		0.738			0.939		2
*O*3		0.273	0.742				0.985	2
*O*4	0.390		0.805		0.806			2
*O*5	0.300	0.246		0.738	0.716			2
*O*6		0.259 ×2↓ ×2→		0.752	0.729			2
*O*7		0.280		0.772		0.949		2
*O*8		0.259			0.749		0.992	2
*O*9	0.344 ×2↓ ×2→	0.290					1.023	2
*O*10		0.444 ×2↓ ×2→				1.113		2
∑	2	3	3	3	3	3	3	

24819: $Na_5Nb^{5+}O_5$					
	*Na*1	*Na*2	*Na*3	*Nb*	∑
*O*1	0.181 ×2↓	0.181 ×2↓ ×2→	0.238 ×2↓ ×2→	0.981 ×2↓	2
*O*2	0.229 ×2↓	0.229 ×2↓ ×2→	0.286	1.029 ×2↓	2
*O*3	0.181	0.181 ×2→	0.238 ×2→	0.981	2
∑	1	1	1	5	

24973: $Ca_4Mn^{3+}{}_3B_3O_{12}CO_3$						
	*Ca*1	*Ca*2	*Mn*	*B*	*C*	∑
*O*1	0.177 ×3↓	0.318	0.480	1.025		2
*O*2	0.177 ×3↓	0.318	0.480	1.025		2
*O*3		0.242	0.404 ×2↓ ×2→	0.949		2
*O*4	0.313 ×3↓	0.455	0.616 ×2↓ ×2→			2
*O*5		0.222 ×3↓ ×3→			1.333 ×3↓	2
∑	2	2	3	3	4	

33194: $Pb^{2+}HfO_3$					
	*Pb*1	*Pb*2	*Hf*1	*Hf*2	∑
*O*1	0.174 ×4↓ ×4→		0.645	0.661	2
*O*2		0.166 ×4↓ ×4→	0.661	0.676	2
*O*3	0.221	0.197 ×2↓ ×2→	0.692 ×2↓ ×2→		2
*O*4	0.179 ×2↓ ×2→	0.155 ×2↓ ×2→		0.666 ×2↓ ×2→	2
*O*5	0.184 ×2→	0.161 ×2→	0.655 ×2→		2

*O*6	0.179 ×2→	0.155 ×2→		0.666 ×2→	2
*O*7	0.184 ×2→	0.161 ×2→	0.655 ×2→		2
*O*8	0.179 ×2→	0.155 ×2→		0.666 ×2→	2
∑	2	2	4	4	

33783: $La(Nb^{5+}{}_5O_{14})$					
	La	*Nb*1	*Nb*2	*Nb*3	∑
*O*1	0.211 ×2↓		0.894 ×2↓ ×2→		2
*O*2	0.210 ×4↓ ×2→	0.688	0.893		2
*O*3	0.348 ×2↓	0.826 ×2↓ ×2→			2
*O*4		0.591	0.796	0.614 ×2↓	2
*O*5		0.591	0.796	0.614 ×2↓	2
*O*6	0.261 ×4↓ ×2→	0.739 ×2↓ ×2→			2
*O*7				1.000 ×2↓ ×2→	2
*O*8			0.727 ×2→	0.545	2
∑	3	5	5	5	

33800: $La_3Ti^{4+}O_4Cl_5$					
	*La*1	*La*2	*La*3	*Ti*	∑
*O*1			0.542 ×2↓ ×2→	0.915	2
*O*2		0.540 ×2↓ ×2→		0.920	2
*O*3	0.253	0.245	0.252	0.625 ×2↓ ×2→	2
*O*4	0.543 ×2↓ ×2→			0.915	2
*Cl*1	0.253	0.244	0.252 ×2↓ ×2→		1
*Cl*2	0.254	0.246 ×2↓ ×2→	0.253		1
*Cl*3		0.248 ×3↓ ×3→	0.255		1
*Cl*4	0.250 ×3↓ ×3→		0.249		1
*Cl*5	0.202 ×2↓ ×2→	0.194	0.201 ×2↓ ×2→		1
∑	3	3	3	4	

33802: $Sr_2(Ru^{4+}O_4)$			
	Sr	*Ru*	∑
*O*1	0.179 ×4↓ ×4→	0.641 ×4↓ ×2→	2
*O*2	0.256 ×5↓ ×5→	0.718 ×2↓	2
∑	2	4	

33863: $Ba_4Ir^{4+}{}_3O_{10}$					
	*Ba*1	*Ba*2	*Ir*1	*Ir*2	∑
*O*1	0.182 ×3↓ ×3→	0.153	0.663 ×2↓	0.638	2
*O*2	0.187 ×2↓ ×2→	0.158 ×2↓ ×2→	0.668 ×2↓	0.643	2
*O*3	0.187 ×2↓ ×2→	0.158 ×2↓ ×2→	0.668 ×2↓	0.643	2

*O*4	0.326	0.297 ×3↓ ×3→		0.782	2
*O*5	0.191 ×2↓ ×2→	0.162 ×2↓ ×2→		0.647 ×2↓ ×2→	2
∑	2	2	4	4	

34392: $K_6(Mn^{3+}{}_2O_6)$					
	*K*1	*K*2	*K*3	*Mn*	∑
*O*1	0.135	0.135	0.155 ×2↓ ×2→	0.710 ×2↓ ×2→	2
*O*2	0.234 ×2↓ ×2→	0.234 ×2↓ ×2→	0.254	0.809	2
*O*3	0.198 ×2↓ ×2→	0.198 ×2↓ ×2→	0.218 ×2↓ ×2→	0.772	2
∑	1	1	1	3	

35084: $Cd_3Te^{6+}O_6$				
	*Cd*1	*Cd*2	*Te*	∑
*O*1	0.373 ×2↓	0.294 ×2↓ ×2→	1.039 ×2↓	2
*O*2	0.314 ×2↓	0.235 ×3↓ ×3→	0.980 ×2↓	2
*O*3	0.314 ×2↓	0.235 ×3↓ ×3→	0.980 ×2↓	2
∑	2	2	6	

35407: $CdPt^{4+}{}_3O_6$				
	Cd	*Pt*1	*Pt*2	∑
*O*1	0.286 ×4↓ ×2→		0.714 ×2↓ ×2→	2
*O*2	0.214 ×4↓	0.500 ×4↓	0.643 ×4↓ ×2→	2
∑	2	2	4	

36608: $Sm^{3+}(Ti^{4+}O_3Cl)$			
	Sm	*Ti*	∑
*O*1	0.320	0.560 ×3↓ ×3→	2
*O*2	0.587 ×2↓ ×2→	0.827	2
*O*3	0.507	0.747 ×2↓ ×2→	2
Cl	0.250 ×4↓ ×4→		1
∑	3	4	

36626: $Nb^{5+}(PO_4)O$			
	Nb	*P*	∑
*O*1	0.750	1.250	2
*O*2	1.000 ×2↓ ×2→		2
*O*3	0.750	1.250	2
*O*4	0.750	1.250	2
*O*5	0.750	1.250	2
∑	5	5	

40249: $KNa_3(W^{6+}O_5)$					
	*Na*1	*Na*2	*K*	*W*	∑
*O*1	0.192	0.197 ×2→	0.111 ×2↓ ×2→	1.192	2
*O*2	0.197 ×2↓	0.202 ×3↓ ×3→		1.197 ×2↓	2
*O*3	0.192	0.197 ×2→	0.111 ×2↓ ×2→	1.192	2
*O*4	0.221		0.139 ×4↓ ×4→	1.221	2
∑	1	1	1	6	

40312: $SrZn(V^{5+}_2O_7)$					
	Sr	*Zn*	*V*1	*V*2	∑
*O*1	0.260	0.414	1.326		2
*O*2	0.260	0.414	1.326		2
*O*3	0.260	0.414	1.326		2
*O*4	-0.046		1.021	1.025	2
*O*5	0.310 ×2↓ ×2→			1.381	2
*O*6	0.259	0.412		1.329	2
*O*7	0.194 ×2↓ ×2→	0.347		1.265	2
∑	2	2	5	5	

40850: $Mn^{2+}(V^{5+}_2O_6)$			
	Mn	*V*	∑
*O*1	0.417 ×4↓ ×2→	1.167	2
*O*2	0.167 ×2↓	0.917 ×2↓ ×2→	2
*O*3		0.667 ×3↓ ×3→	2
∑	2	5	

49746: $Na_5(Os^{7+}O_6)$					
	*Na*1	*Na*2	*Na*3	*Os*	∑
*O*1	0.167 ×4↓ ×2→	0.167 ×4↓	0.167 ×4↓ ×2→	1.167 ×4↓	2
*O*2	0.167 ×2↓ ×2→	0.167 ×2↓	0.167 ×2↓ ×2→	1.167 ×2↓	2
∑	1	1	1	7	

50010: $Cs(V^{5+}_3O_8)$				
	Cs	*V*1	*V*2	∑
*O*1	0.500	1.500		2
*O*2	-0.375	0.625	0.875 ×2→	2
*O*3		0.500 ×2↓	0.750 ×2↓ ×2→	2
*O*4	0.188 ×6↓×3		1.438	2
*O*5	-0.062 ×4↓ ×2→	0.938 ×2↓	1.188	2
∑	1	5	5	

50038: $K_2Fe^{2+}{}_2Nb^{5+}{}_4O_{13}$					
	K	*Fe*	*Nb*1	*Nb*2	∑
*O*1	-0.083 ×2↓	0.259 ×2↓ ×2→	0.693	0.872	2
*O*2	0.176 ×2↓ ×2→	0.518		1.130	2
*O*3	0.090 ×2↓		0.866	1.044	2
*O*4	0.221 ×2↓ ×2→	0.562	0.996		2
*O*5		0.039		0.651 ×3↓ ×3→	2
*O*6	0.075 ×2↓ ×4→		0.851 ×2→		2
*O*7	0.021 ×2↓ ×2→	0.363	0.797 ×2↓ ×2→		2
∑	1	2	5	5	

50459: $Cu^{2+}{}_4O(PO_4)_2$						
	*Cu*1	*Cu*2	*Cu*3	*P*1	*P*2	∑
*O*1	0.551			1.449		2
*O*2		0.293	0.295 ×2→	1.118		2
*O*3		0.391 ×2↓	0.393	1.216 ×2↓		2
*O*4	0.335	0.408			1.257	2
*O*5			0.384 ×2→		1.231	2
*O*6	0.335 ×2↓		0.409		1.256 ×2↓	2
*O*7	0.445	0.517	0.519 ×2→			2
∑	2	2	2	5	5	

55272: $Ca_2ZrB(Al_9O_{18})$						
	Ca	*Al*1	*Al*2	*Zr*	*B*	∑
*O*1		0.444 ×2↓ ×2→	0.444 ×2↓	0.667 ×3↓		2
*O*2	0.500 ×4↓	0.667 ×2↓ ×2→	0.667 ×2↓			2
*O*3		0.444 ×2→	0.444	0.667 ×3↓		2
*O*4		0.333 ×2→	0.333		1.000 ×3↓	2
∑	2	3	3	4	3	

59111: $HfSiO_4$			
	Hf	*Si*	∑
O	0.500 ×8↓ ×2→	1.000 ×4↓	2
∑	4	4	

59244: $LiV^{3+}(Si_2O_6)$				
	Li	*V*	*Si*	∑
*O*1	0.125 ×2↓	0.450 ×4↓ ×2→	0.975	2
*O*2	0.275 ×2↓	0.600 ×2↓	1.125	2
*O*3	0.100 ×2↓		0.950 ×2↓ ×2→	2
∑	1	3	4	

59819: $Ce^{4+}_2(Cr^{6+}O_4)_4(H_2O)_2$							
	*Ce*1	*Ce*2	*Cr*1	*Cr*2	*Cr*3	*Cr*4	∑
*O*1			2.000				2
*O*2		0.632	1.368				2
*O*3		0.632	1.368				2
*O*4	0.737		1.263				2
*O*5		0.474		1.526			2
*O*6		0.474		1.526			2
*O*7		0.474		1.526			2
*O*8	0.579			1.421			2
*O*9	0.553				1.447		2
*O*10		0.447			1.553		2
*O*11	0.553				1.447		2
*O*12		0.447			1.553		2
*O*13		0.421				1.579	2
*O*14	0.526					1.474	2
*O*15	0.526					1.474	2
*O*16	0.526					1.474	2
∑	4	4	6	6	6	6	

62577: $CaNb^{5+}_2(P_4O_{13})(P_2O_7)O$								
	*Nb*1	*Nb*2	*Ca*	*P*1	*P*2	*P*3	*P*4	∑
*O*1			0.267 ×2↓	1.733				2
*O*2		0.782 ×2↓		1.218				2
*O*3				1 ×2→				2
*O*4				1.049	0.951			2
*O*5	0.805 ×2↓				1.195			2
*O*6			0.316 ×2↓		1.684			2
*O*7		0.831 ×2↓			1.169			2
*O*8	0.837 ×2↓					1.163 ×2↓		2
*O*9			0.348			1.652		2
*O*10						1.169	0.978	2
*O*11	0.859 ×2↓						1.141 ×2↓	2
*O*12		0.261					1.739	2
*O*13		1.515	0.458					2
∑	5	5	2	5	5	5	5	

63103: $Y_2Ba_2Cu^{2+}Pt^{4+}O_8$							
	*Ba*1	*Ba*2	*Cu*	*Y*1	*Y*2	*Pt*	∑
*O*1	0.232	0.206 ×3↓ ×3→	0.440			0.711	2

*O*2	0.177 ×2↓	0.151 ×2↓	0.385 ×2↓	0.430 ×4↓ ×2→	0.427 ×2↓		2
*O*3	0.174 ×4↓ ×2→	0.148 ×2↓		0.427 ×2↓	0.424 ×2↓	0.653 ×2↓	2
*O*4	0.174 ×2↓ ×2→	0.148		0.427	0.424	0.653	2
*O*5	0.186 ×2↓	0.160 ×4↓ ×2→	0.394 ×2↓		0.436 ×2↓	0.665 ×2↓	2
∑	2	2	2	3	3	4	

64634: $V^{3+}_2(V^{4+}O(P_2O_7)_2$					
	*V*1	*V*2	*P*1	*P*2	∑
*O*1		0.583		1.417	2
*O*2	0.500 ×2↓	0.333	1.167		2
*O*3	0.500 ×2↓	0.333		1.167	2
*O*4		0.583	1.417		2
*O*5		0.583		1.417	2
*O*6		0.583	1.417		2
*O*7			1.000 ×2→		2
*O*8	2.000				2
*O*9				1.000 ×2→	2
∑	4	3	5	5	

65237: $Na_6(O_2(Cu^{3+}O_2)_2)$										
	$Na1$	$Na2$	$Na3$	$Na4$	$Na5$	$Na6$	$Cu1$	$Cu2$	$Cu3$	∑
$O1$	0.167 ×2↓	0.250 ×2↓	0.167 ×2↓	0.194	0.194	0.250	0.778 ×2↓			2
$O2$				0.139 ×2↓ ×2→	0.139 ×2↓ ×2→		0.722 ×2↓	0.722 ×2↓		2
$O3$	0.167 ×2↓		0.167 ×2↓	0.194	0.194	0.250 ×2↓ ×2→		0.778 ×2↓		2
$O4$				0.139 ×2→	0.139 ×2→				0.722 ×2↓ ×2→	2
$O5$	0.167 ×2↓	0.250 ×2↓	0.167 ×2↓	0.194	0.194	0.250			0.778 ×2↓	2
∑	1	1	1	1	1	1	3	3	3	

65407: $Na_3Sc_2(PO_4)_3$					
	*Na*1	*Na*2	*Sc*	*P*	∑
*O*1		0.106 ×4↓ ×2→	0.519 ×3↓	1.269 ×2↓	2
*O*2	0.153 ×6↓	0.067 ×4↓ ×2→	0.481 ×3↓	1.231 ×2↓	2
∑	0.92	0.693	3	5	

65476: $Ni^{2+}{}_5HfB_2O_{10}$								
	*Ni*1	*Ni*2	*Ni*3	*Ni*4	*Hf*	*B*1	*B*2	∑
*O*1	0.392 ×2↓		0.425 ×2↓	0.427	0.756 ×2↓			2
*O*2	0.308 ×2↓	0.339 ×4↓ ×2→		0.343	0.672 ×2↓			2
*O*3		0.322		0.326 ×2→		1.025		2
*O*4		0.322		0.326 ×2→			1.025	2
*O*5	0.299			0.334 ×2→		1.033		2
*O*6				0.243 ×2→	0.572		0.942	2
*O*7			0.242 ×2↓ ×2→		0.573	0.943		2
*O*8	0.300		0.333 ×2↓ ×2→				1.034	2
∑	2	2	2	2	4	3	3	

65512: $Zr(Mo^{6+}O_4)_2$				
	*Zr*1	*Zr*2	*Mo*	∑
*O*1			2.000	2
*O*2		0.667 ×3↓	1.333	2
*O*3		0.667 ×3↓	1.333	2
*O*4	0.667 ×6↓		1.333	2
∑	4	4	6	

65614: $Y_2Ba_2Cu^{2+}Pt^{4+}O_8$						
	*Ba*1	*Ba*2	*Cu*	*Y*	*Pt*	∑
*O*1	0.228 ×4↓	0.163 ×4↓ ×2→	0.380 ×2↓	0.402 ×2↓	0.663 ×4↓	2
*O*2		0.174 ×3↓ ×3→	0.391	0.413	0.674 ×2↓	2
*O*3	0.272 ×4↓	0.207 ×4↓ ×2→	0.424 ×2↓	0.446 ×4↓ ×2→		2
∑	2	2	2	3	4	

66994: $Cs(Np^{5+}O_2)(Mo^{6+}O_4)$				
	Cs	*Np*	*Mo*	∑
*O*1	0.384 ×2↓ ×2→	1.232		2
*O*2	0.288 ×3↓ ×3→	1.137		2
*O*3	-0.446	0.402	1.022 ×2↓ ×2→	2
*O*4	-0.292	0.557 ×2↓ ×2→	1.177	2
*O*5	-0.292	0.557 ×2↓ ×2→	1.177	2
*O*6	0.133 ×3↓ ×3→		1.601	2

∑	1	5	6	

67726: $Cu^{2+}_3Ba(V^{5+}O_4)_2(OH)_2$						
	Ba	*Cu*1	*Cu*2	*V*	*H*	∑
*O*1		0.459 ×2↓	0.459 ×2↓ ×2→		0.623	2
*O*2	0.195 ×4↓	0.270 ×4↓	0.270 ×2↓	1.264 ×2↓		2
*O*3	0.195 ×2↓		0.270 ×2↓ ×2→	1.264		2
*O*4	0.138 ×6↓ ×3→			1.208	0.377	2
∑	2	2	2	5	1	

68279: $Pr^{3+}_2(Mo^{6+}_4O_{15})$							
	*Pr*1	*Pr*2	*Mo*1	*Mo*2	*Mo*3	*Mo*4	∑
*O*1		0.433	1.567				2
*O*2		0.433	1.567				2
*O*3	0.507		1.493				2
*O*4	0.388	0.239	1.373				2
*O*5	0.490			1.510			2
*O*6	0.490			1.510			2
*O*7		0.416		1.584			2
*O*8	0.376	0.228		1.396			2
*O*9					1.413	0.587	2
*O*10		0.333			1.667		2
*O*11	0.321	0.172			1.507		2
*O*12					1.413	0.587	2
*O*13						2.000	2
*O*14		0.746				1.254	2
*O*15	0.427					0.786 ×2↓ ×2→	2
∑	3	3	6	6	6	6	

68614: $Cu^{+}La(W^{6+}_2O_8)$					
	Cu	*La*	*W*1	*W*2	∑
*O*1		0.148	0.959	0.892	2
*O*2	-0.136		0.734 ×2↓ ×2→	0.668	2
*O*3		0.148	0.959	0.892	2
*O*4		0.595	1.405		2
*O*5		0.396 ×2↓ ×2→	1.207		2
*O*6	0.379	0.439		1.183	2
*O*7	0.379	0.439		1.183	2
*O*8	0.379	0.439		1.183	2
∑	1	3	6	6	

69088: $Ba(Mo^{5+}{}_2P_4O_{16})$					
	Ba	*Mo*	*P*1	*P*2	∑
*O*1		2.000			2
*O*2	0.124 ×2↓	0.577	1.299		2
*O*3	0.150 ×2↓	0.604		1.246	2
*O*4		0.639	1.361		2
*O*5	0.150 ×2↓	0.604		1.246	2
*O*6	0.124 ×2↓	0.577	1.299		2
*O*7			1.040	0.960	2
*O*8	0.452 ×2↓			1.548	2
∑	2	5	5	5	

71450: $Sr_2(V^{4+}O_4)$			
	Sr	*V*	∑
*O*1	0.179 ×4↓ ×4→	0.641 ×4↓ ×2→	2
*O*2	0.256 ×5↓ ×5→	0.718 ×2↓	2
∑	2	4	

71562: $Ca_2Y(As^{5+}O_4)(W^{6+}O_4)_2$					
	Ca	*Y*	*W*	*As*	∑
*O*1	0.240 ×4↓ ×2→		1.519 ×2↓		2
*O*2	0.202 ×2↓	0.317 ×4↓	1.481 ×2↓		2
*O*3	0.317 ×2↓	0.433 ×4↓		1.250 ×4↓	2
∑	2	3	6	5	

72302: $Cr^{2+}{}_3Cr^{3+}{}_4(PO_4)_6$									
	*Cr*1	*Cr*2	*Cr*3	*Cr*4	*P*1	*P*2	*P*3	*P*4	∑
*O*1				0.509			1.491		2
*O*2					1.020		0.980		2
*O*3						1.000		1.000	2
*O*4	0.459 ×2↓			0.249		1.293			2
*O*5		0.425 ×2↓	0.383		1.192				2
*O*6	0.583 ×2↓					1.417			2
*O*7	0.459 ×2↓			0.249				1.293	2
*O*8			0.467	0.255	1.277				2
*O*9		0.438 ×2↓	0.396				1.166		2
*O*10		0.636 ×2↓					1.364		2
*O*11			0.710			1.290			2
*O*12			0.584					1.416	2
*O*13			0.460	0.248				1.292	2
*O*14				0.489	1.511				2

∑	3	3	3	2	5	5	5	5	

72312: $Ba_2(Hg_3Pd^{4+}{}_5Pd^{2+}{}_2O_{14})$								
	Ba	*Hg*1	*Hg*2	*Pd*1	*Pd*2	*Pd*3	*Pd*4	∑
*O*1	0.250			0.750		0.500 ×2↓ ×2→		2
*O*2	-0.021 ×2↓ ×2→	0.563	1.000 ×2↓	0.479				2
*O*3	0.378 ×2↓ ×2→						0.622 ×2↓ ×2→	2
*O*4	0.250 ×2↓			0.750 ×2↓	0.500 ×4↓	0.500 ×2↓		2
*O*5	0.134 ×4↓ ×2→	0.718 ×2↓		0.635 ×2↓			0.378 ×2↓	2
∑	2	2	2	4	2	2	2	

72682: $Cs_2(Ti^{4+}O)(P_2O_7)$						
	*Cs*1	*Cs*2	*Ti*	*P*1	*P*2	∑
*O*1	0.009	0.017	0.739	1.235		2
*O*2	0.191 ×2↓ ×2→	0.199		1.418		2
*O*3	0.009	0.017	0.739	1.235		2
*O*4	-0.115	-0.107		1.111	1.111	2
*O*5	0.191 ×2↓ ×2→	0.199			1.418	2
*O*6	0.314	0.321 ×2↓ ×2→	1.044			2
*O*7	0.009	0.017	0.739		1.235	2
*O*8	0.009	0.017	0.739		1.235	2
∑	1	1	4	5	5	

72714: $Ti^{3+}PO_4$							
	*Ti*1	*Ti*2	*P*1	*P*2	*P*3	*P*4	∑
*O*1	0.429 ×2→			1.143			2
*O*2	0.429 ×2→		1.143				2
*O*3	0.429 ×2→					1.143	2
*O*4	0.429 ×2→					1.143	2
*O*5	0.643					1.357 ×2↓	2
*O*6	0.643		1.357 ×2↓				2
*O*7		0.643		1.357 ×2↓			2
*O*8		0.643			1.357 ×2↓		2
*O*9		0.429 ×2→			1.143		2
*O*10		0.429 ×2→			1.143		2
*O*11		0.429 ×2→		1.143			2
*O*12		0.429 ×2→	1.143				2
∑	3	3	5	5	5	5	

72872: $Co^{3+}Re^{5+}O_4$			
	Co	*Re*	∑

*O*1	0.417 ×2↓	0.792 ×4↓ ×2→	2
*O*2	0.542 ×4↓ ×2→	0.917 ×2↓	2
∑	3	5	

72886: $Ca(V^{4+}O)_2(PO_4)_2$				
	Ca	*V*	*P*	∑
*O*1	0.250 ×2↓	0.500	1.250	2
*O*2	0.250 ×2↓	0.500	1.250	2
*O*3		1.000 ×2↓ ×2→		2
*O*4	0.250 ×2↓	0.500	1.250	2
*O*5	0.250 ×2↓	0.500	1.250	2
∑	2	4	5	

73183: $Ba_3Ca(Ru^{5+}_2O_9)$					
	*Ba*1	*Ba*2	*Ca*	*Ru*	∑
*O*1	0.119 ×6↓ ×2→	0.095 ×3↓ ×2→		0.786 ×3↓ ×2→	2
*O*2	0.214 ×6↓	0.190 ×9↓ ×3→	0.333 ×6↓	0.881 ×3↓	2
∑	2	2	2	5	

73261: $Cr^{2+}_3Cr^{3+}_4(PO_4)_6$								
	*Cr*1	*Cr*2	*Cr*3	*Cr*4	*P*1	*P*2	*P*3	∑
*O*1			0.415 ×2↓ ×2→				1.170	2
*O*2			0.460	0.358		1.182		2
*O*3			0.443	0.341			1.216	2
*O*4	0.511			0.409	1.080			2
*O*5	0.460			0.358		1.182		2
*O*6	0.639					1.361		2
*O*7	0.409 ×2↓ ×2→						1.182	2
*O*8		0.568 ×2↓					1.432	2
*O*9		0.174 ×2↓	0.552			1.274		2
*O*10			0.715		1.285			2
*O*11	0.572				1.428			2
*O*12		0.259 ×2↓		0.535	1.207			2
∑	3	2	3	2	5	5	5	

73686: $Th(V^{5+}_2O_7)$							
	*Th*1	*Th*2	*V*1	*V*2	*V*3	*V*4	∑
*O*1	0.425 ×2↓ ×2→		1.151				2
*O*2	0.637		1.363				2
*O*3		0.665	1.335				2
*O*4	0.425 ×2↓ ×2→		1.151				2

*O*5		0.649		1.351			2
*O*6	0.621			1.379			2
*O*7		0.433 ×2↓ ×2→		1.135			2
*O*8		0.433 ×2↓ ×2→		1.135			2
*O*9	0.291 ×2↓ ×2→				1.417		2
*O*10		0.466			1.534		2
*O*11					1.024	0.976	2
*O*12					1.024	0.976	2
*O*13	0.462					1.538	2
*O*14		0.490				1.510	2
∑	4	4	5	5	5	5	

74212: $CaTi^{4+}O_3$			
	Ca	*Ti*	
*O*1	0.167 ×4↓ ×4→	0.667 ×2↓ ×2→	2
*O*2	0.167 ×8↓ ×4→	0.667 ×4↓ ×2→	2
	2	4	

75264: $Li_3Nb^{5+}O_4$			
	Li	*Nb*	∑
$O1_{br}$	-0.042 ×3→	0.708 ×3↓ ×3→	2
*O*2	0.208 ×5↓ ×5→	0.958 ×3↓	2
∑	1	5	

75583: $La_2(Ti^{4+}{}_2SiO_9)$						
	*La*1	*La*2	*Ti*1	*Ti*2	*Si*	∑
*O*1	0.280 ×2↓	0.186 ×2↓	0.619 ×2↓		0.914 ×2↓	2
*O*2		0.668			1.332	2
*O*3	0.268	0.174 ×2↓ ×2→		0.544	0.839	2
*O*4	0.454 ×4↓ ×2→	0.361 ×2		0.731 ×2↓		2
*O*5	0.354	0.260	0.693 ×2↓ ×2→			2
*O*6		0.315 ×2↓ ×2→		0.685 ×2↓ ×2→		2
*O*7			0.688 ×2↓ ×2→	0.625		2
∑	3	3	4	4	4	

78180: $La_2(W^{6+}O_4)_3$				
	La	*W*1	*W*2	∑
*O*1	0.095	0.952 ×2↓ ×2→		2
*O*2	0.381 ×2↓ ×2→	1.238		2
*O*3	0.571	1.429		2
*O*4	0.429		1.571 ×2↓	2

*O*5	0.571	1.429		2
*O*6	0.286 ×2↓ ×2→		1.429 ×2↓	2
∑	3	6	6	

78842: $Rb_2(Ti^{4+}O_3)$				
	*Rb*1	*Rb*2	*Ti*	∑
*O*1	0.185 ×2↓ ×2→	0.1885 ×3↓ ×3→	1.074	2
*O*2	0.185 ×3↓ ×3→	0.185 ×2↓ ×2→	1.074	2
*O*3	0.037 ×2↓ ×2→	0.037 ×2↓ ×2→	0.926 ×2↓ ×2→	2
∑	1	1	4	

79517: $Cs(Mo^{6+}{}_2O_3(PO_4)_2)$						
	Cs	*Mo*1	*Mo*2	*P*1	*P*2	∑
*O*1	0.382 ×2↓ ×2→	1.237				2
*O*2	-0.087	0.768		1.319		2
*O*3		0.724		1.276		2
*O*4	-0.083	0.772			1.311	2
*O*5	-0.087	0.768		1.319		2
*O*6		0.731			1.269	2
*O*7	0.255 ×2↓ ×2→		1.491			2
*O*8	0.255 ×2↓ ×2→		1.491			2
*O*9			0.915	1.085		2
*O*10	-0.210		1.026		1.184	2
*O*11	-0.157 ×2↓ ×2→		1.078		1.236	2
∑	1	5	6	5	5	

79702: $K_2Ni^{2+}(W^{6+}O_2(PO_4)_2)$					
	K	*Ni*	*W*	*P*	∑
*O*1	-0.059		0.908 ×2↓	1.151	2
*O*2	-0.059		0.908 ×2↓	1.151	2
*O*3	0.125 ×3↓ ×3→	0.292 ×2↓		1.334	2
*O*4	0.156 ×2↓ ×2→	0.324 ×2↓		1.365	2
*O*5	0.216 ×2↓ ×2→	0.384 ×2↓	1.183 ×2↓		2
∑	1	2	6	5	

79734: $K_3(Nb^{5+}{}_3O_6)(Si_2O_7)$				
	K	*Nb*	*Si*	∑
*O*1	0.017 ×3→		0.975 ×2→	2
*O*2	0.105 ×3↓ ×3→	0.843 ×2↓ ×2→		2
*O*3	0.131 ×2↓ ×2→	0.869 ×2↓ ×2→		2
*O*4	0.051 ×8↓ ×4→	0.788 ×2↓	1.008 ×3↓	2

∑	1	5	4	

80423: $CsTa^{5+}(B_2O_5)$				
	Cs	*Ta*	*B*	∑
*O*1	0.114 ×4↓ ×2→	0.750 ×2↓	1.023	2
*O*2	0.114 ×4↓ ×2→	0.750 ×2↓	1.023	2
*O*3		1.000 ×2↓ ×2→		2
*O*4	0.045 ×2↓ ×2→		0.955 ×2→	2
∑	1	5	3	

80430: $KMn^{3+}(Se^{6+}O_4)_2$				
	K	*Mn*	*Se*	∑
*O*1		0.512 ×2↓	1.488	2
*O*2	0.142 ×6↓×3		1.574	2
*O*3	0.037 ×2↓	0.494 ×2↓	1.469	2
*O*4	0.037 ×2↓	0.494 ×2↓	1.469	2
∑	1	3	6	

81473: $BaCo^{2+}{}_2(Si_2O_7)$							
	Ba	*Co*1	*Co*2	*Co*3	*Si*1	*Si*2	∑
*O*1			0.526 ×2↓	0.449	1.025		2
*O*2	0.246 ×2↓ ×2→		0.474 ×2↓			1.035	2
*O*3	0.227			0.379 ×2↓ ×2→		1.016	2
*O*4	0.210	0.429 ×2↓		0.362		0.999	2
*O*5	0.161				0.889	0.950	2
*O*6	0.351	0.571 ×2↓			1.079		2
*O*7	0.280 ×2↓ ×2→			0.432	1.008		2
∑	2	2	2	2	4	4	

82403: $Co^{2+}{}_2Si(P_2O_7)_2$					
	Co	*Si*	*P*1	*P*2	∑
*O*1		1.000 ×2↓	1.000		2
*O*2	0.429		1.571		2
*O*3	0.286 ×2↓ ×2→		1.429		2
*O*4			1.000	1.000	2
*O*5	0.429			1.571	2
*O*6	0.286 ×2↓ ×2→			1.429	2
*O*7		1.000 ×2↓		1.000	2
∑	2	4	5	5	

82488: $Na_4Zr_2Ti^{4+}O_4(CO_3)_4$							
	*Na*1	*Na*2	*Zr*	*Ti*	*C*1	*C*2	∑

*O*1	0.064	0.064		0.595 ×2↓	1.277		2
*O*2	0.091	0.091	0.484			1.333	2
*O*3	0.171		0.563 ×2↓ ×2→	0.702 ×2↓			2
*O*4		0.171	0.563 ×2↓ ×2→	0.702 ×2↓			2
*O*5	0.197 ×2↓ ×2→	0.197			1.410		2
*O*6	-0.007		0.386 ×2↓ ×2→			1.235	2
*O*7	0.098	0.098	0.491		1.312		2
*O*8	0.189	0.190 ×2↓ ×2→				1.431	2
∑	1	1	4	4	4	4	

82685: $SrV^{3+}_2O(PO_4)_2$						
	Sr	*V*1	*V*2	*P*1	*P*2	∑
*O*1	0.273 ×2↓	0.472 ×2↓			1.255 ×2↓	2
*O*2	0.269	0.468		1.263		2
*O*3		0.609			1.391	2
*O*4	0.269	0.468		1.263		2
*O*5	0.312	0.511	0.588 ×2↓ ×2→			2
*O*6	0.117		0.392 ×2↓ ×2→		1.099	2
*O*7	0.243 ×2↓		0.519 ×2↓	1.237 ×2↓		2
∑	2	3	3	5	5	

83285: $K(Fe^{3+}_{11}O_{17})$						
	K	*Fe*1	*Fe*2	*Fe*3	*Fe*4	∑
*O*1		0.379 ×2↓ ×2→	0.742 ×3↓		0.500 ×6↓	2
*O*2	0.167 ×6↓	0.583 ×2↓ ×2→		0.667 ×3↓		2
*O*3		0.409 ×3→	0.773			2
*O*4		0.667 ×3→				2
*O*5	0.000 ×3↓ ×3→			1.000 ×2→		2
∑	1	3	3	3	3	

85042: $Mn^{2+}Zn_2Ta^{5+}_2O_8$				
	Zn	*Mn*	*Ta*	∑
*O*1	0.410 ×3↓ ×3→		0.769	2
*O*2	0.256 ×3↓ ×3→		0.615 ×2↓ ×2→	2
*O*3		0.417 ×4↓ ×2→	1.167	2
*O*4		0.167 ×2↓	0.917×2↓ ×2→	2
∑	2	2	5	

85497: $NaY(GeO_4)$				
	Na	*Y*	*Ge*	∑
*O*1	0.197 ×2↓ ×2→	0.561	1.045	2

*O*2	0.197 ×2↓ ×2→	0.561	1.045	2
*O*3	0.106 ×2↓	0.470 ×4↓ ×2→	0.955 ×2↓	2
∑	1	3	4	

85735: $ZnLiNb^{5+}O_4$				
	Li	*Zn*	*Nb*	∑
*O*1	0.212 ×4↓ ×2→	0.818 ×2↓	0.758 ×2↓	2
*O*2	0.076 ×2↓	0.682 ×2↓	0.621 ×4↓ ×2→	2
∑	1	2	5	

86144: $W^{6+}O_3$		
	W	∑
*O*1	1.000 ×2↓ ×2→	2
*O*2	1.000 ×4↓ ×2→	2
∑	6	

88879: $Nb^{4+}O2$			
	*Nb*1	*Nb*2	∑
*O*1	0.667	0.667 ×2↓ ×2→	2
*O*2	0.667 ×2↓ ×2→	0.667	2
*O*3	0.667	0.667 ×2↓ ×2→	2
*O*4	0.667 ×2↓ ×2→	0.667	2
∑	4	4	

89466: $V^{5+}{}_2Se^{4+}{}_2O_9$					
	*Se*1	*Se*2	*V*1	*V*2	∑
*O*1			2.000		2
*O*2	1.200		0.400	0.400	2
*O*3		1.400	0.600		2
*O*4	1.400		0.600		2
*O*5			1.000	1.000	2
*O*6		1.200	0.400	0.400	2
*O*7	1.400			0.600	2
*O*8		1.400		0.600	2
*O*9				2.000	2
∑	4	4	5	5	

89506: $K(Mn^{7+}O_4)$			
	K	*Mn*	∑

*O*1	0.083 ×3↓ ×3→	1.750	2
*O*2	0.083 ×3↓ ×3→	1.750	2
*O*3	0.083 ×6↓×3	1.750 ×2↓	2
∑	1	7	

90110: $Tl^{+}_{2}(Te^{4+}Mo^{6+}_{2}O_{6}(PO_{4})_{2})$					
	Tl	*Mo*	*P*	*Te*	∑
*O*1	0.005	0.924		1.071 ×2↓	2
*O*2	-0.066 ×2↓ ×2→	0.853	1.279		2
*O*3	0.360 ×2↓ ×2→	1.280			2
*O*4	0.360 ×2↓ ×2→	1.280			2
*O*5	-0.088	0.831	1.257		2
*O*6	-0.088	0.831	1.257		2
*O*7	-0.137		1.208	0.929 ×2↓	2
∑	1	6	5	4	

91748: $Mg_{4}Nb^{5+}_{2}O_{9}$				
	*Mg*1	*Mg*2	*Nb*	∑
*O*1		0.250 ×3↓ ×2→	0.750 ×3↓ ×2→	2
*O*2	0.333 ×6↓ ×2→	0.417 ×3↓	0.917 ×3↓	2
∑	2	2	5	

92317: $(V^{4+}O)(Re^{7+}O_{4})_{2}$				
	V	*Re*1	*Re*2	∑
*O*1	0.333 ×2↓	1.667 ×2↓		2
*O*2	0.333	1.667		2
*O*3		2.000		2
*O*4	0.500 ×2↓		1.500 ×2↓	2
*O*5			2.000	2
*O*6			2.000	2
*O*7	2.000			2
∑	4	7	7	

92489: $Eu^{3+}_{4}(Au^{3+}_{2}O_{9})$				
	Au	*Eu*1	*Eu*2	∑
*O*1		0.500 ×2→	0.500 ×2→	2
*O*2	0.750	0.417 ×2↓ ×2→	0.417	2
*O*3	0.750	0.417	0.417 ×2↓ ×2→	2
*O*4	0.750	0.417 ×2↓ ×2→	0.417	2
*O*5	0.750	0.417	0.417 ×2↓ ×2→	2
∑	3	3	3	

92508: $Pr_3(Re^{7+}O_8)$					
	*Pr*1	*Pr*2	*Pr*3	*Re*	∑
*O*1	0.484 ×2↓ ×2→	0.518	0.513		2
*O*2	0.484 ×2↓ ×2→	0.518	0.513		2
*O*3	0.276 ×2→		0.305 ×2↓	1.144	2
*O*4	0.266	0.300 ×2↓ ×2→		1.134	2
*O*5		0.390	0.385	1.225	2
*O*6	0.267	0.301	0.296	1.136	2
*O*7	0.255	0.289	0.294	1.133	2
*O*8		0.384	0.388	1.228	2
∑	3	3	3	7	

94743: $NaKLaNb^{5+}O_5$					
	La	*Nb*	*Na*	*K*	∑
*O*1	0.375 ×8↓ ×2→	0.978 ×4↓	0.178 ×4↓	0.047 ×8↓ ×2→	2
*O*2		1.088	0.288	0.156 ×4↓ ×4→	2
∑	3	5	1	1	

95493: $Gd(Mn^{3+}O_3)$			
	Gd	*Mn*	∑
*O*1	0.441 ×2↓ ×2→	0.559 ×2↓ ×2→	2
*O*2	0.353 ×6↓×3	0.471 ×4↓ ×2→	2
∑	3	3	

95929: $KMg(V^{5+}{}_5O_{14})(H_2O)_8$																							
	*V*1	*V*2	*V*3	*V*4	*V*5	*K*	*Mg*	*H*1	*H*2	*H*3	*H*4	*H*5	*H*6	*H*7	*H*8	*H*9	*H*10	*H*11	*H*12	*H*13	*H*14	*H*15	*H*16	∑
*O*1		1.510				0.049													0.441					2
*O*2		0.870			0.756					0.137		0.236												2
*O*3	0.845	0.573	0.609															-0.027						2
*O*4	1.111				0.725			0.164																2
*O*5	1.102			0.682									0.216											2
*O*6	0.553 ×2↓ ×2→	0.280	0.316	0.132	0.166																			2
*O*7			1.568			0.071											0.361							2
*O*8			0.988	0.804					0.137							0.071								2
*O*9			0.920		0.770															0.155	0.155			2
*O*10		1.203		1.055		-0.258																		2
*O*11				0.876	0.910						0.214													2
*O*12				1.451		0.139								0.410										2
*O*13	0.836	0.564	0.600																					2
*O*14					1.673	0.327																		2
*O*15 (*O*I1)							0.301	0.836	0.863															2

*O*16 (*O*I2)						0.135	0.217			0.863	0.786													2
*O*17 (*O*I3)						-0.063						0.764	0.784		0.309								0.207	2
*O*18 (*O*I4)						0.320								0.590	0.691							0.398		2
*O*19 (*O*I5)							0.432									0.929	0.639							2
*O*20 (*O*I6)						0.166	0.249											1.027	0.559					2
*O*21 (*O*I7)						0.114	0.196													0.845	0.845			2
*O*22 (*O*I8)							0.605															0.602	0.793	2
∑	5	5	5	5	5	1	2	1	1	1	1	1	1	1	1	1	1	1	1	1	1	1	1	

96359: $SrFe^{3+}_3(PO_4)_3O$								
	*Sr*1	*Fe*1	*Fe*2	*Fe*3	*P*1	*P*2	*P*3	∑
*O*1		0.671 ×2↓ ×2→	0.658					2
*O*2	0.239 ×2↓	0.467 ×2↓			1.295 ×2↓			2
*O*3	0.077 ×2↓ ×2→		0.292	0.434	1.120			2
*O*4	0.247		0.462		1.290			2
*O*5	0.259 ×2↓		0.474 ×2↓			1.267 ×2↓		2
*O*6	0.134	0.362 ×2↓ ×2→				1.141		2
*O*7				0.675		1.325		2
*O*8	0.235 ×2↓			0.591 ×2↓			1.174 ×2↓	2
*O*9			0.638				1.362	2
*O*10				0.709			1.291	2
∑	2	3	3	3	5	5	5	

96454: $Pb^{2+}_2(Mo^{4+}_2O(PO_4)_2(P_2O_7))$					
	*Pb*2	*Mo*	*P*1	*P*2	∑
*O*1		1.000 ×2→			2
*O*2	0.206	0.612		1.182	2
*O*3	0.206	0.612		1.182	2
*O*4		0.629	1.371		2
*O*5		0.629	1.371		2
*O*6	0.112 ×2↓ ×2→	0.518	1.259		2
*O*7			1.000 ×2→		2
*O*8	0.341 ×2↓ ×2→			1.318	2
*O*9	0.341 ×2↓ ×2→			1.318	2
∑	2	4	5	5	

97525: $Ba_6Ru^{5+}_2Na_2Mn^{5+}_2O_{17}$								
	Na	*Ba*1	*Ba*2	*Ba*3	*Ba*4	*Mn*	*Ru*	∑
*O*1	0.167 ×3↓		0.167 ×6↓ ×2→	0.333 ×6↓		1.167 ×3↓		2
*O*2	0.167 ×3↓	0.267 ×6↓ ×2→	0.167 ×3↓		0.233 ×6↓		0.900 ×3↓	2
*O*3		0.133 ×3↓ ×2→			0.100 ×6↓ ×2→		0.767 ×3↓ ×2→	2
*O*4			0.500			1.500		2
∑	1	2	2	2	2	5	5	

99594: $Mn^{2+}V^{5+}Sb^{5+}O_6$				
	Mn	*V*	*Sb*	∑
*O*1	0.133 ×2↓	0.833 ×2↓	1.033 ×2↓	2
*O*2	0.433 ×4↓ ×2→	1.133 ×2↓		2
*O*3		0.533 ×2↓	0.733 ×4↓ ×2→	2
∑	2	5	5	

100082: $CaMn^{2+}_2(BeSiO_4)_3$										
	Ca	*Mn*1	*Mn*2	*Be*1	*Be*2	*Be*3	*Si*1	*Si*2	*Si*3	∑
*O*1	0.194 ×2↓ ×2→					0.556	1.056			2
*O*2	0.194 ×2↓ ×2→			0.556				1.056		2
*O*3	0.194 ×2↓ ×2→				0.556				1.056	2
*O*4		0.306	0.306	0.444			0.944			2
*O*5		0.306	0.306		0.444			0.944		2
*O*6		0.306	0.306			0.444			0.944	2
*O*7	0.139		0.361		0.500		1.000			2
*O*8	0.139	0.361				0.500		1.000		2
*O*9	0.139		0.361	0.500					1.000	2
*O*10	0.139	0.361		0.500			1.000			2
*O*11	0.139		0.361		0.500			1.000		2
*O*12	0.139	0.361				0.500			1.000	2
∑	2	2	2	2	2	2	4	4	4	

100158: $Na_2Ca_4ZrNb^{5+}(Si_2O_7)_2FO_3$													
	*Na*1	*Na*2	*Ca*1	*Ca*2	*Ca*3	*Ca*4	*Zr*	*Nb*	*Si*1	*Si*2	*Si*3	*Si*4	∑
*O*1				0.355		0.349		0.762	0.534				2
*O*2	-0.019			0.435		0.428				1.156			2
*O*3	-0.252			0.202				0.758	1.292				2
*O*4	-0.233					0.364		0.777		1.092			2
*O*5			0.124				0.750		1.126				2
*O*6	0.170		0.140				0.767			0.923			2
*O*7		0.445	0.819		0.578						0.158		2
*O*8		0.738			0.871		0.004					0.386	2
*O*9		-0.206	0.168				0.795				1.242		2
*O*10			0.151		-0.090		0.778					1.160	2
*O*11		-0.003		0.282		0.276					1.445		2
*O*12				0.265	0.113	0.259						1.363	2
*O*13	0.309				0.038		0.906	0.747					2
*O*14	0.499	0.095	0.469					0.937					2
*O*15		0.176		0.461	0.309			1.018					2
*O*16	0.076		0.046						1.048	0.829			2
*O*17		-0.292	0.082								1.155	1.091	2
F	0.450	0.046			0.179	0.325							1
∑	1	1	2	2	2	2	4	5	4	4	4	4	

100278: $ScAlO_3$			
	Sc	*Al*	∑
*O*1	0.441 ×2↓ ×2→	0.559 ×2↓ ×2→	2
*O*2	0.353 ×6↓ ×3→	0.471 ×4↓ ×2→	2
∑	3	3	

100571: $Ba_{10}(Re^{7+}O_5)_6Br_2$				
	*Ba*1	*Ba*2	*Re*	∑
*O*1		0.195 ×3↓ ×3→	1.414	2
*O*2	0.218 ×6↓ ×2→	0.172 ×2↓	1.391 ×2↓	2
*O*3	0.230 ×3↓	0.184 ×4↓ ×2→	1.402 ×2↓	2
*B*r		0.167 ×2↓ ×6→		1
∑	2	2	7	

156736: $Ca_3Mn^{2+}(Sb^{5+}{}_4O_{14})$							
	Mn	*Ca*1	*Ca*2	*Sb*1	*Sb*2	*Sb*3	∑
*O*1	0.280 ×2↓	0.154 ×2↓			0.771 ×2↓	0.795	2
*O*2			0.244			0.878 ×2↓ ×2→	2
*O*3	0.278 ×2↓		0.159		0.769 ×2↓	0.793	2
*O*4		0.343 ×2↓	0.349 ×2↓ ×2→		0.960 ×2↓		2
*O*5	0.442 ×2↓	0.316 ×2↓	0.322	0.920 ×2↓			2
*O*6		0.187 ×2↓	0.194	0.791 ×2↓		0.828	2
*O*7			0.192 ×2↓ ×2→	0.789 ×2↓		0.827	2
∑	2	2	2	5	5	5	

157733: $NaFe^{3+}Si_2O_6$				
	Na	*Fe*	*Si*	∑
*O*1	0.113 ×2↓	0.45 ×4↓ ×2→	0.988	2
*O*2	0.263 ×2↓	0.6 ×2↓	1.138	2
*O*3	0.062 ×4↓ ×2→		0.938 ×2↓ ×2→	2
∑	1	3	4	

170119: $K_2Mo^{6+}O_2(I^{5+}O_3)_4$					
	K	*I*1	*I*2	*Mo*	∑
*O*1	-0.143	0.502	0.593	1.048 ×2↓	2
*O*2	0.178 ×2↓ ×2→	0.822 ×2↓ ×2→			2
*O*3	0.155 ×2↓ ×2→	0.800	0.891		2
*O*4		0.454	0.545	1.001 ×2↓	2
*O*5	0.155 ×2↓ ×2→	0.800	0.891		2
*O*6	0.155 ×2↓ ×2→	0.800	0.891		2
*O*7	-0.141		0.595 ×2↓ ×2→	0.951 ×2↓	2
∑	1	5	5	6	

171028: $Cu^{2+}{}_2V^{5+}{}_2O_7$					
	*Cu*1	*Cu*2	*V*1	*V*2	∑
*O*1	0.356 ×2↓ ×2→			1.288	2
*O*2	0.355 ×2↓ ×2→		1.291		2
*O*3		0.363 ×2↓ ×2→	1.274		2
*O*4		0.365 ×2↓ ×2→		1.271	2
*O*5	0.044		0.980	0.976	2

*O*6	0.534			1.466	2	
*O*7		0.545	1.455		2	
∑	2	2	5	5		

171758: $Na_2Mo^{6+}{}_3Te^{4+}{}_3O_{16}$							
	*Na*1	*Na*2	*Mo*1	*Mo*2	*Te*1	*Te*2	∑
*O*1				0.975	1.025 ×2↓		2
*O*2	-0.087 ×2↓				0.975 ×2↓	1.112	2
*O*3			0.772 ×2↓	0.521		0.707	2
*O*4	-0.058 ×2↓	0.323 ×2↓		0.956		1.142	2
*O*5			1.125 ×2↓	0.875			2
*O*6		-0.142 ×2↓	1.103 ×2↓			1.039	2
*O*7	0.323 ×2↓	0.341 ×2↓		1.336			2
*O*8	0.323 ×2↓	0.341 ×2↓		1.336			2
∑	1	1	6	6	4	4	

200128: $LiSc(SiO_3)_2$				
	Li	*Sc*	*Si*	∑
*O*1	0.125 ×2↓	0.450 ×4↓ ×2→	0.975	2
*O*2	0.275 ×2↓	0.600 ×2↓	1.125	2
*O*3	0.100 ×2↓		0.950 ×2↓ ×2→	2
∑	1	3	4	

200743: $Cd_2P_6O_{17}$					
	*Cd*1	*P*1	*P*2	*P*3	∑
*O*1		0.898	1.102		2
*O*2	0.398	1.602			2
*O*3	0.398	1.602			2
*O*4		0.898	1.102		2
*O*5	0.296		1.704		2
*O*6			1.093	0.907	2
*O*7				1.000 ×2→	2
*O*8	0.389			1.611	2
*O*9	0.259 ×2↓ ×2→			1.481	2
∑	2	5	5	5	

200854: $RbNb^{5+}O_3$						
	*Rb*1	*Rb*2	*Rb*3	*Nb*1	*Nb*2	∑
*O*1		0.094 ×2↓	0.033 ×2↓ ×2→	0.917	0.923	2
*O*2	-0.240 ×2↓			0.557 ×2↓ ×2→	0.563 ×2↓ ×2→	2
*O*3		0.102 ×2↓	0.041	0.925	0.931	2
*O*4	0.121 ×2↓		0.035	0.919	0.925	2
*O*5	0.291 ×2↓		0.205 ×3↓ ×3→		1.095	2
*O*6	0.328 ×2↓	0.303 ×2↓	0.242	1.126		2
∑	1	1	1	5	5	

201658: $V^{4+}O(HPO_4)(H_2O)_{0.5}$				
	V	*P*	*H*	∑
OH		0.739	0.261	1
*O*2	0.522 ×2↓	1.478 ×2		2
*O*3	0.348 ×2↓ ×2→	1.304		2
*O*4	2.000			2
*O*5	0.261 ×2→		0.739 ×2→	2
∑	4	5	1	

201733: $Cu^{2+}_3(As^{5+}O_4)_2$				
	*Cu*1	*Cu*2	*As*	∑
*O*1	0.500 ×2↓	0.327	1.173	2
*O*2		0.577	1.423	2
*O*3		0.385 ×2↓ ×2→	1.231	2
*O*4	0.500 ×2↓	0.327	1.173	2
∑	2	2	5	

201793: $Tl^{3+}_2(Cr^{6+}O_4)_3$				
	Tl	*Cr*1	*Cr*2	∑
*O*1	0.400 ×2↓ ×2→	1.200		2
*O*2		2.000		2
*O*3	0.600	1.400		2
*O*4	0.500		1.500 ×2↓	2
*O*5	0.600	1.400		2
*O*6	0.500		1.500 ×2↓	2
∑	3	6	6	

202414: $W^{5+}_8P_8O_{40}$			
	W	*P*	∑
*O*1	1.000 ×2↓ ×2→		2
*O*2	0.500	1.500	2
*O*3	0.750	1.250	2
*O*4	1.000 ×2→		2
*O*5	0.750	1.250	2
*O*6		1.000 ×2→	2
∑	5	5	

203048: $PW^{5+}O_5$			
	W	*P*	∑
*O*1	0.75	1.25	2
*O*2	0.75	1.25	2
*O*3	0.75	1.25	2
*O*4	0.75	1.25	2

*O*5	1 ×2↓ ×2→		2
∑	5	5	

203232: $DyTa^{5+}_{7}O_{19}$				
	Dy	*Ta*1	*Ta*2	∑
*O*1			1.000 ×2→	2
*O*2	0.417 ×6↓	0.833 ×6↓	0.750	2
*O*3			0.667 ×3↓ ×3→	2
*O*4			0.667 ×3→	2
*O*5	0.250 ×2↓		0.583 ×3→	2
∑	3	5	5	

247056: $LiCr^{3+}(Mo^{6+}_{4})_2$					
	Li	*Cr*	*Mo*1	*Mo*2	∑
*O*1		0.385 ×2↓ ×2→		1.230	2
*O*2	0.317			1.683	2
*O*3		0.562	1.438		2
*O*4		0.562	1.438		2
*O*5	0.038	0.559		1.404	2
*O*6	0.027	0.548	1.425		2
*O*7	0.301		1.699		2
*O*8	0.317			1.683	2
∑	1	3	6	6	

248227: $K_3V^{5+}_{5}O_{14}$				
	K	*V*1	*V*2	
*O*1	0.190 ×2↓ ×3→	1.430		2
*O*2	0.260 ×3↓ ×3→		1.220	2
*O*3	0.02 ×2↓ ×2→		0.980 ×2↓ ×2→	2
*O*4	-0.050 ×4↓ ×2→	1.190 ×3↓	0.910 ×2↓	2
	1	5	5	

249142: $Pb^{2+}_{2}(V^{4+}O(PO_4)_2)$						
	*P*b1	*P*b2	*V*	*P*1	*P*2	∑
*O*1	0.123		0.648		1.229	2
*O*2		0.531		1.469		2
*O*3	0.329 ×2↓ ×2→	0.202		1.140		2
*O*4	0.329 ×2↓ ×2→	0.202		1.140		2
*O*5	0.123		0.648		1.229	2
*O*6		0.039	0.690		1.271	2
*O*7		0.039	0.690		1.271	2
*O*8	0.438	0.312		1.250		2
*O*9		0.675	1.325			2
∑	2	2	4	5	5	

250466: $Na_2(Co^{2+}(NO_3)_4)$								
	*Na*1	*Na*2	*Co*	*N*1	*N*2	*N*3	*N*4	∑
*O*1	0.101		0.271	1.628				2
*O*2	0.236			1.764				2
*O*3		0.140	0.252	1.609				2
*O*4	0.101		0.271		1.628			2
*O*5		0.140	0.252		1.609			2
*O*6	0.236				1.764			2
*O*7	0.119	0.177				1.704		2
*O*8		0.120	0.232			1.648		2
*O*9		0.120	0.232			1.648		2
*O*10	0.085		0.255				1.661	2
*O*11		0.123	0.235				1.641	2
*O*12	0.122	0.180					1.698	2
∑	1	1	2	5	5	5	5	

280066: $Cs_2(Mo^{6+}{}_3O_{10})$				
	Cs	*Mo*1	*Mo*2	∑
*O*1	0.192 ×3↓ ×3→	1.424 ×2↓		2
*O*2	-0.172 ×2↓ ×2→	1.060 ×2↓	1.285	2
*O*3		0.516 ×2↓	0.742 ×2↓ ×2→	2
*O*4	0.181 ×2↓ ×2→		1.638	2
*O*5	0.136 ×3↓ ×3→		1.593	2
∑	1	6	6	

280154: $Na_2Ca_3Ta^{5+}{}_2O_9$					
	Na	*Ca*1	*Ca*2	*Ta*	∑
*O*1	0.167 ×6↓ ×2→	0.500 ×3↓	0.333 ×6↓	0.833 ×3↓	2
*O*2		0.167 ×3↓ ×2→		0.833 ×3↓ ×2→	2
∑	1	2	2	5	

280292: $Hg^{2+}(PO_3)_2$				
	Hg	*P*1	*P*2	∑
*O*1	0.429	1.571		2
*O*2	0.286 ×2↓ ×2→	1.429		2
*O*3	0.286 ×2↓ ×2→		1.429	2
*O*4	0.429		1.571	2
*O*5		1.000	1.000	2
*O*6		1.000	1.000	2
∑	2	5	5	

280309: $SrCr^{2+}(P_2O_7)$					
	Sr	*Cr*	*P*1	*P*2	∑

*O*1	0.252	0.412	1.336		2
*O*2	0.253	0.413		1.334	2
*O*3	0.189 ×2↓ ×2→	0.349	1.273		2
*O*4			1.002	0.998	2
*O*5	0.305 ×2↓ ×2→		1.389		2
*O*6	0.253	0.413		1.334	2
*O*7	0.253	0.413		1.334	2
∑	2	2	5	5	

280501: $Rb(Ti^{4+}O)(As^{5+}O_4)$							
	*Rb*1	*Rb*2	*Ti*1	*Ti*2	*As*1	*As*2	∑
*O*1	0.226	0.187	0.363		1.224		2
*O*2	0.226	0.187	0.363		1.224		2
*O*3	0.209	0.171		0.379	1.241		2
*O*4		0.240		0.449	1.310		2
*O*5	0.433	0.394	0.570	0.603			2
*O*6	0.039	0.000	0.964	0.997			2
*O*7	-0.042	-0.081	0.883			1.241	2
*O*8	-0.070		0.856			1.213	2
*O*9	-0.010	-0.049		0.786		1.273	2
*O*10	-0.010	-0.049		0.786		1.273	2
∑	1	1	4	4	5	1.241	

280589: $YMn^{3+}O_3$				
	*Y*1	*Y*2	*Mn*	∑
*O*1	0.444 ×3↓	0.444 ×3↓ ×2→	0.667	2
*O*2	0.444 ×3↓	0.444 ×3↓ ×2→	0.667	2
*O*3	0.333		0.556 ×3→	2
*O*4		0.333	0.556 ×2↓ ×3→	2
∑	3	3	3	

280775: $V^{5+}AlMo^{6+}O_7$				
	Al	*V*	*Mo*	∑
*O*1	0.500 ×2↓		1.500 ×2↓	2
*O*2	0.500		1.500	2
*O*3	0.500		1.500	2
*O*4	0.500 ×2↓	0.750 ×4↓ ×2→		2
*O*5		2.000		2
∑	3	5	6	

280902: $NaZnFe^{3+}{}_2(PO_4)_3$								
	Na	*Zn*	*Fe*1	*Fe*2	*P*1	*P*2	*P*3	∑
*O*1	0.252	0.416			1.332			2
*O*2				0.775	1.225			2

*O*3	0.186		0.549		1.265			2
*O*4	0.098	0.263	0.462		1.178			2
*O*5			0.621			1.379		2
*O*6	0.084			0.712		1.204		2
*O*7	0.088	0.252	0.451			1.209		2
*O*8	0.088	0.252	0.451			1.209		2
*O*9		0.550					1.450	2
*O*10	0.103			0.731			1.166	2
*O*11				0.782			1.218	2
*O*12	0.102	0.266	0.465				1.166	2
∑	1	2	3	3	5	5	5	

281197: $Pr_3Mo^{5+}O_7$					
	*Pr*1	*Pr*2	*Pr*3	*Mo*	∑
*O*1	0.354	0.355	0.414	0.877	2
*O*2		0.355 ×2↓ ×2→	0.414	0.877	2
*O*3	0.470 ×2↓ ×2→		0.530 ×2↓ ×2→		2
*O*4	0.354	0.355	0.414	0.877	2
*O*5		0.224	0.283	0.746 ×2↓ ×2→	2
*O*6	0.354	0.355	0.414	0.877	2
*O*7	0.499 ×2↓ ×2→	0.501 ×2↓ ×2→			2
∑	3	3	3	5	

281210: $NaAl(Mo^{6+}O_4)_2$				
	Na	*Al*	*Mo*	∑
*O*1	0.062 ×2↓	0.500 ×2↓	1.438	2
*O*2	0.062 ×2↓	0.500 ×2↓	1.438	2
*O*3	0.063 ×2↓	0.500 ×2↓	1.438	2
*O*4	0.313 ×2↓		1.688	2
∑	1	3	6	

281503: $BaTe^{4+}Mo^{6+}{}_2O_9$					
	Ba	*Te*	*Mo*1	*Mo*2	∑
*O*1		0.829	0.580	0.592	2
*O*2	0.095	1.071		0.834	2
*O*3		0.829	0.580	0.592	2
*O*4	-0.147 ×2↓ ×2→	1.272	1.023		2
*O*5	0.277 ×2↓ ×2→		1.447		2
*O*6	0.208 ×3↓ ×3→		1.377		2
*O*7			0.994	1.006	2
*O*8	0.409			1.591	2
*O*9	0.205 ×3↓ ×3→			1.386	2
∑	2	4	6	6	

400438: $Cu^{2+}_2Co^{2+}O(B_2O_5)$						
	*Cu*1	*Cu*2	*Co*	*B*1	*B*2	∑
*O*1		0.373 ×2↓ ×2→	0.231	1.023		2
*O*2	0.470	0.604	0.463 ×2↓ ×2→			2
*O*3	0.304 ×3↓ ×3→			1.089		2
*O*4		0.412	0.270 ×2↓ ×2→		1.047	2
*O*5	0.309 ×2↓ ×2→		0.302		1.079	2
*O*6		0.238		0.888	0.874	2
∑	2	2	2	3	3	

400764: $SrCo^{2+}_2(As^{5+}O_4)_2$						
	Sr	*Co*1	*Co*2	*As*1	*As*2	∑
*O*1		0.384	0.381		1.235	2
*O*2		0.273	0.269 ×2↓ ×2→	1.189		2
*O*3	0.169	0.305 ×2↓ ×2→		1.221		2
*O*4	0.170	0.306	0.302	1.222		2
*O*5	0.293	0.428			1.279	2
*O*6	0.294		0.426		1.280	2
*O*7	0.316 ×2↓ ×2→			1.368		2
*O*8	0.221 ×2↓ ×2→		0.352		1.206	2
∑	2	2	2	5	5	

400802: $KCu^{2+}_5V^{5+}_3O_{13}$										
	K	*Cu*1	*Cu*2	*Cu*3	*Cu*4	*Cu*5	*V*1	*V*2	*V*3	∑
*O*1			0.303		0.303	0.242			1.151	2
*O*2		0.450	0.494	0.562	0.494					2
*O*3	0.094	0.475					1.431			2
*O*4	-0.013	0.367			0.412			1.234		2
*O*5		0.341		0.452				1.207		2
*O*6			0.251	0.318	0.251		1.179			2
*O*7	0.078 ×3↓ ×3→					0.441		1.325		2
*O*8	0.334		0.273		0.273				1.121	2
*O*9			0.267	0.334		0.205	1.195			2
*O*10	0.091 ×2↓ ×2→					0.454			1.364	2
*O*11				0.334	0.267	0.205	1.195			2
*O*12	0.091 ×2↓ ×2→					0.454			1.364	2
*O*13	-0.013	0.367	0.412					1.234		2
∑	1	2	2	2	2	2	5	5	5	

401042: $K_4(Cu^{2+}V^{5+}_5O_{15}Cl)$					
	K	*Cu*	*V*1	*V*2	∑
*O*1	0.206 ×3↓ ×3→		1.381		2
*O*2	0.158 ×2↓ ×2→	0.352 ×4↓	1.332		2
*O*3	0.025 ×2↓ ×2→		1.200	0.750 ×4↓	2

*O*4	-0.087 ×2→		1.087 ×2→		2
*O*5				2.000	2
Cl	0.102 ×4→	0.296 ×2↓ ×2→			1
∑	1	2	5	5	

401951: $Zn_5Mn^{4+}(BO_3)_2O_4$						
	*Zn*1	*Zn*2	*Zn*3	*Zn*4/*Mn*	*B*	∑
*O*1		0.288 ×4↓ ×2→		0.427	0.988	2
*O*2	0.427	0.425 ×2↓		0.574 ×2↓ ×2→		2
*O*3	0.326 ×2↓ ×2→		0.322 ×2↓		1.025	2
*O*4	0.343		0.339 ×4↓ ×2→	0.490 ×2↓ ×2→		2
*O*5	0.289 ×2↓ ×2→			0.436	0.987	2
∑	2	2	2	3	3	

405153: $Ba_2(Nb^{5+}{}_2Te^{6+}O_{10})$				
	Ba	*Nb*	*Te*	∑
*O*1	0.190 ×2↓ ×2→	0.810 ×2↓ ×2→		2
*O*2	0.175	0.796	1.029 ×2↓	2
*O*3	0.131 ×2↓ ×2→	0.752	0.985 ×2↓	2
*O*4	0.131 ×2↓ ×2→	0.752	0.985 ×2↓	2
*O*5	0.460 ×2↓ ×2→	1.080		2
∑	2	5	6	

405329: $PbCu^{2+}(Cu^{2+}Te^{6+}O_7)$					
	*Pb*1	*Cu*1	*Cu*2	*Te*	∑
*O*1		0.321 ×2→	0.372	0.986	2
*O*2	0.405	0.515 ×2→	0.565		2
*O*3		0.214 ×2↓ ×4→	0.265	0.879	2
*O*4	0.239 ×2↓	0.348	0.399 ×2↓	1.014 ×2↓	2
*O*5	0.279 ×4↓ ×2→	0.388		1.054 ×2↓	2
∑	2	2	2	6	

409521: $Hg^{2+}(V^{5+}{}_2O_6)$			
	Hg	*V*	∑
*O*1	0.167 ×2↓	0.917 ×2↓ ×2→	2
*O*2	0.417 ×4↓ ×2→	1.167	2
*O*3		0.667 ×3↓ ×3→	2
∑	2	5	

409745: $Rb_2(Cr^{6+}{}_2O_7)$					
	*Ag*1	*Ag*2	*Cr*1	*Cr*2	∑
*O*1	-0.225		1.131	1.094	2
*O*2		0.162 ×2↓ ×2→	1.676		2
*O*3	0.267	0.110	1.623		2

*O*4	0.215 ×2↓ ×2→		1.571		2
*O*5	0.249	0.091 ×2↓ ×2→		1.568	2
*O*6	0.279	0.122		1.599	2
*O*7		0.261		1.739	2
∑	1	1	6	6	

411285: $KY(W^{6+}O_4)_2$				
	K	*Y*	*W*	∑
*O*1	0.191 ×4↓ ×2→	0.470 ×2↓	1.148	2
*O*2	-0.048 ×2↓	0.230 ×2↓	0.909 ×2↓ ×2→	2
*O*3	0.122 ×2↓	0.400 ×4↓ ×2→	1.078	2
*O*4	0.022 ×4↓ ×2→		0.978 ×2↓ ×2→	2
∑	1	3	6	

413000: $Rb_2Se^{4+}Mo^{6+}O_6$					
	*Rb*1	*Rb*2	*Mo*	*Se*	∑
*O*1	0.038 ×2↓ ×2→		0.962 ×2↓ ×2→		2
*O*2	-0.039 ×4↓ ×2→	-0.074 ×2↓	0.885 ×2↓	1.267 ×2↓	2
*O*3	0.230 ×4↓ ×2→	0.194 ×4↓ ×2→	1.153 ×2↓		2
*O*4	0.160	0.125 ×3↓ ×3→		1.466	2
∑	1	1	6	4	

415239: $Pd^{2+}(P_2O_7)$				
	*Pd*1	*Pd*2	*P*	∑
*O*1	0.400 ×2↓	0.400 ×2↓	1.200	2
*O*2	0.600 ×2↓		1.400	2
*O*3			1.000 ×2→	2
*O*4		0.600 ×2↓	1.400	2
∑	2	2	5	

415427: $Ce^{3+}Ta^{5+}O_4$			
	Ce	*Ta*	∑
*O*1	0.353	0.824 ×2↓ ×2→	2
*O*2	0.353	0.824 ×2↓ ×2→	2
*O*3	0.382 ×3↓ ×3→	0.853	2
*O*4	0.382 ×3↓ ×3→	0.853	2
∑	3	5	

415460: $Yb(Ta^{5+}O_4)$			
	Yb	*Ta*	∑
*O*1	0.500 ×4↓ ×2→	1.000 ×2↓	2
*O*2	0.250 ×4↓ ×2→	0.750 ×4↓ ×2→	2
∑	3	5	

416590: $Li(Nb^{5+}U^{6+}O_6)$				
	Li	*Nb*	*U*	∑
*O*1	0.240 ×2↓ ×2→		1.520	2
*O*2		0.971	1.029	2
*O*3		0.647 ×2↓ ×2→	0.706	2
*O*4		0.627	0.686 ×2↓ ×2→	2
*O*5		0.627	0.686 ×2↓ ×2→	2
*O*6	0.260 ×2↓ ×2→	1.480		2
∑	1	5	6	

417072: $RbW^{5+}O(P_2O_7)$					
	Rb	*W*	*P*1	*P*2	∑
*O*1	0.394 ×2↓ ×2→	1.212			2
*O*2	-0.030	0.788		1.242	2
*O*3	-0.030	0.788		1.242	2
*O*4		0.727	1.273		2
*O*5		0.727	1.273		2
*O*6	-0.061	0.758	1.303		2
*O*7	-0.212		1.152	1.061	2
*O*8	0.182 ×3↓ ×3→			1.455	2
∑	1	5	5	5	

Table S2 : Values of Δ_{topol} and Δ_{cryst} for 266 transition metal coordination polyhedra taken from 140 crystal structures

	Oxidation state	Coordination number	Δ_{topol}	Δ_{cryst}	ICSD code
Sc	3	6	0.019	0.020	65407
		6	0.067	0.038	200128
		8	0.033	0.102	100278
Ti	3	6	0.095	0.030	72714
		6	0.095	0.042	""
	4	4	0.074	0.107	78842
		5	0.140	0.109	33800
		5	0.098	0.217	72682
		6	0.107	0.102	36608
		6	0.032	0.080	75583
		6	0.055	0.162	""
		6	0.048	0.090	82488
		6	0.235	0.250	280501
		6	0.190	0.295	""
V	3	6	0.067	0.018	59244
		6	0.111	0.030	64634
		6	0.040	0.071	82685
		6	0.072	0.052	""
	4	5	0.480	0.065	64634
		5	0.210	0.186	249142
		6	0.034	0.074	71450
		6	0.222	0.219	72886
		6	0.444	0.123	92317
		6	0.444	0.117	201658
	5	4	0.115	0.033	40312
		4	0.112	0.070	""
		4	0.021	0.156	67726
		4	0.099	0.129	73686
		4	0.115	0.093	""
		4	0.226	0.071	""
		4	0.274	0.154	""
		4	0.135	0.039	171028
		4	0.137	0.069	""
		4	0.091	0.111	400802
		4	0.038	0.040	""
		4	0.114	0.217	""
		4	0.107	0.104	401042
		5	0.250	0.112	50010
		5	0.400	0.179	280775
		5	0.400	0.073	401042
		6	0.167	0.336	40850
		6	0.292	0.314	50010

		6	0.444	0.171	89466
		6	0.444	0.160	""
		6	0.187	0.143	95929
		6	0.361	0.097	""
		6	0.325	0.027	""
		6	0.294	0.129	""
		6	0.305	0.060	""
		6	0.200	0.158	99594
		6	0.167	0.306	409521
Cr	2	5	0.057	0.076	73261
		5	0.020	0.077	280309
		6	0.170	0.118	72302
		6	0.156	0.041	73261
	3	6	0.056	0.065	8269
		6	0.055	0.067	72302
		6	0.091	0.052	""
		6	0.098	0.037	""
		6	0.074	0.038	73261
		6	0.089	0.061	""
		6	0.077	0.068	247056
	6	4	0.250	0.144	59819
		4	0.039	0.045	""
		4	0.053	0.080	""
		4	0.039	0.014	""
		4	0.250	0.164	201793
		4	0.000	0.081	""
		4	0.185	0.074	409745
		4	0.203	0.081	""
Mn	2	6	0.111	0.160	40850
		6	0.111	0.099	85042
		6	0.133	0.183	99594
		6	0.028	0.061	100082
		6	0.028	0.046	""
		6	0.072	0.110	156736
	3	4	0.040	0.092	34392
		5	0.053	0.176	280589
		6	0.077	0.211	24973
		6	0.008	0.211	80430
		6	0.039	0.186	95493
	5	4	0.250	0.097	97525
	7	4	0.000	0.028	89506
Fe	2	6	0.000	0.067	17062
		6	0.000	0.071	""
		6	0.148	0.148	50038

	3	4	0.011	0.075	83285
		4	0.125	0.039	""
		4	0.028	0.029	280902
		5	0.073	0.050	96359
		6	0.111	0.026	83285
		6	0.000	0.003	""
		6	0.114	0.070	96359
		6	0.099	0.066	""
		6	0.067	0.038	157733
		6	0.167	0.090	280902
Co	2	4	0.071	0.072	81473
		4	0.026	0.082	""
		5	0.032	0.070	81473
		6	0.026	0.044	20670
		6	0.063	0.028	82403
		6	0.086	0.063	400328
		6	0.049	0.053	400764
		6	0.053	0.089	""
		8	0.013	0.091	250466
	3	6	0.056	0.126	72872
Ni	2	4	0.016	0.052	14159
		6	0.039	0.024	65476
		6	0.007	0.017	""
		6	0.061	0.031	""
		6	0.035	0.035	""
		6	0.034	0.044	79702
Cu	2	4	0.112	0.055	1292
		4	0.000	0.028	201733
		5	0.060	0.100	1292
		5	0.099	0.033	""
		5	0.078	0.076	50459
		5	0.050	0.133	""
		5	0.051	0.063	""
		5	0.016	0.059	63103
		5	0.019	0.101	65614
		5	0.058	0.122	171028
		5	0.071	0.093	201733
		5	0.087	0.088	400438
		5	0.050	0.063	400802
		5	0.086	0.068	""
		5	0.066	0.091	405329
		6	0.063	0.070	2279
		6	0.084	0.039	67726
		6	0.084	0.041	""

		6	0.096	0.127	171028
		6	0.046	0.161	400438
		6	0.080	0.089	400802
		6	0.080	0.087	""
		6	0.116	0.115	""
		6	0.025	0.143	401042
		6	0.084	0.083	405329
	3	4	0.028	0.021	65237
		4	0.028	0.023	""
		4	0.028	0.018	""
Zn	2	4	0.250	0.277	85735
		5	0.021	0.075	40312
		6	0.077	0.129	85042
		6	0.100	0.055	280902
		6	0.034	0.038	401951
		6	0.061	0.022	""
		6	0.007	0.007	""
Y	3	6	0.040	0.046	85497
		7	0.001	0.044	63103
		7	0.004	0.056	""
		7	0.020	0.077	65614
		8	0.111	0.083	15505
		8	0.085	0.071	""
		8	0.058	0.088	71562
		8	0.072	0.131	411285
		9	0.078	0.110	15505
		10	0.086	0.079	20670
Zr	4	6	0.021	0.054	15545
		6	0.000	0.274	55272
		6	0.000	0.030	65512
		6	0.000	0.041	""
		6	0.221	0.186	100158
		8	0.063	0.040	82488
Nb	4	6	0.000	0.085	88879
		6	0.000	0.085	""
	5	5	0.023	0.094	24819
		5	0.035	0.112	94743
		6	0.061	0.210	33783
		6	0.111	0.095	36626
		6	0.071	0.189	50038
		6	0.182	0.218	""
		6	0.019	0.071	62577
		6	0.227	0.098	""
		6	0.125	0.174	75264

		6	0.030	0.056	79734
		6	0.167	0.204	85735
		6	0.083	0.161	91748
		6	0.096	0.198	100158
		6	0.184	0.178	200854
		6	0.180	0.179	""
		6	0.082	0.212	405153
		6	0.261	0.266	416590
		7	0.078	0.192	33783
		7	0.163	0.133	""
Mo	4	6	0.111	0.023	96454
	5	6	0.389	0.075	69088
		6	0.058	0.159	281197
	6	4	0.250	0.109	65512
		4	0.067	0.040	68279
		4	0.052	0.079	""
		4	0.087	0.134	""
		4	0.099	0.056	247056
		4	0.183	0.178	""
		4	0.000	0.055	280775
		4	0.094	0.047	281210
		5	0.161	0.176	66994
		5	0.232	0.256	79517
		5	0.367	0.159	280066
		6	0.418	0.235	68279
		6	0.134	0.204	79517
		6	0.186	0.329	90110
		6	0.033	0.531	170119
		6	0.152	0.340	171758
		6	0.224	0.261	""
		6	0.322	0.215	280066
		6	0.282	0.214	281503
		6	0.328	0.161	""
		6	0.102	0.496	413000
Ru	4	6	0.034	0.141	33802
	5	6	0.048	0.156	73183
		6	0.067	0.140	97525
Pd	2	4	0.100	0.058	415239
		4	0.100	0.065	""
		4	0.000	0.033	72312
		4	0.000	0.042	""
		4	0.122	0.103	""
		6	0.084	0.085	72312
Cd	2	6	0.026	0.061	35084

		6	0.062	0.020	200743
		8	0.022	0.108	35084
		8	0.036	0.027	35407
Hf	4	6	0.017	0.178	33194
		6	0.003	0.162	""
		6	0.063	0.026	65476
		8	0.000	0.092	59111
Ta	5	6	0.111	0.092	80423
		6	0.183	0.147	85042
		6	0.000	0.060	203232
		6	0.000	0.245	280154
		6	0.013	0.099	415427
		6	0.111	0.195	415460
		7	0.092	0.185	203232
W	5	6	0.056	0.026	8269
		6	0.111	0.046	203048
		6	0.167	0.098	202414
		6	0.126	0.067	417072
	6	4	0.019	0.054	71562
		4	0.071	0.141	78180
		5	0.008	0.086	40249
		5	0.149	0.169	78180
		6	0.204	0.170	68614
		6	0.183	0.239	""
		6	0.122	0.262	79702
		6	0.000	0.319	86144
		6	0.075	0.357	411285
Re	5	6	0.056	0.051	72872
	7	4	0.125	0.084	92317
		4	0.250	0.149	""
		5	0.007	0.235	100571
		6	0.025	0.128	15505
		6	0.040	0.077	92508
Os	7	6	0.000	0.105	49746
	8	4	0.000	0.077	20611
		5	0.146	0.248	20611
		6	0.200	0.320	20540
Ir	4	6	0.002	0.046	33863
		6	0.077	0.193	""
Pt	2	4	0.000	0.010	35407
	4	6	0.032	0.017	35407
		6	0.015	0.030	63103
		6	0.005	0.075	65614
Au	3	4	0.000	0.093	92489

Hg	2	2	0.000	0.203	72312
		3	0.069	0.204	72312
		6	0.000	0.010	1640
		6	0.063	0.066	280292
Average:			0.102	0.113	

Transition metals for ACS_OCG-FCH - Supporting.pdf (7.57 MiB) view on ChemRxiv • download file

Bond-length distributions for ions bonded to oxygen: Results for the transition metals and quantification of the factors underlying bond-length variation in inorganic solids

Olivier C. Gagné*,‡ & Frank C. Hawthorne§

‡Geophysical Laboratory, Carnegie Institution for Science, Washington, D.C. 20015, USA

§Department of Geological Sciences, University of Manitoba, Winnipeg, MB, R3T 2N2, Canada

ABSTRACT: Bond-length distributions are examined for 63 transition-metal ions bonded to O^{2-} in 147 configurations, for 7522 coordination polyhedra and 41,488 bond distances, providing baseline statistical knowledge of bond lengths for transition metals bonded to O^{2-}. *A priori* bond valences are calculated for 140 crystal structures containing 266 coordination polyhedra for 85 transition-metal ion configurations with anomalous bond-length distributions. Two new indices, Δ_{topol} and Δ_{cryst}, are proposed to quantify bond-length variation arising from bond-topological and crystallographic effects in extended solids. Bond-topological mechanisms of bond-length variation are [1] non-local bond-topological asymmetry, and [2] multiple-bond formation; crystallographic mechanisms are [3] electronic effects (with inherent focus on coupled electronic-vibrational degeneracy in this work), and [4] crystal-structure effects. The Δ_{topol} and Δ_{cryst} indices allow one to determine the primary cause(s) of bond-length variation for individual coordination polyhedra and ion configurations, quantify the distorting power of cations via electronic effects (by subtracting the bond-topological contribution to bond-length variation), set expectation limits regarding the extent to which functional properties linked to bond-length variations may be optimized in a given crystal structure (and inform how optimization may be achieved), and more. We find the observation of multiple bonds to be primarily driven by the bond-topological requirements of crystal structures in solids. However, we sometimes observe multiple bonds to form as a result of electronic effects (e.g. the pseudo Jahn-Teller effect); resolution of the origins of multiple-bond formation follows calculation of the Δ_{topol} and Δ_{cryst} indices on a structure-by-structure basis. Non-local bond-topological asymmetry is the most common cause of bond-length variation in transition-metal oxides and oxysalts, followed closely by the pseudo Jahn-Teller effect (PJTE). Non-local bond-topological asymmetry is further suggested to be the most widespread cause of bond-length variation in the solid state, with no *a priori* limitations with regard to ion identity. Overall, bond-length variations resulting from the PJTE are slightly larger than those resulting from non-local bond-topological asymmetry, comparable to those resulting from the strong JTE, and less than those induced by π-bond formation. From a comparison of *a priori* and observed bond valences for ~150 coordination polyhedra in which the strong JTE or the PJTE is the main reason underlying bond-length variation, the Jahn-Teller effect is found *not* to have a cooperative relation with the bond-topological requirements of crystal structures. The magnitude of bond-length variations caused by the PJTE decreases in the following order for octahedrally coordinated d^0 transition metals oxyanions: $Os^{8+} > Mo^{6+} > W^{6+} >> V^{5+} > Nb^{5+} > Ti^{4+} > Ta^{5+} > Hf^{4+} > Zr^{4+} > Re^{7+} >> Y^{3+} > Sc^{3+}$. Such ranking varies by coordination number; for [4], it is $Re^{7+} > Ti^{4+} > V^{5+} > W^{6+} > Mo^{6+} > Cr^{6+} > Os^{8+} >> Mn^{7+}$; for [5], it is $Os^{8+} > Re^{7+} > Mo^{6+} > Ti^{4+} > W^{6+} > V^{5+} > Nb^{5+}$. We conclude that non-octahedral coordinations of d^0 ion configurations are likely to occur with bond-length variations that are similar in magnitude to their octahedral counterparts. However, smaller bond-length variations are expected from the PJTE for non-d^0 transition-metal oxyanions.

Introduction

Transition metals are a unique set of elements whose compounds have an extraordinarily varied range of chemical and physical properties. The behavior of transition-metal compounds is characterized by the metastability of partially-filled *d* orbitals, affording them distinctive electronic, magnetic, vibronic, optical, and other properties of fundamental and technological interest. For instance, the wide array of metastable oxidation states characteristic of transition metals facilitates electron-transfer reactions central to catalysis,[1] while meta-stable spin states associated with *d* orbital occupancy are used as bi-stable atomic switches in spin-crossover compounds, controllable via external perturbations[2–4] (and whose lifetime may be increased several orders of magnitude via coupled electronic-vibrational degeneracy).[5]

The functional properties of materials are often linked to irregular bond distances; some of these properties necessarily arise from non-centrosymmetric behavior (e.g. piezoelectricity, ferroelectricity, pyroelectricity, second-harmonic generation response, dielectric behavior),[6–8] while others are sometimes simply enhanced by it (e.g. ferromagnetism,[9] flexoelectricity,[10] negative thermal expansion,[11] the photovoltaic effect,[12] photoluminescence,[13] photocatalysis,[14] thermoelectricity,[15] magnetic-dielectric bistability[16]). As such, deciphering the causal mechanisms underlying

bond-length variation, and the extent to which bond lengths vary in solids, has significant implications in the materials sciences. For one, systematization of chemical-bonding behavior via large-scale bond-length dispersion analysis facilitates tracing anomalous bonding behavior to the causal mechanisms underlying material properties, and further facilitates recognition of anomalously-bonded coordination units bearing functional properties for their transposing into new chemical spaces. Further resolving the extent for which these mechanisms affect bond-length variations is crucial in order to maximize the harnessing of these effects within the constraints of physically realistic crystal structures. In addition, knowledge derived from large-scale bond-length dispersion analysis facilitates ion identification in crystal-structure refinements (with additional help from the bond-valence model) as the metrics of bonding behavior are often characteristic of an ion configuration (particularly for transition metals); this information facilitates quantitative resolution of disordered and/or mixed-valent site occupancy in crystals, with particular relevance to understanding the mineralogical makeup of Earth and other planetary bodies, and the many geological processes we may infer from them.

The growing use of crystal-structure databases in the 1980s resulted in many sizeable bond-length dispersion analyses whose publication impacted fields such as organic chemistry,[17] coordination chemistry[18,19] and protein crystallography.[20,21] Many such studies emerged from the Cambridge Structure Database,[22] which has been key for demonstrating the considerable potential of database analysis in the structural sciences.[23,24] Although similar large-scale studies were done for inorganic crystals in the 1970s and 1980s,[25,26] publication of raw data and their statistics has been lacking. For reasons unknown, no large-scale bond-length dispersion analysis of inorganic compounds has been published since the development of the Inorganic Crystal Structure Database (ICSD) in the late 1970s. Recently, Waroquiers et al. analyzed the ICSD to derive coordination-environment statistics in oxides and oxysalts but stopped short of investigating constituent bond lengths.[27] It has been the primary goal of our work to provide baseline statistical knowledge of bond lengths in inorganic solids, such that the underlying reasons for variation may be rigorously examined. While this series has focused on bonds to oxygen, it is desirable that similar studies be done in the future for other anions; Gagné recently published a similar study for cations bonded to N^{3-} in inorganic compounds.[28]

This article is the fifth and last of a series in which we describe bond-length data for ions bonded to oxygen in inorganic crystals. In this series, we have examined the distribution of bond lengths for 135 ions bonded to oxygen in 460 configurations (on the basis of coordination number), using 177,446 bond lengths extracted from 9210 crystal structures refined since 1975; these data cover most ions of the periodic table and the coordination environment in which they occur in inorganic compounds. Here, we report bond-length data for 63 transition-metal ions bonded to O^{2-} in 147 configurations, using 41,488 bond lengths and 7522 coordination polyhedra taken from 3814 crystal structure refinements. As we have done for the previous articles of this series,[29–32] we deposit all bond-length data and their associated collection codes in the Inorganic Crystal Structure Database (ICSD) so that they may easily be used by others. For a description of data collection and filtering, we refer the reader to the first article of this series.[29]

Scope of this work

There are three objectives in this work: (1) to provide a comprehensive description of bond-length variations for transition metals bonded to O^{2-}; (2) to resolve the causal mechanisms underlying bond-length variation for transition metals bonded to O^{2-}; (3) to quantify the extent to which causal mechanisms result in bond-length variation for those transition-metal configurations with anomalous bond-length distributions. We split this article into three parts in accord with these objectives.

The information we derive in (1) will provide crystallographers *sensu lato* with more comprehensive and accurate bond-length data than currently achievable via addition of ionic radii. These data are useful for refining and interpreting new crystal structures (particularly Rietveld refinements), modeling crystal structures, and assessing the validity of computational studies, without which much effort is wasted on unrealistic atomic arrangements.[33] Some implications for (2) and (3) were discussed in the Introduction; essentially, resolution and quantification of anomalous bonding behavior will facilitate targeted design of materials whose functional properties are linked to asymmetric coordination environments, and will further facilitate optimization of these properties within the constraints of physically realistic crystal structures.

Part 1: Bond-length dispersion analysis

The collection and filtering criteria described in the first part of this series[29] resulted in a sample size of 41,488 bonds and 7522 coordination polyhedra for transition-metal ions bonded to O^{2-}. Table 1 gives the mean bond-length and standard deviation, the minimum and maximum bond-length (and range), the skewness and kurtosis (where justified by sample size), and the number of bonds and coordination polyhedra for the 63 transition-metal ions observed in 147 configurations in terms of oxidation state and coordination number. All bond-length and bond-valence distributions are deposited in Figs. S1 and S2, respectively (we use the bond-valence parameters of Gagné & Hawthorne[34] throughout his work); bond-length distributions of adequate sample size (see below) are given in Fig. 1. As we have done in the previous parts of this series, we have given particular attention to confirming the reliability of the data at the limits of the bond-length distributions, i.e., the shortest and longest few bonds for each ion configuration. Anomalous bond lengths that result from positional and/or substitutional disorder, anomalous displacement parameters, uncorrected twinning effects, etc., were removed from our dataset.

Table 1: Bond-length statistics for the transition metal ions bonded to O^{2-}.

Ion	Coordination number	Number of bonds	Number of co-ordination pol-yhedra	Mean bond-length (Å)	Standard deviation (Å)	Range (Å)	Maximum bond-length (Å)	Minimum bond-length (Å)	Skewness	Kurtosis
Sc^{3+}	6	450	75	2.098	0.041	0.236	2.231	1.995	0.429	0.610
	7	35	5	2.163	0.056	0.268	2.315	2.047	-0.242	0.731
	8	64	8	2.234	0.101	0.497	2.554	2.057	1.352	2.513
Ti^{3+}	6	126	21	2.037	0.051	0.263	2.167	1.904	-0.115	0.160
	7	14	2	2.108	0.022	0.077	2.134	2.057	-1.113	0.575
	8	8	1	2.195	0.077	0.153	2.271	2.118	0.000	-2.800
Ti^{4+}	4	16	4	1.821	0.038	0.159	1.906	1.747	0.220	1.124
	5	85	17	1.917	0.106	0.405	2.050	1.645	-1.256	0.139
	6	1758	293	1.971	0.107	0.826	2.474	1.648	0.124	1.531
	7	7	1	2.064	0.165	0.550	2.230	1.680	-2.098	5.088
V^{3+}	6	402	67	2.007	0.051	0.339	2.224	1.885	0.479	0.681
V^{4+}	5	475	95	1.893	0.147	0.577	2.116	1.539	-1.348	0.163
	6	768	128	1.980	0.202	1.030	2.588	1.558	-0.173	0.559
V^{5+}	4	1380	345	1.717	0.056	0.354	1.917	1.563	0.300	-0.250
	5	325	65	1.827	0.147	0.801	2.352	1.551	-0.068	-0.607
	6	1758	293	1.924	0.213	0.993	2.547	1.554	0.324	-0.519
Cr^{2+}	4	24	6	2.004	0.010	0.028	2.025	1.997	1.441	0.378
	5	10	2	2.113	0.144	0.432	2.426	1.994	1.637	1.313
	6	54	9	2.188	0.193	0.696	2.651	1.955	0.809	-0.889
Cr^{3+}	6	624	104	1.976	0.026	0.190	2.074	1.884	0.277	1.855
Cr^{4+}	4	4	1	1.784	0.035	0.086	1.844	1.758	1.825	3.332
	6	36	6	1.950	0.032	0.094	1.988	1.894	-0.362	-1.336
Cr^{5+}	4	4	1	1.693	0.006	0.012	1.699	1.687	0.000	-6.000
Cr^{6+}	4	676	169	1.652	0.059	0.357	1.892	1.535	1.593	2.852
Mn^{2+}	4	40	10	2.046	0.039	0.241	2.194	1.953	1.304	4.668
	5	120	24	2.141	0.053	0.243	2.267	2.024	0.264	-0.341
	6	1908	318	2.199	0.085	0.830	2.798	1.968	2.070	7.951
	7	14	2	2.352	0.240	0.663	2.782	2.119	0.756	-1.323
	8	144	18	2.321	0.104	0.539	2.691	2.152	0.899	0.927

Mn^{3+}	4	8	2	1.901	0.046	0.099	1.951	1.852	0.015	-2.750
	5	50	10	1.959	0.075	0.255	2.109	1.854	0.301	-1.091
	6	492	82	2.031	0.149	0.755	2.598	1.843	0.841	-0.500
Mn^{4+}	4	4	1	1.750	0.000	0.000	1.750	1.750	-	-
	6	120	20	1.903	0.030	0.167	2.008	1.841	0.552	1.613
Mn^{5+}	4	32	8	1.698	0.014	0.076	1.725	1.649	-1.042	3.241
Mn^{6+}	4	8	2	1.662	0.012	0.034	1.687	1.653	1.599	1.380
Mn^{7+}	4	28	7	1.610	0.009	0.041	1.633	1.592	0.868	1.384
Fe^{2+}	3	24	8	1.844	0.029	0.127	1.918	1.791	0.578	0.456
	4	24	6	1.985	0.027	0.141	2.041	1.900	-1.051	0.726
	5	95	19	2.097	0.099	0.572	2.493	1.921	1.370	3.133
	6	876	146	2.147	0.089	0.713	2.646	1.933	1.440	4.840
	8	40	5	2.333	0.188	0.684	2.722	2.038	0.598	-0.400
Fe^{3+}	4	260	65	1.875	0.033	0.201	1.965	1.764	-0.060	0.471
	5	105	21	1.966	0.070	0.350	2.207	1.857	1.245	2.428
	6	2268	378	2.015	0.064	0.539	2.391	1.852	0.971	2.078
	8	16	2	2.125	0.029	0.095	2.173	2.078	0.036	-1.333
Co^{2+}	3	42	14	1.854	0.058	0.223	1.980	1.757	0.457	-0.754
	4	108	27	1.967	0.022	0.189	2.081	1.892	0.502	5.715
	5	80	16	2.066	0.117	0.628	2.574	1.946	2.717	7.945
	6	1458	243	2.108	0.062	0.571	2.516	1.945	1.612	5.825
	8	8	1	2.272	0.185	0.517	2.573	2.056	0.203	-1.481
Co^{3+}	6	90	15	1.908	0.021	0.108	1.969	1.861	0.717	1.335
Co^{4+}	6	6	1	1.874	0.000	0.000	1.874	1.874	-1.369	-3.333
Ni^{2+}	2	4	2	1.686	0.001	0.002	1.687	1.685	0.000	-6.000
	4	12	3	1.950	0.039	0.092	1.982	1.890	-0.800	-1.573
	5	40	8	2.028	0.041	0.186	2.149	1.963	0.597	0.354
	6	1452	242	2.070	0.054	0.589	2.462	1.873	0.874	4.880
Ni^{4+}	6	30	5	1.870	0.012	0.067	1.906	1.839	0.446	3.019
Cu^{+}	2	84	42	1.839	0.024	0.123	1.911	1.788	-0.080	-0.134
	3	6	2	1.969	0.076	0.183	2.077	1.894	0.742	-1.897
	4	52	13	2.084	0.110	0.541	2.438	1.897	0.554	0.966

Cu^{2+}	4	516	129	1.943	0.029	0.180	2.055	1.875	0.910	2.172
	5	1090	218	2.037	0.155	0.865	2.700	1.835	1.784	2.494
	6	2190	365	2.130	0.232	0.893	2.748	1.855	0.969	-0.494
	8	32	4	2.302	0.304	0.794	2.743	1.949	0.052	-1.973
Cu^{3+}	4	44	11	1.850	0.029	0.135	1.946	1.811	1.485	3.710
Zn^{2+}	4	908	227	1.952	0.031	0.229	2.076	1.847	0.331	0.887
	5	180	36	2.051	0.082	0.619	2.525	1.906	1.609	5.499
	6	1158	193	2.110	0.086	0.810	2.696	1.886	2.005	6.961
Y^{3+}	6	150	25	2.264	0.041	0.226	2.400	2.174	0.695	1.020
	7	245	35	2.332	0.082	0.499	2.661	2.162	1.248	2.181
	8	800	99	2.390	0.065	0.507	2.729	2.222	1.353	6.271
	9	135	15	2.422	0.092	0.585	2.799	2.214	1.005	3.144
	10	10	1	2.496	0.187	0.604	2.857	2.253	0.715	-0.598
	12	12	1	2.541	0.000	0.000	2.541	2.541	-	-
Zr^{4+}	6	438	73	2.078	0.031	0.218	2.224	2.006	1.291	3.830
	7	91	13	2.146	0.048	0.233	2.283	2.050	0.000	-0.356
	8	168	21	2.199	0.053	0.313	2.407	2.094	0.536	0.471
	9	27	3	2.263	0.138	0.472	2.593	2.121	1.385	1.474
	10	70	7	2.283	0.046	0.204	2.415	2.211	1.150	0.597
Nb^{4+}	6	18	3	2.054	0.080	0.241	2.163	1.922	-0.125	-1.553
Nb^{5+}	4	8	2	1.831	0.068	0.184	1.926	1.742	0.167	-1.224
	5	20	4	1.926	0.054	0.164	1.993	1.829	-0.467	-1.286
	6	1440	240	1.993	0.115	0.742	2.444	1.702	0.646	1.077
	7	21	3	2.069	0.163	0.668	2.435	1.767	0.469	0.090
	8	8	1	2.080	0.001	0.002	2.081	2.079	0.000	-2.800
Mo^{3+}	6	30	5	2.095	0.024	0.112	2.163	2.051	0.347	1.099
Mo^{4+}	6	54	9	2.003	0.065	0.264	2.077	1.813	-1.750	2.047
Mo^{5+}	5	10	2	1.916	0.122	0.328	1.981	1.653	-1.799	1.552
	6	444	74	1.992	0.167	0.806	2.429	1.623	-0.627	0.085
Mo^{6+}	4	1736	434	1.764	0.033	0.268	1.905	1.637	0.520	0.770
	5	75	15	1.872	0.146	0.620	2.286	1.666	0.679	-0.042
	6	3036	506	1.972	0.232	1.005	2.608	1.603	0.431	-1.027

Tc^{7+}	4	24	6	1.705	0.019	0.068	1.740	1.672	-0.044	-0.591
Ru^{3+}	6	18	3	2.025	0.043	0.191	2.107	1.916	-1.010	2.152
Ru^{4+}	6	48	8	1.982	0.025	0.134	2.070	1.936	1.317	5.102
Ru^{5+}	6	138	23	1.964	0.076	0.273	2.113	1.840	0.384	-0.755
Rh^{3+}	6	66	11	2.025	0.023	0.093	2.071	1.978	0.647	-0.607
Rh^{4+}	6	18	3	2.007	0.014	0.032	2.020	1.988	-0.442	-1.946
Pd^{2+}	4	116	29	2.011	0.024	0.104	2.060	1.956	0.347	-0.596
Pd^{4+}	6	12	2	2.000	0.027	0.094	2.059	1.965	0.959	0.035
Ag^{+}	2	10	5	2.136	0.018	0.053	2.164	2.111	0.435	-1.386
	3	45	15	2.278	0.112	0.391	2.535	2.144	0.888	-0.181
	4	148	37	2.402	0.127	0.601	2.741	2.140	-0.057	-0.002
	5	225	45	2.489	0.152	0.801	2.975	2.174	0.657	0.058
	6	378	63	2.537	0.135	0.652	2.894	2.242	0.330	-0.288
	7	63	9	2.589	0.155	0.564	2.888	2.324	0.308	-0.888
	8	104	13	2.656	0.175	0.708	3.083	2.375	0.736	0.205
	9	27	3	2.704	0.143	0.402	2.863	2.461	-0.894	-0.873
Cd^{2+}	5	20	4	2.257	0.078	0.342	2.486	2.144	1.352	2.401
	6	810	135	2.302	0.069	0.591	2.754	2.163	1.472	4.484
	7	42	6	2.377	0.134	0.713	2.888	2.175	2.033	5.213
	8	144	18	2.432	0.118	0.531	2.724	2.193	0.312	-0.575
	9	9	1	2.530	0.214	0.500	2.826	2.326	0.688	-1.714
Hf^{4+}	6	66	11	2.082	0.051	0.322	2.241	1.919	0.195	4.551
	7	28	4	2.128	0.019	0.072	2.167	2.095	0.016	-0.842
	8	56	7	2.190	0.064	0.256	2.324	2.068	-0.012	-0.840
Ta^{5+}	6	828	138	1.988	0.076	0.585	2.386	1.801	1.474	4.235
	7	98	14	2.057	0.155	0.619	2.486	1.867	1.763	2.077
W^{5+}	6	24	4	1.956	0.095	0.448	2.140	1.692	-0.821	1.154
W^{6+}	4	140	35	1.773	0.027	0.141	1.846	1.705	-0.220	0.095
	5	60	12	1.859	0.072	0.467	2.166	1.699	0.885	4.719
	6	2178	363	1.951	0.182	0.919	2.557	1.638	0.750	-0.146
Re^{5+}	6	18	3	1.940	0.068	0.183	2.027	1.844	0.045	-1.764
Re^{7+}	4	164	41	1.716	0.021	0.150	1.790	1.640	-0.114	1.066

	5	40	8	1.810	0.052	0.275	1.904	1.629	-1.249	3.058
	6	60	10	1.882	0.046	0.195	1.982	1.787	0.380	-0.224
Os^{5+}	6	24	4	1.960	0.044	0.180	2.044	1.864	-0.486	0.512
Os^{6+}	6	6	1	1.926	0.125	0.266	2.015	1.749	-0.968	-1.875
Os^{7+}	5	5	1	1.825	0.034	0.092	1.855	1.763	-1.448	2.287
	6	18	3	1.887	0.021	0.058	1.923	1.865	0.864	-0.668
Os^{8+}	4	4	1	1.698	0.014	0.027	1.711	1.684	0.000	-6.000
	5	15	3	1.793	0.162	0.569	2.227	1.658	2.132	3.720
	6	24	4	1.880	0.170	0.442	2.169	1.727	0.747	-1.167
Ir^{3+}	6	6	1	2.042	0.000	0.000	2.042	2.042	-	-
Ir^{4+}	4	20	5	1.909	0.008	0.032	1.929	1.897	1.151	1.194
	6	72	12	2.015	0.024	0.176	2.096	1.920	-0.698	4.820
Ir^{5+}	6	36	6	1.990	0.013	0.039	2.010	1.971	-0.237	-1.358
Pt^{2+}	4	12	3	2.007	0.009	0.022	2.017	1.995	-0.473	-1.650
Pt^{4+}	6	198	33	2.021	0.020	0.142	2.087	1.945	0.222	2.499
Au^{3+}	4	96	24	1.999	0.023	0.153	2.082	1.929	0.879	2.577
Hg^{2+}	2	2	1	1.955	0.000	0.000	1.955	1.955	-	-
	4	24	6	2.316	0.311	0.862	2.834	1.972	0.427	-1.568
	5	15	3	2.380	0.271	0.688	2.726	2.038	-0.031	-1.928
	6	150	25	2.429	0.249	0.912	2.932	2.020	-0.041	-1.051
	7	63	9	2.505	0.267	0.998	2.988	1.990	-0.409	-1.095
	8	64	8	2.502	0.163	0.685	2.906	2.221	0.493	-0.182

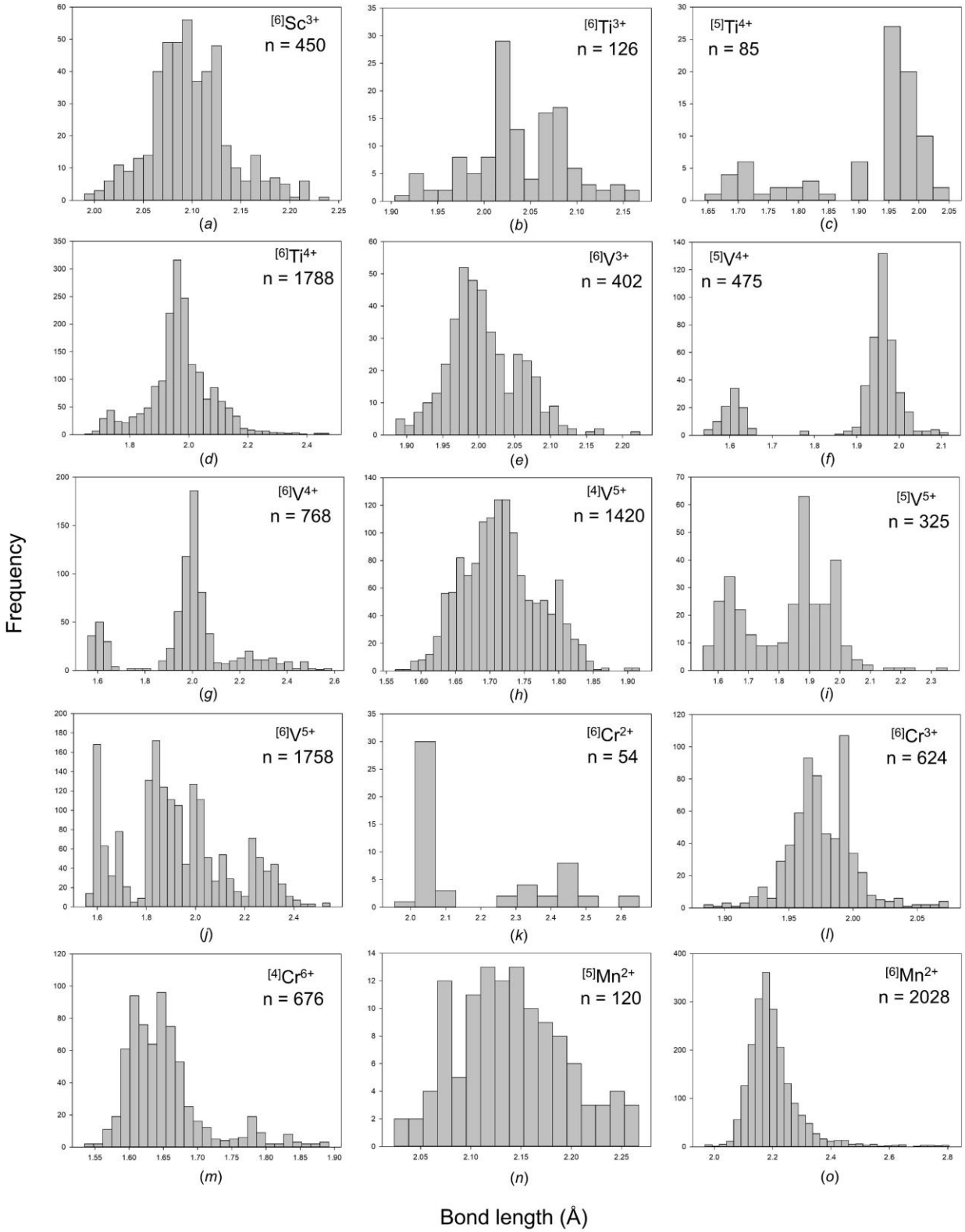
[6]Sc3+
n = 450
(a)
[6]Ti3+
n = 126
(b)
[5]Ti4+
n = 85
(c)
[6]Ti4+
n = 1788
(d)
[6]V3+
n = 402
(e)
[5]V4+
n = 475
(f)
[6]V4+
n = 768
(g)
[4]V5+
n = 1420
(h)
[5]V5+
n = 325
(i)
[6]V5+
n = 1758
(j)
[6]Cr2+
n = 54
(k)
[6]Cr3+
n = 624
(l)
[4]Cr6+
n = 676
(m)
[5]Mn2+
n = 120
(n)
[6]Mn2+
n = 2028
(o)
Frequency
Bond length (Å)

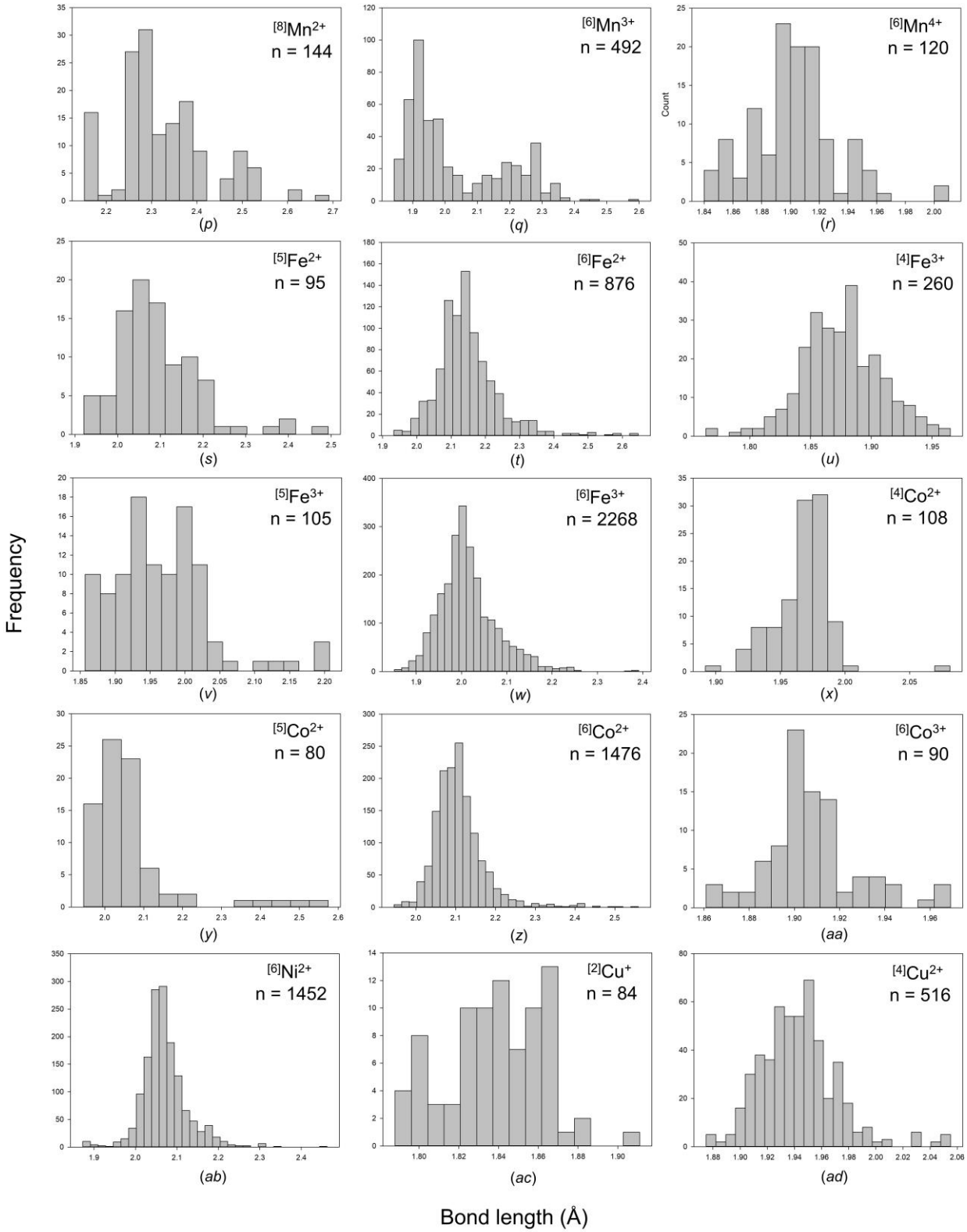
[8]Mn2+
n = 144
(p)
[6]Mn3+
n = 492
(q)
[6]Mn4+
n = 120
Count
(r)
[5]Fe2+
n = 95
(s)
[6]Fe2+
n = 876
(t)
[4]Fe3+
n = 260
(u)
[5]Fe3+
n = 105
(v)
[6]Fe3+
n = 2268
(w)
[4]Co2+
n = 108
(x)
[5]Co2+
n = 80
(y)
[6]Co2+
n = 1476
(z)
[6]Co3+
n = 90
(aa)
[6]Ni2+
n = 1452
(ab)
[2]Cu+
n = 84
(ac)
[4]Cu2+
n = 516
(ad)
Frequency
Bond length (Å)

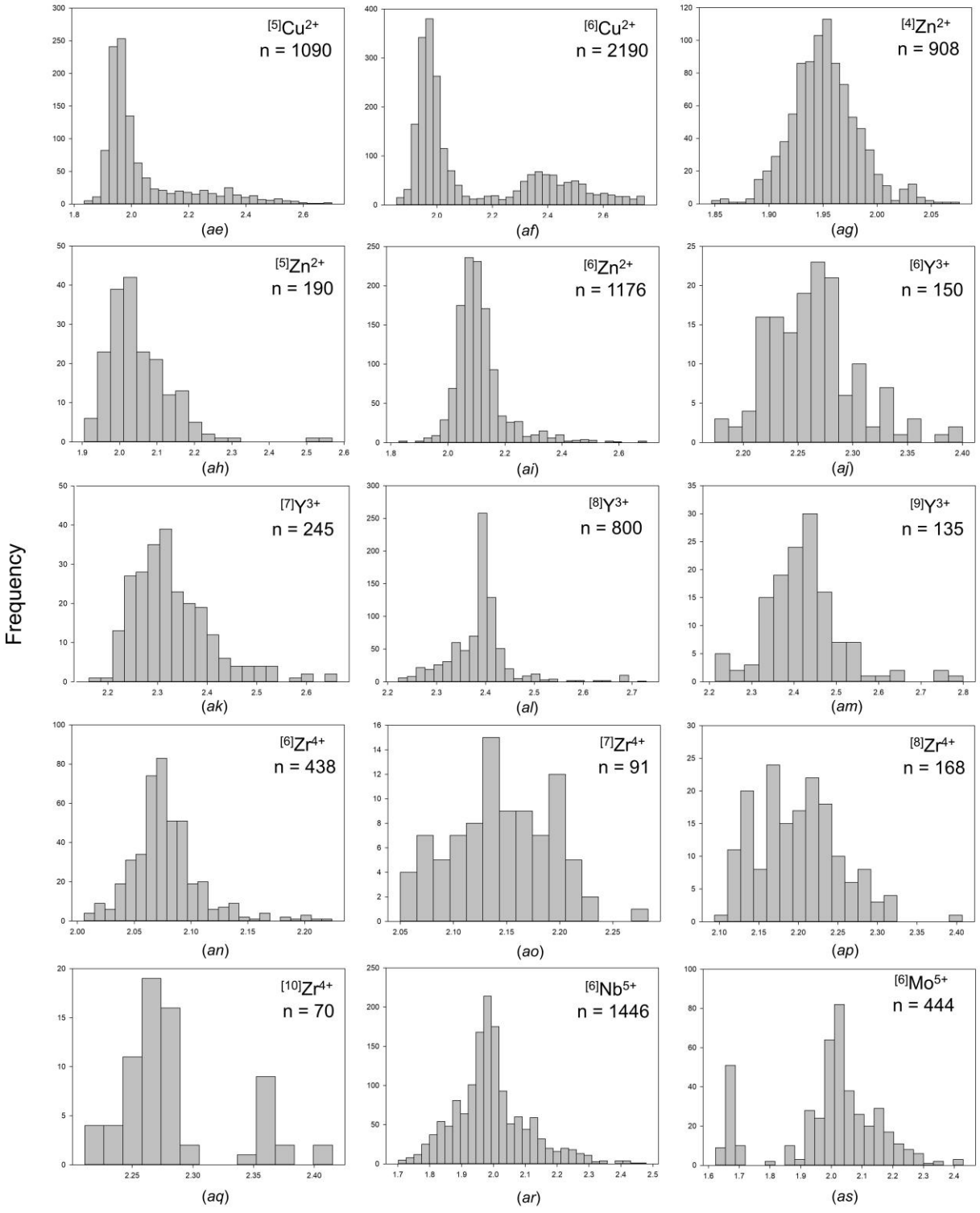
[5]Cu2+
n = 1090
(ae)
[6]Cu2+
n = 2190
(af)
[4]Zn2+
n = 908
(ag)
[5]Zn2+
n = 190
(ah)
[6]Zn2+
n = 1176
(ai)
[6]Y3+
n = 150
(aj)
[7]Y3+
n = 245
(ak)
[8]Y3+
n = 800
(al)
[9]Y3+
n = 135
(am)
[6]Zr4+
n = 438
(an)
[7]Zr4+
n = 91
(ao)
[8]Zr4+
n = 168
(ap)
[10]Zr4+
n = 70
(aq)
[6]Nb5+
n = 1446
(ar)
[6]Mo5+
n = 444
(as)
Frequency
Bond length (Å)

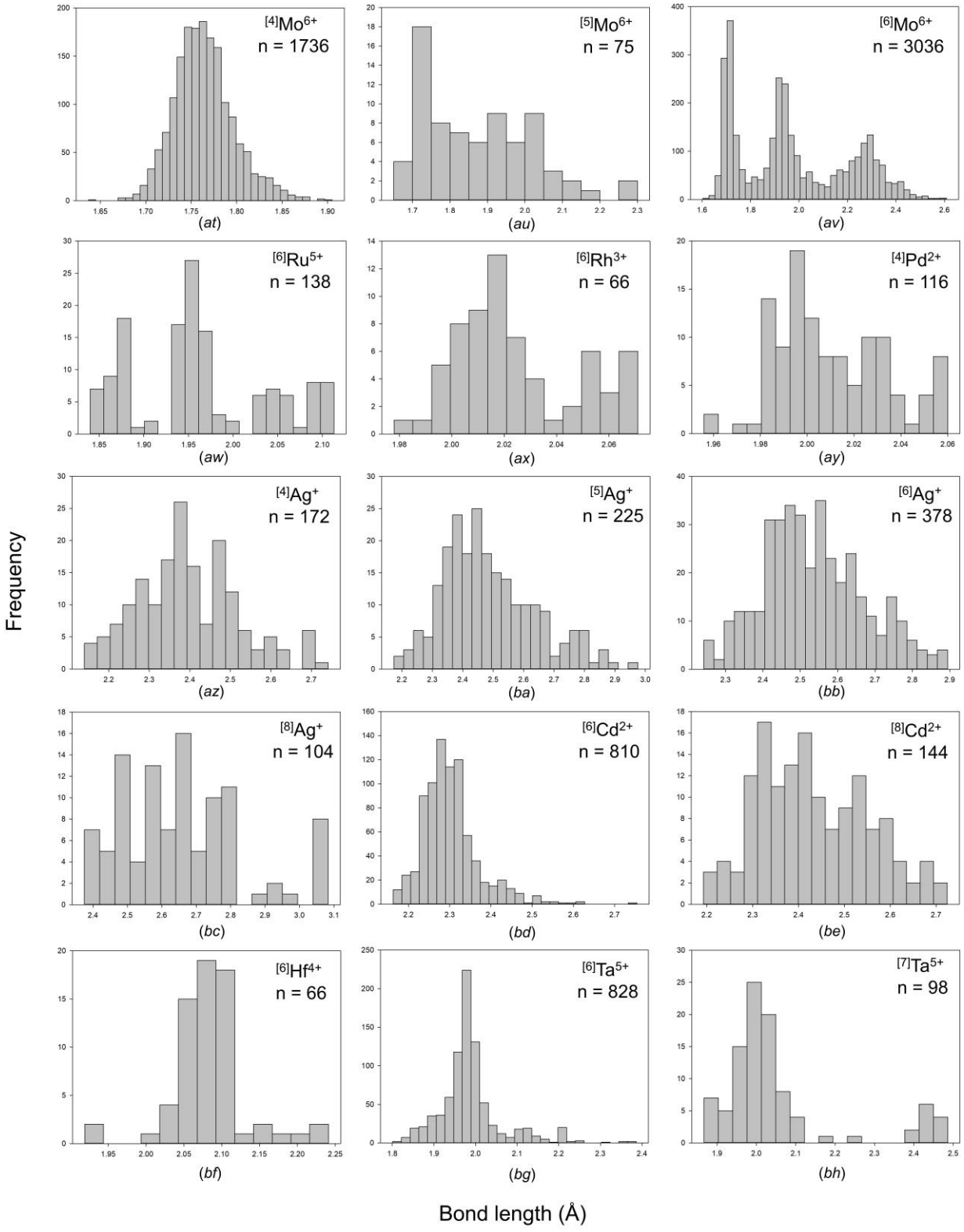
[4]Mo6+
n = 1736
(at)
[5]Mo6+
n = 75
(au)
[6]Mo6+
n = 3036
(av)
[6]Ru5+
n = 138
(aw)
[6]Rh3+
n = 66
(ax)
[4]Pd2+
n = 116
(ay)
[4]Ag+
n = 172
(az)
[5]Ag+
n = 225
(ba)
[6]Ag+
n = 378
(bb)
[8]Ag+
n = 104
(bc)
[6]Cd2+
n = 810
(bd)
[8]Cd2+
n = 144
(be)
[6]Hf4+
n = 66
(bf)
[6]Ta5+
n = 828
(bg)
[7]Ta5+
n = 98
(bh)
Frequency
Bond length (Å)

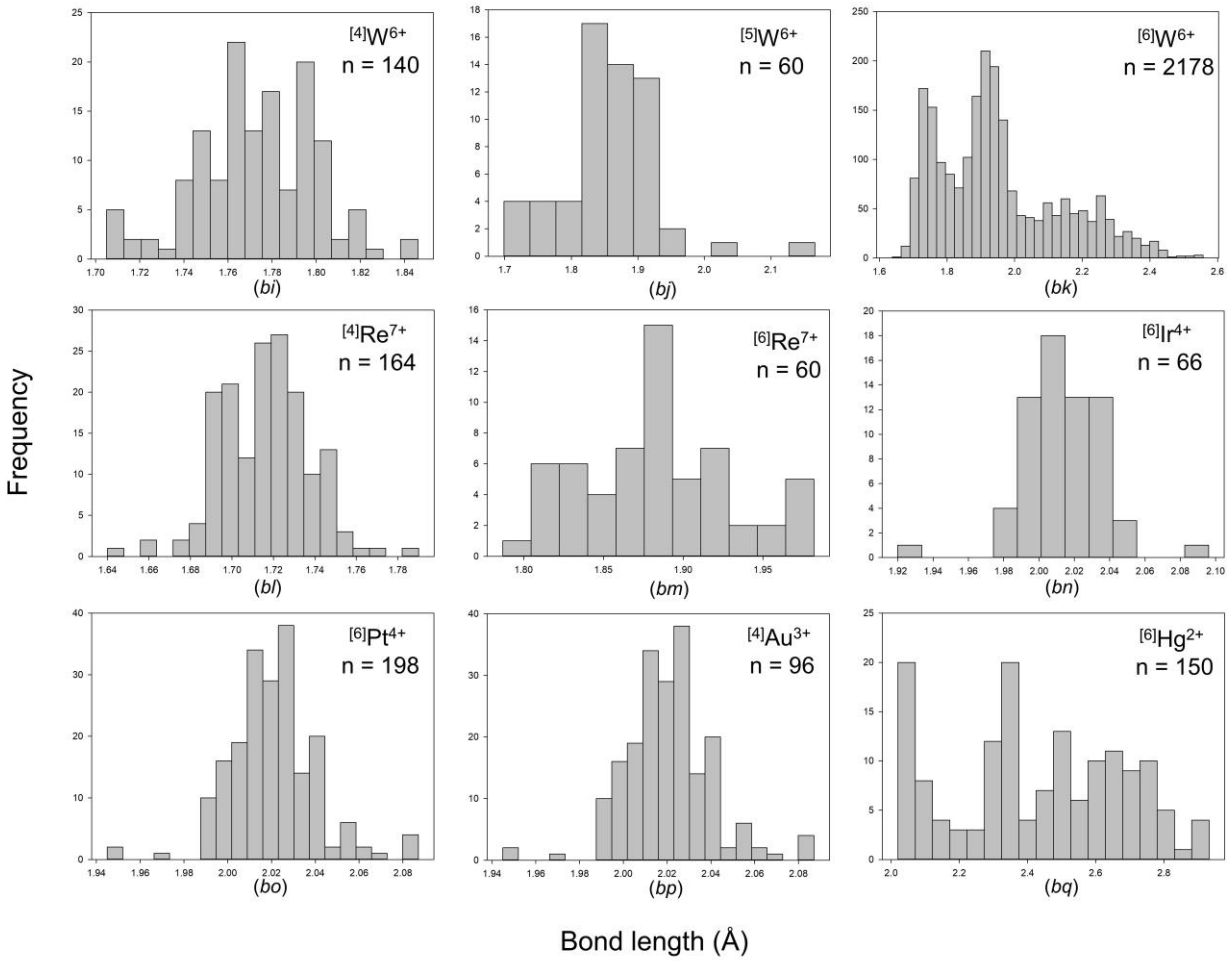

Figure 1: Bond-length distributions for selected configurations of the transition metal ions bonded to O^{2-}: (*a*) $^{[6]}Sc^{3+}$, (*b*) $^{[6]}Ti^{3+}$, (*c*) $^{[5]}Ti^{4+}$, (*d*) $^{[6]}Ti^{4+}$, (*e*) $^{[6]}V^{3+}$, (*f*) $^{[5]}V^{4+}$, (*g*) $^{[6]}V^{4+}$, (*h*) $^{[4]}V^{5+}$, (*i*) $^{[5]}V^{5+}$, (*j*) $^{[6]}V^{5+}$, (*k*) $^{[6]}Cr^{2+}$, (*l*) $^{[6]}Cr^{3+}$, (*m*) $^{[4]}Cr^{6+}$, (*n*) $^{[5]}Mn^{2+}$, (*o*) $^{[6]}Mn^{2+}$, (*p*) $^{[8]}Mn^{2+}$, (*q*) $^{[6]}Mn^{3+}$, (*r*) $^{[6]}Mn^{4+}$, (*s*) $^{[5]}Fe^{2+}$, (*t*) $^{[6]}Fe^{2+}$, (*u*) $^{[4]}Fe^{3+}$, (*v*) $^{[5]}Fe^{3+}$, (*w*) $^{[6]}Fe^{3+}$, (*x*) $^{[4]}Co^{2+}$, (*y*) $^{[5]}Co^{2+}$, (*z*) $^{[6]}Co^{2+}$, (*aa*) $^{[6]}Co^{3+}$, (*ab*) $^{[6]}Ni^{2+}$, (*ac*) $^{[2]}Cu^{+}$, (*ad*) $^{[4]}Cu^{2+}$, (*ae*) $^{[5]}Cu^{2+}$, (*af*) $^{[6]}Cu^{2+}$, (*ag*) $^{[4]}Zn^{2+}$, (*ah*) $^{[5]}Zn^{2+}$, (*ai*) $^{[6]}Zn^{2+}$, (*aj*) $^{[6]}Y^{3+}$, (*ak*) $^{[7]}Y^{3+}$, (*al*) $^{[8]}Y^{3+}$, (*am*) $^{[9]}Y^{3+}$, (*an*) $^{[6]}Zr^{4+}$, (*ao*) $^{[7]}Zr^{4+}$, (*ap*) $^{[8]}Zr^{4+}$, (*aq*) $^{[10]}Zr^{4+}$, (*ar*) $^{[6]}Nb^{5+}$, (*as*) $^{[6]}Mo^{5+}$, (*at*) $^{[4]}Mo^{6+}$, (*au*) $^{[5]}Mo^{6+}$, (*av*) $^{[6]}Mo^{6+}$, (*aw*) $^{[6]}Ru^{5+}$, (*ax*) $^{[6]}Rh^{3+}$, (*ay*) $^{[4]}Pd^{2+}$, (*az*) $^{[4]}Ag^{+}$, (*ba*) $^{[5]}Ag^{+}$, (*bb*) $^{[6]}Ag^{+}$, (*bc*) $^{[8]}Ag^{+}$, (*bd*) $^{[6]}Cd^{2+}$, (*be*) $^{[8]}Cd^{2+}$, (*bf*) $^{[6]}Hf^{4+}$, (*bg*) $^{[6]}Ta^{5+}$, (*bh*) $^{[7]}Ta^{5+}$, (*bi*) $^{[4]}W^{6+}$, (*bj*) $^{[5]}W^{6+}$, (*bk*) $^{[6]}W^{6+}$, (*bl*) $^{[4]}Re^{7+}$, (*bm*) $^{[6]}Re^{7+}$, (*bn*) $^{[6]}Ir^{4+}$, (*bo*) $^{[6]}Pt^{4+}$, (*bp*) $^{[4]}Au^{3+}$, (*bq*) $^{[6]}Hg^{2+}$

Effect of sample size

To ensure quality and reliability of the data reported throughout this series, we (1) set stringent data-collection and filtering criteria for the crystal structures used in our analysis, (2) carefully scrutinized data populating the tails of reported bond-length distributions, and (3) examined the effects of sampling on the reported data.

We previously described the typical shape of a bond-length distribution as a positively-skewed Gaussian distribution which originates from the variation in Born repulsion and Coulomb attraction as a function of interatomic distance, i.e., that which results from a two-body Morse potential.[29] In practice, this shape is seldom observed. Before we ascribe deviations in shape to causal mechanisms, it is crucial that we first understand the extent to which sample size influences the shape and statistics of bond-length distributions.

We examined the effects of sampling (*e.g.*, the presence of outliers, non-random sampling) on grand mean-bond-length (and its standard deviation), skewness and kurtosis for the alkali- and alkaline-earth-metal ions bonded to O^{2-} in the first article of this series[29]. We described the effect of sample size on these values for $^{[6]}Na^{+}$,[29] $^{[4]}S^{6+}$ and $^{[6]}I^{5+}$,[31] $^{[4]}Si^{4+}$ and $^{[8]}Bi^{3+}$,[32] and $^{[8]}La^{3+}$ bonded to O^{2-}.[30] We also showed a dependence of grand mean-bond-length, skewness and kurtosis values on (1) the number of data, (2) mean bond-valence (Pauling bond-strength), and (3) multimodality of the bond-length distribution. Here, we report a similar analysis for $^{[6]}Ti^{4+}$, with a mean bond-valence of 0.67 v.u. which lies within a range of values not yet examined by other works in this series.

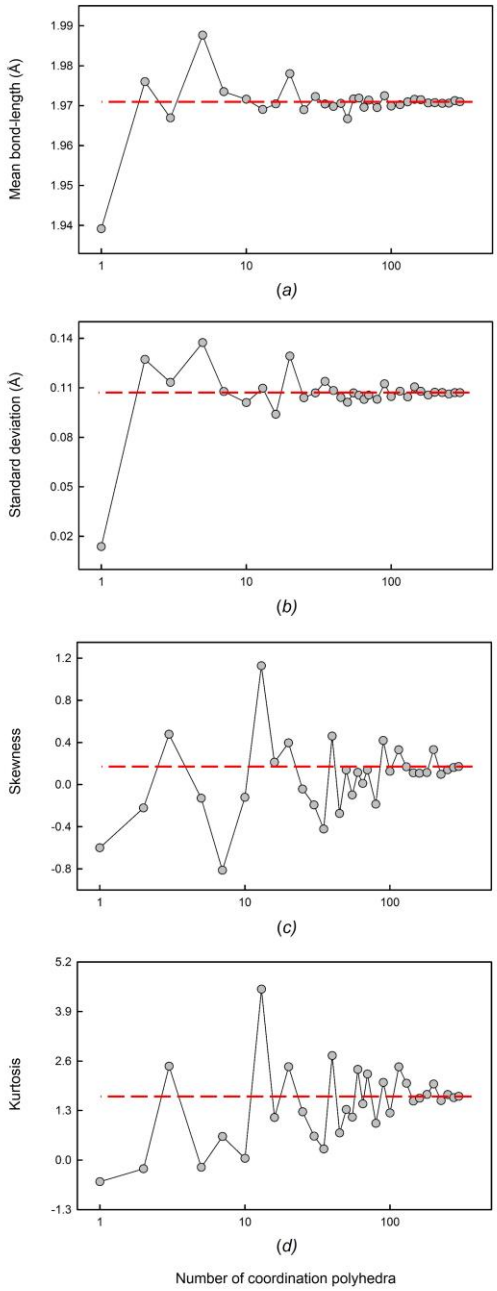

Figure 2: The effect of sample size on (*a*) mean bond-length, (*b*) standard deviation of the mean bond-length, (*c*) skewness, and (*d*) kurtosis for $^{[6]}Ti^{4+}$. The dashed line shows the value for the parent distribution.

Fig. 2 shows that for $^{[6]}Ti^{4+}$, a sample size greater than 20 coordination polyhedra is required for values of grand mean-bond-lengths to fluctuate by less than ±0.005 Å, while reliable values for skewness (±0.2) and kurtosis (±0.6) are obtained for sample sizes greater than ~115 coordination polyhedra. Table 2 gives a summary for all ion configurations of this series analyzed in such manner; values for *mean* bond-length distributions are in parentheses, and ion configurations with multi-modal bond-length distributions (here caused by lone-pair stereoactivity) are bolded. For the different ion configurations, we observe that less data are necessary to get an accurate estimate of grand mean-bond-length with increasing mean bond-strength. It is difficult to ascribe significance to the values of skewness and kurtosis; while these values are sometimes useful in describing well-developed, smooth and generally "similar" unimodal distributions, their extreme sensitivity to sample size requires caution in their interpretation. While multi-modal behaviour changes the minimum sample-size requirements significantly, we note that stronger bonds require smaller sample-sizes to satisfy a given threshold. Skewness and kurtosis converge very rapidly for multi-modal bond-length distributions, as the bonding pattern of individual coordination polyhedra overwhelms the sensitivity to variability among polyhedra. We used the results of Table 2 to help decide whether or not to give values of skewness and kurtosis associated with bond-length and mean-bond-length distributions in our work.

Variation in bond lengths and mean bond-lengths

Where bonded to O^{2-}, transition metals have an average range of bond-lengths of 0.475 Å for ion configurations with sample size greater than 10 coordination polyhedra (n = 74 ion configurations). As a function of electronic configuration, the average bond-length ranges are 0.492 (d^0), 0.736 (d^1), 0.399 (d^2), 0.221 (d^3), 0.505 (d^4), 0.391 (d^5), 0.338 (d^6), 0.414 (d^7), 0.245 (d^8), 0.646 (d^9) and 0.585 Å (d^{10}). For octahedral coordination (n = 33 ion configurations), these numbers are 0.585 (d^0), 0.788 (d^1), 0.399 (d^2), 0.221 (d^3), 0.755 (d^4), 0.517 (d^5), 0.264 (d^6), 0.614 (d^7), 0.589 (d^8), 0.893 (d^9), 0.756 Å (d^{10}). Wide variation in these bond-length ranges demonstrates inconsistent bonding behaviour as a function of electronic configuration and coordination number. This anomalous behaviour is, to some extent, expected from the Jahn-Teller effect (JTE); bond-length variations attributable to the JTE will be discussed in detail below, along with other significant causes of bond-length variation. The largest bond-length ranges are for $^{[6]}V^{4+}$ (1.030 Å; d^1), $^{[6]}Mo^{6+}$ (1.005 Å; d^0), $^{[7]}Hg^{2+}$ (0.998 Å; d^{10}), $^{[6]}V^{5+}$ (0.993 Å; d^0), $^{[6]}W^{6+}$ (0.919 Å; d^0), $^{[6]}Hg^{2+}$ (0.912 Å; d^{10}), and $^{[6]}Cu^{2+}$ (0.893 Å; d^9), and it is notable that all these ion configurations show multimodal distributions.

Mean-bond-length distributions are given in Fig. S3, and those with adequate sample size (see *Effect of sample size* section above) are given in Fig. 3. Table 3 gives the grand mean-bond-length and standard deviation, the minimum and maximum mean bond-lengths (and range), the skewness and kurtosis of each distribution (where justified by sample size), and the number of coordination polyhedra for each configuration observed. Where bonded to O^{2-}, transition metals have an average range of mean bond-lengths of 0.085 Å for sample sizes greater than 10 coordination polyhedra. For octahedrally coordinated d^0 transition metals, this range is 0.078 Å (0.086 Å excluding Sc^{3+}, Y^{3+}, Zr^{4+}, Hf^{4+}), while that of ions exhibiting the classic Jahn-Teller effect in octahedral coordination (weak or strong) is 0.097 Å. For the latter group, the largest mean-bond-length ranges are observed for $^{[6]}Cu^{2+}$ 0.174, $^{[6]}V^{4+}$ 0.103, $^{[6]}Mn^{3+}$ 0.094 and $^{[6]}Mo^{5+}$ 0.070 Å. For the d^0 transition metals, the largest ranges (irrespective of coordination number, for sample sizes greater than 10 coordination polyhedra) are $^{[6]}Nb^{5+}$ 0.102, $^{[6]}W^{6+}$ 0.100, $^{[6]}Ta^{5+}$ 0.100, $^{[8]}Y^{3+}$ 0.096, $^{[6]}Ti^{4+}$ 0.094, $^{[6]}Mo^{6+}$ 0.091, and $^{[6]}Zr^{4+}$ 0.082 Å.

Despite the significant effect of the JTE on bond-length variation, its corresponding effect on mean bond-length is not marked. The mean-bond-length range observed for transition metals bonded to O^{2-} (0.085 Å) is typical of ions not showing electronic and/or crystal-structure effects, and is due to their high Lewis acidity (values given in ref [35]). For comparison, strongly bonded oxyanions have typical mean-bond-length ranges of 0.06-0.10 Å,[31,32] actinides 0.07 Å and lanthanides 0.10 Å;[30] ranges are larger for ions with stereoactive lone-pair electrons, ~0.1-0.3 Å,[31,32] for alkaline-earth metals, ~0.20-0.25 Å, and for alkali metals, ~0.30-0.40 Å.[29]

Table 2: Minimum sample size required to satisfy given variability thresholds for bond-length distributions (mean bond-length distributions)

	Sample size (parent population)	Mean bond-valence (v.u.)	Mean bond-length (±0.005 Å)	Skewness (±0.2) and kurtosis (±0.6)	Reference
$^{[6]}Na^{+}$	920	0.17	200	225 (400)	GH16
$^{[8]}Bi^{3+}$	**84**	**0.38**	**70**	**7 (60)**	GH18a
$^{[8]}La^{3+}$	78	0.38	20	30 (60)	G18
$^{[6]}Ti^{4+}$	298	0.67	20	115 (130)	This work
$^{[6]}I^{5+}$	**77**	**0.83**	**40**	**2 (50)**	GH18b
$^{[4]}Si^{4+}$	2506	1	25	70 (400)	GH18a
$^{[4]}S^{6+}$	906	1.5	5	300 (700)	GH18b

Table 3: Mean-bond-length statistics for the transition metal ions bonded to O^{2-}.

Ion	Coordination number	Number of co-ordination pol-yhedra	Grand mean bond-length (Å)	Standard de-viation (Å)	Mean bond-length range (Å)	Maximum mean bond-length (Å)	Minimum mean bond-length (Å)	Skewness	Kurtosis
Sc^{3+}	6	75	2.098	0.017	0.071	2.133	2.063	0.074	-0.586
	7	5	2.163	0.017	0.043	2.188	2.146	0.846	-0.505
	8	8	2.234	0.026	0.066	2.273	2.207	0.622	-1.817
Ti^{3+}	6	21	2.037	0.019	0.081	2.072	1.991	-0.666	1.075
	7	2	2.108	0.008	0.012	2.114	2.102	--	--
	8	1	2.195	--	0.000	2.195	2.195	--	--
Ti^{4+}	4	4	1.821	0.011	0.026	1.836	1.811	1.416	2.442
	5	17	1.917	0.014	0.048	1.940	1.892	0.241	-0.518
	6	293	1.971	0.017	0.094	2.020	1.926	-0.209	0.118
	7	1	2.064	--	0.000	2.064	2.064	--	--
V^{3+}	6	67	2.007	0.017	0.079	2.048	1.968	0.084	-0.235
V^{4+}	5	95	1.893	0.010	0.066	1.929	1.863	0.411	1.187
	6	128	1.980	0.019	0.103	2.023	1.921	-0.323	0.130
V^{5+}	4	345	1.717	0.010	0.075	1.758	1.682	0.075	1.991
	5	65	1.827	0.013	0.073	1.869	1.796	0.569	1.397
	6	293	1.924	0.013	0.079	1.976	1.896	1.045	1.486
Cr^{2+}	4	6	2.004	0.010	0.027	2.024	1.997	2.082	4.523
	5	2	2.113	0.004	0.006	2.116	2.110	--	--
	6	9	2.188	0.020	0.067	2.233	2.165	1.644	3.308
Cr^{3+}	6	104	1.976	0.014	0.064	2.013	1.949	0.409	-0.583
Cr^{4+}	4	1	1.784	--	0.000	1.784	1.784	--	--
	6	6	1.950	0.019	0.052	1.988	1.937	2.130	4.777
Cr^{5+}	4	1	1.693	--	0.000	1.693	1.693	--	--
Cr^{6+}	4	169	1.652	0.011	0.072	1.696	1.624	0.295	1.051
Mn^{2+}	4	10	2.046	0.025	0.085	2.085	2.001	-0.040	-0.021
	5	24	2.141	0.023	0.096	2.175	2.079	-0.830	1.283
	6	318	2.199	0.027	0.172	2.305	2.134	0.434	0.597

	7	2	2.352	0.061	0.087	2.395	2.309	--	--
	8	18	2.321	0.025	0.081	2.356	2.275	-0.415	-0.636
Mn^{3+}	4	2	1.901	0.003	0.005	1.903	1.898	--	--
	5	10	1.959	0.017	0.047	1.980	1.933	-0.240	-1.269
	6	82	2.031	0.019	0.094	2.086	1.992	0.106	-0.320
Mn^{4+}	4	1	1.750	--	0.000	1.750	1.750	--	--
	6	20	1.903	0.012	0.043	1.928	1.885	0.202	-0.364
Mn^{5+}	4	8	1.698	0.007	0.023	1.706	1.683	-1.095	1.556
Mn^{6+}	4	2	1.662	0.008	0.015	1.670	1.655	--	--
Mn^{7+}	4	7	1.610	0.007	0.020	1.622	1.603	0.913	0.421
Fe^{2+}	3	8	1.844	0.018	0.049	1.860	1.811	-1.274	0.568
	4	6	1.985	0.021	0.066	2.008	1.942	-1.667	3.509
	5	19	2.097	0.027	0.117	2.142	2.024	-1.036	1.866
	6	146	2.147	0.028	0.156	2.246	2.090	0.543	0.419
	8	5	2.333	0.041	0.087	2.383	2.296	0.519	-2.945
Fe^{3+}	4	65	1.875	0.016	0.070	1.910	1.840	0.086	-0.642
	5	21	1.966	0.015	0.049	1.984	1.935	-0.717	-0.491
	6	378	2.015	0.019	0.114	2.091	1.977	1.123	2.171
	8	2	2.125	0.008	0.011	2.130	2.119	--	--
Co^{2+}	3	14	1.854	0.017	0.055	1.869	1.814	-1.659	1.756
	4	27	1.967	0.017	0.069	1.995	1.926	-0.648	0.341
	5	16	2.066	0.026	0.101	2.129	2.027	0.557	0.775
	6	243	2.108	0.021	0.121	2.182	2.061	0.678	0.947
	8	1	2.272	--	0.000	2.272	2.272	--	--
Co^{3+}	6	15	1.908	0.013	0.049	1.942	1.893	1.575	2.638
Co^{4+}	6	1	1.874	--	0.000	1.874	1.874	--	--
Ni^{2+}	2	2	1.686	0.001	0.002	1.687	1.685	--	--
	4	3	1.950	0.047	0.082	1.977	1.895	-1.732	--
	5	8	2.028	0.012	0.031	2.044	2.013	0.089	-1.701
	6	242	2.070	0.020	0.118	2.148	2.030	0.900	1.669
Ni^{4+}	6	5	1.870	0.004	0.011	1.875	1.865	0.408	1.817
Cu^{+}	2	42	1.839	0.022	0.087	1.882	1.794	-0.286	-0.503

	3	2	1.969	0.002	0.003	1.971	1.968	--	--
	4	13	2.084	0.042	0.137	2.171	2.034	0.619	-0.190
Cu^{2+}	4	129	1.943	0.017	0.085	1.986	1.901	0.285	0.160
	5	218	2.037	0.022	0.122	2.106	1.984	0.534	0.244
	6	365	2.130	0.030	0.174	2.225	2.051	0.678	0.322
	8	4	2.302	0.033	0.069	2.349	2.280	1.689	2.751
Cu^{3+}	4	11	1.846	0.018	0.055	1.872	1.817	0.070	-1.052
Zn^{2+}	4	227	1.952	0.016	0.115	2.020	1.905	0.166	1.334
	5	36	2.051	0.015	0.073	2.085	2.012	-0.304	0.138
	6	193	2.110	0.023	0.144	2.200	2.056	1.050	1.676
Y^{3+}	6	25	2.264	0.019	0.069	2.291	2.222	-0.208	-0.894
	7	35	2.332	0.018	0.065	2.366	2.302	0.002	-0.708
	8	99	2.390	0.019	0.096	2.438	2.342	-0.690	0.473
	9	15	2.422	0.019	0.071	2.468	2.397	1.140	1.142
	10	1	2.496	--	0.000	2.496	2.496	--	--
	12	1	2.541	--	0.000	2.541	2.541	--	--
Zr^{4+}	6	73	2.078	0.013	0.082	2.129	2.048	1.057	3.431
	7	13	2.146	0.012	0.032	2.162	2.129	0.187	-1.758
	8	21	2.199	0.006	0.022	2.211	2.189	-0.219	-0.686
	9	3	2.263	0.019	0.036	2.278	2.242	-1.132	--
	10	7	2.283	0.005	0.011	2.288	2.277	-0.147	-2.054
Nb^{4+}	6	3	2.054	0.006	0.011	2.061	2.049	1.449	--
Nb^{5+}	4	2	1.831	0.005	0.007	1.834	1.827	--	--
	5	4	1.926	0.011	0.025	1.933	1.907	-1.982	3.938
	6	240	1.993	0.018	0.102	2.046	1.944	0.137	0.150
	7	3	2.069	0.013	0.026	2.082	2.056	-0.217	--
	8	1	2.080	--	0.000	2.080	2.080	--	--
Mo^{3+}	6	5	2.095	0.009	0.023	2.109	2.086	1.468	2.769
Mo^{4+}	6	9	2.003	0.007	0.023	2.016	1.992	0.559	0.323
Mo^{5+}	5	2	1.916	0.004	0.009	1.920	1.911	--	--
	6	74	1.992	0.015	0.070	2.026	1.955	-0.034	-0.410
Mo^{6+}	4	434	1.764	0.009	0.057	1.790	1.732	-0.255	0.861

	5	15	1.872	0.016	0.053	1.898	1.845	0.069	-0.882
	6	506	1.972	0.015	0.091	2.024	1.933	0.096	-0.282
Tc^{7+}	4	6	1.705	0.004	0.009	1.711	1.702	0.672	-1.320
Ru^{3+}	6	3	2.025	0.002	0.003	2.027	2.024	--	--
Ru^{4+}	6	8	1.982	0.011	0.034	1.995	1.961	-0.713	-0.066
Ru^{5+}	6	23	1.964	0.013	0.044	1.987	1.943	0.241	-1.333
Rh^{3+}	6	11	2.025	0.021	0.065	2.071	2.006	1.324	0.754
Rh^{4+}	6	3	2.007	0.011	0.020	2.020	2.000	1.705	--
Pd^{2+}	4	29	2.011	0.020	0.078	2.060	1.982	0.578	-0.419
Pd^{4+}	6	2	1.999	0.004	0.005	2.001	1.996	--	--
Ag^{+}	2	5	2.136	0.009	0.043	2.164	2.121	0.862	-1.700
	3	15	2.278	0.025	0.083	2.319	2.236	0.003	-0.865
	4	37	2.402	0.030	0.125	2.466	2.341	-0.180	-0.607
	5	45	2.489	0.036	0.147	2.555	2.408	-0.190	-0.438
	6	63	2.537	0.031	0.136	2.594	2.458	-0.292	-0.539
	7	9	2.589	0.028	0.084	2.618	2.534	-1.001	0.480
	8	13	2.656	0.030	0.113	2.730	2.617	1.199	1.882
	9	3	2.704	0.024	0.041	2.731	2.690	1.732	--
Cd^{2+}	5	4	2.257	0.014	0.034	2.278	2.244	1.291	2.291
	6	135	2.302	0.021	0.108	2.368	2.260	0.618	0.035
	7	6	2.377	0.047	0.132	2.466	2.334	1.758	3.604
	8	18	2.432	0.027	0.086	2.469	2.383	-0.105	-1.040
	9	1	2.530	--	0.000	2.530	2.530	--	--
Hf^{4+}	6	11	2.082	0.013	0.035	2.099	2.064	0.085	-1.193
	7	4	2.128	0.003	0.006	2.131	2.125	-0.017	-5.552
	8	7	2.190	0.004	0.013	2.199	2.186	1.365	2.285
Ta^{5+}	6	138	1.988	0.018	0.100	2.052	1.951	0.477	0.131
	7	14	2.057	0.007	0.023	2.069	2.046	0.459	-0.831
W^{5+}	6	4	1.956	0.019	0.043	1.976	1.933	-0.225	-2.734
W^{6+}	4	35	1.773	0.012	0.050	1.797	1.747	-0.172	0.581
	5	12	1.859	0.013	0.040	1.879	1.839	0.133	-1.593
	6	363	1.951	0.017	0.100	1.995	1.894	-0.455	0.408

Re^{5+}	6	3	1.940	0.005	0.009	1.945	1.936	1.597	--
Re^{7+}	4	41	1.716	0.011	0.053	1.740	1.686	-0.443	0.444
	5	8	1.810	0.010	0.035	1.827	1.792	-0.155	1.651
	6	10	1.882	0.012	0.037	1.906	1.869	0.909	0.092
Os^{5+}	6	4	1.960	0.004	0.008	1.963	1.954	-1.846	3.508
Os^{6+}	6	1	1.926	--	0.000	1.926	1.926	--	--
Os^{7+}	5	1	1.825	--	0.000	1.825	1.825	--	--
	6	3	1.887	0.014	0.034	1.904	1.870	--	--
Os^{8+}	4	1	1.698	--	0.000	1.698	1.698	--	--
	5	3	1.793	0.020	0.039	1.811	1.772	-0.726	--
	6	4	1.885	0.018	0.040	1.902	1.862	-0.798	-0.968
Ir^{3+}	6	1	2.042	--	0.000	2.042	2.042	--	--
Ir^{4+}	4	5	1.909	0.007	0.017	1.919	1.902	0.448	-0.638
	6	12	2.015	0.010	0.034	2.031	1.997	-0.353	-0.043
Ir^{5+}	6	6	1.990	0.013	0.030	2.001	1.971	-0.928	-1.725
Pt^{2+}	4	2	2.007	0.011	0.022	2.017	1.995	-1.008	--
Pt^{4+}	6	33	2.021	0.014	0.057	2.055	1.998	0.345	-0.452
Au^{3+}	4	24	1.999	0.013	0.040	2.020	1.980	0.161	-1.363
Hg^{2+}	2	1	1.955	--	0.000	1.955	1.955	--	--
	4	6	2.316	0.081	0.227	2.403	2.176	-1.116	1.176
	5	3	2.380	0.090	0.168	2.445	2.277	-1.565	--
	6	25	2.429	0.072	0.242	2.584	2.342	0.532	-0.474
	7	9	2.505	0.045	0.140	2.593	2.453	0.723	0.440
	8	8	2.502	0.021	0.050	2.530	2.479	0.435	-2.040

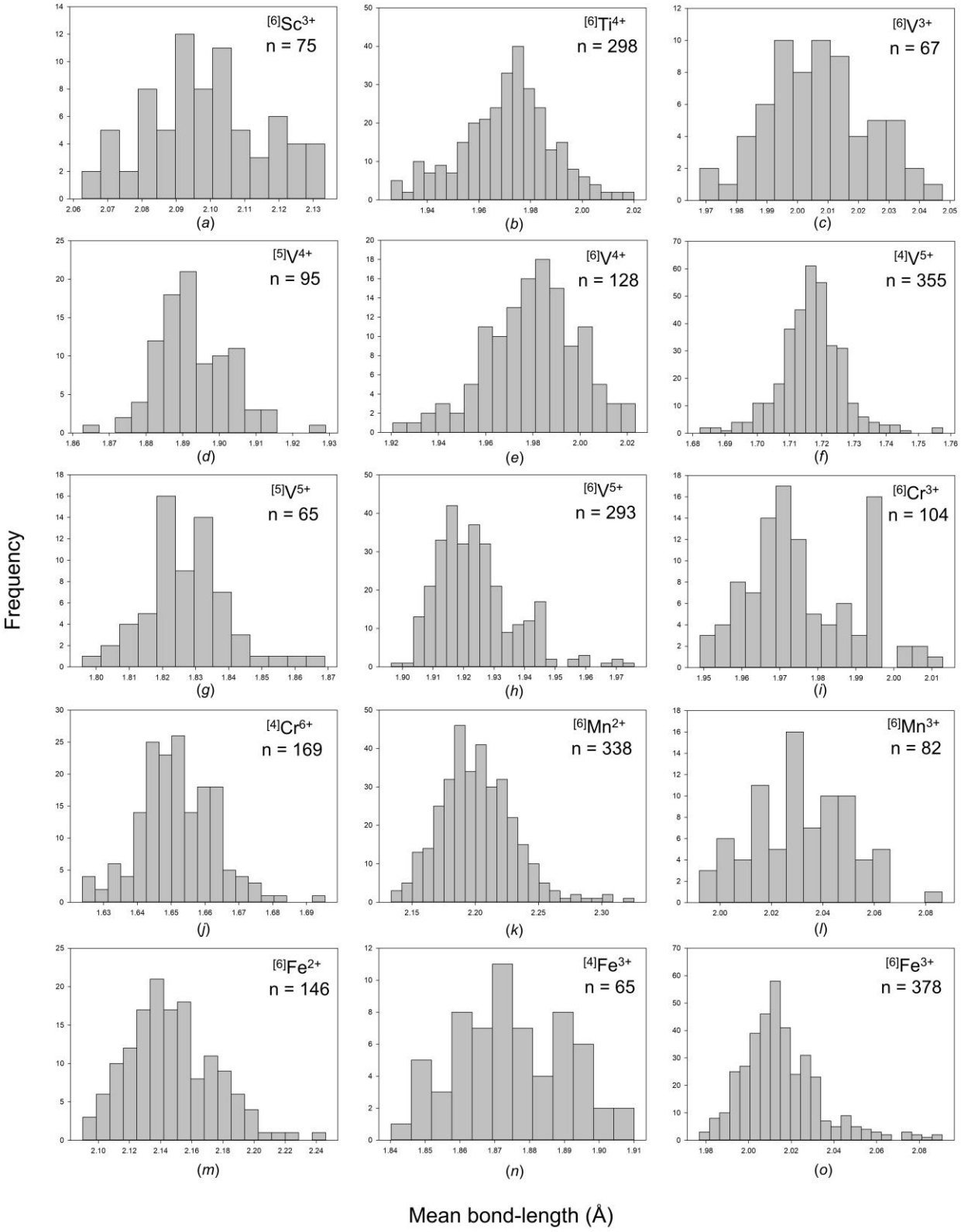
[6]Sc3+
n = 75
(a)
[6]Ti4+
n = 298
(b)
[6]V3+
n = 67
(c)
[5]V4+
n = 95
(d)
[6]V4+
n = 128
(e)
[4]V5+
n = 355
(f)
[5]V5+
n = 65
(g)
[6]V5+
n = 293
(h)
[6]Cr3+
n = 104
(i)
[4]Cr6+
n = 169
(j)
[6]Mn2+
n = 338
(k)
[6]Mn3+
n = 82
(l)
[6]Fe2+
n = 146
(m)
[4]Fe3+
n = 65
(n)
[6]Fe3+
n = 378
(o)
Frequency
Mean bond-length (Å)

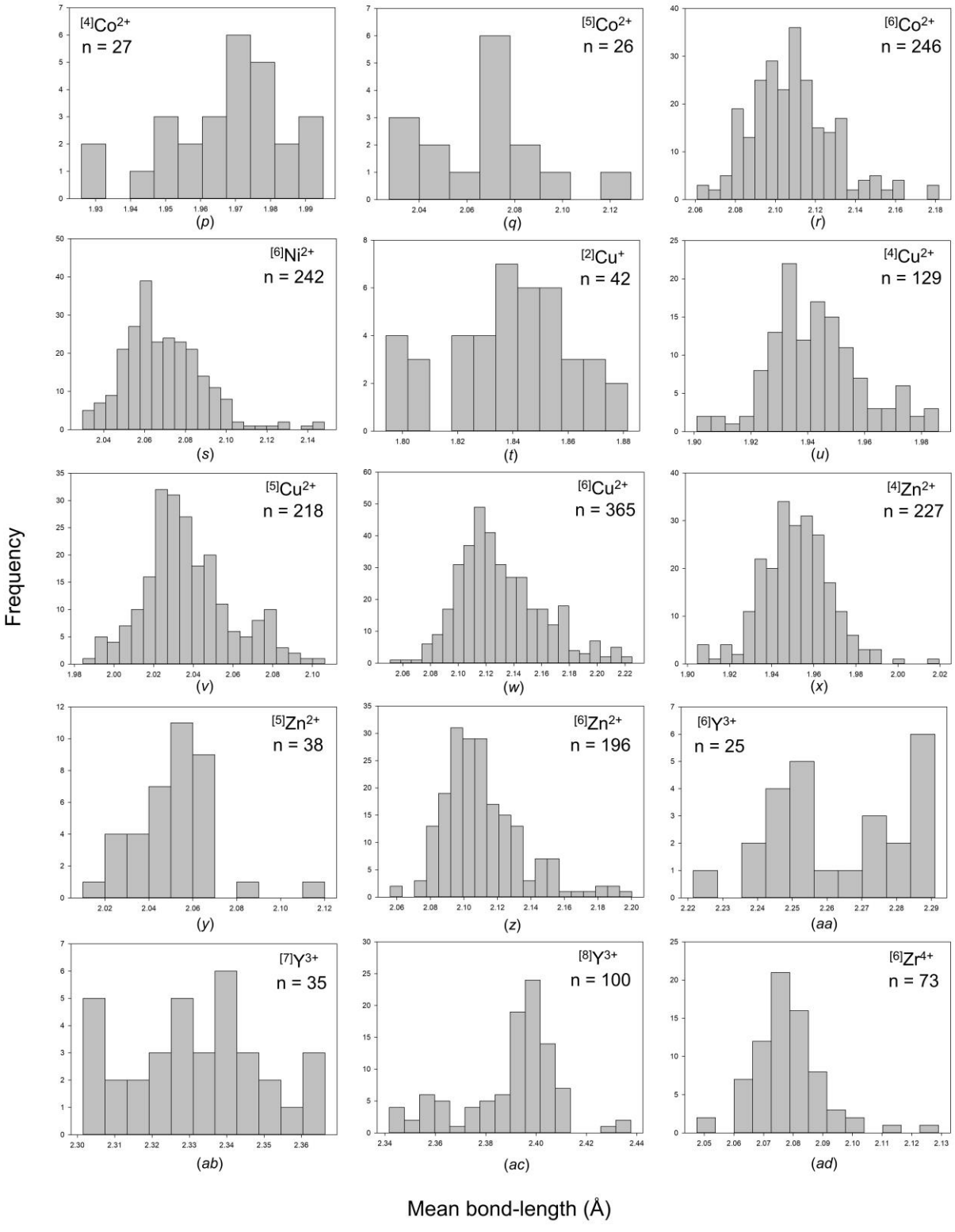
[4]Co2+
n = 27
(p)
[5]Co2+
n = 26
(q)
[6]Co2+
n = 246
(r)
[6]Ni2+
n = 242
(s)
[2]Cu+
n = 42
(t)
[4]Cu2+
n = 129
(u)
[5]Cu2+
n = 218
(v)
[6]Cu2+
n = 365
(w)
[4]Zn2+
n = 227
(x)
[5]Zn2+
n = 38
(y)
[6]Zn2+
n = 196
(z)
[6]Y3+
n = 25
(aa)
[7]Y3+
n = 35
(ab)
[8]Y3+
n = 100
(ac)
[6]Zr4+
n = 73
(ad)
Frequency
Mean bond-length (Å)

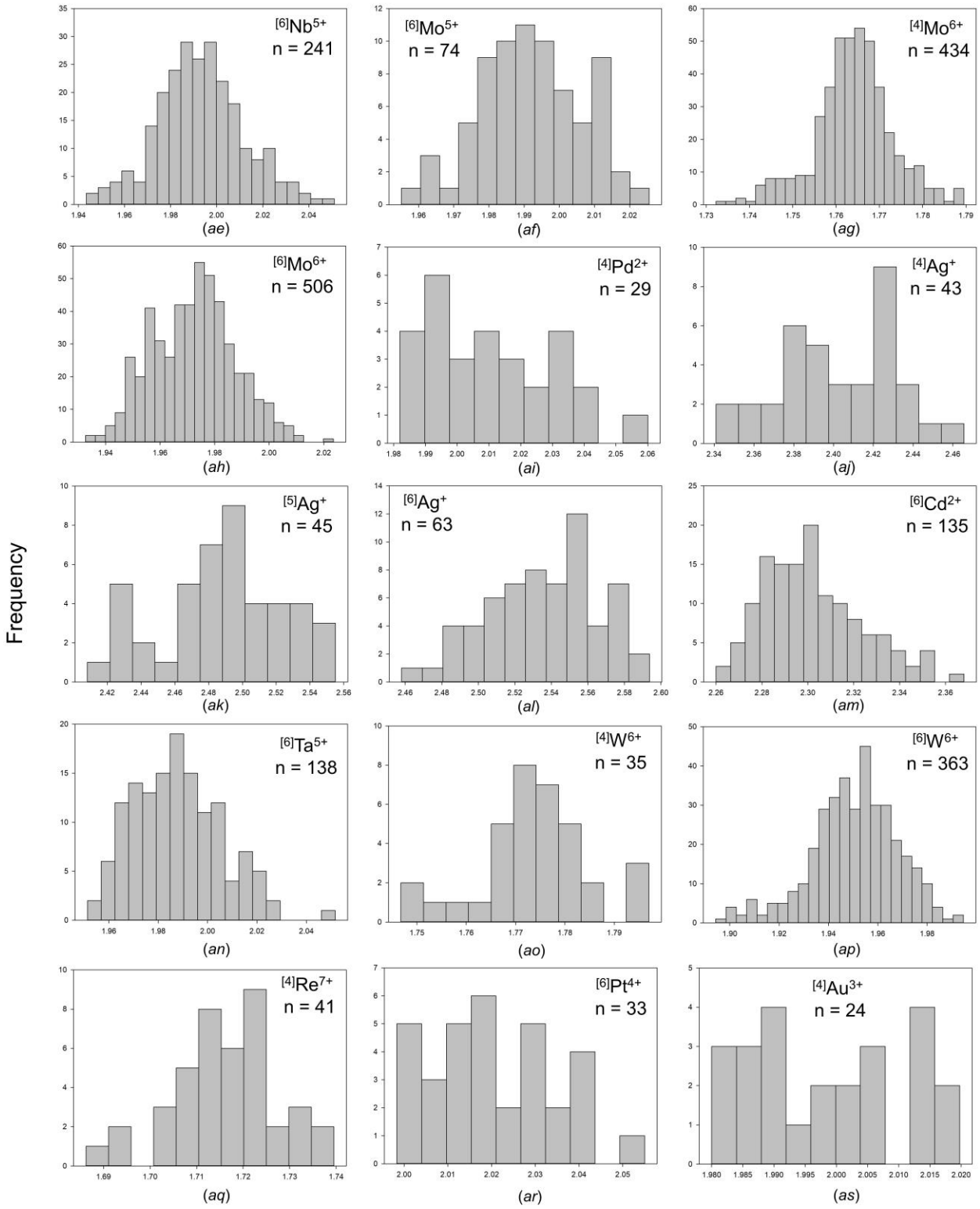
[6]Nb5+
n = 241
(ae)
[6]Mo5+
n = 74
(af)
[4]Mo6+
n = 434
(ag)
[6]Mo6+
n = 506
(ah)
[4]Pd2+
n = 29
(ai)
[4]Ag+
n = 43
(aj)
[5]Ag+
n = 45
(ak)
[6]Ag+
n = 63
(al)
[6]Cd2+
n = 135
(am)
[6]Ta5+
n = 138
(an)
[4]W6+
n = 35
(ao)
[6]W6+
n = 363
(ap)
[4]Re7+
n = 41
(aq)
[6]Pt4+
n = 33
(ar)
[4]Au3+
n = 24
(as)
Frequency
Mean bond-length (Å)

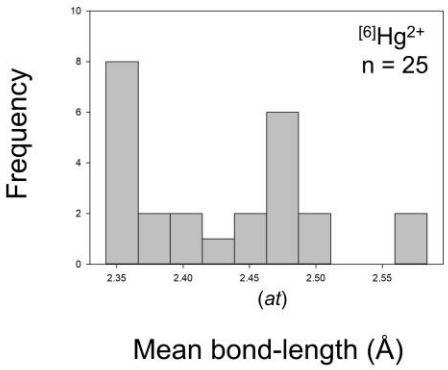

Figure 3: Mean-bond-length distributions for selected configurations of the transition metal ions bonded to O^{2-}: (*a*) $^{[6]}Sc^{3+}$, (*b*) $^{[4]}Ti^{4+}$, (*c*) $^{[6]}V^{3+}$, (*d*) $^{[5]}V^{4+}$, (*e*) $^{[6]}V^{4+}$, (*f*) $^{[4]}V^{5+}$, (*g*) $^{[5]}V^{5+}$, (*h*) $^{[6]}V^{5+}$, (*i*) $^{[6]}Cr^{3+}$, (*j*) $^{[4]}Cr^{6+}$, (*k*) $^{[6]}Mn^{2+}$, (*l*) $^{[6]}Mn^{3+}$, (*m*) $^{[6]}Fe^{2+}$, (*n*) $^{[4]}Fe^{3+}$, (*o*) $^{[6]}Fe^{3+}$, (*p*) $^{[4]}Co^{2+}$, (*q*) $^{[5]}Co^{2+}$, (*r*) $^{[6]}Co^{2+}$, (*s*) $^{[6]}Ni^{2+}$, (*t*) $^{[2]}Cu^{+}$, (*u*) $^{[4]}Cu^{2+}$, (*v*) $^{[5]}Cu^{2+}$, (*w*) $^{[6]}Cu^{2+}$, (*x*) $^{[4]}Zn^{2+}$, (*y*) $^{[5]}Zn^{2+}$, (*z*) $^{[6]}Zn^{2+}$, (*aa*) $^{[6]}Y^{3+}$, (*ab*) $^{[7]}Y^{3+}$, (*ac*) $^{[8]}Y^{3+}$, (*ad*) $^{[6]}Zr^{4+}$, (*ae*) $^{[6]}Nb^{5+}$, (*af*) $^{[6]}Mo^{5+}$, (*ag*) $^{[4]}Mo^{6+}$, (*ah*) $^{[6]}Mo^{6+}$, (*ai*) $^{[4]}Pd^{2+}$, (*aj*) $^{[4]}Ag^{+}$, (*ak*) $^{[5]}Ag^{+}$, (*al*) $^{[6]}Ag^{+}$, (*am*) $^{[6]}Cd^{2+}$, (*an*) $^{[6]}Ta^{5+}$, (*ao*) $^{[4]}W^{6+}$, (*ap*) $^{[6]}W^{6+}$, (*aq*) $^{[4]}Re^{7+}$, (*ar*) $^{[6]}Pt^{4+}$, (*as*) $^{[4]}Au^{3+}$, (*at*) $^{[6]}Hg^{2+}$.

Bond-length distortion

Bond-length distortion, defined as the mean-square relative deviation of bond lengths from their mean value,[36] is a common measure of bond-length dispersion used on the basis of individual coordination polyhedra. Although it is more so a scalar index of bond-length dispersion than it is a measure of *distortion*, we retain the terminology "bond-length distortion" for historical reasons (notably, the link between bond-length distortion and the *distortion theorem* of the bond-valence model, which regards the inherent increase of mean-bond-lengths with increasing bond-length dispersion[37]).

Fig. S4 shows mean bond-length as a function of bond-length distortion for all transition-metal ions bonded to O^{2-}, and Fig. 4 shows those of adequate sample size. Transition-metal ions show a wide range of bond-length distortion when bonded to O^{2-}, from weakly distorted (0-10 × 10^{-3}) to moderately distorted (10-20 × 10^{-3}) to highly distorted (>20 × 10^{-3}). There is strong correlation between bond-length distortion and mean bond-length for moderately distorted ion configurations (10-20 × 10^{-3}) or higher. In previous articles of this series, we found that the correlation between bond-length distortion and mean bond-length is strong for ion configurations with values of distortion > 20 × 10^{-3} for the metalloids and post-transition metal ions bonded to O^{2-},[32] > 10 × 10^{-3} for the alkaline-earth metal,[29] non-metal[31] and actinide[30] ions bonded to O^{2-} and < 10 × 10^{-3} for the lanthanide ions bonded to O^{2-}.[30] There is no particularly strong correlation between bond-length distortion and mean bond-length for alkali-metal ions bonded to O^{2-}. [29]

Causal mechanisms underlying mean-bond-length variations

Gagné & Hawthorne examined potential factors leading to mean-bond-length variation for 55 ion configurations bonded to O^{2-}, including 20 configurations for transition metals bonded to O^{2-}: $^{[6]}Ti^{4+}$, $^{[6]}V^{4+}$, $^{[4]}V^{5+}$, $^{[6]}V^{5+}$, $^{[6]}Cr^{6+}$, $^{[6]}Mn^{2+}$, $^{[6]}Fe^{2+}$, $^{[6]}Fe^{3+}$, $^{[6]}Co^{2+}$, $^{[6]}Ni^{2+}$, $^{[5]}Cu^{2+}$, $^{[6]}Cu^{2+}$, $^{[4]}Zn^{2+}$, $^{[6]}Zn^{2+}$, $^{[6]}Nb^{5+}$, $^{[4]}Mo^{6+}$, $^{[6]}Mo^{6+}$, $^{[6]}Cd^{2+}$, $^{[6]}Ta^{5+}$ and $^{[6]}W^{6+}$.[38] They found mean bond-length to be correlated to bond-length distortion for 17 of those 20 ion configurations at a 99% confidence level ($\langle R^2 \rangle$ = 0.50), citing the *distortion theorem*[37] as the mechanism causing this correlation. Other factors investigated were found to be statistically insignificant, including the ionization energy and electronegativity of the next-nearest neighbours, and the coordination number of the bonded anions, leading them to propose that the inability of crystal structures to attain their ideal (*a priori*) bond lengths within the constraints of space-group and translational symmetry is the leading cause of mean-bond-length variation in crystals. Below, we expand on their analysis to investigate the underlying causal mechanisms of *bond-length* variation in transition-metal oxide and oxysalt crystals.

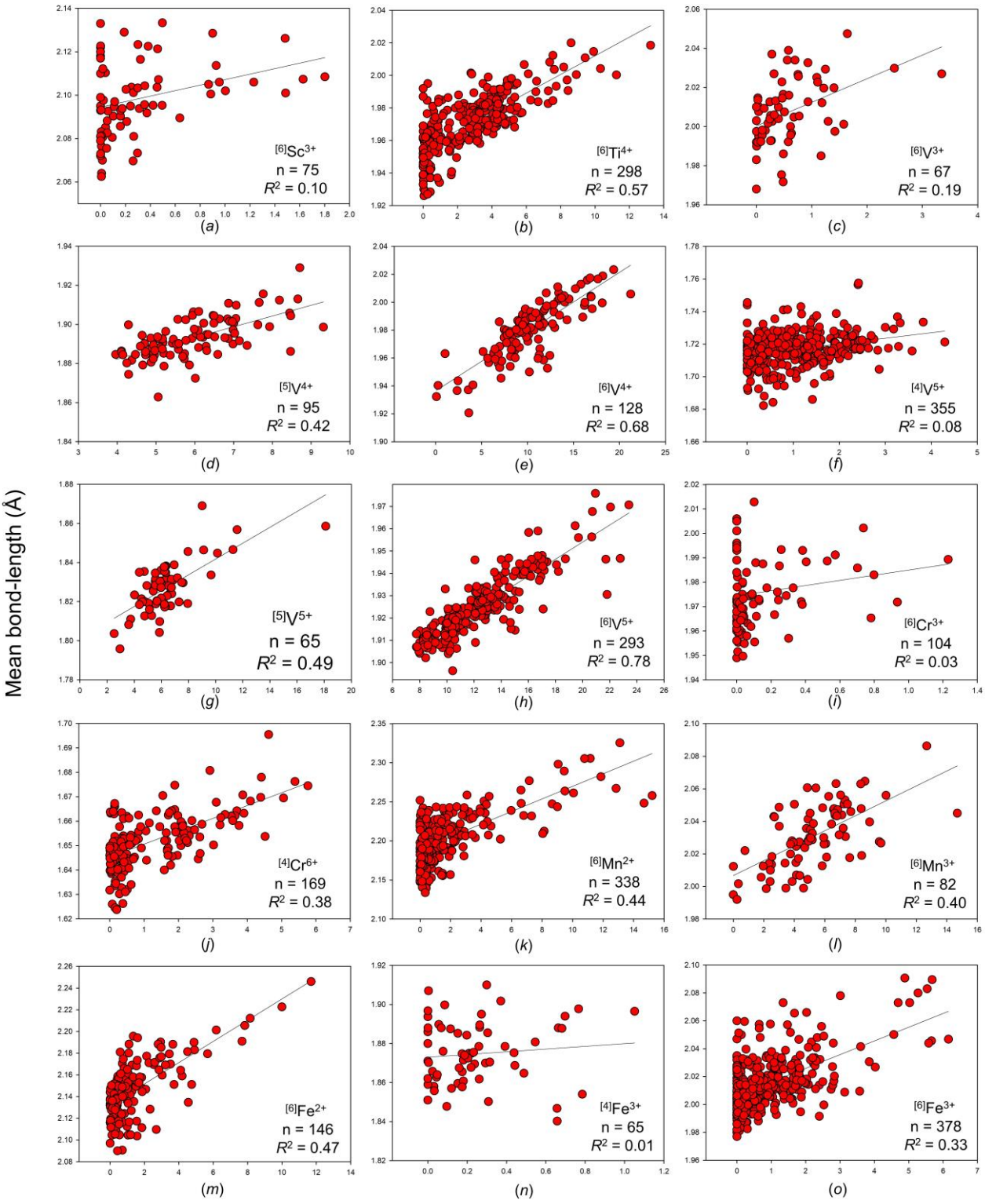
Mean bond-length (Å)
Distortion (x10-3)
(a) [6]Sc3+ n = 75 R2 = 0.10
(b) [6]Ti4+ n = 298 R2 = 0.57
(c) [6]V3+ n = 67 R2 = 0.19
(d) [5]V4+ n = 95 R2 = 0.42
(e) [6]V4+ n = 128 R2 = 0.68
(f) [4]V5+ n = 355 R2 = 0.08
(g) [5]V5+ n = 65 R2 = 0.49
(h) [6]V5+ n = 293 R2 = 0.78
(i) [6]Cr3+ n = 104 R2 = 0.03
(j) [4]Cr6+ n = 169 R2 = 0.38
(k) [6]Mn2+ n = 338 R2 = 0.44
(l) [6]Mn3+ n = 82 R2 = 0.40
(m) [6]Fe2+ n = 146 R2 = 0.47
(n) [4]Fe3+ n = 65 R2 = 0.01
(o) [6]Fe3+ n = 378 R2 = 0.33

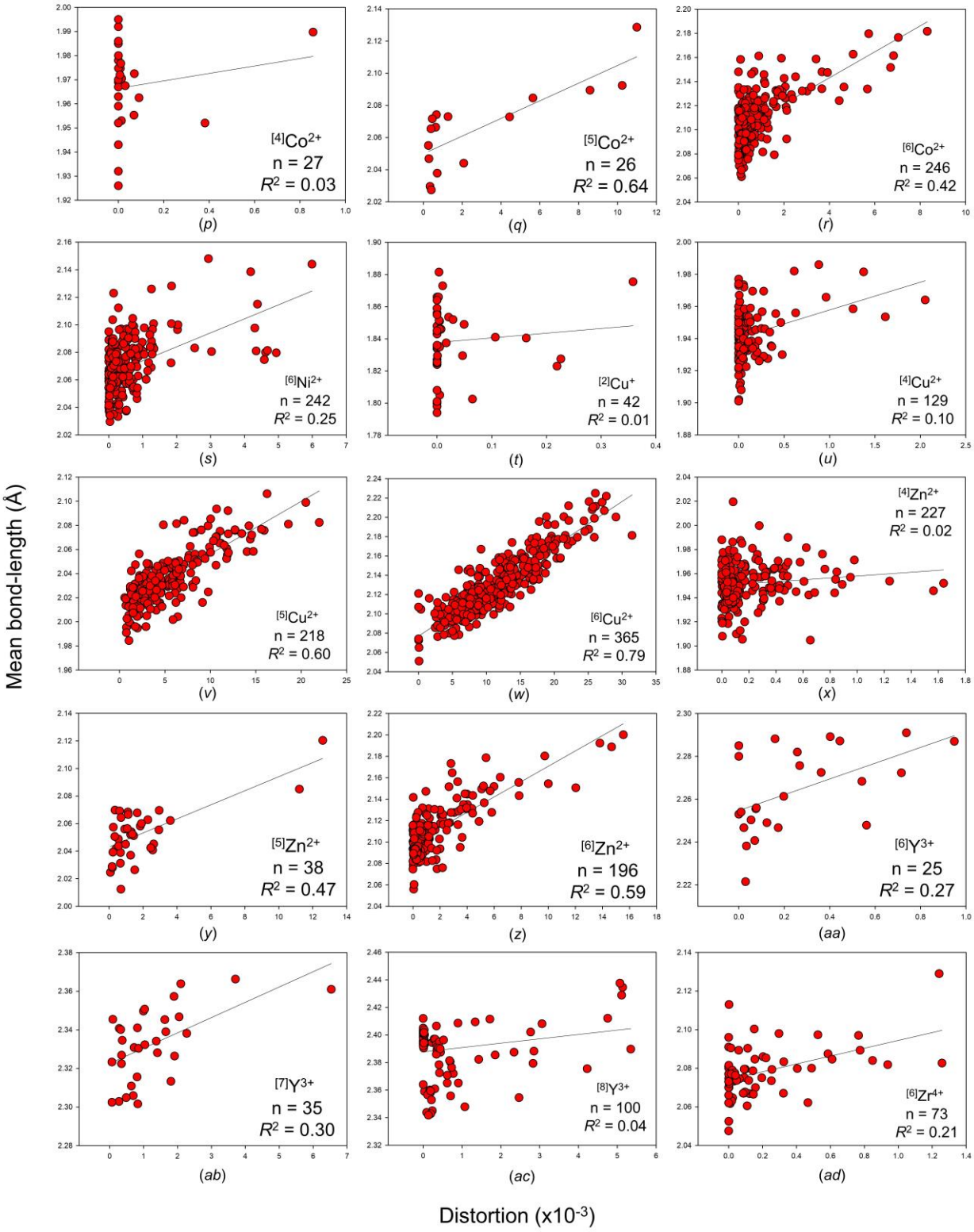
Mean bond-length (Å)
Distortion (x10-3)
[4]Co2+
n = 27
R2 = 0.03
(p)
[5]Co2+
n = 26
R2 = 0.64
(q)
[6]Co2+
n = 246
R2 = 0.42
(r)
[6]Ni2+
n = 242
R2 = 0.25
(s)
[2]Cu+
n = 42
R2 = 0.01
(t)
[4]Cu2+
n = 129
R2 = 0.10
(u)
[5]Cu2+
n = 218
R2 = 0.60
(v)
[6]Cu2+
n = 365
R2 = 0.79
(w)
[4]Zn2+
n = 227
R2 = 0.02
(x)
[5]Zn2+
n = 38
R2 = 0.47
(y)
[6]Zn2+
n = 196
R2 = 0.59
(z)
[6]Y3+
n = 25
R2 = 0.27
(aa)
[7]Y3+
n = 35
R2 = 0.30
(ab)
[8]Y3+
n = 100
R2 = 0.04
(ac)
[6]Zr4+
n = 73
R2 = 0.21
(ad)

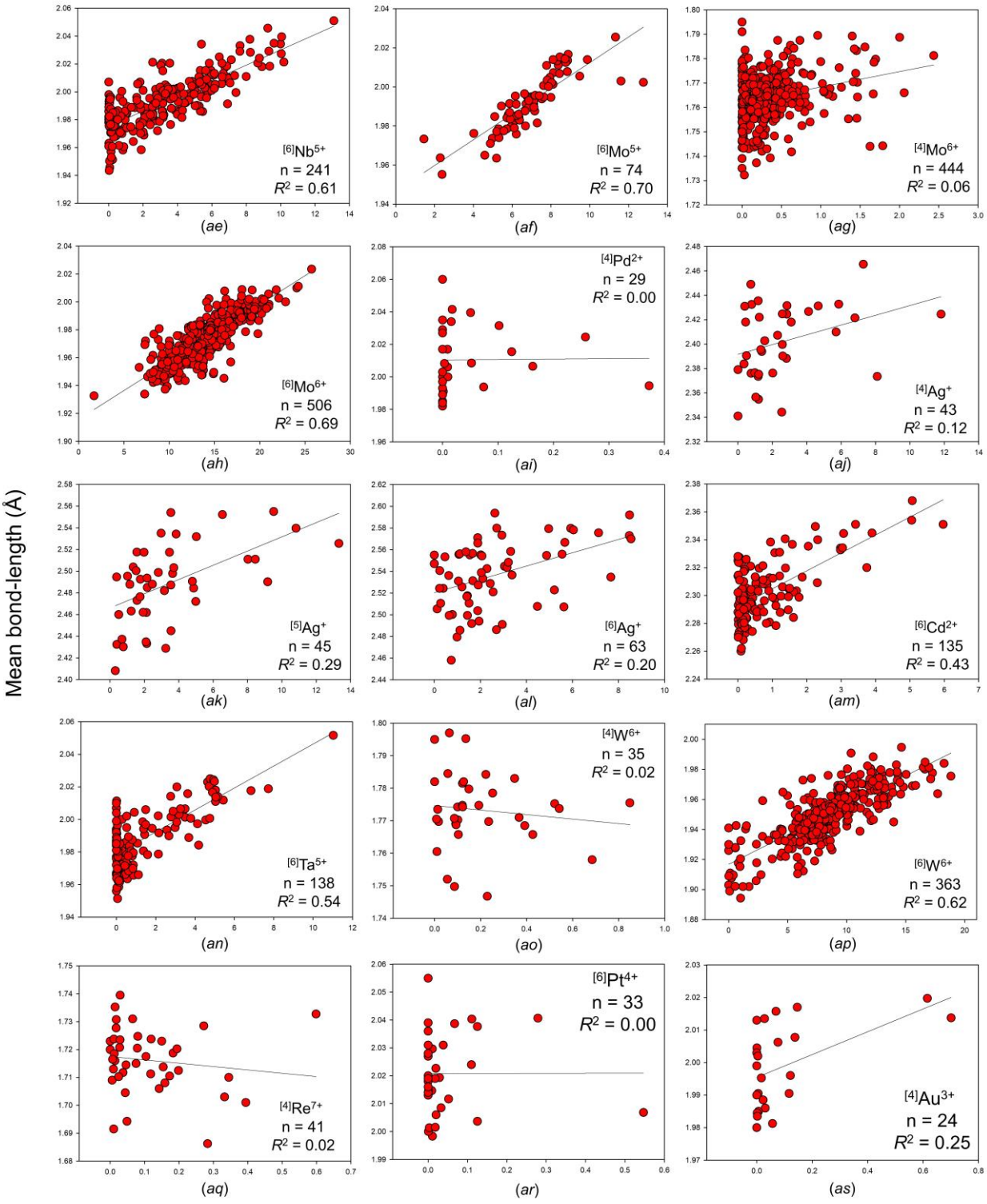
Mean bond-length (Å)
Distortion (x10-3)
[6]Nb5+
n = 241
R2 = 0.61
(ae)
[6]Mo5+
n = 74
R2 = 0.70
(af)
[4]Mo6+
n = 444
R2 = 0.06
(ag)
[6]Mo6+
n = 506
R2 = 0.69
(ah)
[4]Pd2+
n = 29
R2 = 0.00
(ai)
[4]Ag+
n = 43
R2 = 0.12
(aj)
[5]Ag+
n = 45
R2 = 0.29
(ak)
[6]Ag+
n = 63
R2 = 0.20
(al)
[6]Cd2+
n = 135
R2 = 0.43
(am)
[6]Ta5+
n = 138
R2 = 0.54
(an)
[4]W6+
n = 35
R2 = 0.02
(ao)
[6]W6+
n = 363
R2 = 0.62
(ap)
[4]Re7+
n = 41
R2 = 0.02
(aq)
[6]Pt4+
n = 33
R2 = 0.00
(ar)
[4]Au3+
n = 24
R2 = 0.25
(as)

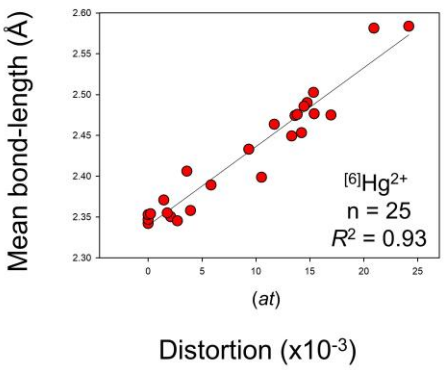

Figure 4: The effect of bond-length distortion on mean bond-length for selected configurations of the transition metal ions bonded to O^{2-}: (*a*) $^{[6]}Sc^{3+}$, (*b*) $^{[4]}Ti^{4+}$, (*c*) $^{[6]}V^{3+}$, (*d*) $^{[5]}V^{4+}$, (*e*) $^{[6]}V^{4+}$, (*f*) $^{[4]}V^{5+}$, (*g*) $^{[5]}V^{5+}$, (*h*) $^{[6]}V^{5+}$, (*i*) $^{[6]}Cr^{3+}$, (*j*) $^{[4]}Cr^{6+}$, (*k*) $^{[6]}Mn^{2+}$, (*l*) $^{[6]}Mn^{3+}$, (*m*) $^{[6]}Fe^{2+}$, (*n*) $^{[4]}Fe^{3+}$, (*o*) $^{[6]}Fe^{3+}$, (*p*) $^{[4]}Co^{2+}$, (*q*) $^{[5]}Co^{2+}$, (*r*) $^{[6]}Co^{2+}$, (*s*) $^{[6]}Ni^{2+}$, (*t*) $^{[2]}Cu^{+}$, (*u*) $^{[4]}Cu^{2+}$, (*v*) $^{[5]}Cu^{2+}$, (*w*) $^{[6]}Cu^{2+}$, (*x*) $^{[4]}Zn^{2+}$, (*y*) $^{[5]}Zn^{2+}$, (*z*) $^{[6]}Zn^{2+}$, (*aa*) $^{[6]}Y^{3+}$, (*ab*) $^{[7]}Y^{3+}$, (*ac*) $^{[8]}Y^{3+}$, (*ad*) $^{[6]}Zr^{4+}$, (*ae*) $^{[6]}Nb^{5+}$, (*af*) $^{[6]}Mo^{5+}$, (*ag*) $^{[4]}Mo^{6+}$, (*ah*) $^{[6]}Mo^{6+}$, (*ai*) $^{[4]}Pd^{2+}$, (*aj*) $^{[4]}Ag^{+}$, (*ak*) $^{[5]}Ag^{+}$, (*al*) $^{[6]}Ag^{+}$, (*am*) $^{[6]}Cd^{2+}$, (*an*) $^{[6]}Ta^{5+}$, (*ao*) $^{[4]}W^{6+}$, (*ap*) $^{[6]}W^{6+}$, (*aq*) $^{[4]}Re^{7+}$, (*ar*) $^{[6]}Pt^{4+}$, (*as*) $^{[4]}Au^{3+}$, (*at*) $^{[6]}Hg^{2+}$.

Part 2: Resolving the principal mechanisms underlying bond-length variation

Transition-metal oxides and oxysalts are ideally suited for examining bond-length variations in solids as they are highly susceptible to two important mechanisms underlying bond-length variation: (1) coupled electronic-vibrational degeneracy (leading to the Jahn-Teller effects), and (2) formation of multiple (π) bonds. In recent years, the non-local bond-topological asymmetry of coordination environments (sometimes referred to as asymmetry in the bond network) has been proposed as an additional mechanism underlying bond-length variation in crystals.[39,40] In this section, we exploit the size and comprehensiveness of our bond-length dispersion analysis to resolve the various causal mechanisms underlying bond-length variation in transition-metal oxides and oxysalts by way of rationalizing the shape of anomalous bond-length distributions (Fig. S1). We further summarize the theoretical underpinnings of these mechanisms.

Discussion for the present section is split into four subsections reflecting the principal causal mechanisms identified in this work: [1] non-local bond-topological effects; [2] multiple-bond formation; [3] electronic effects (with inherent focus on coupled electronic-vibrational degeneracy); and [4] crystal-structure effects. As shown below, mechanisms [1]-[3] may each lead to large bond-length variations and/or multi-modal bond-length distributions. However, these effects rarely occur in isolation, and their combination is often what leads to wide variations in bond lengths. It is worth noting that these mechanisms may be present in a limited number of crystal structures, or for all crystal structures in which the given ion configuration occurs; as a result, the shape of bond-length distributions depends on the relative importance/magnitude of the effect(s) sampled. Thus we focus our attention below on quantifiable features that may be recognized within the constituent data of these bond-length distributions.

In Table 4, we list 52 of the most interesting transition-metal ion configurations observed in this work, for either (1) having a shape that departs prominently from that expected for a two-body Morse potential, (2) displaying a very wide range of observed bond lengths, and/or (3) being of interest to some of the more general questions addressed in this work. These are the data we focus on for parts 2 and 3 of this work. In part 3, we will identify the causal mechanism(s) underlying bond-length variation for each of these ion configurations, and quantify their extent.

Table 4: Ion configurations with anomalous bond-length distribution when bonded to O^{2-}

Ion configuration	Electronic configuration	Anomalous shape?	Sample size (# cp)	Bond-length range (Å)	$\Delta_{topol} > \Delta_{cryst}$?	Mechanism(s)‡
$^{[6]}Sc^{3+}$	d^0	y	75	0.236	y	BTE, PJTE
$^{[4]}Ti^{4+}$	d^0		4	0.159		PJTE, BTE
$^{[5]}Ti^{4+}$	d^0	y	17	0.405		PJTE, BTE
$^{[6]}Ti^{4+}$	d^0	y	293	0.826		PJTE, BTE
$^{[7]}Ti^{4+}$	d^0	y	1	0.55	no data	PJTE

$^{[6]}V^{3+}$	d^2	y	67	0.399	y	BTE, JTEw
$^{[5]}V^{4+}$	d^1	y	95	0.577	y	π, PJTE/BTE/CSE
$^{[6]}V^{4+}$	d^1	y	128	1.030	y	π, PJTE/BTE
$^{[4]}V^{5+}$	d^0	y	355	0.391	y	BTE, PJTE
$^{[5]}V^{5+}$	d^0	y	65	0.801	y	π, PJTE, BTE
$^{[6]}V^{5+}$	d^0	y	293	0.993	y	π, BTE/PJTE
$^{[5]}Cr^{2+}$	d^4		2	0.432		PJTE, BTE
$^{[6]}Cr^{2+}$	d^4	y	9	0.696	y	JTEs/BTE
$^{[6]}Cr^{3+}$	d^3	y	104	0.19	similar	BTE, CSE
$^{[4]}Cr^{6+}$	d^0	y	169	0.357	y	BTE, PJTE, π
$^{[6]}Mn^{3+}$	d^4	y	82	0.755		JTEs, BTE
$^{[4]}Fe^{3+}$	d^5	y	65	0.201	y	BTE
$^{[5]}Co^{2+}$	d^7		16	0.628		PJTE
$^{[6]}Co^{2+}$	d^7		243	0.614	y	BTE, JTEs
$^{[5]}Cu^{2+}$	d^9		218	0.865		PJTE, BTE
$^{[6]}Cu^{2+}$	d^9	y	365	0.893		JTEs, BTE
$^{[6]}Zn^{2+}$	d^{10}		193	0.868	similar	BTE/PJTE
$^{[6]}Y^{3+}$	d^0	y	25	0.226	similar	PJTE/BTE
$^{[7]}Y^{3+}$	d^0	y	35	0.499		PJTE
$^{[8]}Y^{3+}$	d^0	y	99	0.507		PJTE/BTE
$^{[9]}Y^{3+}$	d^0		15	0.585		PJTE, BTE
$^{[10]}Y^{3+}$	d^0		1	0.604	y	BTE/PJTE
$^{[6]}Zr^{4+}$	d^0	y	73	0.218		PJTE, BTE
$^{[4]}Nb^{5+}$	d^0		2	0.184	no data	PJTE/BTE
$^{[5]}Nb^{5+}$	d^0	y	4	0.164		PJTE/BTE
$^{[6]}Nb^{5+}$	d^0	y	240	0.742		PJTE, BTE
$^{[7]}Nb^{5+}$	d^0		3	0.668		PJTE, BTE
$^{[6]}Mo^{4+}$	d^2	y	9	0.264	y	BTE
$^{[5]}Mo^{5+}$	d^1	y	2	0.328	no data	π
$^{[6]}Mo^{5+}$	d^1	y	74	0.806	y	π, BTE, JTEw
$^{[4]}Mo^{6+}$	d^0	possibly	434	0.268	y	BTE, PJTE
$^{[5]}Mo^{6+}$	d^0		15	0.620	y	π, BTE/PJTE
$^{[6]}Mo^{6+}$	d^0	y	506	1.005		PJTE, BTE
$^{[6]}Ru^{5+}$	d^3	y	23	0.305		CSE/BTE
$^{[6]}Cd^{2+}$	d^{10}		135	0.591	y	BTE, PJTE
$^{[6]}Hf^{4+}$	d^0	possibly	11	0.322		PJTE, BTE
$^{[6]}Ta^{5+}$	d^0	y	138	0.585		PJTE, BTE
$^{[7]}Ta^{5+}$	d^0	possibly	14	0.619		PJTE, BTE
$^{[5]}W^{6+}$	d^0		12	0.467		PJTE, BTE
$^{[6]}W^{6+}$	d^0	y	363	0.919		PJTE, BTE
$^{[4]}Re^{7+}$	d^0	y	41	0.150	y	BTE, PJTE
$^{[5]}Re^{7+}$	d^0	possibly	8	0.275		PJTE
$^{[6]}Re^{7+}$	d^0		10	0.195	y	PJTE, BTE
$^{[6]}Os^{6+}$	d^2	possibly	1	0.266	no data	BTE
$^{[5]}Os^{8+}$	d^0	possibly	3	0.569		PJTE, BTE

$^{[6]}Os^{8+}$	d^0	y	4	0.442		PJTE, BTE
$^{[6]}Hg^{2+}$	d^{10}	y	25	0.912	similar	BTE/PJTE

‡Mechanisms are listed in decreasing order of importance; BTE, bond-topological effects; π, pi-bond formation; JTEs, strong Jahn-teller effect; JTEw, weak Jahn-teller effect; PJTE, pseudo Jahn-Teller effect; CSE, crystal-structure effects.

[1] Non-local bond-topological effects

The connection between bond topology and bond-length variation was first demonstrated by Kunz & Brown.[39] Unfortunately, lack of follow-up work left unclear the extent to which this mechanism operates in terms of frequency of occurrence and bond-length-variation magnitude, leading few to acknowledge this mechanism as a noteworthy driver of bond-length variation in inorganic solids. We dedicate a significant part of this work to resolving this issue; we will clarify the mechanism of bond-length variation via bond-topological arguments using the bond-valence model, introduce new indices to quantify the effect of bond topology on bond-length variation, and provide worked examples to show the prevalence and scope of this effect.

The bond-valence model

The bond-valence model is an electrostatic model of chemical bonding used extensively in the study of minerals and inorganic materials.[41] The main axioms of the bond-valence model, analogous to Kirchhoff's rules for electrical circuits, are: [1] the *valence-sum rule*, which states that the sum of the directed bond valences around an ion is equal to its oxidation state (essentially, a modernization of Pauling's 2nd rule), and [2] the *path rule* which states that the sum of the directed bond valences along any path of bonds in a structure is zero where the path begins and ends on symmetrically equivalent ions.[42] Although the model finds many applications both in solution and in the solid state (summarized in refs [41,43]), its most common use is to serve as a check on newly refined crystal structures via verification of the valence-sum rule.

Key to this model is the relation between the length of a bond and its strength (called its *bond valence*):

$$s = exp\left[\frac{(R_o - R)}{B}\right] \qquad \text{(Equation 1)}$$

where s is the bond valence for a bond of length R, and R_0 and B are the bond-valence parameters of the ion pair. The bond-valence parameters are constants that are typically derived empirically (large sets of bond-valence parameters include those of Gagné & Hawthorne,[34] Brese & O'Keeffe[44] and Brown & Altermatt[26]). From this, the valence-sum rule can then be written as

$$\sum S_{ij} = \sum_j \exp\left(\frac{R_0 - R_{ij}}{B}\right) = V_i \qquad \text{(Equation 2)}$$

where V_i is the oxidation state of the ion (sometimes called the formal valence), and where the sum is taken over the j bonds involving ion i. For structure verification, deviation up to ~6-7% is deemed acceptable for any given site of a crystal structure;[34] this variation cannot be removed from the model, and is largely due to the effect of structure type on mean bond-length variations,[38] discussed as causal mechanism [4] in the present work. We used equation (2) throughout this series to spot possible experimental errors and oversights (e.g. substitutional disorder) to remove doubtful data from our dataset; similarly, equation (2) is used as a screening criterion in pymatgen,[45] the analysis code powering the Materials Project.[46] In addition, the valence-sum rule allows inferring the oxidation state of redox-active ions;[47–50] this is particularly relevant for confirming the oxidation state of transition metals, and to resolve mixed-valence site occupancy. Of greatest relevance to this work, the bond-topological underpinnings of the bond-valence model allow prediction of the *a priori* bond valences (thus bond lengths) of crystal structures;[42] as we show below, crystal structures often have intrinsic requirements for uneven distribution of bond valences (and thus bond lengths). Next, we investigate the inner-workings of this phenomenon, and the extent to which it results in bond-length variation for transition metals bonded to O^{2-}.

Non-local bond-topological asymmetry

In the bond-valence model, the principle of maximum symmetry states that a system in stable equilibrium adopts the highest symmetry consistent with the constraints acting on it;[51] these constraints include crystal-chemical and thermodynamics factors not limited to peculiar electronic behavior, *T-P* stability ranges, rate of crystallization, external field(s), etc. Where such constraints are absent or have negligible effect, a crystal structure is observed with the lowest-possible number of crystallographically distinct sites, i.e., equal to the number of distinct elements in the compound (e.g., for spinel: $MgAl_2O_4$). In this configuration, cations and anions distribute their *a priori* (ideal) bond valences evenly (see ref [42] for their calculation), resulting in coordination polyhedra with identical or similar bond lengths. With considerable constraints acting on the system at the time of crystallization, crystallographically distinct sites may rapidly outgrow the number of distinct elements in the compound. The decrease in crystallographic symmetry inherently results in increasingly asymmetric patterns of *a priori* bond valences (thus a *priori* bond lengths; equation 1) for cation and anion polyhedra, increasing the potential for large bond-length variations within those polyhedra. We term this phenomenon "*non-local bond-topological asymmetry*" where the variation in bond lengths does not originate from the local bond topology (the coordination polyhedron), but rather from asymmetry elsewhere in the bond topology, either in the form of varying coordination number(s) or ion identity (Fig. 5).

We emphasize that while crystallographically distinct variables (e.g. sites) may be bond-topologically equivalent (i.e. independent of physical metrics), the opposite is not true; variables that are bond-topologically distinct cannot be crystallographically equivalent. For example, introduction of one or more symmetry-breaking elements acting on sites that are bond-topologically equivalent will inevitably break their crystallographic equivalence, while retaining bond-topological equivalence (e.g., polymorphs; Fig. 6). This concept is an important demonstration of the hierarchy between bond-topological and crystallographic equivalence in crystal structures. As we show next, distinction between bond-topological and crystallographic equivalence defines two classes of causal mechanisms underlying bond-length variation in inorganic solids.

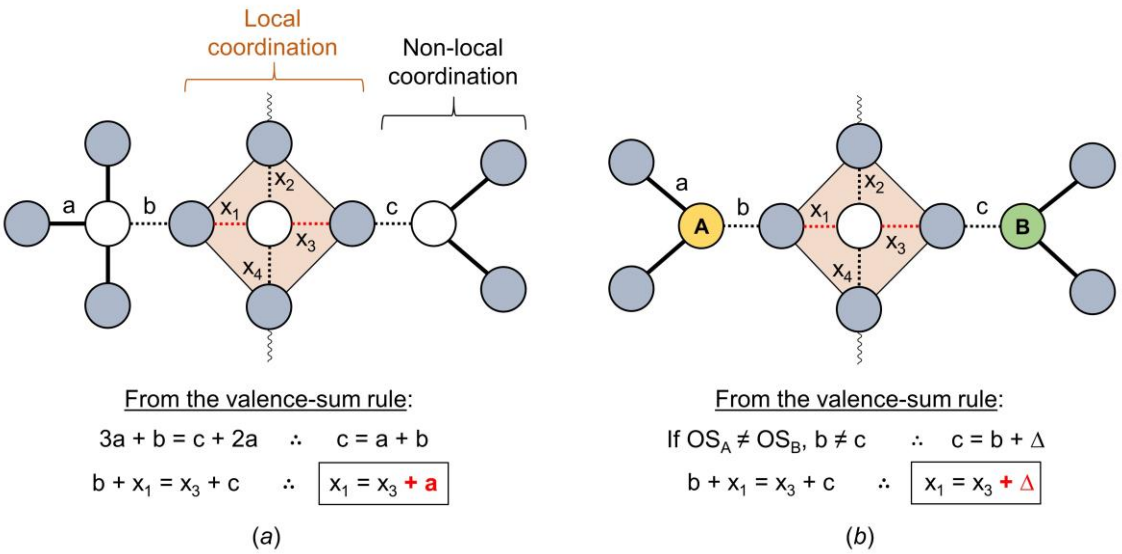

Figure 5: Inherent bond-valence (thus bond-length) variation resulting from the valence-sum rule for (*a*) different coordination numbers and (*b*) different oxidation states (OS) of next-nearest neighbors for a simple bond topology. Grey circles are anions, and white circles cations of the same oxidation state; colored circles are cations of different oxidation states. Fragment shown is self-contained; wavy lines indicate further bonds which are inconsequential to x_1 and x_3. Black bonds are terminal, thus are consequently equal to the oxidation state of the anion, "a"; from here, "b" and "c" are deduced, and x_1 and x_3 are show to be necessarily unequal in strength, thus causing bond-length variation within the local coordination.

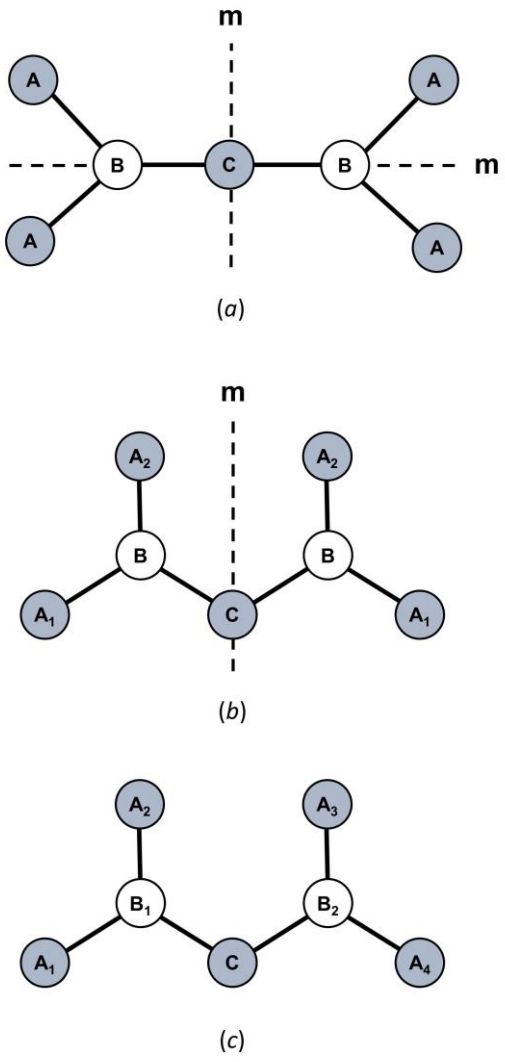

Figure 6: Demonstration of bond-topological and crystallographic equivalence for the ions of a dimeric unit (cations = white, anions = grey). Topologically equivalent ions share the same lettering, and crystallographically equivalent ions share the same lettering and subscript. Crystallographic equivalence of the constituent ions lowers from (*a*) the configuration of maximum symmetry about ion C to (*c*) the point of minimum crystallographic symmetry. Intermediate configurations are observed with progressively less symmetry operators (m = mirror plane), thus lowering the number of equivalent metrics (bond lengths, bond angles) from configurations (*a*) to (*c*). Bond-topological equivalence is unchanged from (*a*) to (*c*).

Quantifying bond-length variation as a result of bond-topological vs crystallographic effects

Mechanisms underlying bond-length variation rarely occur in isolation. As a result, it is often difficult to pin-point the source(s) of bond-length variation in a coordination polyhedron, and the relative extent to which they operate. As we show below, calculation of the *a priori* bond valences of a crystal structure is a useful approach for resolving and quantifying sources of bond-length variation in extended solids, as it allows separation of the causal mechanisms underlying bond-length variation into those that are *bond-topological* and *crystallographic* in nature.

We may quantitatively assess the amount of bond-length variation caused by bond-topological asymmetry, Δ_{topol}, as the mean (absolute) weighted deviation between the bond valences of a given polyhedron and that of its regular variant with equal bond lengths, i.e. its Pauling bond strength:

$$\Delta_{topol} = \frac{\sum_i^N w_i |s_i - s|}{\sum_i^N w_i} \qquad \text{Equation (5)}$$

where S_i is the *a priori* bond valence, s is the Pauling bond strength, w_i is the multiplicity of the bond in the coordination polyhedron, and where the sum is taken over the N crystallographically distinct bonds in the polyhedron.

Conversely, we may quantify bond-valence deviations of crystallographic origins as

$$\Delta_{cryst} = \frac{\sum_i^N w_i |s_i - s_i|}{\sum_i^N w_i} \qquad \text{Equation (6)}$$

where the difference is between the *a priori* bond valences S_i and the observed bond valences s_i. The quantity represented by the Δ_{cryst} index may be interpreted as the mean distortion caused by those effects that are not of bond-topological origin, i.e., whose bond-length variations are not captured/predicted via *a priori* bond valences. Both Δ_{topol} and Δ_{cryst} can be considered significant when > 0.05 v.u., large when > 0.10 v.u., and very large when > 0.20 v.u.

The Δ_{topol} index quantifies bond-length variation caused by [1] non-local bond-topological asymmetry, and [2] multiple-bond formation; Δ_{cryst} quantifies bond-length variation caused by [3] electronic effects (inclusive of effects such as lone-pair stereoactivity and magnetism, but with inherent focus on coupled electronic-vibrational degeneracy in this work), and [4] crystal-structure effects. Our choice of splitting bond-topological mechanisms [1] and [2] is arbitrary, and follows historical reasons of treating multiple-bond formation as an independent mechanism rooted in molecular-orbital theory (see section *[2] Multiple-bond formation*, below). However, it is impossible to clearly resolve the contributions of [1] and [2] from the Δ_{topol} index, because the arrangement of *a priori* bond valences is disconnected from the underlying physical processes leading to the crystal structure at hand. In accord with the hierarchy between bond-topological and crystallographic factors (discussed above), multiple-bond formation is primarily driven by the bond-topological requirements of the crystal structure, whose consideration precedes the bond-valence stability-range of ions. In practice, both the requirements of the crystal structure and those of the ions must coincide for the observation of (bond-topologically-driven) multiple bonds; otherwise, the structure will simply not occur, i.e. the ions crystallize into a different structure type (or types). While bond topology primarily dictates the observation of multiple bonds in solids, there are cases where multiple-bond formation clearly results from crystallographic mechanisms, e.g., the pseudo Jahn-Teller effect. In those cases, bond-length variation escapes prediction via *a priori* bond valences, and instead is amalgamated into the Δ_{cryst} index under a different causal mechanism. As such, it is impossible to generalize the origins of multiple-bond formation in solids; however, our method allows one to resolve whether this phenomenon results from a bond-topological or crystallographic mechanism on a structure-by-structure basis.

The effect of bond-topological and crystallographic mechanisms on bond-length variation is well illustrated by $CaNb^{5+}{}_2(P_4O_{13})(P_2O_7)O$ (62577),[52] with two crystallographically distinct sites fully occupied by monomeric Nb^{5+} ions in octahedral coordination to O^{2-}. For *Nb*1, all bonds are to non-bridging O^{2-} ions from PO_4 dimers; for *Nb*2, five bonds are to non-bridging O^{2-} ions of PO_4 dimers, and *O*13 has only one bond to Ca^{2+}. The *a priori* (observed) bond valences are as follows (Table 5; Fig. 7): 2 × 0.805 (0.993), 2 × 0.837 (0.824), and 2 × 0.859 (0.869) v.u. for *Nb*1, with Δ_{topol} = 0.019 and Δ_{cryst} = 0.071 v.u.; 2 × 0.782 (0.714), 2 × 0.831 (0.837), 0.261 (0.462) and 1.515 v.u. (1.753) for *Nb*2, with Δ_{topol} = 0.227 and Δ_{cryst} = 0.098 v.u. With regard to crystallographic effects, the strongest and weakest bonds involving *Nb*2 (0.261 and 1.515 v.u., for bond lengths 2.406 and 1.756 Å) are in *trans* configuration; the discrepancy between *a priori* and observed bond valences for these two bonds is caused by the off-centering of *Nb*2 toward *O*13 via the pseudo Jahn-Teller effect (more on this below). With regard to bond-topological effects, we can see from the *a priori* bond valences and the Δ_{topol} index that the formation of a highly-distorted octahedron on the one hand (*Nb*2), and of a regular octahedron on the other, for two monomers of the same cation in the same structure, simply results from non-local bond-topological asymmetry. Thus, we conclude from the Δ_{topol} and Δ_{cryst} values calculated for $CaNb_2(P_4O_{13})(P_2O_7)O$ that (1) the main driver of bond-length variation is the pseudo Jahn-Teller effect (PJTE) for *Nb*1, and non-local bond-topological asymmetry for *Nb*2, and (2) the magnitude of the PJTE is similar in both octahedra.

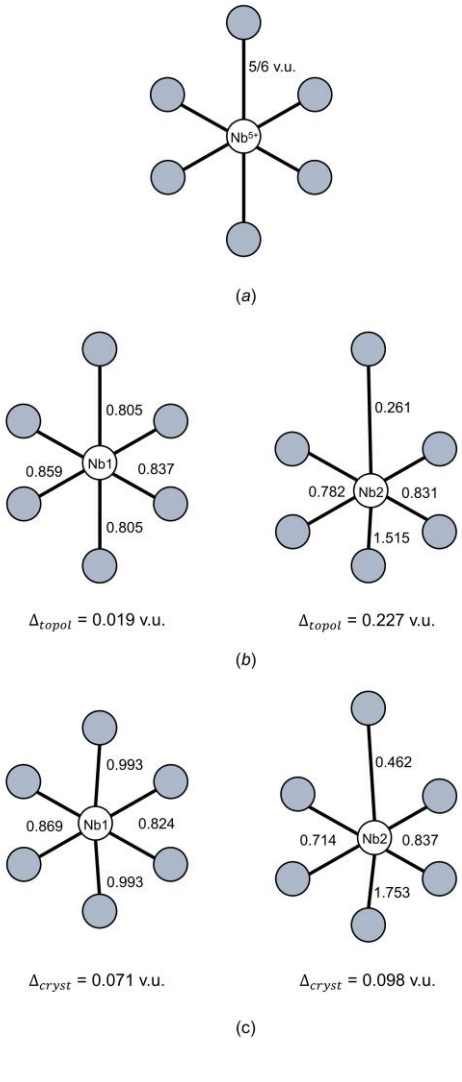

Figure 7: Local coordination of *Nb*1 and *Nb*2 in $CaNb^{5+}{}_2(P_4O_{13})(P_2O_7)O$. In this structure, the two crystallographically distinct $Nb^{5+}O_6$ octahedra do not have equal bonds 5/6 v.u. in strength (*a*); instead, non-local bond-topological asymmetry imposes bond-valence (thus bond-length) variability within the polyhedra (*b*), which serve as starting configurations for crystallographic effects to lead to the observed local geometries (*c*). The shaded spheres represent O^{2-}.

Table 5: *A priori* bond valences (v.u.) for $CaNb^{5+}{}_2(P_4O_{13})(P_2O_7)O$

	*Nb*1	*Nb*2	*Ca*	*P*1	*P*2	*P*3	*P*4	∑
*O*1			0.267 ×2↓	1.733				2
*O*2		0.782 ×2↓		1.218				2
*O*3				1 ×2→				2
*O*4				1.049	0.951			2
*O*5	0.805 ×2↓				1.195			2
*O*6			0.316 ×2↓		1.684			2
*O*7		0.831 ×2↓			1.169			2
*O*8	0.837 ×2↓					1.163 ×2↓		2
*O*9			0.348			1.652		2
*O*10						1.169	0.978	2
*O*11	0.859 ×2↓						1.141 ×2↓	2
*O*12		0.261					1.739	2
*O*13		1.515	0.458					2
∑	5	5	2	5	5	5	5	

The insight provided by *a priori* bond valences as well as the Δ_{topol} and Δ_{cryst} indices should be useful to experimentalists when refining, proposing, and describing new crystal structures; calculating these values should become routine practice where possible, in the same way the calculation of observed bond valence sums is routine practice today. These analyses should further be useful for identifying the structural and electronic underpinnings of functional properties linked to asymmetric coordination units. At present, no model rigorously defines the extent to which functional properties may be optimized via compositional and/or structural modifications. As we discuss later in text, calculation of Δ_{topol} and Δ_{cryst} indices resolves and quantifies the extent to which bond-topological and/or crystallographic phenomena are responsible for a given functional property in a crystal structure. Such knowledge allows informed optimization of the proper causal mechanisms giving rise to these properties, and sets expectation limits with regard to the optimizable extent of these functional properties.

To resolve the main cause(s) of bond-length variation underlying the numerous multi-modal bond-length distributions identified in this work (Fig. 1), we calculated values of Δ_{topol} and Δ_{cryst} for 268 transition-metal coordination polyhedra representing some of the largest bond-length variations observed for factors [1]-[4] above. These data cover 85 transition-metal ion configurations taken from 140 specific crystal structures for which we solved for the *a priori* bond valences (Table S1). Values of Δ_{topol} and Δ_{cryst} are given in Table S2, and are scattered in the next sections in aid to our analyses. From a representative cross-section of factors [1]-[4] in the set of selected crystal structures, we find $\langle\Delta_{topol}\rangle$ = 0.102 v.u. and $\langle\Delta_{cryst}\rangle$ = 0.113 v.u. for the 268 transition-metal coordination polyhedra, giving a glimpse into the extent and magnitude for which bond-length variations are affected by non-local bond-topological asymmetry. These values will be discussed in greater detail below (section *Bond-topological vs crystallographic effects)*. Next, we discuss two special cases where non-local bond-topological asymmetry has a particularly marked effect on bond-length variations for strongly-bonded units.

Polymerization of strongly-bonded units where $\langle BV\rangle_{cat.}$ is greater than $\langle BV\rangle_{br.an.}$

Bond-length variation driven by bond-topological asymmetry can be plainly illustrated via localized bonding interactions in strongly bonded units, for which bond-length variations result from the inter-connectedness of the bond-valence constraints of cations and anions with regard to the valence-sum rule (equation 2). For certain conditions, competition between the bond-valence constraints of cations and their bonded anions necessarily requires an uneven distribution of bond valences in cation and/or anion coordination polyhedra. These conditions are typical of oxide and oxysalt structures, in which the combination of high cation oxidation states and low coordination numbers results in high mean bond-valences, thus strongly bonded oxyanions. Where the mean bond-valence of a cation configuration ($\langle BV\rangle_{cat}$) exceeds that of the mean bond-valence of the bridging anion ($\langle BV\rangle_{br.an.}$), polymerization of the oxyanion requires significant weakening (i.e. lengthening) of the bridging M-O-M bonds for the valence-sum rule to hold at the bridging O^{2-} ion. For example, $^{[4]}Cr^{6+}$ readily polymerizes into corner-sharing dimers (e.g. $Ag^{+}{}_2Cr^{6+}{}_2O_7$; 2433)[53] where the bridging $^{[2]}O^{2-}$ ion forms two bonds 1 v.u. in strength (bond-valence sum 2 v.u.). Ideally, the $Cr^{6+}O_4$ tetrahedron would have four bonds 1.5 v.u. in strength, but this is prohibited by the bond-valence constraints of the bridging $^{[2]}O^{2-}$. As a result, $Cr^{6+}O_4$ dimers form three bonds 5/3 v.u. (1.608 Å) in strength and one bridging bond 1 v.u. (1.799 Å) in strength, thus resulting in a bimodal distribution of bond lengths for corner-sharing $Cr^{6+}O_4$ dimers. While this mechanism may seem to be different from that of non-local bond-topological asymmetry (see above), the difference is a matter of interpretation; bridging and non-bridging bonds are necessarily bond-topologically inequivalent. As such, we sometimes use the terms "bond-topological asymmetry"

and "bond-topological effects" interchangeably in text, although we tend to use the latter for more general discussion.

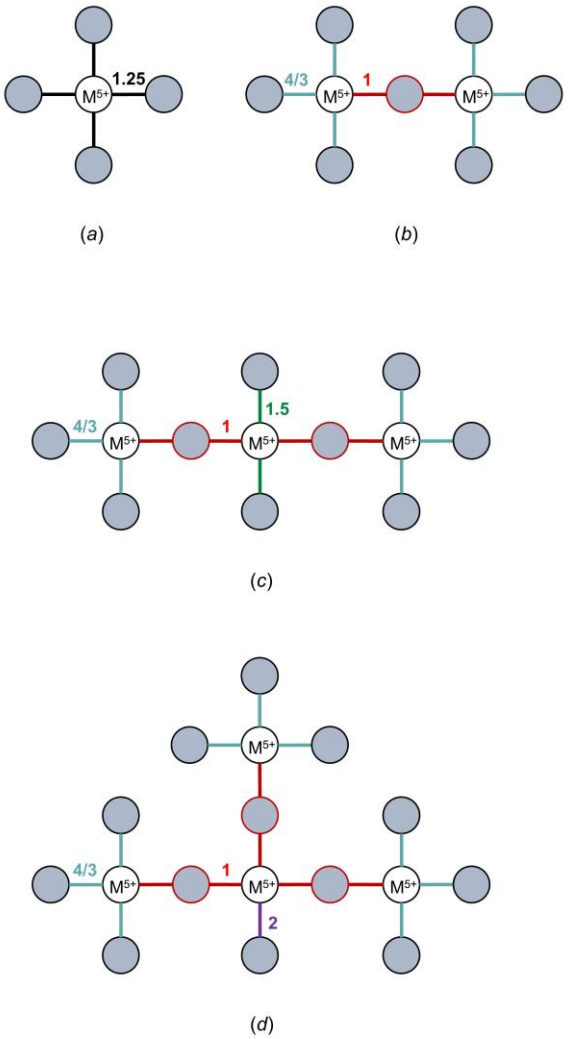

Figure 8: Bond-valence patterns arising from various corner-sharing tetrahedra for +5 oxidation state for (a) monomers, (b) dimers, (c) linear oligomers and chains, (d) branched polymers. Shaded spheres represent O^{2-}.

One may list all possible bond-valence patterns arising from various polyhedra, polyhedral connectivity, and degree of polymerization to realize the richness of bond-valence constraints in the solid state and the scale of bond-length variations that arises solely from bond-topological constraints. For example, we enumerate possible bond-valence patterns arising from various corner-sharing tetrahedra for +5 and +6 oxidation states in Figs. 8 and 9, respectively. For a central cation with oxidation state +5, isolated tetrahedra ideally form bonds of 1.25 v.u. For a dimer, the bridging M-O-M bond is 1 v.u., and the other three bonds therefore adjust to 4/3 v.u. For a trimer, the central tetrahedron forms two bonds of 1 v.u. (both bridging), and the two other bonds adjust to 1.5 v.u. For a branched tetramer (a linear/cyclic tetramer does not lead to new bond-valence constraints), the central tetrahedron makes 3 bonds of 1 v.u., and its fourth bond is 2 v.u., i.e. the maximum bond valence achievable by O^{2-}. For a +6 oxidation state, monomers ideally form four bonds 1.5 v.u. in strength, while dimers make bonds 1 v.u. + 3 × 5/3 v.u. in strength. For trimers, the doubly-bridged central tetrahedron forms two bonds of 2 v.u., and a branched tetramer is therefore impossible to achieve. These bond-valence patterns increase in complexity when considering (1) polymerization with different (but similarly strongly-bonded) ions and ion configurations; (2) polymerization via multiple bridging anions, i.e. edge- and face-sharing, including the formation of complex oxygen-sharing clusters typical of $^{[5\text{-}6]}V^{5+}$, $^{[6]}W^{6+}$, $^{[6]}Mo^{6+}$, and sometimes $^{[6]}Ti^{4+}$, $^{[6]}Nb^{5+}$, and $^{[6]}Ta^{5+}$; (3) additional (non-bridging) bonds made by the bridging anion(s), etc. In other words, these bond-valence constraints will experience further variability based on the exact bond topology of the crystal structure. Fortunately, one does not have to keep track of all such variables, unless they wish to rationalize the exact pattern of *a priori* bond valences whose simple calculation is otherwise sufficient for all intents and purposes. Thus for oxides, polymerization of strongly-bonded units invariably leads to bond-length variation when OS/CN > 1 for $^{[2]}O^{2-}$br., > 2/3 for $^{[3]}O^{2-}$br., etc. This condition is necessary but not sufficient, as some combinations of charge and coordination number cannot result in polymerization of the strongly bonded unit, e.g., for $^{[4]}Os^{8+}$.

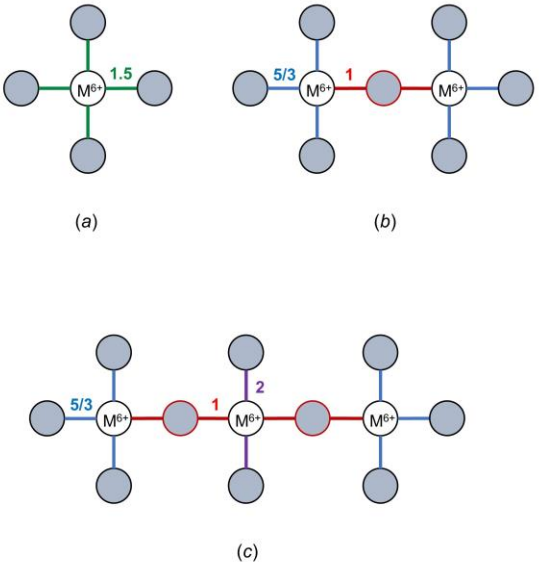

Figure 9: Bond-valence patterns arising from various corner-sharing tetrahedra for +6 oxidation state for (*a*) monomers, (*b*) dimers, (*c*) linear oligomers and chains. Shaded spheres represent O^{2-}.

We illustrate this concept with $Li_3Nb^{5+}O_4$ (75264)[54] which consists of edge-sharing $[Nb^{5+}{}_4O_{16}]^{12-}$ clusters inter-connected via Li^+. The mean bond-valence to the bridging ion (*O*1; Table 6) is roughly 2/3 v.u. when ignoring the weak bonds made to Li^+; thus Nb^{5+} adjusts from its mean bond-valence of 0.833 v.u. to make three weaker bonds of 0.708 v.u. to the bridging *O*1, with the three other bonds adjusting to 0.958 v.u. (with corresponding *a priori* bond lengths of 2.037 and 1.925 Å, respectively). This split is further accentuated by displacement of the Nb^{5+} ion toward the face made by the *O*1 ions as a result of a pseudo Jahn-Teller effect, resulting in an effective split in bond lengths of 1.858-2.130 Å (Δ_{topol} = 0.125, Δ_{cryst} = 0.174 v.u.).

Table 6: *A priori* bond valences (v.u.) for $Li_3Nb^{5+}O_4$

	Li	*Nb*	∑
$O1_{br}$	-0.042 ×3→	0.708 ×3↓ ×3→	2
*O*2	0.208 ×5↓ ×5→	0.958 ×3↓	2
∑	1	5	

Polymerization of strongly-bonded units where <BV>$_{cat.}$ is smaller than <BV>$_{br.an.}$

In the previous section, we showed that bond-length variation driven by bond-topological asymmetry is inherent in cases where <BV>$_{cat.}$ is greater than <BV>$_{br.an}$. In those cases, the bond-valence constraints on bridging anions induce an increase in the bond valences at the non-bridging bonds, leading to considerable bond-length variation. The inverse situation, where <BV>$_{cat.}$ is smaller than <BV>$_{br.an}$, also results in clear-cut bond-length variation driven by bond-topological asymmetry, this time in the form of a decrease in the bond valences at the non-bridging bonds. This phenomenon may lead to bond-length variability of similar magnitude; although the bond-valence variability is typically less, the cations involved are of lower Lewis acidity (defined as the ratio of oxidation state and mean observed coordination number; see ref [35]), resulting in larger bond-length variations for a given bond-valence variation.

A simple illustration of this effect is seen in $PW^{5+}O_5$ (203048),[55] the structure of which consists of chains of corner-sharing $W^{5+}O_6$ octahedra. The *a priori* bond valences for W^{5+} are 2 × 1 v.u. for the bridging bonds, and 4 × 0.75 v.u. for the non-bridging bonds (Table 7), compared with six bonds of 0.833 v.u. (1.949 Å) for holosymmetric coordination. These compare to the experimental values of 0.949 and 1.027 v.u. for the bridging bonds, and 0.823, 0.811, 0.809 and 0.753 for the non-bridging bonds, showing how $^{[6]}W^{5+}$ adjusts to the anion bond-valence requirements by making two stronger bridging bonds, and four weaker non-bridging bonds to O^{2-} (Δ_{topol} = 0.111, Δ_{cryst} = 0.046 v.u.). The resulting dispersion of bond lengths for W^{5+} is 1.833-2.005 Å.

Table 7: *A priori* bond valences (v.u.) for $PW^{5+}O_5$

	W	*P*	∑
*O*1	0.75	1.25	2
*O*2	0.75	1.25	2
*O*3	0.75	1.25	2
*O*4	0.75	1.25	2
*O*5	1 ×2↓ ×2→		2
∑	5	5	

To show this effect for a cation of lower Lewis acidity, we calculate the *a priori* bond valences for Fe^{3+} in aegirine, $NaFe^{3+}Si_2O_6$ (157733).[56] In this structure, Fe^{3+} forms chains of edge-sharing $Fe^{3+}O_6$ octahedra sharing via four bridging *O*1 ions (which further bond to Si^{4+} and Na^+), while the two non-bridging *O*2 sites bond only to Si^{4+} and Na^+ (Table 8). To accommodate the different bond-valence requirements of O^{2-}, the *a priori* bond valences for the bonds to *O*2 increase to 2 × 0.6 v.u., from 6 × 0.5 v.u. (2.016 Å) in holosymmetric coordination, whereas bonds to O1 decrease to 4 × 0.45 v.u. The predicted dispersion of bond lengths is 1.950-2.053 Å (observed 1.939-2.113 Å) with Δ_{topol} = 0.067 and Δ_{cryst} = 0.038 v.u.

Table 8: *A priori* bond valences (v.u.) for $NaFe^{3+}Si_2O_6$

	Na	*Fe*	*Si*	∑
*O*1	0.113 ×2↓	0.45 ×4↓ ×2→	0.988	2
*O*2	0.263 ×2↓	0.6 ×2↓	1.138	2
*O*3	0.062 ×4↓ ×2→		0.938 ×2↓ ×2→	2
∑	1	3	4	

[2] Multiple-bond formation

Many molecular features of coordination complexes are preserved as they are incorporated into crystal structures, and their electronic properties are often more important than the ensuing steric constraints of the crystal structure.[57] A simplifying assumption commonly made in studying the geometry of transition-metal complexes in crystals is to overlook translational symmetry, treating these complexes as "molecules in solids";[58–60] this allows a more chemically intuitive treatment of chemical bonding of the crystal's molecular fragments via ligand-field theory.

Fig. 10 shows the standard molecular-orbital (MO) bonding scheme for a transition metal and its oxygen ligands in octahedral coordination (reproduced with permission from ref [61]). Symmetry-adapted linear combinations (SALC) of atomic orbitals for the O^{2-} ligands show that π donor orbitals t_{1g}, t_{2g}, t_{1u} and t_{2u} are sufficiently close in energy to interact with the atomic orbitals (AO) of the transition metal. However, only the t_{2g} orbital has the appropriate symmetry and spatial overlap to mix with that of the transition metal, and the three other orbitals remain non-bonded. The MO levels are filled with ligand electrons up to t_{2g} (18 electrons, not counting an additional 18 non-bonded electrons), at which point transition-metal *d* electrons begin to fill levels starting from t_{2g}* in a way that progressively negates the favorable π-interaction, i.e., a t_{2g} state of lower energy in comparison to non-bonding. For this reason, the most favorable π-bonding interactions for octahedrally coordinated transition-metal oxyanions (called oxo complexes in coordination chemistry) involve transition metals with few to no *d* electrons; this is well supported by our data, as we will see below. Following favorable π-type interaction, the complex is described as forming "multiple bonds" to one or more of its ligands (all ligands forming primary bonds to the transition metal via their σ donor orbitals; Fig. 10). These are sometimes described as "yl" complexes, e.g., vanadyl,[62] uranyl.[63] The additional bonding component shortens the bonded distance to the ligand(s) involved, thus resulting in bond-length variation. This phenomenon usually manifests itself in our data in the form of a multi-modal distribution of bond lengths, typically with a mode at anomalously short bond lengths.

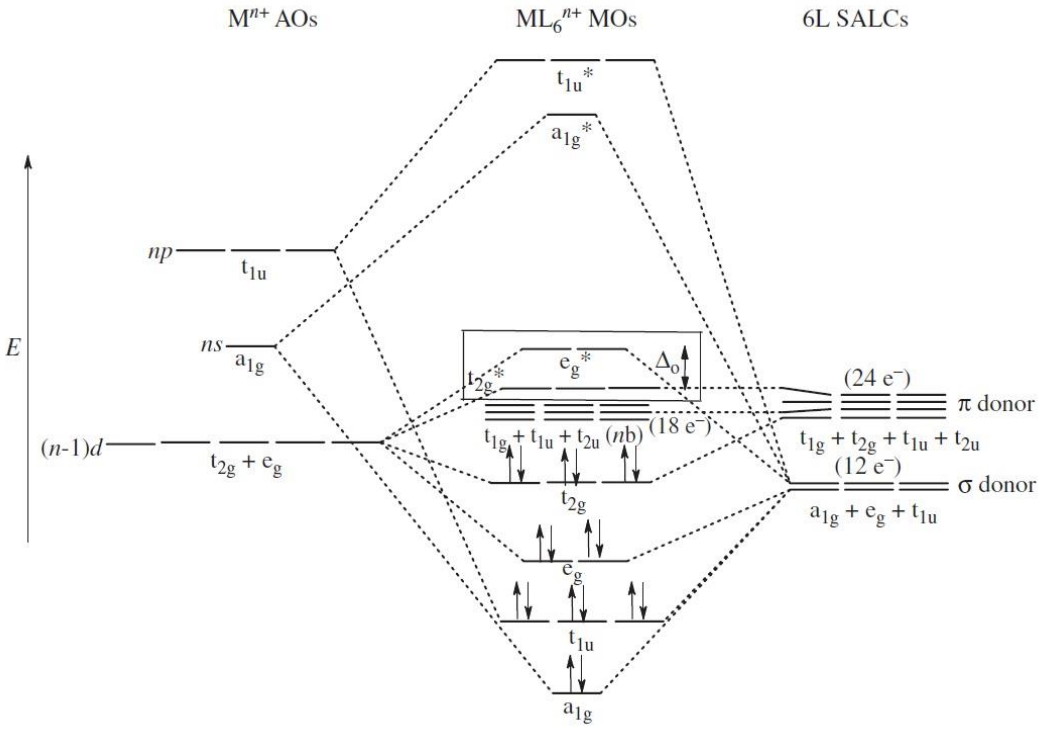

Figure 10: Molecular orbital (MO) diagram for $[ML_6]^{n+}$ compounds where the ligands (O^{2-}) can act as both σ- and π-donors. Transition metal *d* electrons fill levels starting from t_{2g}* in a way that progressively negates favorable π-interaction, thus favoring complexes with few to no *d* electrons. Reproduced with permission from ref [61], Fig. 16.26, p.531

We note that the above treatment is best-suited to covalently-bonded molecules; this description therefore holds to the extent for which crystals can be described as (strongly-bonded) molecular fragments. Additional bonding schemes, e.g., those that arise in extended solids as a result of substantial electron delocalization, and ionic interactions, complicate the bonding picture. An important result of their consideration is the observation of non-integer bond orders in crystals (first described by Pauling in metals)[64], which is well captured by the bond-valence model via the observation of non-integer bond valences, which may be interpreted to result in part from a continuum of orbital spatial overlap along the bond axis.

As discussed above in the section *Quantifying bond-length variation as a result of bond-topological vs crystallographic effects*, multiple-bond formation inherently gets modeled into the bond-topological component Δ_{topol}. The continuous (non-integer) nature of bond valences, combined with the overlapping effects of non-local bond-topological asymmetry and multiple-bond formation, renders a clear-cut divide of whether multiple-bond formation is the main reason for bond-length variation difficult to achieve. Our analysis suggests that multiple-bond formation may be the main reason underlying bond-length variation where (1) $\Delta_{topol} > \Delta_{cryst}$; (2) BV_{max} > 1.25 MBV (mean bond-valence) > 1.75 v.u.; and (3) the formation of π-bonds is not an inherent result of the polymerization of strongly-bonded units, in which case we consider non-local bond-topological asymmetry as the main cause of bond-length variation. For (2), the condition BV_{max} > 1.25 MBV is implemented not to mistakenly classify those ion configurations that form strong π bonds by necessity (e.g. $^{[4]}Re^{7+}$) as due to multiple-bond formation. For example, we calculated the *a priori* bond valences for seven $^{[6]}V^{4+}$ polyhedra in six crystal structures to find $\langle\Delta_{topol}\rangle$ = 0.207 and $\langle\Delta_{cryst}\rangle$ = 0.145 v.u. For this ion configuration, BV_{max} is frequently > 1.75 v.u., higher than 1.25 × 2/3 v.u. $[V^{4+}O_6]^{8-}$ units are often observed as monomers; as the formation of strong π-bonds is not an inherent product of polymerization, we conclude that the formation of π-bonds is the main factor underlying bond-length variation for this ion configuration when bonded to O^{2-}. Following similar logic, we find bond-length variation to result from bond-topological asymmetry for $[Cr^{6+}O_4]^{2-}$, under special case "*Polymerization of strongly-bonded units where* $\langle BV\rangle_{cat.}$ *is greater than* $\langle BV\rangle_{br.an.}$*"* as the formation of the strong π-bonds is indeed caused by polymerization of the $[Cr^{6+}O_4]^{2-}$ unit. When $\Delta_{cryst} > \Delta_{topol}$, multiple-bond formation is always a result of the pseudo Jahn-Teller effect (below) for d^0 transition metals.

[3] Electronic effects

In recent decades, significant developments in electronic-structure theory have reduced the problem of molecular engineering and materials design to increasingly quantitative calculations of the electronic structure of both known and hypothetical compounds. It is expected that electronic

effects represent the dominant force underlying bond-length variation *for a given crystal structure*, i.e., for which the effect of non-local bond-topological asymmetry on bond lengths is disregarded as a quantifiable and predictable constant. However, the extent to which electronic effects affect bond lengths in solids has yet to be quantified on a large scale, hindering rapid identification of these phenomena in crystal structures, and clouding the extent to which bond-length variations may be expected from these effects within the constraints of physically realistic crystal structures (with direct applications in materials design and the verification of computational results).

The two most common types of electronic effects present in inorganic solids are (1) lone-pair stereoactivity; and (2) coupled electronic-vibrational degeneracy. Lone-pair stereoactivity results from strong interaction between cation *s* and anion *p* orbitals leading to a high-energy antibonding state which, via structure distortion, may interact with empty cation *p* orbitals to form a localized electronic state where the lone pair resides.[65] The extent to which this phenomenon leads to bond-length variation in oxide and oxysalt structures was discussed for ns^2np^0 p-block cations earlier in this series.[31,32] Because transition metals are not subject to lone-pair stereoactivity, our discussion of electronic effects is limited to (2) coupled electronic-vibrational degeneracy, below. Other common electronic phenomena which may result in bond-length variation (e.g., inductive effects) are typically only relevant to hetereo-ligand coordination centers, and are not considered here.

Coupled electronic-vibrational degeneracy: the Jahn-Teller effect

The Jahn-Teller effect is a mechanism of symmetry breaking in molecules and solids, and results from strong electron-vibrational (vibronic) and electron–phonon interactions in molecules and crystals, respectively.[66] The phenomenon was first described from group-theoretical arguments by Jahn & Teller, who showed that non-linear molecules cannot be stable if they have energetically degenerate electronic states, resulting in their spontaneous distortion to a lower-symmetry configuration with split (near-degenerate) states.[67] An energetically favourable occupancy of the non-degenerate states, which depends on the number of electrons available to populate them, characterizes the Jahn-Teller effect (hereon abbreviated as JTE). Recognition of similar mechanisms for near-degenerate orbital electronic states later resulted in a significantly broader definition of the JTE,[68–70] inclusive of pseudo-degenerate states where the energy gap between the mixing states is sufficiently small in comparison to other vibronic parameters of the system.[66] In this work, we avoid the "first-" and "second-" order terminology commonly used to describe the JTE for degenerate and near-degenerate energy states, respectively. This terminology originates from a perturbation-theoretical treatment of the JTE,[70,71] which, despite significantly contributing to the understanding of many chemical questions, has problems.[72] We use the term "JTE" as inclusive of both cases of degeneracy, and "pseudo JTE" (PJTE) for near-degenerate electronic states. One mechanism is not exclusive of the other, as the PJTE may still be an important source of instability in the presence of electronic degeneracy.[72]

The JTE has been proposed to be the only source of instability and distortion for polyatomic systems in near-degenerate states,[66,72] and more generally, to be the only source of spontaneous symmetry-breaking in matter in all its forms.[73] In light of the previous section (*[1] Non-local bond-topological effects*), we find this statement to be incorrect; distortion away from the configuration of highest-symmetry may arise from asymmetry in the bond network, a phenomenon that, as we will see below (section *Ion configurations primarily distorted via non-local bond-topological effects*), occurs much more frequently than coupled electronic-vibrational degeneracy, with no *a priori* limitation with regard to ion identity.

Degenerate electronic states

The classic interpretation of the JTE deals with electron occupancy of degenerate electronic states. It is traditionally described in the context of octahedral and tetrahedral coordination, for they are frequently observed coordinations that are geometrically apt to distortion as a result of the shape and orientation of *d* orbitals. Energy changes for the five degenerate *d* orbitals of the transition metal (*d*xy, *d*xz, *d*yz, dx^2-y^2 and dz^2) upon their surrounding by an array of ligands (here, O^{2-}) is most succinctly described via Crystal Field Theory (CFT). Fig. 11 shows the crystal-field splitting of energy levels for some of the most frequently-observed coordinations of this work (Dq values from ref [57]).

In the classic description of the JTE, degenerate *d* electronic states split into triply-degenerate t_{2g} (*d*xy, *d*xz, *d*yz) and doubly-degenerate e_g (dx^2-y^2 and dz^2) energy levels for an octahedral coordination of ligands; for this coordination, the e_g orbitals are higher in energy as they point directly at the ligands, resulting in electrostatic repulsion with the bonding electrons. For a tetrahedral coordination, the *d* electronic states split into doubly-degenerate *e* (dx^2-y^2 and dz^2) and triply-degenerate t_2 (*d*xy, *d*xz, *d*yz) electronic states, with the t_2 orbital higher in energy (Fig. 11). The occurrence of a JT distortion depends on the occupancy of these electronic states, which in turn depends on the number of *d* electrons available. Where the degeneracy occurs in the orbital set of higher energy, distortion resulting from the JTE is "strong" (with relatively large bond-length variation), and is "weak" otherwise. For an octahedral crystal field, degeneracy is strong for electron configurations HS d^4, LS d^7 and d^9; those prone to weak JTE are d^1, d^2, LS d^4, LS d^5, HS d^6 and HS d^7. For a tetrahedral field, the largest distortions (i.e. bond-length variations) are expected for configurations HS d^3, HS d^4, d^8 and d^9, so on and so forth for every coordination geometry. For example, the strong JTE is observed for $^{[6]}Mn^{3+}$ (d^4) in $Gd(Mn^{3+}O_3)$ (95493),[74] with *a priori* (observed) bond valences 4 × 0.471 (2 × 0.194 and 2 × 0.700) and 2 × 0.559 (0.612) v.u. for Mn^{3+}, and Δ_{topol} = 0.039 and Δ_{cryst} = 0.186 v.u. As a side note, the wide discrepancy observed between *a priori* and observed bond valences in this example demonstrates the inability of *a priori* bond valences to model the Jahn-Teller distortion (more on this below).

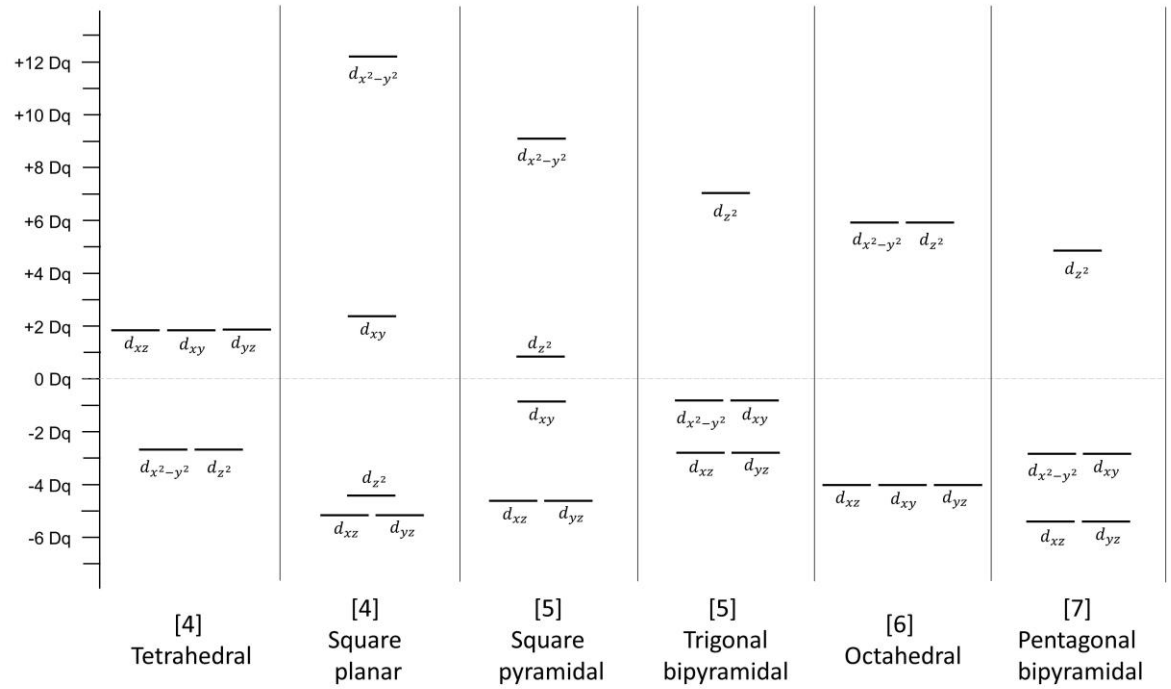

Figure 11: Crystal-field splitting for the five d-orbitals for some of the most frequently-observed coordinations of this work.

After examining our dataset in detail for the strong and weak JTE in various crystal fields, and comparing the magnitude of the effect to that of distortion of bond-topological origin via the Δ_{topol} and Δ_{cryst} indices, we identify three ion configurations from Table 4 whose main underlying cause of bond-length variation is the strong JTE ($^{[6]}Mn^{3+}$, $^{[6]}Cr^{2+}$ and $^{[6]}Cu^{2+}$) and none whose main cause is the weak JTE. We observe these effects as minor contributors to bond-length variation for $^{[6]}Co^{2+}$ (JTEs) and $^{[6]}V^{3+}$ and $^{[6]}Mo^{5+}$ (JTEw). These will be discussed in section *[3.1] Ion configurations primarily distorted via coupled electronic-vibrational degeneracy*, below.

Near-degenerate electronic states

The pseudo Jahn-Teller effect (PJTE) results from the vibronic mixing of two (or more) near-degenerate electronic states under nuclear displacement.[66] As such, the PJTE is not encumbered by *a priori* limitations as is the case for the classic interpretation of the JTE. However, the energy gap between the interacting states, usually (but not always) the highest occupied molecular orbital (HOMO) and the lowest unoccupied molecular orbital (LUMO) must be small, and there must be a distortion mode that has the same symmetry as the HOMO to LUMO transition (the energy gap is a function on ligand identity).[39] Fig. 12 gives a simple visual representation of the PJTE for a TiO_6 octahedron (adapted from ref [66]). We plot the HOMO $|t_{1u}z>$ (from O^{2-}) and LUMO $|3d_{yz}>$ (from Ti^{4+}) of the system; it can then be seen that favorable vibronic mixing results in a positive overlap integral upon displacement of the Ti^{4+} ion along the y axis (i.e. "off-centering"), resulting in an energetically-favored, lower-symmetry configuration. For example, Mo^{6+} displaces toward a corner in $Cs(Mo^{6+}{}_2O_3(PO_4)_2)$ (79517),[75] with *a priori* (observed) bond valences 0.724 (0.702), 0.731 (0.541), 2 × 0.768 (0.640 and 0.730), 0.772 (0.678) and 1.237 (1.988) v.u., and Δ_{topol} = 0.134 and Δ_{cryst} = 0.204 v.u. In this example, Mo^{6+} displaces toward *O*1 along the *O*6-*Mo*1-*O*1 axis, resulting in strong/weak bonds of 1.988/0.541 v.u.

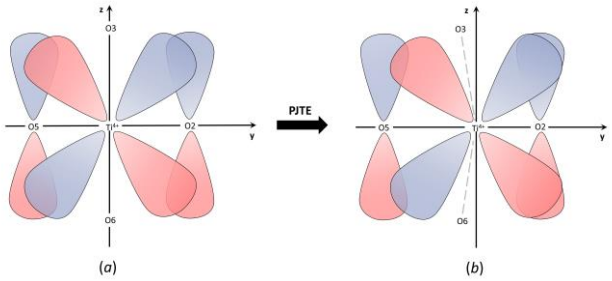

Figure 12: Visual representation of the pseudo Jahn-Teller effect for a TiO_6 octahedron. *O*1 and *O*4 are directly above and below Ti^{4+} in (*a*); blue lobes are (+) and red (-). In high-symmetry configuration (*a*), the overlap integral between the HOMO $|t_{1u}z>$ (from O^{2-}) and LUMO $|3d_{yz}>$ (from Ti^{4+}) is null. However, displacement of Ti^{4+} along the y axis results in both an increase in positive overlap (+/+ and -/-), and decrease in negative overlap (+/-), thus resulting in spontaneous distortion.

The PJTE is widely observed in transition metals with a d^0 electronic configuration, although it should be noted that its occurrence is not limited to this configuration (examples below).[72,76,77] In turn, the d^0 electronic configuration is relatively well-studied vis-a-vis symmetry-breaking bond-length variation due to wide-ranging technologically-relevant properties of compounds containing d^0 transition metals in asymmetric coordination environments (see section *Scope of this work*); for example, the frequently-encountered bi-stable behavior of crystal structures with d^0 transition metals is exploited in the design of atomic switches,[78]

artificial neurons,[79] and can foreseeably be used to control sorption characteristics of catalysts to move beyond the Sabatier principle.[80] In addition to being inversely proportional to the HOMO-LUMO gap, the magnitude of polyhedral distortion follows electronegativity,[8] and the commonly observed d^0 ions have been quantified as strong (Mo^{6+} and V^{5+}), moderate (W^{6+}, Ti^{4+}, Nb^{5+} and Ta^{5+}), and weak (Zr^{4+} and Hf^{4+}) distorters.[81] It has further been suggested that bond topology influences the occurrence and magnitude of the PJTE in a primary[39] and secondary[82] capacity, whereby the PJTE either results from, or is affected by, the arrangement of *a priori* bond valences in structures with d^0 transition metals. We investigate this issue via calculation of *a priori* bond valences for 130+ d^0 transition-metal-oxide polyhedra, below.

[4] Crystal-structure effects

The constraints of long-range order and periodicity have important implications with regard to bond distances. Variations in external conditions (e.g. temperature, pressure, applied field) may further result in variability in bond lengths up to the point of phase transition (beyond which bond-length variations are accounted for via [1] non-local bond-topological asymmetry). Here, we group these effects under the designation of "crystal-structure effects". These effects do not lead to multi-modality of the bond-length distributions, and cause bond-length variations of significantly lower magnitude than those of mechanisms [1]-[3]. As such, quantifying bond-length variations due to crystal-structure effects can only be done in the absence of other crystallographic mechanisms of bond-length variation for a given polyhedron (e.g. lone-pair stereoactivity, coupled electronic-vibrational degeneracy) which otherwise overwhelm the Δ_{cryst} effect. Moreover, bond-length variation caused by these mechanisms are expected to fall semi-randomly about the mean bond-length in a way that does not significantly alter the shape of bond-length distributions.

Structural incommensuration

Some polyhedra are inherently unable to adopt their configuration of highest symmetry as a result of the imperfect projection of their *a priori* bond lengths into three-dimensional space.[39,40] This was recently demonstrated by Gagné & Hawthorne who showed the inability of a crystal structure to attain its *a priori* bond lengths within the constraints of space-group symmetry and periodicity by showing excellent agreement between observed and *a priori* bond lengths *within* a structure type, and the loss of this agreement *across* structure types.[38] The mismatch between *a priori* and observed bond lengths may be used to quantify structural strain via distortion indices, e.g., the Global Instability Index (GII),[83] and Bond Strain Index (BSI).[84] Structural strain may be isotropic or anisotropic in nature; Fig. 4 provides evidence for the isotropic working of this phenomenon whereby nearly a dozen transition-metal-ion configurations are observed to cover a surprisingly wide range (~ 0.1 Å) of mean bond lengths for $\Delta = 0$ (e.g., $^{[6]}Mn^{2+}$, $^{[6]}Fe^{3+}$, $^{[4,6]}Co^{2+}$, $^{[4]}Cu^{2+}$).

Next-nearest-neighbour interactions

Sometimes called steric effects, factors such as metal-metal and anion-anion repulsion and nearby stereoactive lone-pair electrons have been shown to influence bond-length variations and polyhedral distortion,[8,39] for example resulting in preferential displacement of d^0 transition metals under the PJTE. We observe only one ion configuration in Table 4 where next-nearest-neighbour interactions seem to be the underlying cause of polyhedral interaction (Ru^{5+}-Ru^{5+} interactions for $^{[6]}Ru^{5+}$), discussed in section *Ion configurations primarily distorted via crystal-structure effects*, below.

Part 3: Determination of the causal mechanism(s) underlying bond-length variation for ion configurations with anomalous bond-length distributions

In this section, we identify the principal and minor causal mechanism(s) underlying bond-length variation for the 52 ion configurations listed in Table 4. We further quantify the extent to which these causal mechanisms affect bond-length variation for those ion configurations. Our discussion is arranged into four subsections based on causal mechanism: [1] non-local bond-topological effects; [2] multiple-bond formation; [3] electronic effects (coupled electronic-vibrational degeneracy); and [4] crystal-structure effects. The ion configurations of Table 4 are discussed in the subsection which corresponds to their principal cause of bond-length variation.

Our discussion of ion configurations follows consistent form throughout; we (1) calculate *a priori* bond valences and indices Δ_{topol} and Δ_{cryst} for polyhedra with anomalous bond-length dispersion; (2) calculate $<\Delta_{topol}>$ and $<\Delta_{cryst}>$ values to determine whether the bond-length distribution is primarily irregular as a result of bond-topological or crystallographic effects; (3) identify the main and minor causes of bond-length variation based on frequency of observation and magnitude; (4) describe the effect of causal mechanisms on the shape and range of the bond-length distribution; (5) compare main and minor causes of bond-length variation with similar ion configurations where pertinent, and/or other relevant information.

[1] Ion configurations primarily distorted via non-local bond-topological effects

$^{[6]}Sc^{3+}$ (Fig. 1a) has a subtly bimodal distribution of bond lengths. The main distribution peaks at 2.90 Å (0.50 v.u.), and the other maximum is at 2.12 Å (0.47 v.u.), and occurs in conjunction with a hidden peak at 2.07 Å (0.53 v.u.). For example, $Na_3Sc_2(PO_4)_3$ (65407)[85] has *a priori* (observed) bond valences 3 × 0.519 (0.555) and 3 × 0.481 (0.477) v.u., with Δ_{topol} = 0.019 and Δ_{cryst} = 0.020 v.u. The tail at shorter bond lengths is longer than expected; constituent data include those of $LiSc(SiO_3)_2$ (200128),[86] with *a priori* (observed) bond valences 4 × 0.45 (2 × 0.491 and 2 × 0.383) and 2 × 0.6 (0.607) v.u., with Δ_{topol} = 0.067 and Δ_{cryst} = 0.038 v.u. Thus, bond-length variations for this ion configuration mainly result from non-local bond-topological asymmetry, and to a lesser extent from the pseudo Jahn-Teller effect.

$^{[6]}V^{3+}$ (Fig. 1e) occurs as monomers, oligomers, chains, sheets and frameworks. Despite the proclivity of the $[V^{3+}O_6]^{9-}$ unit for polymerization, its bond-length distribution is rather regular, and doesn't cover an overly large range of bond lengths that is typical of others ions exhibiting this behavior (0.399 Å, vs 0.826 Å for $^{[6]}Ti^{4+}$, for example). There is however a subtle second maximum in Fig. 1e

at 2.06 Å (0.44 v.u.). This maximum arises from structures in which $[V^{3+}O_6]^{9-}$ polymerizes into oligomers, chains, sheets and frameworks, all of which result in weaker bonds 0.4-0.5 v.u. (vs 0.55-0.65 v.u. for the strongest bonds). This for example agrees with *a priori* (observed) bond valences calculated for distorted polyhedra of edge-sharing chains in $LiV^{3+}(Si_2O_6)$ (59244),[87] with 4 × 0.45 (0.429) and 2 × 0.6 (0.612) v.u., with Δ_{topol} = 0.067 and Δ_{cryst} = 0.018 v.u. Variations in bond lengths roughly result from bond-topological and crystallographic constraints in equal proportions for chains of edge-sharing octahedra in $SrV^{3+}{}_2O(PO_4)_2$ (82685),[88] with Δ_{topol} = 0.040 and Δ_{cryst} = 0.071 v.u., and Δ_{topol} = 0.072 and Δ_{cryst} = 0.052 v.u. for *V*1 and *V*2 respectively, showing that some variation in bond lengths may be due to the weak JTE (d^2 electronic configuration) for this ion configuration. Average values of Δ_{topol} and Δ_{cryst} for five polyhedra in four structures are 0.064 and 0.040 v.u., respectively.

$^{[4]}V^{5+}$ (Fig. 1h) has a somewhat symmetrical distribution of bond lengths when bonded to O^{2-}. The $[V^{5+}O_4]^{3-}$ unit polymerizes into various linear oligomers, chains and rings, with important implications regarding O_{br} as the mean bond-valence for this ion configuration is > 1 v.u. (special case #1 of non-local bond-topological asymmetry). Symmetrization of the $^{[4]}V^{5+}$-O^{2-} bond-length distribution is well illustrated from the bond-length pattern that results from V_4O_{12} and V_6O_{18} rings in $K_3CaV_5O_{15}$ (401203):[89] the two bridging bond valences of ~1 v.u. result in observed bond lengths of 1.76-1.81 Å, while the two non-bridging O atoms adjust to ~1.5 v.u. for observed bond lengths of 1.61-1.65 Å. These bond lengths fall on each side of the predicted maximum for monomer units, 1.71 Å (5/4 v.u.). We calculated the *a priori* (observed) bond valences for 13 coordination polyhedra in 6 structures; the mean values of Δ_{topol} and Δ_{cryst} of 0.122 and 0.099 v.u. indicate that despite a high value for Δ_{cryst} (largely attributed to the PJTE), non-local bond-topological asymmetry is the main reason underlying bond-length variation for this ion configuration. We do not find coordination polyhedra in our data where multiple-bond formation is the principal driver of bond-length variation; the strong π-bonds are a product of polymerization and displacement of the cation away from the center of the polyhedron via the PJTE. In $KCu^{2+}{}_5V^{5+}{}_3O_{13}$ (400802),[90] with monomeric $[V^{5+}O_4]^{3-}$ units, the *a priori* bond valences for *V*3 are 1.151 (*O*1), 1.121 (*O*8), and 2 × 1.364 (*O*10, *O*12) v.u. In this tetrahedron, V^{5+} moves off-center toward *O*8 and away from *O*1, resulting in observed bond valences of 1.448 (*O*8) v.u. and 0.738 v.u. (*O*1) for a particularly strong case of PJTE; Δ_{topol} = 0.081 and Δ_{cryst} = 0123 v.u. In $Cu^{2+}{}_2V^{5+}{}_2O_7$ (171028),[91] the *a priori* (observed) bond valences are 0.980 (0.908), 1.274 (1.279), 1.288 (1.205) and 1.291 (1.329) v.u. for *V*1, with Δ_{topol} = 0.135 and Δ_{cryst} = 0.039 v.u., and 0.976 (1.054), 1.271 (1.166), 1.288 (1.205) and 1.466 (1.478) v.u. for *V*2, with Δ_{topol} = 0.137 and Δ_{cryst} = 0.069 v.u.

$^{[6]}Cr^{3+}$ (Fig. 1l) has a somewhat regular distribution of bond lengths, with two anomalies: (1) a spike of bond lengths at 1.99 Å (v.u.), and (2) a relatively long tail at shorter bond lengths. For (1), the bond distances originate from a study of the $(Mg,Fe^{2+})Cr_2{}^{3+}O_4$ solid-solution series in spinels whereby 11 structures were refined with holo-symmetric $[Cr^{3+}O_6]^{9-}$ units thus providing 66 distances of 1.99 Å to our dataset.[92] For (2), we calculated the *a priori* bond valences for the structures which have the shortest distances observed. The shortest distances are observed in $Cr^{2+}{}_3Cr^{3+}{}_4(PO_4)_6$ (73261),[93] with *a priori* (observed) bond valences between 0.409-0.639 (0.383-0.617) v.u., with Δ_{topol} = 0.074 and Δ_{cryst} = 0.038 v.u. for *Cr*1, and 0.415-0.715 (0.396-0.643) v.u., with Δ_{topol} = 0.089 and Δ_{cryst} = 0.061 v.u. for *Cr*2, thus showing the non-local bond-topological asymmetry as the origin of bond-length variation. For a total of seven coordination polyhedra for which we calculated Δ_{topol} and Δ_{cryst}, the mean values for these indices are 0.077 and 0.056 v.u., respectively. With a d^3 electronic configuration, Cr^{3+} is not susceptible to the JTE, suggesting that crystal-structure effects are a significant cause of bond-length variation for this ion configuration.

$^{[4]}Cr^{6+}$ (Fig. 1m) has a multimodal distribution of bond lengths where bonded to O^{2-}. $[Cr^{6+}O_4]^{2-}$ units polymerize as linear oligomers (primarily dimers), in addition to forming very strong π-bonds in monomers. As discussed for $^{[4]}V^{5+}$ above, polymerization of the $[Cr^{6+}O_4]^{2-}$ unit inherently results in varying bond lengths whereby the mean bond-valence for this ion configuration is > 1 v.u. (special case #1 of non-local bond-topological asymmetry). Thus the maxima in Fig. 1m result from the superposition of the bond-length constraints of dimers, 1 v.u. (1.799 Å) and 3 × (5/3) v.u. (1.608 Å) on the normal distribution of bond lengths for monomers (1.65 Å; 1.5 v.u.). We calculated the a priori (observed) bonds-valences for eight coordination polyhedra from three structures; average values of Δ_{topol} and Δ_{cryst} are 0.127 and 0.085 v.u., respectively, confirming that the primary reason for bond-length variation is non-local bond-topological asymmetry (special case #1) for this ion configuration, closely followed by the PJTE which presumably accounts for most of Δ_{cryst}. The structure of $Tl^{3+}{}_2(Cr^{6+}O_4)_3$ (201793),[94] made up of two crystallographically distinct monomeric units, is a case where bond-topological asymmetry is the root cause of bond-length variation in one polyhedron, and the PJTE in the other. Its *a priori* (observed) bond valences are 1.2 (1.053), 2 × 1.4 (1.533 and 1.617) and 2 (1.843) v.u. for *Cr*1, and 4 × 1.5 (2 × 1.477 and 2 × 1.639) v.u. for *Cr*2. These values give Δ_{topol} = 0.250 and Δ_{cryst} = 0.164 for *Cr*1, and Δ_{topol} = 0 and Δ_{cryst} = 0.081 for *Cr*2. Multiple-bond formation appears to be the main reason underlying bond-length variation in a small number of structures, for example in $(NH_4)Fe^{3+}(Cr^{6+}O_4)_2$ (934),[95] made up of monomeric units, where each corner of the *Cr*1 tetrahedron shares one O^{2-} with $Fe^{3+}O_6$ octahedra. A mean bond-valence of 1.5 v.u. for Cr^{6+}, and 0.5 v.u. for Fe^{3+}, does not result in a constraint of polymerization at O_{br}, and thus the formation of a strong π bond (2.02 v.u.) by Cr^{6+} must result from proper multiple-bond formation.

$^{[4]}Fe^{3+}$ (Fig. 1u) has a unimodal distribution with anomalously low kurtosis, with a maximum at 1.85 Å (0.791 v.u.; higher than the expected value of 0.75 v.u.). $[Fe^{3+}O_4]^{5-}$ units polymerize into various oligomers, chains and frameworks via corner and/or edge-sharing, thus creating a wide range of bond-length constraints around that of 0.75 v.u. for a regular tetrahedron. These constraints effectively "flatten" the shape of the distribution, similar to what happens in $^{[4]}V^{5+}$. With a mean bond-valence of 0.75 v.u., $^{[4]}Fe^{3+}$ sometimes redistributes its bond valences to satisfy O_{br} requirements

(special case #2 of non-local bond-topological asymmetry, above). For example, Fe-O-Fe bonds adjust to 1.764 Å (1.004 v.u.) (and 3 × 1. 884 Å) for *Fe*3 in $K(Fe^{3+}{}_{11}O_{17})$ (83285),[96] exactly satisfying the bond-valence requirement of O_{br} for this corner-sharing dimer. We calculated *a priori* bond valences for three coordination polyhedra in 2 structures: $K(Fe_{11}O_{17})$ (above) and $NaZnFe^{3+}{}_2(PO_4)_3$ (280902),[97] with average values of Δ_{topol} and Δ_{cryst} of 0.055 and 0.048, respectively. Here, Δ_{cryst} is due to the selection of structures where the bond-valence sums deviate slightly from 3 v.u. (< 10%), and not to crystal-structure effects.

$^{[6]}Co^{2+}$ (Fig. 1z) has a regular bond-length distribution when bonded to O^{2-}, although with a very long tail at longer bond lengths. This ion is susceptible to the strong JTE when in the low-spin state (d^7), and to the weak JTE when in the high-spin state. Co^{2+} is usually presumed to be HS,[98] in agreement with a regular distribution of bond lengths (Fig. 1z), in contrast to the classic bimodal distribution observed for ions under the effect of the strong JTE. Of the 10 longest bonds observed for this ion configuration (with one bond length > 2.35 Å), spin is only reported for one coordination polyhedron, in $Co^{2+}{}_3(BPO_7)$ (51317)[99] where Co^{2+} is in low-spin state, in the shape of an elongated polyhedron (bond lengths 2.018, 2.024, 2.035, 2.039, 2.346 and 2.448 Å). Similar bond-length patterns occur in other structures with no report of spin state, e.g., in $SrCo^{2+}{}_2(As^{5+}O_4)_2$ (400764)[100] and $Co^{2+}(SiO_3)$ (17054)[101] with bond lengths 4 × 2.01-2.09 and 2 × 2.41-2.45, and 4 × 1.98-2.11 and 2 × 2.39-2.52 Å, respectively. We calculated *a priori* (observed) bond valences for five coordination polyhedra from four crystal structures, namely $YCo^{2+}(BO_2)_5$ (20670),[102] $Co^{2+}{}_2Si(P_2O_7)_2$ (82403),[103] $Cu^{2+}{}_2Co^{2+}O(B_2O_5)$ (400438)[104] and $SrCo^{2+}{}_2(As^{5+}O_4)_2$ (400764).[100] On average, Δ_{topol} = 0.055 and Δ_{cryst} = 0.056. This suggests that while non-local bond-topological asymmetry is the main cause of bond-length variation for this ion configuration, the JTE still has a marked effect, especially where Co^{2+} is (presumably) in a low-spin state.

$^{[6]}Zn^{2+}$ (Fig. 1ai) has a regular distribution of bond lengths when bonded to O^{2-}, with a very long tail at longer bond lengths. We calculated the *a priori* bond valences for five polyhedra from five crystal structures, and obtained average Δ_{topol} and Δ_{cryst} values of 0.056 and 0.050 v.u., respectively. In $NaZnFe^{3+}{}_2(PO_4)_3$ (280902),[97] *a priori* (observed) bond valences are 2 × 0.252 (0.168 and 0.274), 0.263 (0.212), 0.266 (0.412) 0.416 (0.433) and 0.550 (0.558) v.u., with Δ_{topol} = 0.100 and Δ_{cryst} = 0.055 v.u. In $Mn^{2+}Zn_2Ta^{5+}{}_2O_8$ (85042),[105] *a priori* (observed) bond valences are 3 × 0.256 (0.092, 0.103 and 0.491) and 3 × 0.410 (0.306, 0.447 and 0.491) v.u., with Δ_{topol} = 0.077 and Δ_{cryst} = 0.129 v.u. The large Δ_{cryst} value is attributable to the PJTE for this polyhedron, as is the case for *Zn*4 in $Zn_3(Se^{4+}O_3)3{\cdot}H_2O$ (280151),[106] which is displaced 0.34 Å off center in its polyhedron, resulting in a wide range of bond lengths (1.985-2.484 Å). Bond-topological and PJT effects seem to be of a similar magnitude for this ion configuration.

$^{[10]}Y^{3+}$ (Fig. S1bv) is only found in one crystal structure, $YCo^{2+}(BO_2)_5$ (20670),[102] although it covers a large range of bond distances. Calculation of *a priori* (observed) bond valences gives Δ_{topol} = 0.086 and Δ_{cryst} = 0.079 v.u.; thus, despite the strong distorting effect of the PJTE, bond-length variations primarily result from non-local bond-topological asymmetry for this ion configuration (this result may change with the refinement of additional crystal structures with this ion configuration). This configuration is the only one for Y^{3+} where $\Delta_{cryst} > \Delta_{topol}$; bond-length variations in coordinations [6]-[9] primarily result from the PJTE.

$^{[6]}Mo^{4+}$ has a bimodal distribution of bond lengths with maxima at 1.85 (0.96) and 2.03 Å (0.62 v.u.). $[Mo^{6+}O_4]^{2-}$ units occur as monomers and corner-sharing dimers. The monomers are more-or-less regular. In corner-sharing dimers, the $[Mo^{6+}O_4]^{2-}$ units adjust their bond valences to 1 × 1 v.u. at O_{br} and 3 × 0.66 v.u. for the three non-bridging bonds. This rearrangement, a result of non-local bond-topological asymmetry (special case #2), results in a bimodal distribution of bond lengths. For example, *a priori* (observed) bond valences in $Pb^{2+}{}_2(Mo^{4+}{}_2O(PO_4)_2(P_2O_7))$ (96454)[107] are 0.518 (0.548), 2 × 0.612 (0.599 and 0.612), 2 × 0.629 (0.586 and 0.594) and 1 (0.985) v.u., with Δ_{topol} = 0.111 and Δ_{cryst} = 0.023 v.u.

$^{[4]}Mo^{6+}$ (Fig. 1at) forms a unimodal bond-length distribution with very wide dispersion of bond lengths when bonded to O^{2-}, with the majority of MoO_4 tetrahedra occurring as monomers. We calculated the *a priori* bond valences for eight polyhedra from five crystal structures, and obtained average Δ_{topol} and Δ_{cryst} values of 0.104 and 0.087 v.u., respectively. Although $<\Delta_{cryst}>$ is much smaller than for $^{[5]}Mo^{6+}$ and $^{[6]}Mo^{6+}$, it shows that a considerable amount of bond-length variation is due to the PJTE for this ion configuration. Nonetheless, the effect of bond-topological asymmetry is stronger in most cases; one convincing example is for the structure of $Zr(Mo^{6+}O_4)_2$ (65512),[108] with *a priori* (observed) bond valences 3 × 1.333 (1.296, 1.314, 1.629) and 2 (1.918) v.u., with Δ_{topol} = 0.250 and Δ_{cryst} = 0.109 v.u.

$^{[6]}Cd^{2+}$ (Fig. 1bd) forms a unimodal bond-length distribution with a few anomalously long bond-lengths. Calculation of *a priori* (observed) bond valences for two structures gave average values of Δ_{topol} and Δ_{cryst} of 0.044 and 0.040 v.u., respectively. In $Cd_3Te^{6+}O_6$ (35084),[109] *a priori* (observed) bond valences are 4 × 0.314 (2 × 0.324 and 2 × 0.409) and 2 × 0.373 (0.296) v.u., with Δ_{topol} = 0.026 and Δ_{cryst} = 0.061 v.u. Presumably, the contribution to Δ_{cryst} is due to the PJTE, which is not uncommon in d^{10} transition-metal complexes (see also $^{[6]}Hg^{2+}$ below).[110] Anomalously long bond-lengths, e.g., 2.754 Å in $Cd_8(OH)_{12}(SO_4)_2(H_2O)$ (27222),[111] and 2.622 Å in $BaCd(P_2O_7)$ (39397)[112] are valid and result from a mixture of unusual bond topologies and the PJTE.

$^{[4]}Re^{7+}$ (Fig. 1bl) forms what appears to be a multi-modal distribution of bond lengths made entirely of $[Re^{7+}O_4]^-$ monomeric units, with a main maximum at 1.72 Å (1.73 v.u.) and other maxima at 1.69 (1.86) and 1.75 (1.61 v.u.) Å. We calculated the *a priori* (observed) bond valences for two coordination polyhedra in $(V^{4+}O)(Re^{7+}O_4)_2$ (92317),[113] with 3 × 1.667 (2 × 1.668 and 1.819) and 2 (1.819) Å for *Re*1, and 2 × 1.5 (1.632) and 2 × 2 (1.814 and 1.855) Å for *Re*2. Mean values of Δ_{topol} and Δ_{cryst} are 0.188 and 0.116 v.u.; while bond-length variation is caused mainly by bond-topological asymmetry, Δ_{cryst} shows that the PJTE also has a marked effect for this ion configuration.

$^{[6]}Os^{6+}$ (Fig. S1dy) has a distinctly bimodal distribution of bond lengths, although it consists of one crystal structure, $Rb_2Na_4((Os^{6+}O_2)((HO)_2Te^{6+}O_4)_2)(H_2O)_{16}$ (78359).[114] The H

positions were not refined for this structure, and we cannot calculate the *a priori* bond valences. We may only speculate that bond-topological asymmetry is at the root of bond-length variation, as the weak JTE (d^2 electronic configuration) is unlikely to result in such marked variation (>0.25 Å).

$^{[6]}Hg^{2+}$ (Fig. 1bq) has a very messy distribution of bond lengths when bonded to O^{2-}. This is partly due to the difficulty of defining a coordination polyhedron for this ion configuration across different structure types. Hg^{2+} typically forms two relatively short bonds (and a series of longer bonds for coordination numbers [3-7]), although this is not always true for [6]. For example, $(Hg^{2+}(H_2O)_6)(Cl^{7+}O_4)_2$ (1640)[115] report a holo-symmetric octahedron with bond lengths 6 × 2.342 Å (0.34 v.u.), in accord with our calculation of *a priori* bond valences for this structure. For a slightly irregular polyhedron (but not quite a [2+4] coordination) in $Hg^{2+}(PO_3)_2$ (280292),[116] *a priori* (observed) bond valences are 4 × 0.286 (0.222, 0.228, 0.320, 0.402) and 2 × 0.429 (0.439 and 0.543) v.u., with Δ_{topol} = 0.063 and Δ_{cryst} = 0.066 v.u. In this structure, the Hg^{2+} ion presumably moves off-center as a result of the PJTE (discussed further in section *PJTE: beyond octahedrally coordinated d^0 transition metal complexes*).[110]

[2] Ion configurations primarily distorted via multiple-bond formation

Ion configurations with BV_{max} 1.33-1.75 v.u. are $^{[5-7]}Ti^{4+}$, $^{[4]}Mn^{5+}$, $^{[4]}Mn^{6+}$, $^{[4,6-7]}Nb^{5+}$, $^{[6]}Ta^{5+}$, $^{[7]}Re^{7+}$, $^{[6]}Os^{6+}$, $^{[5-6]}Os^{7+}$. Those with BV_{max} > 1.75 v.u. are $^{[5-6]}V^{4+}$, $^{[4-6]}V^{5+}$, $^{[4]}Cr^{6+}$, $^{[4]}Mn^{7+}$, $^{[5-6]}Mo^{5+}$, $^{[4-7]}Mo^{6+}$, $^{[4]}Tc^{7+}$, $^{[4-6]}W^{6+}$, $^{[4-5]}Re^{7+}$, and $^{[4-6]}Os^{8+}$. From the latter group, bond-length distributions for which the main driver of bond-length variation is the formation of π-bonds according to criteria described above are $^{[5-6]}V^{4+}$, $^{[5-6]}V^{5+}$, $^{[5-6]}Mo^{5+}$ and $^{[5]}Mo^{6+}$. These are discussed below.

$^{[5]}V^{4+}$ (Fig. 1f) forms a bimodal distribution of bond lengths with maxima at 1.61 (1.58) and 1.96 Å (0.60 v.u.), integrating for 1 and 4 bonds, respectively. $^{[5]}V^{4+}$ forms one (vanadyl) π-bond for all but for one structure in our dataset, that of NaV_6O_{11} (202215),[117] where $[V^{4+}O_5]^{6-}$ occurs as a trigonal bipyramid (as opposed to the common square-pyramidal configuration) with bond valences 3 × 0.975 (1.785) and 2 × 0.423 v.u. (2.089 Å). We calculated *a priori* (observed) bond valences for two polyhedra from two crystal structures. In $V^{3+}{}_2(V^{4+}O(P_2O_7)_2$ (64634),[118] they are 4 × 0.5 (0.537) and 2 (1.823) v.u., with Δ_{topol} = 0.480 and Δ_{cryst} = 0.065 v.u., clearly demonstrating the bond-topological effect of π-bond formation and its effect on bond-length variation. In $Pb^{2+}{}_2(V^{4+}O(PO_4)_2)$ (249142),[119] *a priori* (observed) bond valences are 2 × 0.648 (0.506 and 0.542), 2 × 0.690 (0.579 and 0.613) and 1.325 (1.818) v.u., with Δ_{topol} = 0.210 and Δ_{cryst} = 0.186 v.u. The high value of Δ_{topol} is primarily driven by π-bond formation, but presumably also by non-local bond-topological asymmetry (their respective contributions cannot be resolved). The very high value of Δ_{cryst} is somewhat suspicious; while the $^{[5]}V^{4+}$ ion (d^1) is not susceptible to the JTE in square-pyramidal coordination, some of the bond-length variation due to crystallographic effects is probably due to the PJTE, whereby the V^{4+} ion typically moves off-center toward the O^{2-} ion of the vanadyl bond. In this particular structure, however, a more important factor is at play. We may trace the value of Δ_{cryst} to a calculated *a priori* bond valence of 1.325 v.u. for the π-bond; this value is very low because the O^{2-} ion involved in the π-bond is predicted to form a bond of 0.675 v.u. to Pb^{2+} (observed 0.167 v.u.). These values are not those observed in practice; instead, the $[V^{4+}{}_{05}]^{6-}$ units form corrugated (and presumably highly-strained) layers, and the high value of Δ_{cryst} results from structural incommensuration.

$^{[6]}V^{4+}$ (Fig. 1g) forms a trimodal distribution of bond lengths, with maxima around 1.61 (1.58), 2.00 (0.54), and 2.25 Å (0.27 v.u.). $[V^{4+}O_6]^{8-}$ units occur as monomers, oligomers, chains, sheets and frameworks where bonded to O^{2-}. By-and-large, these polyhedra adopt a [1+4+1] octahedral coordination, described by Schindler et al. as the number of vanadyl, equatorial, and *trans* bonds of the polyhedron (listed in order), where the *trans* bond is the weakest bond formed.[62] We calculated *a priori* (observed) bond valences for four polyhedra from as many crystal structures. In $(V^{4+}O)(Re^{7+}O_4)_2$ (92317),[113] made up of monomeric units, they are 3 × 0.333 (0.242 and 2 × 0.502), 2 × 0.5 (0.528) and 2 (1.744) v.u., with Δ_{topol} = 0.444 and Δ_{cryst} = 0.123 v.u. In $V^{4+}O(HPO_4)(H_2O)_{0.5}$ (201658),[120] made up of face-sharing dimers, they are 0.261 (0.207), 2 × 0.348 (0.453), 2 × 0.522 (0.621) and 2 (1.763) v.u., with Δ_{topol} = 0.444 and Δ_{cryst} = 0.117 v.u. These structures show that the formation of π bonds is clearly the main driver of bond-length variation for this ion configuration, in addition to non-local bond-topological effects which create variability among the non-vanadyl bonds. However, in $Ca(V^{4+}O)_2(PO_4)_2$ (72886),[121] made up of corner-sharing dimers, the *a priori* (observed) bond valences are 4 × 0.5 (0.464, 0.472, 0.502 and 0.513) and 2 × 1 (0.388 and 1.624) v.u., with Δ_{topol} = 0.222 and Δ_{cryst} = 0.219 v.u. In this structure, the large value of Δ_{topol} results from non-local bond-topological asymmetry alone; however, the V^{4+} ion moves off-center in the direction of the strong bond, resulting in one much stronger, and one much weaker bond than predicted. It is unclear whether this phenomenon results from the weak JTE, the PJTE, or a combination of both (they are not exclusive; see ref [72]). We presume that the PJTE is responsible for the off-centering, as we do not observe any similarly strong distorting effects from the weak JTE in the entirety of our dataset. Interestingly, we observe $[V^{4+}O_6]^{8-}$ units to be quasi-regular in $Sr_2(V^{4+}O_4)$ (71450),[122] made up of corner-sharing sheets of octahedra. The near regularity is predicted via *a priori* (observed) bond valences 4 × 0.641 (0.675) and 2 × 0.718 (0.563) v.u., with Δ_{topol} = 0.034 and Δ_{cryst} = 0.074 v.u.

$^{[5]}V^{5+}$ (Fig. 1i) forms a bi-modal distribution of bond lengths with maxima at about 1.64 (1.50) and 1.92 Å (0.73 v.u.), and two superimposed peaks at about 1.89 (0.79) and 1.99 Å (0.61 v.u.). $[V^{5+}O_5]^{5-}$ units occur primarily in square-pyramidal coordination (seldom with a sixth O^{2-} ion nearby, far too long for consideration as a bonded distance) but also as triangular bipyramidal and intermediate coordinations. They occur as monomers, oligomers, chains, sheets, clusters and frameworks, sharing corners and/or edges. We calculated *a priori* (observed) bond valences for three polyhedra in as many crystal structures. In $K_4(Cu^{2+}V^{5+}{}_5O_{15}Cl)$ (401042),[123] made up of $[V^{5+}O_5]^{5-}$ monomer units, they are 4 × 0.75 (0.810) and 2 (1.873) v.u., with Δ_{topol} = 0.400 and Δ_{cryst} = 0.073 v.u. In $V^{5+}AlMo^{6+}O_7$ (280775),[124] made up of edge-

sharing chains, they are 4 × 0.75 (2 × 0.628 and 2 × 0.943) and 2 (1.738) v.u, with Δ_{topol} = 0.400 and Δ_{cryst} = 0.179 v.u. While both these examples show the strong distorting effect of π-bond formation, significant off-centering via the PJTE also proves to be a significant cause of bond-length variation in $V^{5+}AlMo^{6+}O_7$. In $Cs(V^{5+}{}_3O_8)$ (50010),[125] made up of sheets of edge-sharing square pyramids with $V^{5+}O_6$, they are 2 × 0.750 (0.601 and 0.657), 0.875 (0.827), 1.188 (1.190) and 1.438 (1.703) v.u., with Δ_{topol} = 0.250 and Δ_{cryst} = 0.112 v.u. In this structure, bond-length variation associated with the strong π-bond results from non-local bond-topological asymmetry and the PJTE.

[6]V^{5+} (Fig. 1j) forms a very messy distribution of bond lengths. We primarily observe the $[V^{5+}O_6]^{7-}$ units as clusters, but also as monomers, dimers, chains, sheets and frameworks, sharing corners and/or edges. Of the 293 coordination polyhedra in our dataset, 251 originate from edge-sharing clusters, and 223 from decavanadate clusters. As we show below, cluster-type polyanions have specific bond-valence constraints for each of their crystallographically distinct polyhedra, which further vary as a function of the symmetry of the structure. These constraints result in a very messy (although resolvable) appearance for Fig. 1j, with added variability resulting from a suite of other effects. To elucidate the occurrence, prevalence and magnitude of these effects, we calculated *a priori* (observed) bond valences for eleven polyhedra from six crystal structures containing this ion configuration, including a structure containing the decavanadate cluster. First, we show the effect of π-bond formation in $V^{5+}{}_2Se^{4+}{}_2O_9$ (89466),[126] with *a priori* (observed) bond valences 2 × 0.4 (0.176/0.230 and 0.685/0.651), 2 × 0.6 (0.549/0.683 and 0.685/0.746), 1 (1.121/0.934) and 2 (1.743/1.756) v.u. for *V*1/*V*2, with Δ_{topol} = 0.444/0.444 and Δ_{cryst} = 0.171/0.160 v.u. In addition, a significant amount of bond-length variation seems to be caused by non-local bond-topological asymmetry and the PJTE in this structure. The strong distorting effect of the PJTE is shown in $Hg^{2+}(V^{5+}{}_2O_6)$ (409521),[127] with *a priori* (observed) bond valences 3 × 0.667 (0.201, 0.712 and 1.068), 2 × 0.917 (0.516 and 0.846) and 1.167 (1.621) v.u., with Δ_{topol} = 0.167 and Δ_{cryst} =

0.306 v.u. In $KMg(V^{5+}{}_5O_{14})(H_2O)_8$ (95929),[128] made up of decavanadate clusters (the most complex calculation done for this work, solving for 77 *a priori* bond valences), the *a priori* (observed) bond valences are 2 × 0.553 (0.433 an 0.449), 0.836 (0.758), 0.845 (0.710), 1.102 (1.350) and 1.111 (1.282) v.u. for *V*1, with Δ_{topol} = 0.187 and Δ_{cryst} = 0.143 v.u., 0.280 (0.319), 0.564 (0.624), 0.573 (0.590), 0.870 (0.922), 1.203 (0.919) and 1.510 (1.638) v.u. for *V*2, with Δ_{topol} = 0.361 and Δ_{cryst} = 0.097 v.u., 0.316 (0.329), 0.600 (0.608), 0.609 (0.573), 0.920 (0.891), 0.988 (0.986) and 1.568 (1.643) v.u. for *V*3, with Δ_{topol} = 0.325 and Δ_{cryst} = 0.027 v.u., 0.132 (0.273), 0.682 (0.513), 0.804 (0.752), 0.876 (0.917), 1.055 (0.901) and 1.451 (1.668) v.u. for *V*4, with Δ_{topol} = 0.294 and Δ_{cryst} = 0.129 v.u., and 0.166 (0.246), 0.725 (0.557), 0.756 (0.831), 0.770 (0.798), 0.910 (0.901), 1.673 (1.672) v.u. for *V*5, with Δ_{topol} = 0.305 and Δ_{cryst} = 0.060 v.u. Thus, bond lengths for $[V^{5+}O_6]^{7-}$ in the decavanadate cluster largely vary as a result of bond-topological asymmetry, including the formation of moderately-strong π-bonds ($<\Delta_{topol}>$ = 0.295 v.u.), and to a more modest extent by the PJTE ($<\Delta_{cryst}>$ = 0.091 v.u.). The average values of Δ_{topol} and Δ_{cryst} are 0.290 and 0.173 v.u. for the 13 polyhedra considered for this ion configuration.

[5]Mo^{5+} (Fig. S1ck)) occurs in two structures in our dataset. In $Pb^{2+}(Mo^{5+}O)_{10}(P_2O_7)$ (417729),[129] it forms square-pyramidal monomeric units with bond lengths (bond valences) of 1.691 (1.872), 2 × 1.974 (0.760) and 2 × 1.981 Å (0.744 v.u.). The sixth shortest interatomic distance is at 3.155 Å, far too long to be considered a bond. The O^{2-} ion participating in the strong π-bond does not bond to other cations; thus bond-length variation is primarily a result of π-bond formation for this ion configuration.

[6]Mo^{5+} (Fig. 1as) forms a bimodal distribution of bond lengths, with maxima at 1.68 (1.95) and 2.04 Å (0.62 v.u.). This ion configuration is characterized by the formation of a strong double-bond (1.953 v.u. on average), sometimes followed by polymerization into corner-sharing or edge-sharing dimers. We calculated *a priori* (observed) bond valences for two polyhedra in as many crystal structures. In $Ba(Mo^{5+}{}_2P_4O_{16})$ (69088),[130] made up of $[Mo^{5+}O_6]^{7-}$ monomeric units, they are 2 × 0.577 (0. 391 and 0.534), 2 × 0.604 (0.651 and 0.659), 0.639 (0.676) and 2 (2.079) v.u., with Δ_{topol} = 0.389 and Δ_{cryst} = 0.075 v.u., showing the strong distorting effect of π-bond formation for this ion configuration. In $Pr_3Mo^{5+}O_7$ (281197),[131] a less-common chain-structure, *a priori* (observed) bond valences are 2 × 0.746 (0.663 and 0.810) and 4 × 0.877 (0.529, 0.682, 0.906 and 1.114) v.u., with Δ_{topol} = 0.058 and Δ_{cryst} = 0.159 v.u. Thus no π-bond is predicted for this structure, and bond-length variation is primarily driven by crystallographic factors, most likely the weak JTE (d^1 electronic configuration).

[5]Mo^{6+} (Fig. 1au) forms what appears to be a unimodal bond-length distribution, despite the formation of a strong π-bond in all of its structures (1.738 v.u. on average). The somewhat unimodal appearance is due to a continuous series of observed bond valences whereby $[Mo^{6+}O_5]^{4-}$ units form multiple strong bonds (e.g., 1.552 v.u. on average for the second shortest bond). $[Mo^{6+}O_5]^{4-}$ units occur as monomers with square-pyramidal and triangular-bipyramidal shape, sometimes polymerizing into chains, sheets and frameworks with $Mo^{6+}O_6$ octahedra. We calculated *a priori* (observed) bond valences for three polyhedra from as many crystal structures. In $Cs_2(Mo^{6+}{}_3O_{10})$ (280066),[132] a representative example, they are 2 × 0.742 (0.653 and 0.903), 1.285 (0.970), 1.593 (1.706) and 1.638 (1.755) v.u., with Δ_{topol} = 0.367 and Δ_{cryst} = 0.159 v.u. Thus bond-length variations result primarily from a mixture of π-bond formation and non-local bond-topological asymmetry, followed by off-centering of the cation via the PJTE. In $Cs(Mo^{6+}{}_2O_3(PO_4)_2)$ (79517),[75] *a priori* (observed) bond valences are 0.915 (0.850), 1.026 (0.801), 1.078 (0.735) and 2 × 1.491 (1.735 and 1.891) v.u., with Δ_{topol} = 0.232 and Δ_{cryst} = 0.256 v.u. In $Cs(Np^{5+}O_2)(Mo^{6+}O_4)$ (66994),[133] they are 2 × 1.022 (0.615 and 1.007), 2 × 1.177 (1.252 and 1.539) and 1.601 (1.579) v.u., with Δ_{topol} = 0.161 and Δ_{cryst} = 0.176 v.u. Thus the PJTE has a more important effect on bond-length variation than the combined effect of π-bond formation and non-local bond-topological asymmetry in these two structures.

[3.1] Ion configurations primarily distorted via coupled electronic-vibrational degeneracy

[6]Cr^{2+} (Fig. 1k) forms a clear bimodal distribution, typical of that observed for octahedrally coordinated cations under the influence of the strong JTE. We calculated *a priori* (observed) bond valences for two of the seven structures in our dataset containing this ion configuration (the two anhydrous structures). In $Cr^{2+}{}_3Cr^{3+}{}_4(PO_4)_6$ (72302),[134] the *a priori* (observed) bond valences are 4 × ~ 0.25 (0.08-0.45) and 2 × ~ 0.5 v.u. (0.48-0.58) v.u., with Δ_{topol} = 0.170 and Δ_{cryst} = 0.118 v.u. In $Cr^{2+}{}_3Cr^{3+}{}_4(PO_4)_6$ (73261),[93] they are 2 × 0.568 (0.484), 2 × 0.174 (0.199) and 2 × 0.259 (0.244) v.u., with Δ_{topol} = 0.156 and Δ_{cryst} = 0.041. The fact that $\Delta_{topol} > \Delta_{cryst}$ in these structures probably results from structure selection (*a priori* bond valences could not be calculated for the hydrated structures); the 9 other polyhedra for this ion configuration clearly follow the [4+2] coordination expected of a "z-out" Jahn-Teller distortion. We list the JTE as the main factor underlying bond-length variation for this ion configuration, although it is closely followed by the effect of non-local bond-topological asymmetry.

[6]Mn^{3+} (Fig. 1q) forms a bimodal distribution of bond lengths, typical of the strong JTE. However, inspection of the data making up the distribution reveals that of the 82 coordination polyhedra, only 39 have a distinct [4+2] ("z-out") coordination, while 17 have a [2+2+2] coordination, 6 have a [2+4] ("z-in"), and 2 are regular (18 are ambiguous). A [4+2] coordination is easily explained by the strong JTE, for example in $KMn^{3+}(Se^{6+}O_4)_2$ (80430),[135] with Δ_{topol} = 0.008 and Δ_{cryst} = 0.211 v.u., or $Gd(Mn^{3+}O_3)$ (95493),[74] with Δ_{topol} = 0.039 and Δ_{cryst} = 0.186 v.u. On the other hand [2+2+2]-coordinated polyhedra appear to result as a mixture of the strong JTE and bond-topological effects. For example, edge-shared chains in $Ca_4Mn^{3+}{}_3B_3O_{12}CO_3$ (24973)[136] have *a priori* (observed) bond valences 2 × 0.404 (0.155 and 0.230), 2 × 0.480 (0.506 and 0.874), and 2 × 0.616 (0.806 and 0.846) v.u., with Δ_{topol} = 0.077 and Δ_{cryst} = 0.211 v.u. Regular polyhedra are likely due to disordered JT distortion, as evidenced by high anisotropic-displacement parameters in $Mn^{2+}{}_3Mn^{3+}{}_2(SiO_4)_3$ (86935).[137]

[6]Cu^{2+} (Fig. 1af) forms a smooth bimodal distribution of bond lengths. Inspection of the data making up the distribution shows that of the 365 coordination polyhedra, 269 have distinct [4+2] ("z-out") coordination, 49 have a [2+2+2] coordination, 10 have a [2+4] ("z-in"), and 7 are regular (30 are ambiguous). [4+2] coordination follows classic (strong) JTE arguments, for example in $Cu^{2+}{}_2V^{5+}{}_2O_7$ (171028),[91] with Δ_{topol} = 0.096 and Δ_{cryst} = 0.127 v.u., and in $Cu^{2+}{}_2Co^{2+}O(B_2O_5)$ (400438),[104] with Δ_{topol} = 0.046 and Δ_{cryst} = 0.161 v.u. An example of [2+4] coordination is that of $Cu^{2+}{}_3Ba(V^{5+}O_4)_2(OH)_2$ (67726),[138] with *a priori* (observed) bond valences 2 × 0.459 (0.54) and 4 × 0.270 (2 × 0.246 and 2 × 0.253) v.u. with Δ_{topol} = 0.084 and Δ_{cryst} = 0.039. It is interesting that $\Delta_{topol} > \Delta_{cryst}$ for two of the three coordination polyhedra above. While this may be accidental, this result shows two things: (1) bond-topological effects are an important driver of bond-length variation for this ion configuration, and (2) some structures appear to accommodate the bond-valence constraints of JTEs ions (how much of this is a result of observational bias is currently unclear). We further calculated the *a priori* (observed) bond valences for a regular octahedron in $Ba_3Cu^{2+}(Sb^{5+}{}_2O_9)$ (2279)[139] as 3 × 0.270 (0.340) and 3 × 0.396 (0.330) v.u., with Δ_{topol} = 0.063 and Δ_{cryst} = 0.070 v.u. It is therefore interesting that for this structure, $Cu^{2+}O_6$ is indeed expected to distort for bond-topological reasons, but doesn't for crystallographic reasons (dynamic JTE).

[3.2] Ion configurations primarily distorted via coupled electronic-vibrational *near*-degeneracy

[4]Ti^{4+} (Fig. S1g) occurs in four coordination polyhedra in three crystal structures. The largest bond-length variation is observed in chains of corner-sharing octahedra in $Rb_2(Ti^{4+}O_3)$ (78842)[140] where it forms its strongest observed bond (1.233 v.u.; 1.747 Å). *A priori* (observed) bond valences for this structure are 2 × 0.926 (0.858) and 2 × 1.074 (1.208 and 1.233) v.u., with Δ_{topol} = 0.074 and Δ_{cryst} = 0.107 v.u. The PJTE has slightly stronger distorting power than the effect of non-local bond-topological asymmetry for this ion configuration.

[5]Ti^{4+} (Fig. 1c) forms a peculiar bond-length distribution with a maximum at 1.96 Å (0.66 v.u.) and a very long tail at shorter bond lengths. The shape of distribution results mainly from the formation of a strongly bonded axial ligand in square-pyramidal geometry, relative to the equatorial ligands. $[Ti^{4+}O_5]^{6-}$ units range in shape from square pyramidal to distorted square-pyramidal to triangular bipyramidal, with the strongest bond decreasing in strength along that series. In $Cs_2(Ti^{4+}O)(P_2O_7)$ (72682),[141] $[Ti^{4+}O_5]^{6-}$ units are square pyramidal with *a priori* (observed) bond valences 4 × 0.739 (0.587, 0.617, 0.622 and 0.663) and 1.044 (1.66) v.u., with Δ_{topol} = 0.098 and Δ_{cryst} = 0.217 v.u. In $La_3Ti^{4+}O_4Cl_5$ (33800),[142] $[Ti^{4+}O_5]^{6-}$ units are triangular bipyramidal with *a priori* (observed) bond valences 2 × 0.625 (0.509), 2 × 0.915 (1.013 and 1.031) and 0.920 (1.019) v.u., with Δ_{topol} = 0.140 and Δ_{cryst} = 0.109 v.u. These examples show that the strongest cause underlying bond-length variation for this ion configuration may vary between non-local bond-topological asymmetry and the PJTE as a function of polyhedral shape. Overall, the PJTE results in larger bond-length variations than bond-topological asymmetry, with mean Δ_{topol} and Δ_{cryst} values of 0.119 and 0.163 v.u., respectively. For the square-pyramidal units, there is sometimes (but not always) a possibility of a sixth bond to complete the octahedron. However, these distances range from 2.70-3.77 Å in different structures, and we consider them far too long for inclusion as bonds.

[6]Ti^{4+} (Fig. 1d) forms a multi-modal bond-length distribution with subtle maxima arising from different effects. Primarily, $[Ti^{4+}O_6]^{8-}$ units form oligomers, chains, rings, sheets, clusters and frameworks, both as strictly corner-sharing and edge-sharing units, and sometimes as a mixture of both, resulting in a wide range of bond-valence constraints. Adding to the intrinsic bond-valence constraints is the off-centering of Ti^{4+} due to the PJTE, resulting in a very large range of observed bond lengths (1.648-2.474 Å). The near-uniqueness of the bonding environment of each and every TiO_6 octahedron in our dataset somewhat takes away the usefulness of rationalizing the shape of its compound bond-length distribution. Some of the noteworthy features of Fig. 1d include a small maximum between 1.7-1.8 Å with maximum at 1.74 Å, a strong maximum at ~1.95 Å and a subtle maximum at 2.10 Å (0.44 v.u.). These maxima originate

from the strongest and weakest bond of corner-sharing chains, for which we typically observe one bond of 1.25-1.35 v.u. (1.72-1.74 Å), and five bonds of gradually decreasing strength in the ~0.40-0.70 v.u. (1.94-2.13 Å) range, with an average bond-length 2.10 Å for the longest bond. A representative example is that of $(Cs_{0.07}Rb_{0.95})(Ti^{4+}O)(As^{5+}O_4)$ (280501),[143] with *a priori* (observed) bond valences of 2 × 0.363 (0.397 and 0.673), 0.570 (0.631), 0.856 (0.525), 0.883 (0.474) and 0.964 (1.318) v.u. for *Ti*1, with Δ_{topol} = 0.235 and Δ_{cryst} = 0.250, and 0.379 (0.522), 0.449 (0.577), 0.603 (1.218), 2 × 0.786 (0.615 and 0.654) and 0.997 (0.418) v.u. for *Ti*2, with Δ_{topol} = 0.190 and Δ_{cryst} = 0.295 v.u. We may compare these numbers to the *a priori* (observed) bond valences of sheets of edge-sharing octahedra in $Sm^{3+}(Ti^{4+}O_3Cl)$ (36608):[144] 3 × 0.560 (0.455 and 2 × 0.555), 2 × 0.747 (0.515 and 0.978) and 0.827 (0.858) v.u., with Δ_{topol} = 0.107 and Δ_{cryst} = 0.102 v.u. Furthermore, we calculated the *a priori* (observed) bond valences for sheets of edge- and corner-sharing octahedra of $[Ti^{4+}O_6]^{8-}$ in $La_2(Ti^{4+}{}_2SiO_9)$ (75583):[145] 2 × 0.619 (0.663), 2 × 0.688 (0.619) and 2 × 0.693 (0.821) v.u. for *Ti*1, with Δ_{topol} = 0.032 and Δ_{cryst} = 0.080 v.u., and 0.544 (0.281), 2 × 0.625 (0.791), 2 × 0.685 (0.554) and 0.731 (0.871) v.u. for *Ti*2, with Δ_{topol} = 0.055 and Δ_{cryst} = 0.162 v.u. Altogether, we get average values of Δ_{topol} and Δ_{cryst} of 0.111 and 0.163 v.u., respectively, confirming that the PJTE has a larger effect on bond-length variation than non-local bond-topological asymmetry, overall.

$^{[7]}Ti^{4+}$ (Fig. S1j) is only example of this coordination polyhedron, in $(C(NH_2)_3)_4(Ti^{4+}O(CO_3)_3)(H_2O)_2$ (66308),[146] bonding to six O^{2-} ions from CO_3 groups (0.30-0.46 v.u.) and making a partial double-bond (1.50 v.u.) to a seventh O^{2-} ion (in turn forming two hydrogen bonds to NH_2 groups). The positions of the H atoms were not refined, and we cannot calculate the *a priori* bond valences for this structure. There is however significant displacement of Ti^{4+} toward *O*1 and away from *O*9 (the apical bonds), suggesting the PJTE as the main reason underlying bond-length variation for this ion configuration.

$^{[6]}Y^{3+}$ (Fig. 1aj) has a somewhat regular distribution of bond lengths, with a main maximum at 2.27 Å (0.49 v.u.), and a more subtle maximum at 2.22 Å (0.55 v.u.). This latter maximum does not occur as a result of polymerization constraints; it either results from non-local bond-topological asymmetry, or because of slight (but consistent) off-centering of the central cation via the PJTE resulting in some bonds in the range 2.20-2.24 Å. We calculated the *a priori* (observed) bond valences for olivine-structured $NaY(GeO_4)$ (85497):[147] 2 × 0.561 (0.490 and 0.548) and 4 × 0.470 (2 × 0.399 and 2 × 0.495) v.u., with Δ_{topol} = 0.040 and Δ_{cryst} = 0.046, showing non-local bond-topological asymmetry to be about equally responsible for bond-length variations for this ion configuration.

$^{[7]}Y^{3+}$ (Fig. 1ak) forms a regular distribution of bonds lengths, with a "wide" maximum, as also observed for $^{[7]}Y^{3+}$ and $^{[9]}Y^{3+}$. We calculated *a priori* (observed) bond valences for three coordination polyhedra from two polymorphs of $Y_2Ba_2Cu^{2+}Pt^{4+}O_8$ (63103 and 65614).[148,149] In the first structure, Δ_{topol} = 0.001 and Δ_{cryst} = 0.044 v.u. for *Y*1, and Δ_{topol} = 0.004 and Δ_{cryst} = 0.056 v.u. for *Y*2. In the second structure, we calculate Δ_{topol} = 0.020 and Δ_{cryst} = 0.077 v.u. Together, these values show that the wide maximum observed in the bond-length distribution of this ion configuration is probably due to slight off-centering of Y^{3+} as opposed to resulting from non-local bond-topological asymmetry.

$^{[8]}Y^{3+}$ (Fig. 1al) forms a very wide bond-length distribution with high kurtosis. A sharp maximum at 2.39 Å (0.36 v.u.) accounts for the majority of polyhedra where Y^{3+} makes eight equal bonds (i.e., does not move off-center). A slightly distorted variant of a regular polyhedron can be seen in $Ca_2Y(As^{5+}O_4)(W^{6+}O_4)_2$ (71562),[150] with *a priori* (observed) bond valences of 4 × 0.317 (0.422) and 0.433 (0.362) v.u., with Δ_{topol} = 0.072 and Δ_{cryst} = 0.131 v.u. *A priori* (observed) bond valences are much more scattered in $Y_3Re^{7+}O_8$ (15505),[151] ranging from 0.254-0.486 (0.269-0.478) v.u., with Δ_{topol} = 0.111 and Δ_{cryst} = 0.083 for *Y*1, to 0.302-0.533 (0.251-0.571) v.u., with Δ_{topol} = 0.085 and Δ_{cryst} = 0.071 v.u. for *Y*2. In $KY(W^{6+}O_4)$ (411285),[152] *a priori* (observed) bond valences are 2 × 0.230 (0.495), 4 × 0.400 (2 × 0.174 and 2 × 0.427), and 2 × 0.470 (0.475) v.u., with Δ_{topol} = 0.058 and Δ_{cryst} = 0.088 v.u. The mean values of Δ_{topol} and Δ_{cryst} are 0.082 and 0.093 v.u. over those structures, showing the PJTE and non-local bond-topological asymmetry to be approximately equally responsible for bond-length variations for this ion configuration.

$^{[9]}Y^{3+}$ (Fig. 1am) forms a regular distribution of bonds lengths with a wide maximum, as observed for other coordination numbers of this cation. *A priori* (observed) bond valences in $Y_3Re^{7+}O_8$ (15505)[151] are 0.270-0.495 (0.133-0.560) v.u., with Δ_{topol} = 0.078 and Δ_{cryst} = 0.110 v.u. Thus it seems that both the PJTE and non-local bond-topological asymmetry cause bond-length variation for this ion configuration, and for the widening of the maximum.

$^{[6]}Zr^{4+}$ (Fig. 1an) forms a regular distribution of bond lengths when bonded to O^{2-}. We calculated *a priori* (observed) bond valences for five coordination polyhedra in four structures: $Na_4Zr_2(SiO_4)_3$ (15545),[153] with Δ_{topol} = 0.021 and Δ_{cryst} = 0.054 v.u., $(Ca_{0.81}Na_{0.19})ZrB(Al_{8.82}Ti^{4+}{}_{0.18}O_{18})$ (55272),[154] with Δ_{topol} = 0 and Δ_{cryst} = 0.003 v.u. for *Zr*1 and Δ_{topol} = 0 and Δ_{cryst} = 0.041 v.u. for *Zr*2, $Zr(Mo^{6+}O_4)_2$ (65512),[108] with Δ_{topol} = 0 and Δ_{cryst} = 0.041 v.u., and $Na_2Ca_4ZrNb^{5+}(Si_2O_7)_2FO_3$ (100158),[155] with Δ_{topol} = 0.221 and Δ_{cryst} = 0.186 v.u. Average values of Δ_{topol} and Δ_{cryst} are 0.048 and 0.117 v.u., respectively, for these structures, showing that the PJTE accounts for more variability in bond lengths than non-local bond-topological asymmetry for this ion configuration.

$^{[4]}Nb^{5+}$ (Fig. S1cd) occurs in a single structure in our dataset, that of $Cs_2Nb^{5+}{}_4O_{11}$ (26379),[156] where $Nb^{5+}O_4$ and $Nb^{5+}O_6$ polyhedra link together to form a framework structure. For the *Nb*5 site ([4]-coordinated), two of the O^{2-} ions (*O*3 and *O*17) bond to 2 × $^{[6]}Nb^{5+}$ and 1 × $^{[4]}Nb^{5+}$, while the other two (*O*21) bond only to 2 × $^{[6]}Nb^{5+}$. This creates a strong bond-topological mismatch between the bond-valence requirement of O^{2-} (2 v.u.) and an even distribution of bond valences for the NbO_6 and NbO_4 polyhedra. Thus the $[Nb^{5+}O_4]^{3-}$ unit makes two bridging bonds via *O*21 of 1.573 v.u. (1.742 Å), while the two bridging bonds made via *O*3 and *O*17 are weaker at 0.961 v.u. (1.926 Å). Although we could not calculate the *a priori* bond valences of this structure, we assume that the PJTE has a similarly strong effect on bond-

length variability as bond-topological asymmetry for this ion configuration.

[5]Nb^{5+} (Fig. S1ce) occurs in four structures in our dataset. We calculated the *a priori* (observed) bond valences for two of these structures: for $Na_5Nb^{5+}O_5$ (24819),[157] they are 3 × 0.981 (2 × 0.797 and 1.083) and 2 × 1.029 (1.028) v.u., with Δ_{topol} = 0.023 and Δ_{cryst} = 0.094 v.u.; for $NaKLaNb^{5+}O_5$ (94743),[158] they are 4 × 0.978 (0.877) and 1.088 (1.243) v.u., with Δ_{topol} = 0.035 and Δ_{cryst} = 0.112 v.u. These values show that the PJTE is the main reason underlying bond-length variation for [5]Nb^{5+}, with non-negligible contribution from non-local bond-topological asymmetry.

[6]Nb^{5+} (Fig. 1ar) forms a symmetric distribution of bond lengths with a maximum at 1.98 Å (5/6 v.u.). As we have seen above for [6]Ti^{4+} and [4]V^{5+}, a symmetric distribution typically results from an ion configuration with a strong proclivity for polymerization. $[Nb^{5+}O_6]^{7-}$ units polymerize into dimers, chains, rings, clusters, sheets and frameworks, via corners, edges, faces, and combinations of these. All of these polymerization circumstances lead to different *a priori* bond valences (and thus bond lengths) for the constituent crystal structures; the resulting distribution of these *a priori* bond lengths approaches that of a Gaussian distribution, in contrast to the positively-skewed shape of simpler bond-length distributions driven by a two-body Morse potential. For example, monomeric $[Nb^{5+}O_6]^{7-}$ units are evenly distributed between [1+4+1] coordination and regular octahedra in our dataset. The off-centering of the Nb^{5+} ion via the PJTE, with no preferential off-centering direction,[81] contributes to further symmetrization of the distribution. The combined effect of these phenomena gives a wide range of observed bond lengths: 1.702-2.479 Å (~0.06 Å smaller than [6]Ti^{4+}). To compare the magnitude of bond-length variability caused by bond-topological asymmetry and the PJTE, we calculated the *a priori* (observed) bond valences for 15 polyhedra in 12 structures containing [6]Nb^{5+}. In $La(Nb^{5+}{}_5O_{14})$ (33783),[159] they are 0.727 (0.607), 2 × 0.796 (0.610 and 1.068), 0.893 (0.891) and 2 × 0.894 (0.573 and 1.250) v.u., with Δ_{topol} = 0.061 and Δ_{cryst} = 0.210 v.u. In $CaNb^{5+}{}_2(P_4O_{13})(P_2O_7)O$ (62577; discussed above), they are 2 × 0.805 (0.993), 2 × 0.837 (0.824) and 2 × 0.859 (0.869) v.u. for *Nb*1, with Δ_{topol} = 0.019 and Δ_{cryst} = 0.071 v.u., and 0.261 (0.462), 2 × 0.782 (0.714), 2 × 0.831 (0.837) and 1.515 (1.753) v.u. for *Nb*2, with Δ_{topol} = 0.227 and Δ_{cryst} = 0.098 v.u. In $Li(Nb^{5+}U^{6+}O_6)$ (416590),[160] they are 2 × 0.627 (0.835 and 0.893), 2 × 0.647 (0.810), 0.971 (0.248) and 1.480 (1.408) v.u., with Δ_{topol} = 0.261 and Δ_{cryst} = 0.266 v.u. We obtain average values of Δ_{topol} and Δ_{cryst} of 0.125 and 0.167 v.u. over the 15 polyhedra, respectively. These values demonstrate the substantial role of bond-topological asymmetry in driving bond-length variation in $[Nb^{5+}O_6]^{7-}$ units, while confirming the PJTE as the main source of variation.

[7]Nb^{5+} (Fig. S1cg) occurs in three coordination polyhedra in two crystal structures. In $La(Nb^{5+}{}_5O_{14})$ (33783),[159] *a priori* (observed) bond valences are 2 × 0.591 (0.240 and 0.849), 0.688 (0.590), 2 × 0.739 (0.497 and 1.037), and 2 × 0.826 (0.865 and 0.888) v.u. for *Nb*1, with Δ_{topol} = 0.078 and Δ_{cryst} = 0.192 v.u., and 0.545 (0.506), 4 × 0.614 (2 × 0.613 and 2 × 0.617) and 2 × 1 (0.582 and 1.470) v.u., with Δ_{topol} = 0.163 and Δ_{cryst} = 0.133 v.u. Average values for Δ_{topol} and Δ_{cryst} are 0.121 and 0.163, respectively.

[6]Mo^{6+} (Fig. 1av) forms a peculiar trimodal distribution of bond lengths when bonded to O^{2-}, with maxima at 1.71 (1.74), 1.92 (0.95) and 2.30 Å (0.32 v.u). The $[Mo^{6+}O_6]^{6-}$ units occur as monomers, dimers and other oligomers, chains, rings, sheets, clusters and frameworks, sharing corner, edges and/or faces. The near-uniqueness of the bonding environment of each and every $Mo^{6+}O_6$ octahedron in our dataset renders the elucidation of all bond-valence constraints leading up to the observed bond-length distribution very lengthy and tedious. Here, we will simply calculate *a priori* (observed) bond valences for various modes of polymerization (from 10 coordination polyhedra and 8 structures) to determine whether bond-topological asymmetry, or the PJTE, is the main reason underlying bond-length variation for this ion configuration. Some of the results are given below, ordered in increasing degree of polymerization of the $[Mo^{6+}O_6]^{6-}$ unit. In $K_2Mo^{6+}O_2(I^{5+}O_3)_4$ (170119),[161] with monomeric $[Mo^{6+}O_6]^{6-}$ units, the *a priori* (observed) bond valences are 2 × 0.951 (1.740), 2 × 1.001 (0.384) and 2 × 1.048 (0.862) v.u., with Δ_{topol} = 0.033 and Δ_{cryst} = 0.531 v.u.; this is the largest value we calculate for our entire dataset. In $Na_2Mo^{6+}{}_3Te^{4+}{}_3O_{16}$ (171758),[162] made up of trimers of edge-sharing octahedra, Δ_{topol} = 0.152 and Δ_{cryst} = 0.340 v.u. for *Mo*1, and Δ_{topol} = 0.224 and Δ_{cryst} = 0.261 v.u. for *Mo*2. In $Rb_2Se^{4+}Mo^{6+}O_6$ (413000),[163] made up of chains of corner-sharing octahedra, we get Δ_{topol} = 0.102 and Δ_{cryst} = 0.496 v.u. In $Cs_2(Mo^{6+}{}_3O_{10})$ (280066),[132] made up of chains of edge-sharing $Mo^{6+}O_6$ and $Mo^{6+}O_5$ polyhedra, Δ_{topol} = 0.322 and Δ_{cryst} = 0.215 v.u. In $Pr^{3+}{}_2(Mo^{6+}{}_4O_{15})$ (68279),[164] made up of sheets of corner- and edge-sharing $Mo^{6+}O_4$ and $Mo^{6+}O_6$ polyhedra, Δ_{topol} = 0.418 and Δ_{cryst} = 0.235 v.u. Finally, in $BaTe^{4+}Mo^{6+}{}_2O_9$ (281503),[165] a framework of corner-sharing $[Mo^{6+}O_6]^{6-}$ octahedra, Δ_{topol} = 0.282 and Δ_{cryst} = 0.214 v.u. for *Mo*1, and Δ_{topol} = 0.328 and Δ_{cryst} = 0.161 v.u. for *Mo*2. Altogether, $\langle\Delta_{topol}\rangle$ = 0.218 and $\langle\Delta_{cryst}\rangle$ = 0.298 v.u.; this $\langle\Delta_{cryst}\rangle$ value is the largest of our dataset, out of the 52 transition-metal configurations for which we calculated these values in two or more structures. Next comes a closer examination of the data to rationalize the shape of the bond-length distribution. We find our dataset to be made of ~ 50% clusters, ~ 30% chains/rings, ~ 10% monomers, and 10% of other degrees of polymerization. We find that for clusters, chains/rings, and monomers, our data forms three groups of two bonds, in agreement with Ok et al. who found that octahedrally coordinated Mo^{6+} preferentially moves off-center toward an edge (and sometimes a face).[81] The mean bond-valence are 1.706, 0.926, and 0.362 v.u. for clusters, and 1.715, 0.901, and 0.362 v.u. for chains and rings. These values compare exceptionally well to the three observed maxima of 1.74, 0.95 and 0.32 v.u. On the other hand, monomers have mean bond-valence values of 1.708, 0.821, and 0.473 v.u. Taken together, these values indicate that the trimodal shape of the bond-length distribution arises as a result of the combination of bond-topological constraints of polymerization (for clusters, chains and rings) and the preferential off-centering of Mo^{6+} toward an edge of the octahedron as a result of the PJTE.

[6]Hf^{4+} (Fig. 1bf) forms a regular distribution of bond lengths. We calculated *a priori* (observed) bond valences for three polyhedra in two structures. In $Pb^{2+}HfO_3$ (33194),[166] Δ_{topol} = 0.017 and Δ_{cryst} = 0.178 v.u. for *Zr*1, and Δ_{topol} = 0.003 and

Δ_{cryst} = 0.162 v.u. for *Zr*2. In $Ni^{2+}{}_5HfB_2O_{10}$ (65476),[167] Δ_{topol} = 0.063 and Δ_{cryst} = 0.026 v.u. These values indicate that the PJTE can have a very strong distorting effect on $Hf^{4+}O_6$ octahedra, and that non-local bond-topological asymmetry has some effect on bond-length variations for this ion configuration.

[6]Ta^{5+} forms a somewhat symmetrical, unimodal distribution of bond lengths, reminiscent of that of [6]Ti^{4+} (Fig. 1g). Similar to [6]Ti^{4+}, [6]Nb^{5+} and other ions with similarly symmetrical bond-length distributions, $[Ta^{5+}O_6]^{7-}$ units are very susceptible to polymerization. $[Ta^{5+}O_6]^{7-}$ octahedra occur as monomers, dimers, chains, sheets, clusters and frameworks, either sharing corners, edges and/or faces. We calculated *a priori* (observed) bond valences for six coordination polyhedra in as many crystal structures. In $Na_2Ca_3Ta^{5+}{}_2O_9$ (280154),[168] made up of face-sharing dimers, they are 6 × 0.833 (3 × 0.533 and 3 × 1.023) v.u., with Δ_{topol} = 0 and Δ_{cryst} = 0.245 v.u. Comparing two structures where the $[Ta^{5+}O_6]^{7-}$ units form chains of either corner- or edge-sharing octahedra, we get 4 × 0.75 (2 × 0.796 and 2 × 0.847) and 2 × 1 (0.762 and 1.029) v.u. for chains of corner-sharing octahedra in $CsTa^{5+}(B_2O_5)$ (80423),[169] with Δ_{topol} = 0.111 and Δ_{cryst} = 0.092 v.u., and 4 × 0.75 (2 × 0.429 and 2 × 0.849) and 2 × 1 (1.167) v.u. for chains of edge-sharing octahedra in $Yb(Ta^{5+}O_4)$ (415460).[170] Including the other structures not discussed here, we obtain average values of Δ_{topol} and Δ_{cryst} of 0.070 and 0.140 v.u. for this ion configuration. Thus the PJTE is the main reason underlying bond-length variation for this ion configuration.

[7]Ta^{5+} (Fig. 1bh) forms what appears to be a bimodal distribution of bond lengths when bonded to O^{2-} with main maximum at 2.01 Å (0.76 v.u.) and secondary maximum at 2.43 Å (0.22 v.u.). Pentagonal bipyramids typically polymerize into sheet and framework structures with TaO_6 octahedra. We calculated the *a priori* (observed) bond valences for one polyhedron, in $DyTa^{5+}{}_7O_{19}$ (203232),[171] 0.583 (0.640), 4 × 0.667 (0.210, 0.606, 0.756, and 1.153), 0.750 (0.680) and 1 (1.075) v.u., with Δ_{topol} = 0.092 and Δ_{cryst} = 0.185 v.u. Thus the formation of the long and weak bond for this ion configuration is not a result of non-local bond-topological asymmetry, and rather results from the PJTE.

[5]W^{6+} (Fig. 1bj) has a regular distribution of bond lengths. We calculated the *a priori* (observed) bond valences for two polyhedra in as many structures. In $KNa_3(W^{6+}O_5)$ (40249),[172] they are 2 × 1.192 (1.004 and 1.146), 2 × 1.197 (1.184) and 1.221 (1.393) v.u., with Δ_{topol} = 0.008 and Δ_{cryst} = 0.086 v.u. In $La_2(W^{6+}O_4)_3$ (78180),[173] they are 2 × 0.952 (0.469 and 1.139), 1.238 (1.290) and 2 × 1.429 (1.512 and 1.652) v.u., with Δ_{topol} = 0.149 and Δ_{cryst} = 0.169 v.u. Thus the PJTE is probably the main driver of bond-length variation for this ion configuration, although the effect of non-local bond-topological asymmetry can be significant in some structures.

[6]W^{6+} (Fig. 1bk) has a peculiar trimodal distribution of bond lengths when bonded to O^{2-}, with two maxima at 1.74 (1.65) and 1.92 Å (0.97 v.u.), and a third, very broad maximum around 2.18 Å (0.45 v.u.). The $[W^{6+}O_6]^{6-}$ units occur as monomers, chains, rings, sheets, clusters and frameworks, sharing corners and/or edges. The shape of the bond-length distribution is influenced by the fact that the majority of our dataset (roughly 2/3) involve clusters of more-or-less similar bond-valence constraints. The strongest and weakest bonds of these clusters are 1.69 (1.73) and 0.38 v.u. (2.24 Å) on average, with significant variability in between, presumably as a result of bond-topological constraints. The bonds in chains and rings tend to split into three groups, with mean bond-valences of 2 × 1.5, 2 × 1 and 2 × 0.5 v.u. The main maximum at 1.92 Å (0.97 v.u.) represents the mean bond-valence (statistically the most probable observation) for this ion configuration, although the $[W^{6+}O_6]^{6-}$ unit is regular in only a few structures. We calculated the *a priori* (observed) bond valences for five polyhedra from four crystal structures. In $K_2Ni^{2+}(W^{6+}O_2(PO_4)_2)$ (79702),[174] made up of monomeric $[W^{6+}O_6]^{6-}$ units, Δ_{topol} = 0.122 and Δ_{cryst} = 0.262 v.u. In $KY(W^{6+}O_4)_2$ (411285),[152] made up of chains of edge- and/or corner-sharing octahedra, Δ_{topol} = 0.075 and Δ_{cryst} = 0.357 v.u. In $Cu^{+}La(W^{6+}{}_2O_8)$ (68614),[175] made up of tetrameric clusters of edge-sharing octahedra, Δ_{topol} = 0.204 and Δ_{cryst} = 0.170 v.u. for *W*1 and Δ_{topol} = 0.183 and Δ_{cryst} = 0.239 v.u. for *W*2. Finally, in WO_3 (86144),[176] a framework of corner-sharing octahedra, *a priori* (observed) bond valences are 6 × 1 (0.443, 2 × 0.927, 2 × 1.174 and 1.865) v.u., with Δ_{topol} = 0 and Δ_{cryst} = 0.319 v.u. Altogether, average values of Δ_{topol} and Δ_{cryst} are 0.117 and 0.269 v.u. for these structures, showing that the PJTE is the principal cause of bond-length variation for this ion configuration, with bond-topological asymmetry having a lesser role. Although many polyhedra have bond valences > 1.75 v.u., these strong bonds result either from polymerization or the PJTE.

[5]Re^{7+} (Fig. S1dv) forms a regular but slightly negatively skewed distribution of bonds lengths when bonded to O^{2-}. The largest bond-length variation is in $Ba_{10}(Re^{7+}O_5)_6Br_2$ (100571),[177] with *a priori* (observed) bond valences of 2 × 1.391 (1.263), 2 × 1.402 (1.178) and 1.414 (1.882) v.u., with Δ_{topol} = 0.007 and Δ_{cryst} = 0.235 v.u. These values clearly show the PJTE to be the main cause of bond-length variation for this ion configuration.

[6]Re^{7+} (Fig. 1bm) forms a regular distribution of bond lengths when bonded to O^{2-}. We calculated *a priori* (observed) bond valences for two coordination polyhedra from as many crystal structures. In $Pr_3(Re^{7+}O_8)$ (92508),[178] they vary between 1.134-1.228 (1.019-1.467) v.u., with Δ_{topol} = 0.040 and Δ_{cryst} = 0.077 v.u. In $Y_3Re^{7+}O_8$ (15505),[151] they vary between 1.143-1.240 (0.928-1.320) v.u., with Δ_{topol} = 0.025 and Δ_{cryst} = 0.128 v.u. Thus the PJTE is the main cause of bond-length variation for this ion configuration.

[5]Os^{8+} (Fig. S1ec) occurs in two structures in our dataset. In $Rb(Os^{8+}{}_2O_8(OH))$ (20611),[179] the *a priori* (observed) bond valences are 1.235 (0.624), 2 × 1.647 (1.735 and 1.739) and 2 × 1.735 (1.693 and 2.140) v.u., with Δ_{topol} = 0.146 and Δ_{cryst} = 0.248 v.u. Thus the PJTE is the main cause of bond-length variation for this ion configuration.

[6]Os^{8+} (Fig. S1ed) forms a multi-modal distribution of bond lengths when bonded to O^{2-}. In $Li_2[Os^{8+}O_4(OH)_2]$ (20540),[180] the *a priori* (observed) bond valences are 2 × 1.033 (0.607), 2 × 1.383 (1.756) and 2 × 1.583 (1.743) v.u., with Δ_{topol} = 0.200 and Δ_{cryst} = 0.320 v.u. While the PJTE is the main driver of bond-length variation for this ion configuration, bond-topological asymmetry also contributes a significant amount.

Ion configurations primarily distorted via coupled electronic-vibrational near-degeneracy for non-d^0 transition metals

A variety of structural problems have been resolved via the pseudo Jahn-Teller effect for transition metals with non-d^0 electronic configurations, in various coordination numbers (e.g. refs [72,76,77] and references therein). In our dataset, there are three [5]-coordinated ion configurations with a peculiar distribution of bond lengths whose shape may not be explained via bond-topological nor classical Jahn-Teller arguments. While we observe the PJTE in a variety of ion configurations (e.g. in $^{[6]}Zn^{2+}$, $^{[6]}Hg^{2+}$, and others), listed below are the three non-d^0, non-octahedrally coordinated configurations of our dataset for which the PJTE is the main cause of bond-length variation.

$^{[5]}Cr^{2+}$ (Fig. S1r) occurs in two structures in our dataset. In $Cr^{2+}(HPO_3)(H_2O)_2$ (63466),[181] Cr^{2+} forms four bonds of 0.425-0.482 v.u., and one longer bond of 0.150 v.u. for a bond-valence sum of 2.001 v.u. In $SrCr^{2+}(P_2O_7)$ (280309),[182] the four strongest bonds of the $[Cr^{2+}O_5]^{8-}$ unit vary over a wider range; *a priori* (observed) bond valences are 0.349 (0.369), 0.412 (0.514) and 3 × 0.413 (0.180, 0.427 and 0.430) v.u., with Δ_{topol} = 0.020 and Δ_{cryst} = 0.077 v.u. The effect of the PJTE on bond-length variations seems to be weaker than in $Cr^{2+}(HPO_3)(H_2O)_2$, but is clearly present. The four shortest bonded distances for these two polyhedra range between 1.994-2.110 Å, and the fifth distance is between 2.361-2.426 Å. The sixth shortest interatomic distance is between 2.964-3.3.053 Å, far too long to be a bond.

$^{[5]}Co^{2+}$ (Fig. 1y) forms a unimodal distribution with anomalously long bond-lengths. There are five bonds making up the tail at longer bond lengths, representing the five (out of fifteen) polyhedra where $[Co^{2+}O_5]^{8-}$ units appear to distort as a result of the PJTE. In $BaCo^{2+}{}_2(Si_2O_7)$ (81473),[183] *a priori* (observed) bond valences are 0.362 (0.397), 2 × 0.379 (0.178 and 0.442), 0.432 (0.448) and 0.449 (0.483) v.u., with Δ_{topol} = 0.032 and Δ_{cryst} = 0.070 v.u., showing that the PJTE is the main driver of bond-length variation for this ion configuration. The four shortest bonds in these five polyhedra range between 1.946-2.045 Å, and the fifth distance is between 2.345-2.574 Å. The sixth shortest interatomic distance is between 2.898-3.444 Å, far too long to be considered as a bond.

$^{[5]}Cu^{2+}$ (Fig. 1ae) forms a unimodal distribution of bond lengths when bonded to O^{2-}, with an very long and flat tail at longer bond lengths. This ion configuration is very common (218 coordination polyhedra), making it an excellent candidate for probing the magnitude of the PJTE for [5]-coordinated cations. We calculated *a priori* (observed) bond valences for thirteen polyhedra from nine crystal structures. In $Cu^{2+}{}_4O(PO_4)_2$ (50459),[184] they are 0.445 (0.591), 3 × 0.335 (0.263 and 2 × 0.308) and 0.551 (0.658) v.u., with Δ_{topol} = 0.078 and Δ_{cryst} = 0.076 v.u. for *Cu*1 (distorted square pyramid), 0.293 (0.482), 2 × 0.391 (0.253), 0.408 (0.517) and 0.517 (0.427) v.u., with Δ_{topol} = 0.050 and Δ_{cryst} = 0.133 v.u. for *Cu*2 (trigonal bipyramid), and 0.295 (0.159), 0.384 (0.458), 0.393 (0.446), 0.409 (0.418) and 0.519 (0.564) v.u., with Δ_{topol} = 0.051 and Δ_{cryst} = 0.063 v.u. for *Cu*3 (square pyramid). In $Cu^{2+}{}_5O_2(PO_4)_2$ (1292),[185] they are 0.329 (0.101), 0.385 (0.486), 2 × 0.367 (0.445 and 0.458) and 0.551 (0.554) v.u., with Δ_{topol} = 0.060 and Δ_{cryst} = 0.100 v.u. for *Cu*2 (distorted square pyramid), and 2 × 0.277 (0.203 and 0.261), 0.444 (0.502) and 2 × 0.501 (0.486 and 0.505) v.u., with Δ_{topol} = 0.099 and Δ_{cryst} = 0.033 v.u. for *Cu*3 (distorted trigonal bipyramid). Although there is a weak correlation in which the weakest bond of the polyhedron becomes progressively stronger from square pyramidal to triangular bipyramidal configuration, there is no correlation between Δ_{topol} and Δ_{cryst} as a function of polyhedron shape. We obtain average values of Δ_{topol} and Δ_{cryst} of 0.061 and 0.084 v.u., with ranges of 0.016-0.099 and 0.033-0.133 v.u., respectively, for the thirteen polyhedra. Thus it seems that the long tail results from a mixture of continuous off-centering of Cu^{2+} via the PJTE, and non-local bond-topological asymmetry. One more structure worth discussing is that of $PbCu^{2+}(Cu^{2+}Te^{6+}O_7)$ (405329)[186] with a particularly long bond (2.687 Å). The *a priori* (observed) bond valences in this structure are 0.265 (0.060), 0.372 (0.342), 2 × 0.399 (0.498) and 0.565 (0.590) v.u., with Δ_{topol} = 0.066 and Δ_{cryst} = 0.091 v.u. Thus the weak bond in this structure results from a mixture of non-local bond-topological asymmetry (*a priori* bond valence 0.265 v.u. < 2/5 v.u.) and the PJTE.

[4] Ion configurations primarily distorted via crystal-structure effects

$^{[6]}Ru^{5+}$ (Fig. 1aw) occurs as monomers, chains of corner- and edge-sharing octahedra, and face-sharing oligomers. Face-sharing octahedra have O_{br} bond valences 3 × 0.53-0.78 v.u., with O_{br} bonding to other cations. Non-bridging bonds vary between 0.83-1.17 v.u. in these structures. For example, *a priori* (observed) bond valences are 3 × 0.786 (0.667) v.u. for bridging and 3 × 0.881 (1.075) v.u. for non-bridging bonds for Ru^{5+} in $Ba_3Ca(Ru^{5+}{}_2O_9)$ (73183),[187] with Δ_{topol} = 0.048 and Δ_{cryst} = 0.156 v.u. In $Ba_6Ru^{5+}{}_2Na_2Mn^{5+}{}_2O_{17}$ (97525),[188] *a priori* (observed) bond valences are 3 × 0.767 (0.633) and 3 × 0.900 (1.047) v.u., with Δ_{topol} = 0.067 and Δ_{cryst} = 0.140 v.u. The large values of Δ_{cryst} are unclear, but may be due to slight Ru^{5+}-Ru^{5+} interactions between the dimers (crystal-structure effects); Ru^{5+} is JT-inactive with a d^3 electronic configuration. Otherwise, monomers and chains of corner-sharing octahedra have regular polyhedra with mean bond-length 1.957 Å (5/6 v.u.).

General discussion

Bond-topological *vs* crystallographic effects

Of the 52 ion configurations of Table 4, 39 bond-length distributions may be considered to have a shape that deviates significantly from that expected for a two-body Morse potential. Non-local bond-topological effects are assigned as the main (minor) driving factor for 15 (19) of those 39 bond-length distributions, the strong JTE 3 (0), the weak JTE 0 (2), the PJTE 17 (9), π-bond formation 6 (1), and cryst al-structure effects 1 (2). Similarly, 39 of the 52 ion configurations may be considered to have an anomalously large range of observed bond lengths (Table 4). Of those configurations, non-local bond-topological effects are assigned as the main (minor) driving factor for 14 (23), the strong JTE 3 (1), the weak JTE 0 (2), the PJTE 23 (8), π-bond formation 6 (1), and crystal-structure effects 1 (1). Fig. 13 summarizes these numbers taking into consideration the overlapping nature of these datasets.

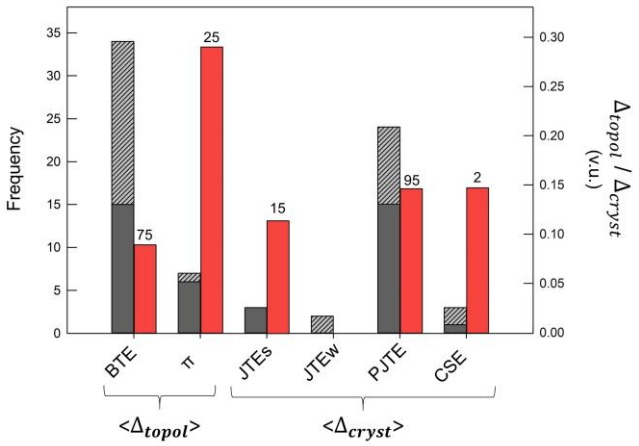

Figure 13: Frequency for which bond-topological effects (BTE), multiple-bond formation (π), the strong (JTEs) and weak (JTEw) Jahn-Teller effects, the pseudo Jahn-Teller effect (PJTE) and crystal-structure effects (CSE) are the main (dark grey) and minor (light grey) cause of bond-length variation underlying the ion configurations of Table 4. These data are necessarily biased toward anomalous bond-length distributions, whereas the BTE is ubiquitous across all ion configurations. Mean Δ_{topol} and Δ_{cryst} values (right axis) are calculated using those polyhedra for which the given effect is the main cause of bond-length variation; numbers atop represent sample size.

The distribution of observed Δ_{topol} and Δ_{cryst} values is given in Fig. 14 for the 266 coordination polyhedra for which *a priori* bond valences were calculated (Table S2); $<\Delta_{topol}>$ = 0.102 and $<\Delta_{cryst}>$ = 0.113 v.u. For the 235 coordination polyhedra with Δ_{topol} and/or Δ_{cryst} > 0.05 v.u., $<\Delta_{topol}>$ = 0.113 and $<\Delta_{cryst}>$ = 0.123 v.u. Next, we wish to calculate the average magnitude of these indices between the main two factors identified in transition- metal oxyanions: non-local bond-topological effects, and the PJTE. We remove the polyhedra of this dataset in which π-bonding is the main cause of bond-length variation, i.e. those for $^{[5]}V^{4+}$, $^{[6]}V^{4+}$, $^{[5]}V^{5+}$, $^{[6]}V^{5+}$, $^{[5]}Mo^{5+}$, $^{[6]}Mo^{5+}$ and $^{[5]}Mo^{6+}$, to get $<\Delta_{topol}>$ = 0.091 and $<\Delta_{cryst}>$ = 0.120 v.u. (these values are 0.291 and 0.155 v.u. for the 25 coordination polyhedra where π-bonding is the main factor). Similarly, if we remove those coordination polyhedra where the main factor underlying bond-length variation is the strong or weak JTE ($^{[6]}Cr^{2+}$, $^{[6]}Mn^{3+}$and $^{[6]}Cu^{2+}$), $<\Delta_{topol}>$ = 0.093 and $<\Delta_{cryst}>$ = 0.120 v.u. for the remaining 195 polyhedra (those values are 0.076 and 0.114 v.u. for 16 coordination polyhedra where the strong/weak JTE is the main cause of bond-length variation). From here, it is not possible to remove the component of Δ_{cryst} which is due to crystal-structure effects, as those effects are both widespread and structure dependent; while Δ_{cryst} may be interpreted as mainly driven by the PJTE in this subset, a non-negligible component is due to crystal-structure effects. Thus we are left comparing $<\Delta_{topol}>$ = 0.091 and $<\Delta_{cryst}>$ = 0.120 v.u. for 195 polyhedra. In terms of frequency, Δ_{topol} and Δ_{cryst} are > 0.05 v.u. for 141 and 171 polyhedra, respectively, while Δ_{topol} > Δ_{cryst} for 78 of those polyhedra; however, we emphasize that this subset of data is biased toward ion configurations with d^0 electronic configuration, for addressing other questions of this work. In terms of magnitude, eight of the fifteen widest ranges of observed bond lengths of Table 4 result primarily from the PJTE, while only one is due to non-local bond-topological effects; however, non-local bond-topological effects act as a minor contributor in every case.

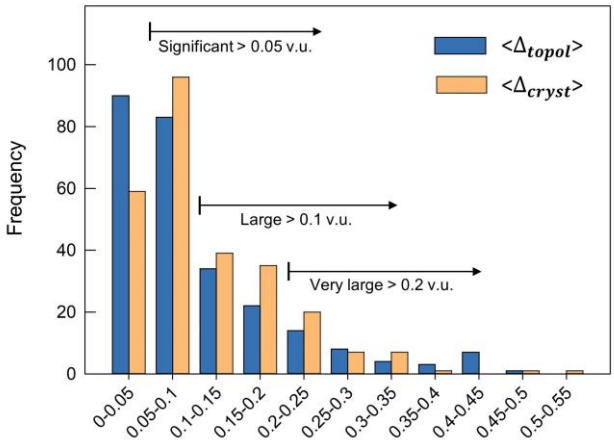

Figure 14: Distribution of observed Δ_{topol} and Δ_{cryst} values for the 266 transition-metal polyhedra of this work for which *a priori* bond-valences were calculated.

Thus we conclude the following: (1) non-local bond-topological asymmetry is the most frequently-encountered cause of bond-length variation in transition-metal oxides and oxysalts, closely followed by the PJTE; (2) bond-length variations resulting from the PJTE are slightly larger than those resulting from non-local bond-topological asymmetry, comparable to those resulting from the strong JTE, and less than those induced by π-bond formation. We further suggest non-local bond-topological asymmetry to be the most widespread cause of spontaneous distortion (and bond-length variation) in the solid state, with no *a priori* limitations with regard to ion identity.

Are bond-topological and crystallographic effects mutually supportive?

Kunz & Brown suggested that the structure of the bond network influences the occurrence and magnitude of the PJTE, whereby the PJTE either results from, or is affected by, the arrangement of *a priori* bond valences in crystal structures with d^0 transition metals.[39] In this work, we calculated *a priori* and observed bond valences for 15 coordination polyhedra in which the strong JTE is the leading cause of bond-length variation, and 132 coordination polyhedra where the leading cause is the PJTE. Where Jahn-Teller distortions are accommodated by the crystal structure, we expect a high value of Δ_{topol}, indicative of the polyhedron distorting away from a regular polyhedron toward a configuration compatible with the Jahn-Teller distortion, and low values of Δ_{cryst}, as the distortion caused by the JTE is captured by Δ_{topol}.

For the 15 coordination polyhedra where the strong JTE is the leading cause of polyhedral distortion, $<\Delta_{topol}>$ = 0.081 v.u. and $<\Delta_{cryst}>$ = 0.115 v.u., and Δ_{cryst} > Δ_{topol} for 10 polyhedra. For the 132 coordination polyhedra where the leading cause is the PJTE, $<\Delta_{topol}>$ = 0.129 v.u. and $<\Delta_{cryst}>$ = 0.145 v.u., and Δ_{cryst} > Δ_{topol} for 79 polyhedra. Thus, while many individual polyhedra support a mutually supportive relation between bond-topological requirements of the structure and the JTE, many more do not.

For the strong JTE, strong correlation is observed for $^{[6]}Cr^{2+}$ in $Cr^{2+}{}_3Cr^{3+}{}_4(PO_4)_6$ (73261),[93] with *a priori* (observed) bond valences 2 × 0.568 (0.484), 2 × 0.174 (0.199) and 2 × 0.259 (0.244) v.u. Thus this polyhedron strongly deviates from regularity (6 × 2/3 v.u.) in a way that accommodates the JT distortion; Δ_{topol} = 0.156 and Δ_{cryst} = 0.041 v.u. However, in $Gd(Mn^{3+}O_3)$ (95493),[74] *a priori* (observed) bond valences for Mn^{3+} are 4 × 0.471 (2 × 0.194 and 2 × 0.700) and 2 × 0.559 (0.612) v.u. for Mn^{3+}. Thus deviation from regularity (6 × 0.5 v.u.) is not captured by the bond topology; Δ_{topol} = 0.039 and Δ_{cryst} = 0.186 v.u. Another such example is that of $Cu^{2+}{}_2Co^{2+}O(B_2O_5)$ (400438),[104] with *a priori* (observed) bond valences of 3 × 0.304 (0.061, 0.436 and 0.469), 2 × 0.309 (0.099 and 0.453) and 0.470 (0.540) v.u. for $^{[6]}Cu^{2+}$, with Δ_{topol} = 0.046 and Δ_{cryst} = 0.161 v.u.

For the PJTE, we find few structures where bond-topological and crystallographic effects appear to work in cooperation. Nonetheless, the decavanadate clusters represents a very good example of apparent cooperation. In $KMg(V^{5+}{}_5O_{14})(H_2O)_8$ (95929),[128] $\Delta_{topol} > \Delta_{cryst}$ for the five crystallographically distinct $^{[6]}V^{5+}$ sites. The Jahn-Teller requirements are nearly perfectly matched for *V*3, with *a priori* (observed) bond valences 0.316 (0.329), 0.600 (0.608), 0.609 (0.573), 0.920 (0.891), 0.988 (0.986) and 1.568 (1.643) v.u., with Δ_{topol} = 0.325 and Δ_{cryst} = 0.027 v.u. We also showed the case for $CaNb^{5+}{}_2(P_4O_{13})(P_2O_7)O$ (62577)[52] earlier in text, where of the two crystallographically-distinct $^{[6]}Nb^{5+}$ sites, one site is significantly distorted as a result of bond-topological asymmetry, with Δ_{topol} = 0.227 and Δ_{cryst} = 0.098, while the other isn't (Δ_{topol} = 0.019 and Δ_{cryst} = 0.071). However, the number of cases in which the JT distortion functions independent of (or against) bond-topological requirements, is overwhelmingly large. In $(Ca_{0.81}Na_{0.19})ZrB(Al_{8.82}Ti^{4+}{}_{0.18}O_{18})$ (55272),[154] *a priori* (observed) bond valences are 6 × 0.667 (3 × 0.187 and 3 × 0.599) v.u., with Δ_{topol} = 0 and Δ_{cryst} = 0.274 v.u. In $K_2Mo^{6+}O_2(I^{5+}O_3)_4$ (170119),[161] *a priori* (observed) bond valences for $^{[6]}Mo^{6+}$ are 2 × 0.951 (1.740), 2 × 1.001 (0.384) and 2 × 1.048 (0.862) v.u., with Δ_{topol} = 0.033 and Δ_{cryst} = 0.531 v.u. In WO_3 (86144),[176] *a priori* (observed) bond valences 6 × 1 (0.443, 2 × 0.927, 2 × 1.174 and 1.865) v.u. for $^{[6]}W^{6+}$, with Δ_{topol} = 0 and Δ_{cryst} = 0.319 v.u.

From the comparison of *a priori* and observed bond valences for ~150 coordination polyhedra where either the strong JTE or pseudo JTE is the main reason underlying polyhedral distortion, we conclude that the Jahn-Teller effect does not have a cooperative relation with the bond-topological requirements of crystal structures.

PJTE: octahedrally coordinated d^0 transition metal complexes

Octahedrally coordinated ions with d^0 electronic configuration are often ranked as a function of their "distorting power" (the magnitude of their bond-length variation) on a qualitative scale, e.g., strong for Mo^{6+} and V^{5+}, moderate for W^{6+}, Ti^{4+}, Nb^{5+} and Ta^{5+}, and weak for Zr^{4+} and Hf^{4+}.[81] Our calculations allow a more quantitative ranking of distorting power via $<\Delta_{cryst}>$ values taken from the data for octahedrally coordinated d^0 ions in Table S2. Thus ordering $<\Delta_{cryst}>$ values in decreasing magnitude gives Os^{8+} (0.320, n = 1), Mo^{6+} (0.298, n = 10), W^{6+} (0.269, n = 5), V^{5+} (0.173, n = 11), Nb^{5+} (0.167, n = 15), Ti^{4+} (0.163, n = 6), Ta^{5+} (0.140, n = 6), Hf^{4+} (0.122, n = 3), Zr^{4+} (0.117, n = 5), Re^{7+} (0.103, n = 2), Y^{3+} (0.046, n = 1), and Sc^{3+} (0.029, n = 2). These $<\Delta_{cryst}>$ values are not set in stone; they may vary slightly as more *a priori* bond valences are calculated for these ion configurations.

Moreover, we find the magnitude of bond-length variations to vary as a function of coordination number for d^0 ions. For [4]-coordination, ($<\Delta_{cryst}>$, in v.u.), we have the following order: Re^{7+} 0.116 (n = 2), Ti^{4+} 0.107 (n = 1), V^{5+} 0.099 (n = 13), W^{6+} 0.098 (n = 2), Mo^{6+} 0.087 (n = 8), Cr^{6+} 0.085 (n = 8), Os^{8+} 0.077 (n = 1), and Mn^{7+} 0.028 (n = 1). For [5], we observe Os^{8+} 0.248 (n = 1), Re^{7+} 0.235 (n = 1), Mo^{6+} 0.197 (n = 3), Ti^{4+} 0.163 (n = 2), W^{6+} 0.127 (n = 2), V^{5+} 0.121 (n = 3), and Nb^{5+} 0.103 (n = 2).

PJTE: beyond octahedrally coordinated d^0 transition-metal complexes

The inseparability of electronic and nuclear coordinates in Jahn-Teller systems makes JT-active compounds unsuitable to density functional theory (DFT), whose foundation rests on the Born-Oppenheimer approximation.[16,189] We further showed that the neither the JTE nor the PJTE may be modeled bond-topologically. As a result of these difficulties, materials design for JT-active compounds is often relegated to heuristic methods. Thus we identify in our dataset the ion configurations for which the PJTE is observed to an appreciable extent in "non-traditional" configurations. These data shine light onto new potentially promising compositional spaces for materials discovery, notably for non-centrosymmetric structures.

Table S2 includes values of Δ_{topol} and Δ_{cryst} for 14 ions with d^0 electronic configuration with coordination numbers ranging from [4] to [10]. We summarize values of $<\Delta_{topol}>$, $<\Delta_{cryst}>$ and the maximum observed value of $<\Delta_{cryst}>$ for these ions in Table 9, together with four ion configurations with non-d^0 electronic configuration whose primary cause of bond-length variation is the PJTE.

For [6]-coordination, with n = 67 polyhedra, $<\Delta_{cryst}>$ = 0.181 v.u., with the highest Δ_{cryst} value of 0.531 v.u. in $K_2Mo^{6+}O_2(I^{5+}O_3)_4$ (170119).[161] The value of $<\Delta_{cryst}>$ is surprisingly close for [5]-coordination, 0.159 v.u., despite a much lower sample size (n = 14), followed by [7]-coordination with $<\Delta_{cryst}>$ = 0.115 v.u. (n = 6), [9]-coordination with $<\Delta_{cryst}>$ = 0.110 v.u. (n = 1), [4]-coordination with $<\Delta_{cryst}>$ = 0.092 v.u. (n = 36), [8]-coordination with $<\Delta_{cryst}>$ = 0.087 v.u. (n = 7), and [10]-coordination with $<\Delta_{cryst}>$ = 0.079 v.u. (n = 1). Considering that crystal structures containing octahedrally coordinated d^0 ions have been the subject of intense scrutiny and targeted syntheses (e.g. refs [161,190]), it seems that non-traditional coordinations of d^0 ion configurations are likely to have a similarly large potential for bond-length variation via the PJTE as that of octahedrally coordinated complexes.

Table 9: Mean values of Δ_{topol} and Δ_{cryst} for polyhedra distorted as a result of the pseudo JTE

	# CP	$<\Delta_{topol}>$	$<\Delta_{cryst}>$	Maximum Δ_{cryst}	Compound and reference
[4]	36 (8 ions)	0.11	0.092	0.217	$KCu^{2+}_5V^{5+}_3O_{13}$ (400802; Martin & Müller-Buschbaum 1994)
[5]	14 (7 ions)	0.173	0.159	0.256	$Cs(Mo^{6+}_2O_3(PO_4)_2)$ (79517; Hoareau et al. 1995)
[6]	67 (12 ions)	0.144	0.181	0.531	$K_2Mo^{6+}O_2(I^{5+}O_3)_4$ (170119; Ok & Halasyamani 2005)
[7]	6 (3 ions)	0.06	0.115	0.192	$La(Nb^{5+}_5O_{14})$ (33783; Hofmann & Gruehn 1990)
[8]	7 (4 ions)	0.06	0.087	0.131	$KY(W^{6+}O_4)$ (411285; Gallucci et al. 2000)
[9]	1	0.078	0.11	0.11	$Y_3Re^{7+}O_8$ (15505; Baud et al. 1981)
[10]	1	0.086	0.079	0.079	$YCo^{2+}(BO_2)_5$ (20670; Abdullaev et al. 1980)
$^{[5]}Cr^{2+}$	2	0.039	0.077	0.077	$SrCr^{2+}(P_2O_7)$ (280309; Maass & Glau 2000)
$^{[5]}Co^{2+}$	1	0.032	0.07	0.07	$BaCo^{2+}_2(Si_2O_7)$ (81473; Adams et al. 1996)
$^{[5]}Cu^{2+}$	13	0.061	0.084	0.133	$Cu^{2+}_4O(PO_4)_2$ (50459; Schwunck et al. 1998)
$^{[6]}Zn^{2+}$	5	0.056	0.050	0.129	$Mn^{2+}Zn_2Ta^{5+}_2O_8$ (85042; Rohweder & Müller-Buschbaum 1989)
$^{[6]}Hg^{2+}$	2	0.032	0.038	0.066	$Hg^{2+}(PO_3)_2$ (280292; Weil & Glaum 2004)

The PJTE is the main reason underlying bond-length variation for five non-d^0 ion configurations: $^{[5]}Cr^{2+}$ (d^4), $^{[5]}Co^{2+}$ (d^7), $^{[5]}Cu^{2+}$ (d^9), $^{[6]}Zn^{2+}$ and $^{[6]}Hg^{2+}$ (d^{10}). The PJTE for [5]-coordinated square-pyramidal complexes has been demonstrated for $^{[5]}Cu^{2+}$ and several ligands;[76,77] we observe the same behavior for [5]-coordinated complexes of what are otherwise octahedrally coordinated cations with electronic configurations prone to a strong JTE. The case for d^{10} transition-metal oxides is also interesting; the PJTE has been shown to be a significant cause of bond-length variation for Hg^{2+} in hexahydrate complexes,[110] with less unequivocal results for analogous Zn^{2+} (and Cd^{2+}) complexes. While the bond-length distributions of $^{[6]}Zn^{2+}$ and $^{[6]}Cd^{2+}$ are regular, the range of bond lengths for $^{[6]}Zn^{2+}$ is much larger than that for $^{[6]}Cd^{2+}$ (0.868 vs 0.591 Å), suggesting that the PJTE is stronger for Zn^{2+} than it is for Cd^{2+} when bonded to O^{2-}. However, both these ions (and other d^{10} transition metals) have been shown to exhibit the PJTE in S^{2-} structures of various d^{10} transition metal ions;[191,192] the extent to which the PJTE affects bond lengths for d^{10} transition-metal oxyanions awaits further work.

For the five ion configurations with non-d^0 electronic configuration whose main causal mechanism for bond-length variation is the PJTE, $<\Delta_{cryst}>$ values are 0.084 v.u. (n = 13) for $^{[5]}Cu^{2+}$, 0.077 v.u. for $^{[5]}Cr^{2+}$ (n = 2), 0.07 v.u. for $^{[5]}Co^{2+}$ (n = 1), 0.050 v.u. for $^{[6]}Zn^{2+}$ (n = 5), and 0.038 v.u. for $^{[6]}Hg^{2+}$ (n =2). Thus it seems that the distorting power of non-d^0 ion configurations is slightly less than that of their d^0 counterparts, although the sample size is far from significant.

Optimizing material properties linked to bond-length variation

Calculation of Δ_{topol} and Δ_{cryst} indices allows one to pinpoint the causal mechanism(s) underlying material properties linked to bond-length variations, and to determine *if*, and *how*, optimization of these properties may be done. Understanding the extent to which these mechanisms materialize into bond-length variations is further crucial to maximize the harnessing of these effects within the constraints of physically realistic crystal structures.

For instance, seeking to optimize functional properties associated with non-centrosymmetric behavior via compositional variations will have little effect if those properties are associated with coordination polyhedra where $\Delta_{topol} >> \Delta_{cryst}$, as said property would arise primarily from the bond-topological underpinnings of the crystal structure. Along those lines, optimization via compositional variation would have maximum potential where the coordination unit responsible for the functional property has $\Delta_{topol} = 0$. For example, Δ_{topol} = 0.000 and Δ_{cryst} = 0.017 v.u for the *B* site of *Pnma* perovskite $^{A}Ca^{B}Ti^{4+}O_3$ (74212).[193] Introducing compositional variation, Δ_{topol} = 0.039 and Δ_{cryst} = 0.186 v.u. for the *B* site of the *Pnma* perovskite $^{A}Gd^{3+B}Mn^{3+}O_3$ (95493),[74] leading to multiferroic behavior.[194]

Values given in this work may be used to set expectation limits regarding the maximum values of Δ_{cryst} attainable on the basis of ion configuration (Table S2) or coordination number (e.g. Table 9 for the PJTE), although we note that larger values of Δ_{topol} and Δ_{cryst} will likely be observed in the future; as such, Table S2 should be used as an evolving guide. In addition, minimum/maximum bond-lengths listed in Table 1 are useful for framing marginal compositional substitutions within the realm of physically realistic crystal structures; this dataset also has the advantage of being more exhaustive than our list of Δ_{topol} and Δ_{cryst} values (Table S2). Such compositional-variation analyses may be complemented by DFT calculations, where constrained to

values outlined in Tables 1 and S2. Getting back to $Gd^{3+}Mn^{3+}O_3$, with Δ_{cryst} = 0.186 v.u., consulting Table S2 informs us that little optimization of the functional properties resulting from Mn^{3+} seems possible; Table S2 lists three values of Δ_{cryst} in as many crystal structures, for $^{[6]}Mn^{3+}$: 0.186, 0.211 and 0.211 v.u. In this instance, increasing Δ_{cryst} would necessarily follow from substitution of $^{A}Gd^{3+}$, whereby a small amount of bond-length variation via mechanism [4] (crystal-structure effects) may trickle down to the Δ_{cryst} index of $^{B}Mn^{3+}$.

In the reverse scenario, where the functional property is linked to non-local bond-topological asymmetry (i.e. $\Delta_{topol} > \Delta_{cryst}$), optimization is complicated by the fact that spontaneous distortion of crystal structures via non-local bond-topological asymmetry is a static, emergent phenomenon which can only be predicted from *a priori* knowledge of ion connectivity. As a result, properties arising from non-local bond-topological asymmetry are less tunable, for they require subtle and less predictable changes in ion connectivity. These changes may occur either at the site of interest (e.g., substituting for a cation of significantly different size, which may change the coordination number of the site), or at other sites of the structure, where subtle changes in coordination numbers via homovalent and/or (multi-site) heterovalent substitution may have an effect on the *a priori* bond valences of the crystal structure which carries to the Δ_{topol} index of the (functional) site of interest. While these substitutions can be modeled with relative ease, a significant constraint is that such fine tuning must not result in the crystallization of a different structure type; as a result, optimization of functional properties linked to non-local bond-topological asymmetry is significantly more challenging than that for crystallographic effects.

We further point out that it is not infrequent for the mechanisms underlying the Δ_{topol} and Δ_{cryst} indices to work together toward the expression or suppression of a functional property, depending on their relative spatial expression within the polyhedron and unit cell. In such cases, calculation of Δ_{topol} and Δ_{cryst} values is useful for resolving the anomalous magnitude of functional properties. For example, for *P*31*m* $K_3V^{5+}{}_5O_{14}$ (248227),[195] *a priori* (observed bond valences are 1.430 (1.601) and 3 × 1.190 (1.169) v.u., Δ_{topol} = 0.090 and Δ_{cryst} = 0.059 v.u for *V*1, and 1.220 (1.647), 2 × 0.980 (0.938) and 2 × 0.910 (0.738) v.u., with Δ_{topol} = 0.088 and Δ_{cryst} = 0.171 v.u for *V*2. For *V*1, non-local bond-topological asymmetry is mainly responsible for variation away from a regular tetrahedron with four bonds of 1.25 v.u.; for *V*2, the PJTE is the principal reason for variation away from observing five bonds of 1 v.u. More importantly, both mechanisms cause variation in the same spatial direction within both their polyhedron and the unit cell; both strongest bonds (*V*1-*O*1 and *V*2-*O*2) point in the same direction, along the **c** axis. As a result, the effect of Δ_{topol} and Δ_{cryst} is entirely additive, and $K_3V^{5+}{}_5O_{14}$ is observed with a series of marked functional properties, i.e. second-harmonic generation, piezoelectricity, and polarization.[195]

Conclusion

In this work, we have resolved the causal mechanisms of bond-length variation for transition metals in oxide and oxysalt structures, and further quantified the extent to which these mechanisms result in bond-length variation for transition-metal configurations with anomalous bond-length distributions.

One of the principal findings presented in this work regards the unrealized extent for which crystal structures spontaneously distort as a result of non-local bond-topological asymmetry – a mechanism we show is entirely separate and independent of electronic and crystal-structure effects. The demonstrated ubiquity of this phenomenon, as well as the magnitude of the bond-valence variations it generates, challenge the common assumption of bond-length transferability in solids. This finding further conflicts with the widespread approximation of bond lengths via the addition of constituent ionic radii, and provides quantitative evidence of the "non-spherical" nature of coordination environments; while the addition of ionic radii certainly remains a useful approximation of bond lengths for yet-to-be-observed ion pairs, it has become evident that the practice should be avoided where comprehensive bond-length statistics are available (such as those given in this work, and throughout this series).

Perhaps one of the most promising opportunities resulting from this work regards the strategic use of the newly proposed Δ_{topol} and Δ_{cryst} indices for the optimization of functional properties tied to bond-length variations. Calculation of these indices allows identification of the causal mechanism(s) upon which optimization should be focused, while the magnitude of these values is used to qualitatively gauge the extent to which these values (typically Δ_{cryst}) may be maximized. Along those lines, examination of the relation between Δ_{topol} and Δ_{cryst} and the magnitude of various functional properties linked to bond-length variation, and the optimization of these properties, seems warranted.

ASSOCIATED CONTENT

Supporting Information

Bond-length, bond-valence, and mean-bond-length distributions for all ion configurations encountered in this work, and their polyhedral distortion scatter plots, and two tables giving the *a priori* bond valences and Δ_{topol} and Δ_{cryst} indices for crystal-structure refinements used in this work, and one table of all bond lengths used in this work.

AUTHOR INFORMATION

Corresponding Author

*Olivier C. Gagné. Email: ogagne@carnegiescience.edu
ORCID : 0000-0002-7902-8166

Author Contributions

All authors have given approval to the final version of the manuscript.

Funding Sources

This work was supported by a Banting post-doctoral fellowship and a PGS-D3 scholarship from the Natural Sciences and Engineering Research Council of Canada, and a Carnegie post-doctoral fellowship from the Carnegie Institution for Science to OCG. FCH was supported by a Discovery Grant and a Canada Research Chair in Crystallography and Mineralogy from the Natural Sciences and Engineering Research Council of Canada.

Notes

Relevant ICSD codes included in parentheses in text.

ABBREVIATIONS

JT, Jahn-Teller; JTE, Jahn-Teller effect; PJTE, Peudo Jahn-Teller effect;

REFERENCES

1. Fukuzumi, S. Fundamental Concepts of Catalysis in Electron Transfer. in *Electron Transfer in Chemistry* vol. 4 2–67 (John Wiley & Sons, Ltd, 2001).
2. Halcrow, M. A. Structure:Function Relationships in Molecular Spin-Crossover Materials. in *Spin-Crossover Materials* 147–169 (John Wiley & Sons, Ltd, 2013). doi:10.1002/9781118519301.ch5.
3. Guionneau, P. Crystallography and spin-crossover. A view of breathing materials. *Dalton Trans.* **43**, 382–393 (2014).
4. Senthil Kumar, K. & Ruben, M. Emerging trends in spin crossover (SCO) based functional materials and devices. *Coord. Chem. Rev.* **346**, 176–205 (2017).
5. Garcia-Fernandez, P. & Bersuker, I. B. Class of Molecular and Solid State Systems with Correlated Magnetic and Dielectric Bistabilities Induced by the Pseudo Jahn-Teller Effect. *Phys. Rev. Lett.* **106**, 246406 (2011).
6. Halasyamani, P. S. & Poeppelmeier, K. R. Noncentrosymmetric oxides. *Chem. Mater.* **10**, 2753–2769 (1998).
7. Wu, B.-L., Hu, C.-L., Mao, F.-F., Tang, R.-L. & Mao, J.-G. Highly Polarizable Hg^{2+} Induced a Strong Second Harmonic Generation Signal and Large Birefringence in $LiHgPO_4$. *J. Am. Chem. Soc.* **141**, 10188–10192 (2019).
8. Halasyamani, P. S. Asymmetric cation coordination in oxide materials: Influence of lone-pair cations on the intra-octahedral distortion in d^0 transition metals. *Chem. Mater.* **16**, 3586–3592 (2004).
9. Coey, J. M. D. d^0 ferromagnetism. *Solid State Sci.* **7**, 660–667 (2005).
10. Wang, L. H. *et al.* Piezoelectricity and local structural distortions in $(Na_{0.5}Bi_{0.5})_{1-x}Sr_xTiO_3$-$Bi_{12}TiO_{20}$ flexoelectric-type polar ceramics. *Appl. Phys. Lett.* **101**, 062903 (2012).
11. Marinkovic, B. A. *et al.* Correlation between AO_6 Polyhedral Distortion and Negative Thermal Expansion in Orthorhombic $Y_2Mo_3O_{12}$ and Related Materials. *Chem. Mater.* **21**, 2886–2894 (2009).
12. Yin, W.-J., Yang, J.-H., Kang, J., Yan, Y. & Wei, S.-H. Halide perovskite materials for solar cells: a theoretical review. *J. Mater. Chem. A* **3**, 8926–8942 (2015).
13. Chen, M., Xia, Z., Molokeev, M. S., Wang, T. & Liu, Q. Tuning of Photoluminescence and Local Structures of Substituted Cations in $xSr_2Ca(PO_4)_2$–$(1-x)Ca_{10}Li(PO_4)_7$:Eu^{2+} Phosphors. *Chem. Mater.* **29**, 1430–1438 (2017).
14. Kudo, A. & Hijii, S. H_2 or O_2 evolution from aqueous solutions on layered oxide photocatalysts consisting of Bi^{3+} with $6s^2$ configuration and d^0 transition metal ions. *Chem Lett* 1103–1104 (1999).
15. Lai, W., Wang, Y., Morelli, D. T. & Lu, X. From Bonding Asymmetry to Anharmonic Rattling in $Cu_{12}Sb_4S_{13}$ Tetrahedrites: When Lone-Pair Electrons Are Not So Lonely. *Adv. Funct. Mater.* **25**, 3648–3657 (2015).
16. Bersuker, I. B. The Jahn-Teller and pseudo Jahn-Teller effect in materials science. *J. Phys. Conf. Ser.* **833**, 012001 (2017).
17. Allen, F. H. *et al.* Tables of bond lengths determined by X-ray and neutron diffraction. Part 1. Bond lengths in organic compounds. *J. Chem. Soc. Perkin Trans. 2* S1 (1987).
18. Mayer, J. M. Metal-oxygen multiple bond lengths: a statistical study. *Inorg. Chem.* **27**, 3899–3903 (1988).
19. Orpen, A. G. *et al.* Supplement. Tables of bond lengths determined by X-ray and neutron diffraction. Part 2. Organometallic compounds and co-ordination complexes of the d- and f-block metals. *J. Chem. Soc. Dalton Trans.* S1 (1989).
20. Engh, R. A. & Huber, R. Accurate bond and angle parameters for X-ray protein structure refinement. *Acta Crystallogr. A* **47**, 392–400 (1991).
21. Laskowski, R. A., Moss, D. S. & Thornton, J. M. Main-chain bond lengths and bond angles in protein structures. *J. Mol. Biol.* **231**, 1049–1067 (1993).
22. Groom, C. R., Bruno, I. J., Lightfoot, M. P. & Ward, S. C. The Cambridge Structural Database. *Acta Crystallogr. Sect. B Struct. Sci. Cryst. Eng. Mater.* **72**, 171–179 (2016).
23. Allen, F. H. & Motherwell, W. D. S. Applications of the Cambridge Structural Database in organic chemistry and crystal chemistry. *Acta Crystallogr. B* **58**, 407–422 (2002).
24. Groom, C. R. & Allen, F. H. The Cambridge Structural Database in retrospect and prospect. *Angew. Chem. Int. Ed Engl.* **53**, 662–671 (2014).
25. Shannon, R. D. Revised effective ionic radii and systematic studies of interatomic distances in halides and chalcogenides. *Acta Crystallogr. Sect. A* **32**, 751–767 (1976).
26. Brown, I. D. & Altermatt, D. Bond-valence parameters obtained from a systematic analysis of the Inorganic Crystal Structure Database. *Acta Crystallogr. B* **41**, 244–247 (1985).
27. Waroquiers, D. *et al.* Statistical analysis of coordination environments in oxides. *Chem. Mater.* **29**, 8346–8360 (2017).
28. Gagné, O. C. On the crystal chemistry of inorganic nitrides: Crystal-chemical parameters and opportunities in the exploration of their compositional space. *ChemRxiv* 11626974 (2020).
29. Gagné, O. C. & Hawthorne, F. C. Bond-length distributions for ions bonded to oxygen: Alkali and alkaline-earth metals. *Acta Crystallogr. Sect. B Struct. Sci. Cryst. Eng. Mater.* **72**, 602–625 (2016).
30. Gagné, O. C. Bond-length distributions for ions bonded to oxygen: Results for the lanthanides and actinides and discussion of the *f*-block contraction. *Acta Crystallogr. Sect. B Struct. Sci. Cryst. Eng. Mater.* **74**, 49–62 (2018).
31. Gagné, O. C. & Hawthorne, F. C. Bond-length distributions for ions bonded to oxygen: Results for the non-metals and discussion of lone-pair stereoactivity and the polymerization of PO_4. *Acta Crystallogr. Sect. B Struct. Sci. Cryst. Eng. Mater.* **74**, 79–96 (2018).
32. Gagné, O. C. & Hawthorne, F. C. Bond-length distributions for ions bonded to oxygen: Metalloids and post-transition metals. *Acta Crystallogr. Sect. B Struct. Sci. Cryst. Eng. Mater.* **74**, 63–78 (2018).
33. Richardson, I. G. The importance of proper crystal-chemical and geometrical reasoning demonstrated using layered single and double hydroxides. *Acta Crystallogr. Sect. B* **69**, 150–162 (2013).
34. Gagné, O. C. & Hawthorne, F. C. Comprehensive derivation of bond-valence parameters for ion pairs involving oxygen. *Acta Crystallogr. Sect. B Struct. Sci. Cryst. Eng. Mater.* **71**, 562–578 (2015).
35. Gagné, O. C. & Hawthorne, F. C. Empirical Lewis acid strengths for 135 cations bonded to oxygen. *Acta Crystallogr. Sect. B Struct. Sci. Cryst. Eng. Mater.* **73**, 956–961 (2017).
36. Brown, I. D. & Shannon, R. D. Empirical bond-strength–bond-length curves for oxides. *Acta Crystallogr. A* **29**, 266–282 (1973).
37. Brown, I. D. Bond valences—a simple structural model for inorganic chemistry. *Chem. Soc. Rev.* **7**, 359–376 (1978).
38. Gagné, O. C. & Hawthorne, F. C. Mean bond-length variations in crystals for ions bonded to oxygen. *Acta Crystallogr. Sect. B Struct. Sci. Cryst. Eng. Mater.* **73**, 1019–1031 (2017).
39. Kunz, M. & Brown, I. D. Out-of-center distortions around octahedrally coordinated d^0 transition metals. *J. Solid State Chem.* **115**, 395–406 (1995).
40. Bosi, F. Mean bond-length variation in crystal structures: a bond-valence approach. *Acta Crystallogr. Sect. B Struct. Sci. Cryst. Eng. Mater.* **70**, 697–704 (2014).

41. Brown, I. D. *The Chemical Bond in Inorganic Chemistry: The Bond Valence Model*. (Oxford University Press, 2016).
42. Gagné, O. C., Mercier, P. H. J. & Hawthorne, F. C. *A priori* bond-valence and bond-length calculations in rock-forming minerals. *Acta Crystallogr. Sect. B Struct. Sci. Cryst. Eng. Mater.* **74**, 470–482 (2018).
43. Brown, I. D. Recent Developments in the Methods and Applications of the Bond Valence Model. *Chem. Rev.* **109**, 6858–6919 (2009).
44. Brese, N. E. & O'Keeffe, M. Bond-valence parameters for solids. *Acta Crystallogr. B* **47**, 192–197 (1991).
45. Ong, S. P. *et al.* PYthon MATerials GENomics (pymatgen): A robust, open-source python library for materials analysis. *Comput. Mater. Sci.* **68**, 314–319 (2013).
46. Jain, A. *et al.* Commentary: The Materials Project: A materials genome approach to accelerating materials innovation. *APL Mater.* **1**, 011002 (2013).
47. Shields, G. P., Raithby, P. R., Allen, F. H. & Motherwell, W. D. S. The assignment and validation of metal oxidation states in the Cambridge Structural Database. *Acta Crystallogr. B* **56**, 455–465 (2000).
48. Wood, R. M., Abboud, K. A., Palenik, R. C. & Palenik, G. J. Bond Valence Sums in Coordination Chemistry. Calculation of the Oxidation State of Chromium in Complexes Containing Only Cr−O Bonds and a Redetermination of the Crystal Structure of Potassium Tetra(peroxo)chromate(V). *Inorg. Chem.* **39**, 2065–2068 (2000).
49. Roulhac, P. L. & Palenik, G. J. Bond Valence Sums in Coordination Chemistry. The Calculation of the Oxidation State of Cerium in Complexes Containing Cerium Bonded Only to Oxygen. *Inorg. Chem.* **42**, 118–121 (2003).
50. Reeves, M. G., Wood, P. A. & Parsons, S. Automated oxidation-state assignment for metal sites in coordination complexes in the Cambridge Structural Database. *Acta Crystallogr. Sect. B Struct. Sci. Cryst. Eng. Mater.* **75**, 1096–1105 (2019).
51. Brown, I. D. Bond Valence Theory. in *Bond Valences* (eds. Brown, I. D. & Poeppelmeier, K. R.) 11–58 (Springer, 2014).
52. Averbuch-Pouchot, M.-T. Crystal Structure of a Tetrapoly-Dipolyphosphate: $CaNb_2O(P_4O_{13})(P_2O_7)$. *Z. Für Anorg. Allg. Chem.* **545**, 118–124 (1987).
53. Durif, A. & Averbuch-Pouchot, M. T. Structure du dichromate d'argent: $Ag_2Cr_2O_7$. *Acta Crystallogr. B* **34**, 3335–3337 (1978).
54. Ukei, K., Suzuki, H., Shishido, T. & Fukuda, T. Li_3NbO_4. *Acta Crystallogr. C* **50**, 655–656 (1994).
55. Wang, S. L., Wang, C. C. & Lii, K. H. Crystal structure of WPO_5, the second member of the monophosphate tungsten bronze series $(WO_3)_{2m}(PO_2)_4$. *J. Solid State Chem.* **82**, 298–302 (1989).
56. Nestola, F., Tribaudino, M., Ballaran, T. B., Liebske, C. & Bruno, M. The crystal structure of pyroxenes along the jadeite–hedenbergite and jadeite–aegirine joins. *Am. Mineral.* **92**, 1492–1501 (2007).
57. Bersuker, I. B. *Electronic Structure and Properties of Transition Metal Compounds: Introduction to the Theory*. (John Wiley & Sons, Inc., 2010).
58. Burdett, J. K. Use of the Jahn-Teller theorem in inorganic chemistry. *Inorg. Chem.* **20**, 1959–1962 (1981).
59. Burdett, J. K. From bonds to bands and molecules to solids. *Prog. Solid State Chem.* **15**, 173–255 (1984).
60. Roesky, H. W., Haiduc, I. & Hosmane, N. S. Organometallic Oxides of Main Group and Transition Elements Downsizing Inorganic Solids to Small Molecular Fragments. *Chem. Rev.* **103**, 2579–2596 (2003).
61. Pfennig, B. W. *Principles of inorganic chemistry*. (Wiley, 2015).
62. Schindler, M., Hawthorne, F. C. & Baur, W. H. Crystal chemical aspects of vanadium: Polyhedral geometries, characteristic bond valences, and polymerization of (VO_n) polyhedra. *Chem. Mater.* **12**, 1248–1259 (2000).
63. Lussier, A. J., Lopez, R. A. K. & Burns, P. C. A revised and expanded structure hierarchy of natural and synthetic hexavalent uranium compounds. *Can. Mineral.* **54**, 177–283 (2016).
64. Pauling, L. Atomic radii and interatomic distances in metals. *J. Am. Chem. Soc.* **69**, 542–553 (1947).
65. Walsh, A., Payne, D. J., Egdell, R. G. & Watson, G. W. Stereochemistry of post-transition metal oxides: revision of the classical lone pair model. *Chem. Soc. Rev.* **40**, 4455 (2011).
66. Bersuker, I. B. *The Jahn-Teller effect*. (Cambridge University Press, 2006).
67. Jahn, H. A., Teller, E. & Donnan, F. G. Stability of polyatomic molecules in degenerate electronic states - I—Orbital degeneracy. *Proc. R. Soc. Lond. Ser. - Math. Phys. Sci.* **161**, 220–235 (1937).
68. Öpik, U. & Pryce, M. H. L. Studies of the Jahn-Teller effect. I. A survey of the static problem. *Proc. R. Soc. Lond. Ser. Math. Phys. Sci.* **238**, 425–447 (1957).
69. Longuet-Higgins, H. C. & Salem, L. The alternation of bond lengths in long conjugated chain molecules. *Proc. R. Soc. Lond. Ser. Math. Phys. Sci.* **251**, 172–185 (1959).
70. Bader, R. F. W. An interpretation of potential interaction constants in terms of low-lying excited states. *Mol. Phys.* **3**, 137–151 (1960).
71. Pearson, R. G. Symmetry rule for predicting molecular structures. *J. Am. Chem. Soc.* **91**, 4947–4955 (1969).
72. Bersuker, I. B. Pseudo-Jahn–Teller effect—A two-state paradigm in formation, deformation, and transformation of molecular systems and solids. *Chem. Rev.* **113**, 1351–1390 (2013).
73. Bersuker, I. B. Spontaneous Symmetry Breaking in Matter Induced by Degeneracies and Pseudodegeneracies. in *Advances in Chemical Physics* 159–208 (John Wiley & Sons, Ltd, 2016).
74. Mori, T., Kamegashira, N., Aoki, K., Shishido, T. & Fukuda, T. Crystal growth and crystal structures of the $LnMnO_3$ perovskites: Ln = Nd, Sm, Eu and Gd. *Mater. Lett.* **54**, 238–243 (2002).
75. Hoareau, T., Leclaire, A., Borel, M. M., Grandin, A. & Raveau, B. A Mixed Valent Molybdenum Monophosphate with a Layer Structure: $CsMo_2O_3(PO_4)_2$. *J. Solid State Chem.* **116**, 87–91 (1995).
76. Reinen, D. & Atanasov, M. Symmetry and vibronic coupling: The stereochemistry and the ground state potential surface of Cu^{2+} in five-coordination. *Chem. Phys.* **155**, 157–171 (1991).
77. Reinen, D. & Friebel, C. Copper(2+) in 5-coordination: a case of a second-order Jahn-Teller effect. 2. Pentachlorocuprate(3-) and other CuIIL5 complexes: trigonal bipyramid or square pyramid? *Inorg. Chem.* **23**, 791–798 (1984).
78. Szymanski, N. J., Walters, L. N., Puggioni, D. & Rondinelli, J. M. Design of Heteroanionic MoON Exhibiting a Peierls Metal-Insulator Transition. *Phys. Rev. Lett.* **123**, (2019).
79. Yang, R. *et al.* Synaptic plasticity and memory functions achieved in a WO_{3-x}-based nanoionics device by using the principle of atomic switch operation. *Nanotechnology* **24**, 384003 (2013).
80. Kakekhani, A. & Ismail-Beigi, S. Ferroelectric-Based Catalysis: Switchable Surface Chemistry. *ACS Catal.* **5**, 4537–4545 (2015).
81. Ok, K. M. *et al.* Distortions in Octahedrally Coordinated d^0 Transition Metal Oxides: A Continuous Symmetry Measures Approach. *Chem. Mater.* **18**, 3176–3183 (2006).
82. Welk, M. E., Norquist, A. J., Arnold, F. P., Stern, C. L. & Poeppelmeier, K. R. Out-of-Center Distortions in d^0 Transition Metal Oxide Fluoride Anions. *Inorg. Chem.* **41**, 5119–5125 (2002).
83. Salinas-Sanchez, A., Garcia-Muñoz, J. L., Rodriguez-Carvajal, J., Saez-Puche, R. & Martinez, J. L. Structural characterization of R_2BaCuO_5 (R = Y, Lu, Yb, Tm, Er, Ho, Dy, Gd, Eu and Sm) oxides by X-ray and neutron diffraction. *J. Solid State Chem.* **100**, 201–211 (1992).
84. Preiser, C., Lösel, J., Brown, I. D., Kunz, M. & Skowron, A. Long-range Coulomb forces and localized bonds. *Acta Crystallogr. B* **55**, 698–711 (1999).
85. Collin, G., Comes, R., Boilot, J. P. & Colomban, Ph. Disorder of tetrahedra in Nasicon-type structure—I.: $Na_3Sc_2(PO_4)_3$: Structures and ion-ion correlations. *J. Phys. Chem. Solids* **47**, 843–854 (1986).

86. Hawthorne, F. C. & Grundy, H. D. Refinement of the crystal structure of $LiScSi_2O_6$ and structural variations in alkali pyroxenes. *Can. Mineral.* **15**, 50–58 (1977).

87. Satto, C., Millet, P. & Galy, J. Lithium Vanadium Metasilicate, $LiVSi_2O_6$. *Acta Crystallogr. C* **53**, 1727–1728 (1997).

88. Boudin, S., Grandin, A., Labbé, Ph., Provost, J. & Raveau, B. The V(III) Monophosphate Series $AV_2O(PO_4)_2$ with A= Cd, Ca, Sr: Structure and Magnetism. *J. Solid State Chem.* **127**, 325–330 (1996).

89. Martin, F.-D. & Müller-Buschbaum, Hk. Ein Beitrag zur Kristallchemie der Alkali-Erdalkalimetall-Oxovanadate: Synthese und Struktur von $K_3CaV_5O_{15}$. *Z. Für Naturforschung B* **50**, 243–246 (1995).

90. Martin, F.-D. & Müller-Buschbaum, Hk. Em neues Alkalimetall-Kupfer-Oxovanadat: $KCu_5V_3O_{13}$. *Z. Für Naturforschung B* **49**, 1137–1140 (1994).

91. Krivovichev, S. V., Filatov, S. K., Cherepansky, P. N., Armbruster, T. & Pankratova, O. Yu. Crystal structure of γ-$Cu_2V_2O_7$ and its comparison to blossite (α-$Cu_2V_2O_7$) and ziesite (β-$Cu_2V_2O_7$). *Can. Mineral.* **43**, 671–677 (2005).

92. Lenaz, D., Skogby, H., Princivalle, F. & Hålenius, U. Structural changes and valence states in the $MgCr_2O_4$–$FeCr_2O_4$ solid solution series. *Phys. Chem. Miner.* **31**, 633–642 (2004).

93. Glaum, R. Beiträge zum thermischen Verhalten wasserfreier Phosphate VIII.* Darstellung und Kristallstruktur von $Cr_7(PO_4)_6$. Das erste gemischtvalente Phosphat mit Cr(II) und Cr(III). *Z. Für Krist. - Cryst. Mater.* **205**, 69–83 (1993).

94. Riou, A., Gerault, Y. & Cudennec, Y. Determination structurale du chromate de thallium trivalent $Tl_2(CrO_4)_3$. *Rev Chim Min.* **23**, 70–79 (1986).

95. Gravereau, P., Hardy, A. & Bonnin, A. La série M'Fe$(CrO_4)_2$: structure cristalline de la variété α du chromate double de fer et d'ammonium $NH_4Fe(CrO_4)_2$. *Acta Crystallogr. B* **33**, 1362–1367 (1977).

96. Ito, S., Kurosawa, H., Akashi, K., Michiue, Y. & Watanabe, M. Crystal structure and electric conductivity of K^+-β-ferrite with ideal composition $KFe_{11}O_{17}$. *Solid State Ion.* **86–88**, 745–750 (1996).

97. Hidouri, M., Lajmi, B. & Ben Amara, M. The iron phosphate $NaZnFe_2(PO_4)_3$. *Acta Crystallogr. C* **58**, i147–i148 (2002).

98. Rulíšek, L. & Vondrášek, J. Coordination geometries of selected transition metal ions (Co^{2+}, Ni^{2+}, Cu^{2+}, Zn^{2+}, Cd^{2+}, and Hg^{2+}) in metalloproteins. *J. Inorg. Biochem.* **71**, 115–127 (1998).

99. Yilmaz, A., Bu, X., Kizilyalli, M., Kniep, R. & Stucky, G. D. Cobalt Borate Phosphate, $Co_3[BPO_7]$, Synthesis and Characterization. *J. Solid State Chem.* **156**, 281–285 (2001).

100. Osterloh, D. & Müller-Buschbaum, Hk. Zur Kenntnis von $SrCo_2V_2O8$ und $SrCo_2(AsO_4)_2$. *Z. Für Naturforschung B* **49**, 923–926 (2014).

101. Sasaki, S. & Takéuchi, Y. Electron-density distributions of three orthopyroxenes, $Mg_2Si_2O_6$, $Co_2Si_2O_6$, and $Fe_2Si_2O_6$. *Z. Für Krist. - Cryst. Mater.* **158**, 279–298 (2015).

102. Abdullaev, G. K., Mamedov, Kh. S., Dzhafarov, G. G. & Aliev, O. A. Synthesis and study of the crystal structure of the double metaborate of yttrium and cobalt $YCo(BO_2)_5$. *Zh Neorg Khim* **25**, 364–367 (1980).

103. Glaum, R. & Schmidt, A. Cobalt Silicon Diphosphate, $Co_2Si(P_2O_7)_2$. *Acta Crystallogr. C* **52**, 762–764 (1996).

104. Schaefer, J. & Bluhm, K. Ein neues Kupfercobaltboratoxid mit isolierten B_2O_5-Baugruppen: $Cu_2Co(B_2O_5)O$. *Z. Für Anorg. Allg. Chem.* **620**, 1051–1055 (1994).

105. Rohweder, U. & Müller-Buschbaum, H. Ein Beitrag zur Kristallchemie der Oxotantalate. V. Geordnete und ungeordnete Metallverteilung in $MnZn_2Ta_2O_8$ und $Mn_{0,33}Zn_{0,67}Ta_2O_6$. *Z. Für Anorg. Allg. Chem.* **572**, 102–108 (1989).

106. Harrison, W. T. A. An extreme case of ZnO_6 octahedral distortion in trizinc tris(selenite) hydrate, $Zn_3(SeO_3)_3$. *Acta Crystallogr. C* **55**, 1980–1983 (1999).

107. Leclaire, A., Chardon, J. & Raveau, B. A new lead Mo(IV) phosphate with a tunnel structure: $Pb_2Mo_2O(PO_4)_2P_2O_7$. *J. Solid State Chem.* **172**, 412–416 (2003).

108. Serezhkin, V. N., Efremov, V. A. & Trunov, V. K. The crystal structure of α-$Zr(MoO_4)_2$ the high temperature modification of zirconium molybdate. *Zh Neorg Khim* **32**, 2695–2699 (1987).

109. Burckhardt, H.-G., Platte, C. & Trömel, M. Cadmiumorthotellurat(VI) Cd_3TeO_6: ein pseudoorthorhombischer Kryolith im Vergleich mit Ca_3TeO_6. *Acta Crystallogr. B* **38**, 2450–2452 (1982).

110. Strömberg, D., Sandström, M. & Wahlgren, U. Theoretical calculations on the structure of the hexahydrated divalent zinc, cadmium and mercury ions. *Chem. Phys. Lett.* **172**, 49–54 (1990).

111. Louër, D., Labarre, J., Auffredic, J.-P. & Louër, M. Etude structurale des hydroxysulfates de cadmium. IV. Structure cristalline de $Cd_8(OH)_{12}(SO_4)_2{\cdot}H_2O$. *Acta Crystallogr. B* **38**, 1079–1084 (1982).

112. Murashova, E. V., Velikodnyi, Y. A. & Trunov, V. K. The crystal structures of the double pyrophosphates BaM'P_2O_7 (M' = Zn, Cd). *Zhurnal Neorganicheskoi Khimii* **36**, 479–481 (1991).

113. Bastide, B., Enjalbert, R., Fuess, H. & Galy, J. $VO(ReO_4)_2$: solid state and structural chemistry. *Solid State Sci.* **2**, 545–552 (2000).

114. Levason, W., Oldroyd, R. D. & Webster, M. Extended X-ray absorption fine structure studies of transition-metal periodate and tellurate complexes. Crystal structure of $Rb_2Na_4[OsO_2(H_2TeO_6)_2]{\cdot}16H_2O$. *J. Chem. Soc. Dalton Trans.* 2983–2988 (1994) doi:10.1039/DT9940002983.

115. Johansson, G. *et al.* The Crystal Structure of Hexaaquamercury(II) Perchlorate, $[Hg(H_2O)_6](ClO_4)_2$. *Acta Chem. Scand.* **32a**, 109–113 (1978).

116. Weil, M. & Glaum, R. Mercury(II) polyphosphate, $Hg(PO_3)_2$. *Acta Crystallogr. C* **56**, 133–135 (2000).

117. de Roy, M. E., Besse, J. P., Chevalier, R. & Gasperin, M. Synthèse et structure cristalline de NaV_6O_{11}. *J. Solid State Chem.* **67**, 185–189 (1987).

118. Johnson, J. W. *et al.* Structure and magnetic properties of $V_2(VO)(P_2O_7)_2$. A mixed-valence vanadium(III,III,IV) pyrophosphate. *Inorg. Chem.* **27**, 1646–1648 (1988).

119. Shpanchenko, R. V., Kaul, E. E., Geibel, C. & Antipov, E. V. The new lead vanadylphosphate $Pb_2VO(PO_4)_2$. *Acta Crystallogr. C* **62**, i88–i90 (2006).

120. Leonowicz, M. E., Johnson, J. W., Brody, J. F., Shannon, H. F. & Newsam, J. M. Vanadyl hydrogenphosphate hydrates: $VO(HPO_4){\cdot}\ 4H_2O$ and $VO(HPO_4){\cdot}0.5H_2O$. *J. Solid State Chem.* **56**, 370–378 (1985).

121. Lii, K. H., Chueh, B. R., Kang, H. Y. & Wang, S. L. Synthesis and crystal structure of $Ca(VO)_2(PO_4)_2$. *J. Solid State Chem.* **99**, 72–77 (1992).

122. Range, K.-J., Rau, F. & Klement, U. Hochdrucksynthese und Strukturverfeinerung von $SrVO_3$, Sr_2VO_4 und $Sr_3V_2O_7$. *Z. Für Naturforschung B* **46**, 1315–1318 (1991).

123. Martin, F.-D. & Müller-Buschbaum, Hk. Zur Kenntnis von $K_4CuV_5O_{15}Cl$. *Z. Für Naturforschung B* **49**, 1459–1462 (1994).

124. Galy, J., Enjalbert, R., Rozier, P. & Millet, P. The mixed oxide $MoVAlO_7$. *Acta Crystallogr. C* **58**, i6–i8 (2002).

125. Oka, Y., Yao, T. & Yamamoto, N. Hydrothermal synthesis and structure refinements of alkali-metal trivanadates AV_3O_8 (A = K, Rb, Cs). *Mater. Res. Bull.* **32**, 1201–1209 (1997).

126. Millet, P., Galy, J. & Johnsson, M. Crystal growth and structure of $V_2^{V}Se_2^{IV}O_9$; comparison with $V_2Te_2O_9$. *Solid State Sci.* **1**, 279–286 (1999).

127. Mormann, Th. J. & Jeitschko, W. Redetermination of the crystal structure of high-temperature modification of the mercury(II) hexaoxodivanadate(V), ß-HgV_2O_6. *Z. Für Krist. - New Cryst. Struct.* **216**, 3–4 (2001).

128. Hughes, J., Schindler, M., Rakovan, J. & Cureton, F. The crystal structure of hummerite, $KMg(V_5O_{14}){\cdot}8H_2O$: Bonding between the $[V_{10}O_{28}]^{6-}$ structural unit and the $\{K_2Mg_2(H_2O)_{16}\}^{6+}$ interstitial complex. *Can. Mineral.* **40**, 1429–1435 (2002).

129. Leclaire, A., Caignaert, V. & Raveau, B. A large series of isotypic Mo(V) diphosphates with a tunnel structure: From $A(MoO)_{10}(P_2O_7)_8$ with A = Ba, Sr, Ca, Cd, Pb to $A(MoO)_5(P_2O_7)_4$ with A = Ag, Li, Na, K. *J. Solid State Chem.* **180**, 2044–2052 (2007).

130. Costentin, G., Borel, M. M., Grandin, A., Leclaire, A. & Raveau, B. A molybdenum V diphosphate, $BaMo_2P_4O_{16}$. *J. Solid State Chem.* **89**, 83–87 (1990).

131. Barrier, N. & Gougeon, P. Pr_3MoO_7. *Acta Crystallogr. Sect. E Struct. Rep. Online* **59**, 22–24 (2003).

132. Enjalbert, R., Guinneton, F. & Galy, J. $Cs_2Mo_3O_{10}$. *Acta Crystallogr. C* **55**, 273–276 (1999).

133. Grigor'ev, M. S., Baturin, N. A., Plotnikova, T. E., Fedoseev, A. M. & Budantseva, N. A. Crystal structure of neptunium(V) complex molybdate $Cs_2(NpO_2)_2Mo_2O_8$. *Radiokhimiya* **2**, 322 (1991).

134. Glaum, R. Beiträge zum thermischen Verhalten wasserfreier Phosphate. IX. Darstellung und Kristallstruktur von $Cr_6(P_2O_7)_4$. Ein gemischtvalentes Pyrophosphat mit zwei- und dreiwertigem Chrom. *Z. Für Anorg. Allg. Chem.* **616**, 46–52 (1992).

135. Giester, G. Crystal structure of $KMn^{3+}[SeO_4]_2$ — a triclinic distorted member of the Yavapaiite family. *Mineral. Petrol.* **53**, 165–171 (1995).

136. Yakubovich, O. V., Simonov, M. A. & Belov, N. V. Structure refinement for Gaudefroyite. *Kristallografiya* **20**, 152–155 (1975).

137. Arlt, T., Armbruster, T., Miletich, R., Ulmer, P. & Peters, T. High pressure single-crystal synthesis, structure and compressibility of the garnet $Mn^{2+}{}_3Mn^{3+}{}_2[SiO_4]_3$. *Phys. Chem. Miner.* **26**, 100–106 (1998).

138. Zhesheng, M., Ruilin, H. & Xiaoling, Z. Redetermination of the Crystal Structure of Vesignieite. *Acta Geol. Sin. - Engl. Ed.* **4**, 145–151 (1991).

139. Køuhl, P. Die Kristallstruktur der Hexagonalen Verbindungen $Ba_3Me^{II}Sb_2O_9$. II. $Ba_3CuSb_2O_9$. *Z. Für Anorg. Allg. Chem.* **442**, 280–288 (1978).

140. Weiß, C. & Hoppe, R. Was heißt eigentlich Festkörper??. Neue molekulare Aspekte am Beispiel $Rb_2[TiO_3]$ [1], [2]. *Z. Für Anorg. Allg. Chem.* **622**, 1019–1026 (1996).

141. Protas, J., Menaert, B., Marnier, G. & Boulanger, B. Structure cristalline de $Cs_2TiO(P_2O_7)$. *Acta Crystallogr. C* **47**, 698–701 (1991).

142. Hübner, N., Schaffrath, U. & Gruehn, R. Darstellung und Struktur von $Ln_3TiO_4Cl_5$(Ln = La – Nd) - die ersten Oxochlorotitanate der Seltenen Erden. *Z. Für Anorg. Allg. Chem.* **591**, 107–117 (1990).

143. Womersley, M. N., Thomas, P. A. & Corker, D. L. Investigation of the $Cs_xRb_{1-x}TiOAsO_4$ Series. I. Crystal Structure Analysis and Pseudo-symmetry. *Acta Crystallogr. B* **54**, 635–644 (1998).

144. Hübner, N. & Gruehn, R. $SmTiO_3Cl$: Präparation und Struktur—das erste Oxochlorotitanat der „mittleren" Seltenen Erden. *Z. Für Anorg. Allg. Chem.* **602**, 119–128 (1991).

145. Benbertal, D., Mosset, A. & Trombe, J. C. Synthese et structure cristalline d'un nouveau silicate de lanthane et de titane. *Mater. Res. Bull.* **29**, 47–54 (1994).

146. Li, P.-J., Huang, S.-H., Huang, K.-Y., Ru-Ji, W. & Mak, T. C. W. Crystal structure of tetraguanidinium tri(carbonato)oxotitanium(IV) dihydrate, $[C(NH_2)_3]_4[TiO(CO_3)_3]\cdot 2H_2O$. *Inorganica Chim. Acta* **175**, 105–110 (1990).

147. Dudka, A. P., Kaminskii, A. A. & Simonov, V. I. Refinement of $NaGdGeO_4$, $NaYGeO_4$, and $NaLuGeO_4$ Single-Crystal Structures. *Phys. Status Solidi A* **93**, 495–502 (1986).

148. Swinnea, J. S. & Steinfink, H. The structure of $Y_2Ba_2CuPtO_8$. *Acta Crystallogr. C* **43**, 2436–2437 (1987).

149. Calestani, G., Rizzoli, C. & Andreetti, G. D. Synthesis and crystal structure of $Y_2Ba_3Cu_2PtO_{10}$. *Solid State Commun.* **66**, 223–226 (1988).

150. Demartin, F., Gramaccioli, C. M. & Pilati, T. Structure of a new natural tungstate arsenate, $[Ca_2Y(AsO_4)(WO_4)_2]$, structurally related to scheelite. *Acta Crystallogr. C* **48**, 1357–1359 (1992).

151. Baud, G., Besse, J.-P., Chevalier, R. & Gasperin, M. Les differentes formes cristallines de Y_3ReO_8: Relations avec la structure fluorine. *J. Solid State Chem.* **38**, 186–191 (1981).

152. Gallucci, E., Goutaudier, C., Boulon, G., Cohen-Adad, M. Th. & Mentzen, B. F. Nonstoichiometric $KY(WO_4)_2$: crystal growth, chemical and physical characterization. *J. Cryst. Growth* **209**, 895–905 (2000).

153. Tran Qui, D., Capponi, J. J., Joubert, J. C. & Shannon, R. D. Crystal structure and ionic conductivity in $Na_4Zr_2Si_3O_{12}$. *J. Solid State Chem.* **39**, 219–229 (1981).

154. Armbruster, T. *et al.* The crystal structure of painite CaZrB[Al_9O_{18}] revisited. *Am. Mineral.* **89**, 610–613 (2004).

155. Mellini, M. & Merlino, S. Refinement of the crystal structure of wöhlerite. *Mineral. Petrol.* **26**, 109–123 (1979).

156. Gasperin, M. Structure du niobate de césium $Cs_2Nb_4O_{11}$. *Acta Crystallogr. B* **37**, 641–643 (1981).

157. Darriet, J., Maazaz, A., Bouloux, J. C. & Delmas, C. Les Phases Na_5NbO_5 et Na_5TaO_5 Structure Cristalline de Na_5NbO_5. *Z. Für Anorg. Allg. Chem.* **485**, 115–121 (1982).

158. Liao, J.-H. & Tsai, M.-C. Synthesis and Crystal Growth of Two Novel Layered Structures, $NaKLaNbO_5$ and $Na_2K_2Gd_4Nb_2O_{13}$, in Molten Hydroxide Salts. *Cryst. Growth Des.* **2**, 83–85 (2002).

159. Hofmann, R. & Gruehn, R. Zur Darstellung und Struktur von $LaNb_5O_{14}$. *Z. Für Anorg. Allg. Chem.* **590**, 81–92 (1990).

160. Surblé, S. *et al.* The $A_{1-x}UNbO_{6-x/2}$ compounds (x = 0, A = Li, Na, K, Cs and x = 0.5, A = Rb, Cs): from layered to tunneled structure. *J. Solid State Chem.* **179**, 3238–3251 (2006).

161. Ok, K. M. & Halasyamani, P. S. New d^0 Transition Metal Iodates: Synthesis, Structure, and Characterization of $BaTi(O_3)_6$, $LaTiO(IO_3)_5$, $Ba_2VO_2(IO_3)_4\cdot(IO_3)$, $K_2MoO_2(IO_3)_4$, and $BaMoO_2(IO_3)_4\cdot H_2O$. *Inorg. Chem.* **44**, 2263–2271 (2005).

162. Chi, E. O., Ok, K. M., Porter, Y. & Halasyamani, P. S. $Na_2Te_3Mo_3O_{16}$: A New Molybdenum Tellurite with Second-Harmonic Generating and Pyroelectric Properties. *Chem. Mater.* **18**, 2070–2074 (2006).

163. Porter, Y. & Halasyamani, P. S. New alkali–metal–molybdenum(VI)–selenium(IV) oxides: syntheses, structures, and characterization of A_2SeMoO_6 (A =Na+, K+, or Rb+). *J. Solid State Chem.* **174**, 441–449 (2003).

164. Efremov, V. A., Davydova, N. N. & Trunov, V. K. Crystal structure of praseodymium molybdate $Pr_2Mo_4O_{15}$. *Zh Neorg Khim* **33**, 3001–3004.

165. Ra, H.-S., Ok, K. M. & Halasyamani, P. S. Combining Second-Order Jahn–Teller Distorted Cations to Create Highly Efficient SHG Materials: Synthesis, Characterization, and NLO Properties of $BaTeM_2O_9$ (M = Mo^{6+} or W^{6+}). *J. Am. Chem. Soc.* **125**, 7764–7765 (2003).

166. Zaitsev, S. M. *et al.* Refinement of the structure of $PbHfO_3$. *Kristallografiya* **24**, 826–828 (1979).

167. Bluhm, K. & Müller-Buschbaum, H. $Ni_5HfB_2O_{10}$ mit geordneter Metallverteilung. *Z. Für Anorg. Allg. Chem.* **575**, 26–30 (1989).

168. Yamane, H., Takahashi, H., Kajiwara, T. & Shimada, M. $Na_2Ca_3Ta_2O_9$ with a simple stacking of oxygen triangular nets. *Acta Crystallogr. C* **55**, 1978–1980 (1999).

169. Akella, A. & Keszler, D. A. Crystal Chemistry of Noncentrosymmetric Alkali-Metal Nb and Ta Oxide Pyroborates. *J. Solid State Chem.* **120**, 74–79 (1995).

170. Hartenbach, I. *et al.* Über Oxotantalate der Lanthanide des Formeltyps $MTaO_4$ (M = La – Nd, Sm – Lu). *Z. Für Anorg. Allg. Chem.* **631**, 2377–2382 (2005).

171. Guo, G.-C. *et al.* Dysprosium Tantalum Oxide, $DyTa_7O_{19}$. *Acta Crystallogr. C* **52**, 5–7 (1996).

172. Hoffmann, R. & Hoppe, R. Ein Oxowolframat mit „Kanalstruktur": KNa_3WO_5 (Mit einer Bemerkung über den Aufbau von Na_4WO_5). *Z. Für Anorg. Allg. Chem.* **573**, 143–156 (1989).

173. Gärtner, M., Abeln, D., Pring, A., Wilde, M. & Reller, A. Synthesis, Structure, and Reactivity of Novel Lanthanum Tungstates. *J. Solid State Chem.* **111**, 128–133 (1994).

174. Peuchert, U., Bohatý, L. & Fröhlich, R. $K_2NiWO_2(PO_4)_2$: a New Structure Type Related to $KTiOPO_4$ (KTP). *Acta Crystallogr. C* **51**, 1719–1721 (1995).

175. Boehlke, A. & Müller-Buschbaum, Hk. Ein beitrag zur kristallstruktur von $CuLaW_2O_8$ und $CuSmW_2O_8$. *J. Common Met.* **162**, 141–147 (1990).

176. Aird, A., Domeneghetti, M. C., Mazzi, F., Tazzoli, V. & Salje, E. K. H. Sheet superconductivity in WO_{3-x}: crystal structure of the tetragonal matrix. *J. Phys. Condens. Matter* **10**, 569–574 (1998).

177. Baud, G., Besse, J.-P., Sueur, G. & Chevalier, R. Structure de nouvelles apatites au rhenium contenant des anions volumineux: $Ba_{10}(ReO_5)_6X_2$ (X = Br, I). *Mater. Res. Bull.* **14**, 675–682 (1979).

178. Jeitschko, W., Heumannskämper, D. H., Rodewald, U. C. & Schriewer-Pöttgen, M. S. Preparation and Crystal Structure of Rare Earth Rhenates: the Series $Ln_5Re_2O_{12}$ with Ln = Y, Gd–Lu, and the Praseodymium Rhenates Pr_3ReO_8, $Pr_3Re_2O_{10}$, and $Pr_4Re_2O_{11}$. *Z. Für Anorg. Allg. Chem.* **626**, 80–88 (2000).

179. Nevskii, N. N. & Porai Koshits, M. A. The crystal structure of rubidium oxohydroxoosmate (8) $Rb(Os_2O_8(OH))$. *Dokl Akad Nauk SSSR* **270**, 1392–1395 (1983).

180. Nevskii, N. N., Ivanov-Emin, B. N., Nevskaya, N. A. & Belov, N. V. The crystal structure of a new lithium hydroxoosmate $Li_2(OsO_4(OH)_2)$. *Dokl Akad Nauk SSSR* **266**, 628–630 (1982).

181. Brynda, J., Kratochvíl, B. & Císařová, I. The determination of crystal structure of chromium(II) phosphite dihydrate, $CrHPO_3$ 2 H_2O. *Collect. Czechoslov. Chem. Commun.* **52**, 1742–1747 (1987).

182. Maaß, K. & Glaum, R. Strontium chromium(II) diphosphate, $SrCrP_2O_7$. *Acta Crystallogr. C* **56**, 404–406 (2000).

183. Adams, R. D., Payen, C. & Datta, T. Syntheses, Structural Analyses, and Unusual Magnetic Properties of $Ba_2CoSi_2O_7$ and $BaCo_2Si_2O_7$. *Inorg. Chem.* **35**, 3492–3497 (1996).

184. Schwunck, H.-M., Moser, P. & Jung, W. Das Kupfer(II)-oxidphosphat $Cu_4O(PO_4)_2$ in einer neuen, orthorhombischen Modifikation durch Oxidation einer Tl/Cu/P-Legierung. *Z. Für Anorg. Allg. Chem.* **624**, 1262–1266 (1998).

185. Brunel-Laügt, M. & Guitel, J.-C. Structure cristalline de $Cu_5O_2(PO_4)_2$. *Acta Crystallogr. B* **33**, 3465–3468 (1977).

186. Wedel, B. & Müller-Buschbaum, Hk. Über ein Blei-Kupfer-Tellurat $PbCu_3TeO_7$ mit Cu^{2+} in deformiert tetragonal pyramidaler und tetraedrischer Sauerstoffkoordination. *Z. Für Naturforschung B* **51**, 1587–1590 (2014).

187. Wilkens, J. & Müller-Buschbaum, H. Über Neue Oxoruthenate vom Typ der 6 L-Perowskite: $Ba_3SrRu_{2-x}Ta_xO_9$ (x = 0,8 und 1,4) mit einem Beitrag über $Ba_3CaRu_2O_9$. *Z. Für Anorg. Allg. Chem.* **619**, 517–520 (1993).

188. Quarez, E., Abraham, F. & Mentré, O. Synthesis, crystal structure and characterization of new 12H hexagonal perovskite-related oxides $Ba_6M_2Na_2X_2O_{17}$ (M = Ru, Nb, Ta, Sb; X = V, Cr, Mn, P, As). *J. Solid State Chem.* **176**, 137–150 (2003).

189. Bersuker, I. B. Limitations of density functional theory in application to degenerate states. *J. Comput. Chem.* **18**, 260–267 (1997).

190. Ok, K. M. & Halasyamani, P. S. New Metal Iodates: Syntheses, Structures, and Characterizations of Noncentrosymmetric $La(IO_3)_3$ and $NaYI_4O_{12}$ and Centrosymmetric β-$Cs_2I_4O_{11}$ and $Rb_2I_6O_{15}$ $(OH)_2{\cdot}H_2O$. *Inorg. Chem.* **44**, 9353–9359 (2005).

191. Boucher, F., Evain, M. & Brec, R. Second-order Jahn—Teller effect in $CdPS_3$ and $ZnPS_3$ demonstrated by a non-harmonic behaviour of Cd^{2+} and Zn^{2+} d^{10} ions. *J. Alloys Compd.* **215**, 63–70 (1994).

192. Fan, Y.-H. *et al.* Phase Transition and Second Harmonic Generation in Thiophosphates $Ag_2Cd(P_2S_6)$ and $AgCd_3(PS_4)S_2$ Containing Two Second-Order Jahn–Teller Distorted Cations. *Inorg. Chem.* **56**, 114–124 (2017).

193. Liu, X. & Liebermann, R. C. X-ray powder diffraction study of $CaTiO_3$ perovskite at high temperatures. *Phys. Chem. Miner.* **20**, 171–175 (1993).

194. Li, X. *et al.* Novel multiferroicity in $GdMnO_3$ thin films with self-assembled nano-twinned domains. *Sci. Rep.* **4**, 1–6 (2014).

195. Yeon, J., Kim, S.-H. & Halasyamani, P. S. $A_3V_5O_{14}$ (A = K^+, Rb^+, or Tl^+), New Polar Oxides with a Tetragonal Tungsten Bronze Related Structural Topology: Synthesis, Structure, and Functional Properties. *Inorg. Chem.* **49**, 6986–6993 (2010).

Table of contents graphic

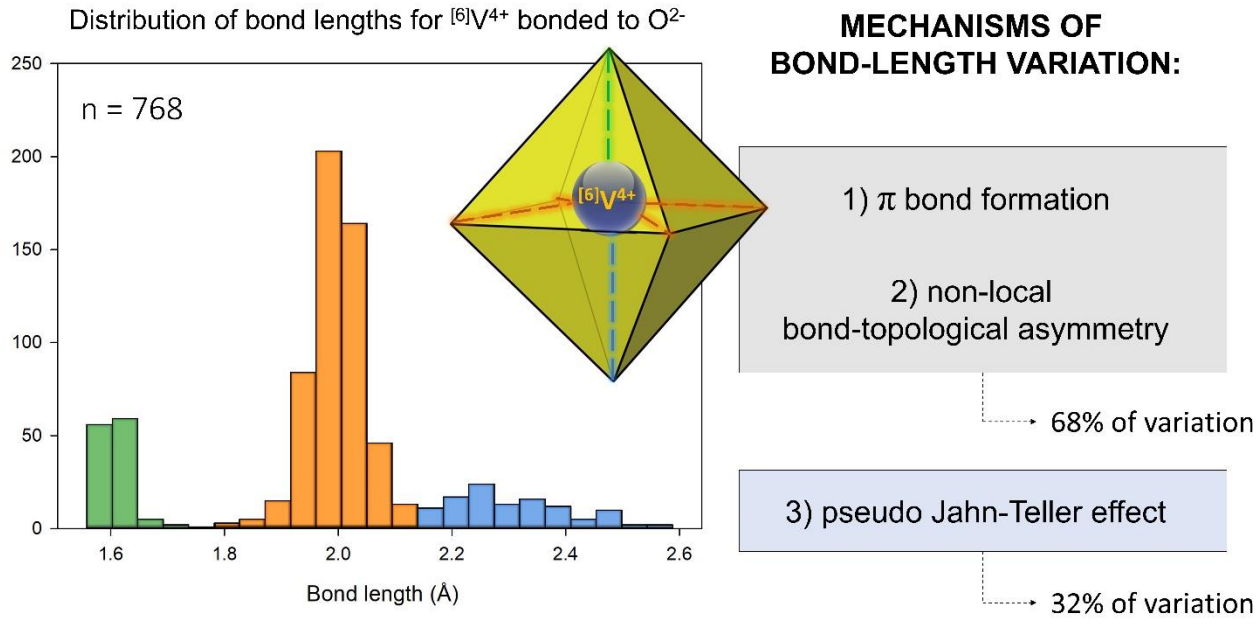

Transition metals for ACS_OCG-FCH.pdf (3.84 MiB) view on ChemRxiv • download file